Exploring van der Waals Materials

From Nanofabrication to Strain Mapping using Transmission Electron Microscopy

Bolhuis, M.

DOI
10.4233/uuid:35d1c57b-8f79-4e37-85e4-65bf95f471c4

Publication date
2025

Document Version
Final published version

Citation (APA)
Bolhuis, M. (2025). *Exploring van der Waals Materials: From Nanofabrication to Strain Mapping using Transmission Electron Microscopy*. [Dissertation (TU Delft), Delft University of Technology]. https://doi.org/10.4233/uuid:35d1c57b-8f79-4e37-85e4-65bf95f471c4

Important note
To cite this publication, please use the final published version (if applicable).
Please check the document version above.

Exploring Van der Waals Materials

From Nanofabrication to Strain Mapping
using Transmission Electron Microscopy

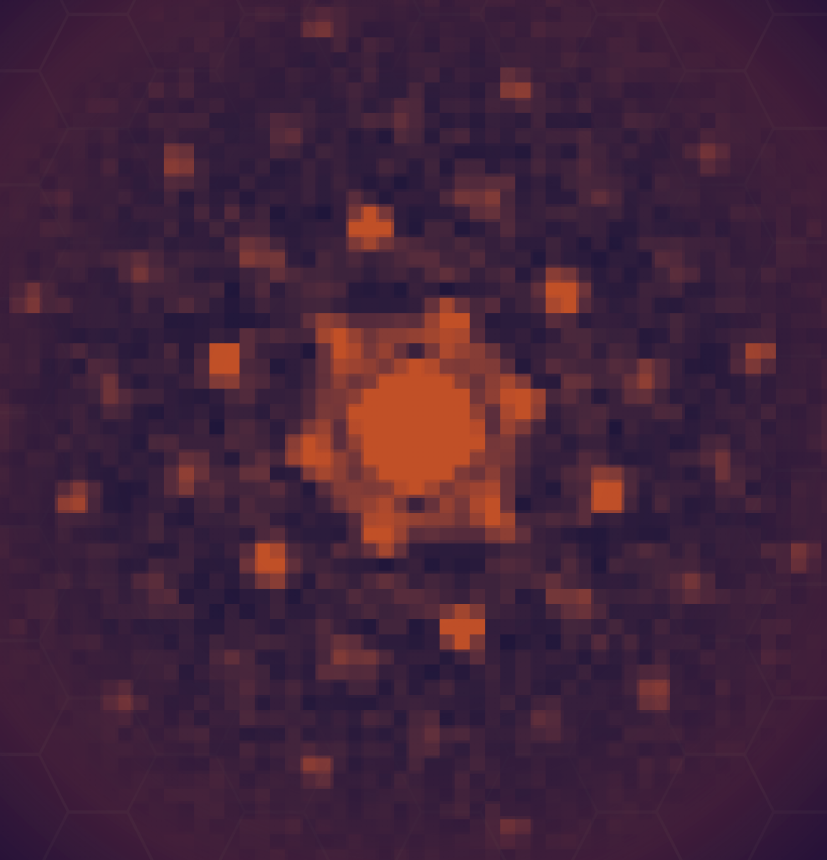

Maarten Bolhuis

Exploring Van der Waals Materials:
From Nanofabrication to Strain Mapping using Transmission Electron Microscopy

EXPLORING VAN DER WAALS MATERIALS:
FROM NANOFABRICATION TO STRAIN MAPPING USING TRANSMISSION ELECTRON MICROSCOPY

Proefschrift

ter verkrijging van de graad van doctor

aan de Technische Universiteit Delft,

op gezag van de Rector Magnificus Prof.dr.ir T. H. J. J. van der Hagen,

voorzitter van het College voor Promoties,

in het openbaar te verdedigen op

vrijdag 21 maart 2025 om 12:30 uur

door

Maarten BOLHUIS

Master of Science in Applied Physics,
Technische Universiteit Delft, Nederland

geboren te Utrecht, Nederland.

Dit proefschrift is goedgekeurd door de

promotor: dr. S. C. Conesa-Boj
promotor: prof. dr. L. Kuipers

Samenstelling promotiecommissie:

Rector Magnificus,	Voorzitter
Dr. S. C. Conesa-Boj,	Technische Universiteit Delft, promotor
Prof. dr. L. Kuiper,	Technische Universiteit Delft, promotor
Onafhankelijke leden:	
Prof. dr. P.G. Steeneken,	Technische Universiteit Delft
Prof. dr. Y.M. Blanter,	Technische Universiteit Delft
Dr. A. Castellanos-Gómez,	The Material Science Institute of Madrid
Dr. M. Tinoco Rivas,	Universidad Complutense de Madrid
Dr. A.A.F.M. Artaud,	Technische Universiteit Delft

Keywords: Transition Metal Dichalcogenides Nanostructures, Vertically oriented MoS_2, Transmission Electron Microscopy, 4D-STEM, Center-Of-Mass, Strain, Exit-Waver Power Cepstrum
Printed by: Proefschriftspecialist - The Netherlands

ISBN 978-94-6384-762-9

An electronic version of this dissertation is available at
http://repository.tudelft.nl/.

CONTENTS

SUMMARY

One of the driving forces behind advancements in modern nanotechnology is the quest to decrease the size of optical and electronic devices. In this quest, the remarkable optoelectronic properties of transition metal dichalcogenides (TMDs) materials, such as molybdenum disulfide (MoS_2), offer a suitable platform to realize the next generation of electronic and photonic nanodevices. The optoelectronic properties of these materials depend sensitively on the local (atomic-level) crystal structure and, therefore, will generally be modulated at the nanoscale.

Illustrating these powerful functionalities, the ability of MoS_2 to change and adapt its electronic band structure by modifying the underlying crystal arrangement makes it an ideal candidate for a wide range of applications. The natural bandgap of bulk MoS_2 indicates that this layered material is highly suitable for two-dimensional (2D) electronic devices. Moreover, when MoS_2 is reduced to a single atomic layer, the material transitions from an indirect to a direct bandgap semiconductor, highlighting its relevance to nanophotonic devices. It is thus clear that precisely controlling the crystal growth and, thereby, adjusting the intrinsic bandgap of TMD materials enables novel platforms for tunable 2D nanoelectronics and nanophotonics.

To fully exploit these materials' unique properties, it is crucial to control their synthesis and fabricate TMD-based nanomaterials in a variety of configurations and morphologies. While significant strides have been made in synthesizing horizontally-aligned MoS_2 nanosheets, less emphasis has been devoted to the controlled synthesis of vertically-aligned MoS_2. Vertically-aligned MoS_2 nanosheets are of direct interest for non-linear optical applications due to their increased density of inversion symmetry-breaking edge terminations. In chapter 3, we carry out a systematic assessment determining the diffusion confinement and the activation energy needed for the diffusion-limited sulfurization of predeposited molybdenum (Mo) thin films. The sulfurization of the Mo thin films leads to the formation of vertically-aligned MoS_2 nanosheets that exhibit an increased non-linear optical response when compared to a reference of horizontally-aligned MoS_2 nanosheets. When combined with advanced nanofabrication techniques, this strategy also enables the fabrication of Mo/MoS_2 core-shell nanopillars that induce an enhanced non-linear optical response highly localized at the wafer scale.

Characterizing the properties of TMD materials, such as MoS_2, at the nanoscale is vital for understanding the intricate interplay between the underlying crystal structure and the resulting electronic and optical properties. Here, advanced transmission electron microscopy (TEM) techniques, like electron energy loss spectroscopy (EELS) and four-dimensional scanning TEM (4D–STEM), are ideally suited to explore the local properties of these 2D nanostructures with atomic precision. In chapter 5, we describe the development of an advanced 4D–STEM framework (`StrainMAPPER`) to map strain across

entire micrometer-sized structures with atomic resolution. In chapter 6, we utilize `Strain MAPPER` to map the strain in a MoS_2 monolayer with limited diffraction contrast, a Moire MoS_2 bilayer, and in a heterostructure composed by molybdenum oxide and MoS_2. When combined with spatially-resolved EELS measurements, the flexibility of the `StrainMAPPER` method provides an excellent tool to investigate the subtle relation between the bandgap energy modulation in MoS_2 as a function of the local strain fields.

In chapter 7, we use 4D–STEM to measure shifts in the center-of-mass (CoM) of convergent beam electron diffraction (CBED) patterns. While often assumed to be related to local electric fields, we show that a shift in the CoM of CBED patterns can be induced by many different interactions with the specimen. For instance, we show that a defocused probe can induce a CoM shift at the edge of a single layer of MoS_2. Finally, we show that the CoM is influenced by slight misalignments of the crystal structure. This way, we demonstrate that one can leverage the shift of the CoM to accurately identify and locate crystal domains and grain boundaries in TMD nanomaterials.

In summary, the work presented in this thesis represents an important step towards a deeper understanding of the unique properties of MoS_2 and of related TMD materials. In particular, the availability of TMD nanomaterials in non-standard configurations provides both a challenge and an opportunity for advanced TEM characterization techniques, pushing the state-of-the-art toward an extensive spatially resolved characterization of their structural and optoelectronic functionalities. Indeed, the methodological advancements obtained in this thesis facilitate further research into the remarkable interplay between local crystal deformations and the resultant optoelectronic properties of MoS_2 and related materials.

SAMENVATTING

Een van de drijvende krachten achter de vooruitgang in de moderne nanotechnologie is de zoektocht naar het verkleinen van de omvang van optische en elektronische apparaten. In deze zoektocht bieden de opmerkelijke opto-elektronische eigenschappen van transitiemetaaldichalcogeniden (TMDs), zoals molybdeendisulfide (MoS_2), een geschikt platform om de volgende generatie elektronische en fotonische nanodevices te realiseren. De opto-elektronische eigenschappen van deze materialen zijn afhankelijk van de lokale (atomaire) kristalstructuur en zullen daarom over het algemeen op nanoschaal worden gemoduleerd.

Ter illustratie: Een van deze opmerkelijke functionaliteiten is dat de elektronische bandstructuur van MoS_2 veranderd door de wijzigingen in de onderliggende kristalsamenstelling. Dit maakt MoS_2 een ideale kandidaat voor een breed scala aan toepassingen. De natuurlijke bandgap van bulk MoS_2 maakt dat dit gelaagde materiaal zeer geschikt is voor tweedimensionale (2 D) elektronische apparaten. Bovendien, wanneer MoS_2 wordt gereduceerd tot een enkele atomaire laag, gaat het materiaal over van een indirecte naar een directe bandgap-halfgeleider, wat de relevantie van MoS_2 voor nanofotonische apparaten benadrukt. Het is dus duidelijk dat het nauwkeurig controleren van de kristalgroei en daarmee het aanpassen van de intrinsieke bandgap van TMD-materialen nieuwe platformen mogelijk maakt voor afstembare 2D-nano-elektronica en nanofotonica.

Om de unieke eigenschappen van deze materialen volledig te benutten, is het cruciaal om hun synthese te controleren en TMD-gebaseerde nanomaterialen te fabriceren in verschillende configuraties en morfologieën. Hoewel er aanzienlijke stappen zijn gezet in het synthetiseren van horizontaal uitgelijnde MoS_2-nanosheets, is er minder nadruk gelegd op de gecontroleerde synthese van verticaal uitgelijnd MoS_2. Verticaal uitgelijnde MoS_2 nanosheets zijn van direct belang voor niet-lineaire optische toepassingen vanwege hun verhoogde dichtheid van inversie symmetriebrekende kristalranden. In hoofdstuk 3 voeren we een systematische studie uit waarbij we de diffusie en de activeringsenergie bepalen die nodig is voor de diffusiegelimiteerde verzwaveling van vooraf gedeponeerde molybdeen (Mo) dunne films . De verzwaveling van de Mo dunne films leidt tot de vorming van verticaal uitgelijnde MoS_2 nanosheets die een verhoogde niet-lineaire optische respons vertonen in vergelijking met een referentie van horizontaal uitgelijnde MoS_2 nanosheets. In combinatie met geavanceerde nanofabricatietechnieken maakt deze strategie ook de fabricage mogelijk van Mo/MoS_2 core-shell nanopilaren die een verbeterde niet-lineaire optische respons induceren die zeer gelokaliseerd is op de waferschaal.

Het karakteriseren van de eigenschappen van TMD-materialen, zoals MoS_2, op nanoschaal is van vitaal belang voor het begrijpen van de ingewikkelde wisselwerking tussen

de onderliggende kristalstructuur en de resulterende elektronische en optische eigenschappen. Hiervoor zijn geavanceerde transmissie-elektronenmicroscopie (TEM) technieken, zoals elektronenenergieverliesspectroscopie (EELS) en vierdimensionale scanning TEM (4D–STEM), bij uitstek geschikt om de lokale eigenschappen van deze 2D-nanostructuren met atomaire precisie te onderzoeken. In hoofdstuk 5 beschrijven we de ontwikkeling van een geavanceerd 4D–STEM-framework (`StrainMAPPER`) om de rek in hele structuren van micrometerformaat met atomaire resolutie in kaart te brengen. In hoofdstuk 6 gebruiken we `StrainMAPPER` om de rek in kaart te brengen in een MoS_2 monolaag met beperkt diffractiecontrast, een Moire MoS_2 dubbellaag, en in een heterostructuur samengesteld uit molybdeenoxide en MoS_2. In combinatie met ruimtelijk-resolutie EELS-metingen biedt de flexibiliteit van de `StrainMAPPER`-methode een uitstekend hulpmiddel om de modulatie van de bandgap-energie in MoS2 als functie van de lokale vervormingsvelden te onderzoeken.

In hoofdstuk 7 gebruiken we 4D–STEM om verschuivingen in het massamiddelpunt (CoM) van convergente elektronendiffractie patronen (CBED) te meten. Hoewel vaak wordt aangenomen dat dit verband houdt met lokale elektrische velden, laten we zien dat een verschuiving in de CoM van CBED-patronen kan worden veroorzaakt door veel verschillende interacties met het preparaat. We laten bijvoorbeeld zien dat een onscherpe elektronen bundel een CoM-verschuiving kan veroorzaken aan de rand van een enkele laag MoS_2. Tot slot laten we zien dat de CoM wordt beïnvloed door kleine afwijkingen van de kristalstructuur. Op deze manier demonstreren we dat de verschuiving van de CoM gebruikt kan worden om de kristaldomeinen in TMD-nanomaterialen nauwkeurig in kaart te brengen.

Samenvattend vertegenwoordigt het werk dat in dit proefschrift wordt gepresenteerd een belangrijke stap in de richting van een dieper begrip van de unieke eigenschappen van MoS_2 en verwante TMD-materialen. In het bijzonder biedt de beschikbaarheid van TMD-nanomaterialen in niet-standaard configuraties zowel een uitdaging als een kans voor geavanceerde TEM-karakteriseringstechnieken, waardoor de state-of-the-art methodes wordt voortgestuwd in de richting van een zeer uitgebreide karakterisering van TMD structuren. De methodologische vooruitgang die in dit proefschrift is geboekt, maakt verder onderzoek naar de opmerkelijke wisselwerking tussen lokale kristaldeformaties en de resulterende opto-elektronische eigenschappen van MoS_2 en verwante materialen mogelijk.

1

INTRODUCTION

1

The development of semiconductor transistors has been one of the main drivers of technological processes in modern society, from computing to communications and imaging. Indeed, the advances in the performance of modern electronic devices would have been impossible without the steady decrease of the transistor size, enhancing computational capacity and energy efficiency [1, 2]. This miniaturization has followed industry trends but is now constrained by the physical limitations of silicon, the primary material used in transistor fabrication [3, 4]. Consequently, there is a pressing need for alternative materials, going beyond silicon-based transistors [5, 6], to enable further improvements in the performance of electronic devices.

With this motivation, the discovery and subsequent isolation of two-dimensional (2D) materials, starting with graphene in 2004 [7], has represented a paradigm shift in material science. Graphene, characterized by being fully functional down to a single atomic layer and by its unprecedented electrical and thermal properties [8–10], showcases the potential of 2D materials for a wide variety of applications. However, its lack of a bandgap limits its direct use in semiconductor devices, motivating the search for alternative 2D materials with suitable electronic properties to eventually provide a reliable alternative for silicon [11, 12].

In this quest, transition metal dichalcogenides (TMDs) have emerged as a family of 2D materials that promise to overcome graphene's limitations. Among the [A-Z]2,materials studied to date, molybdenum disulfide (MoS_2) is particularly attractive for its inherent and tunable bandgap, making it suitable for electronic switching applications [13–15]. The characteristic layered structure of TMDs, in which a transition metal layer is sandwiched between chalcogen atoms, enables the isolation of monolayers only three atoms thick. This specific atomic structure enables unique edge terminations that influence the electronic properties of the layered material. This structural diversity allows TMDs to display versatile electronic behaviors, bridging the gap between metallic and semiconducting regimes [16–18].

In applications related to nanophotonics and optoelectronics, material configurations with a high density of exposed edges exhibit enhanced functionalities, and in particular, these edges play a crucial role in tuning light-matter interactions [19], catalytic activity [20], and electronic properties [21]. In TMDs such as MoS_2, the type and arrangement of edge atoms can significantly influence the material's physical and chemical properties, offering diverse functionalities not present in their basal planes.

Among the most common edge types, zigzag and armchair edges enable different material properties. The zigzag edges lead to localized magnetic states and, in some cases, metallic behavior, enhancing performance in electronic and catalytic applications. In contrast, armchair edges generally exhibit semiconducting behavior, crucial for tuning electronic and optical responses.

Beyond their electronic and catalytic applications, edges in TMD nanosheets also significantly impact nonlinear optical (NLO) properties. Specifically, these materials exhibit numerous remarkable electronic and optical properties thanks to their broken inversion symmetry [22–24]. Indeed, exposed edge sites in TMD materials amplify light-matter interactions, enhancing nonlinear optical effects, such as second- and third-harmonic

generation [25]. For this reason, significant attention has been recently devoted to characterizing their NLO response [26–28], which makes TMDs ideal building blocks for ultrathin nonlinear photonic devices.

In the last years, efforts to maximize edge-induced effects in 2D materials have focused on designing non-standard morphologies that provide a higher density of exposed edges, enabling the full harnessing of edge-driven functionalities [19, 29]. Traditional planar structures often offer limited edge exposure, but alternative configurations, such as vertically oriented nanosheets, overcome this limitation by increasing the accessible surface area of edge sites. To this aim, chemical vapor deposition (CVD) and other nanofabrication methods now allow for precise control over thickness, crystal quality, and morphology, supporting the scalable production of high-quality, edge-rich structures suitable for nanophotonic and catalytic applications [30–32].

In this thesis, one of the driving motivations was to address the challenges posed by maximizing edge-related functionalities in 2D materials. Within this program, one of the first goals was the development of a synthesis strategy for MoS_2 nanostructures using CVD, with an emphasis on creating vertically-aligned MoS_2 nanosheets (chapter 3). These vertical nanostructures are designed to maximize exposed edges, significantly enhancing their performance in nanophotonic applications.

Through a systematic exploration of the reaction temperature, time, and other growth parameters, we elucidated the diffusion-limited sulfurization process that governs the formation of these structures. This detailed analysis of vertical MoS_2 nanostructures revealed unique edge-related properties that boost their nonlinear optical response, thus laying a foundation for the fabrication of wafer-scale localized MoS_2 nanopillars suitable for advanced photonic devices.

The synthesis approach discussed in chapter 3 was also instrumental in enabling the subsequent realization of MoS_2 nanopillar arrays [33]. These core-shell 1D nanostructures were found to localize nonlinear signals at the wafer scale, offering a controlled, scalable method to tailor edge-driven properties for a range of optoelectronic applications. Although beyond the scope of this thesis, the development of such MoS_2 nanopillars underscores the adaptability and extended applications of vertically aligned TMD nanostructures in areas including biological sensing, single-electron emitters, and clean energy solutions.

The results presented in chapter 3, combined with complementary studies focusing on MoS_2 monolayers, suggest that vertically-oriented MoS_2 nanosheets—characterized by a high density of exposed edge sites—could provide an optimal configuration for achieving high-efficiency, second-order nonlinear responses for photonic applications [34]. This finding emphasizes the broader potential of vertically aligned TMDs as versatile platforms in the field of nanophotonics and beyond.

Precise characterization techniques are essential to fully realize the potential of such 2D nanostructures with non-trivial morphologies beyond the traditional planar configuration, especially as devices are designed with increasingly sophisticated geometries. In this context, while powerful, traditional transmission electron microscopy (TEM) meth-

ods often fail to capture the nanoscale strain and structural variations in non-planar or twisted geometries of TMD nanostructures. Addressing these challenges with TEM-based techniques requires innovative approaches that can provide detailed insights into strain and structural complexity at the atomic scale.

With this motivation, the second major result achieved in this thesis is the development and application of a comprehensive characterization framework of TMD nanostructures based on four-dimensional scanning transmission electron microscopy (4D-STEM). This framework is designed specifically to tackle the unique challenges of analyzing strain and structural complexity in TMDs, where subtle variations at the atomic scale can lead to significant differences in electronic and optical properties. Chapter 4 introduces the foundational principles of 4D-STEM, integrating advanced data analysis techniques crucial for mapping strain with nanometer precision in TMD nanostructures.

Building upon this foundation, chapter 5 describes the development of the custom Exit-Wave Power Cepstrum (EWPC) conditions used in 4D-STEM, which combined with nanobeam electron diffraction (NBED) form the basis of the open-source `StrainMAPPER` software framework developed in this thesis. This novel framework enables precise quantification of strain and rigid rotations in non-planar nanostructures with nanometer precision.

Chapter 6 then applies our `StrainMAPPER` framework to MoS_2 nanostructures with non-trivial morphologies beyond the traditional planar one, including twisted Moiré layers and TMD heterostructures such as MoS_2/MoO_3. These analyses validate the framework's robustness in capturing localized strain fields, advancing the study of strain-engineered nanostructures.

Finally, chapter 7 expands on the technical discussions from the previous chapters to explore the challenges associated with a robust theoretical interpretation of 4D-STEM measurements. There, we critically evaluate potential artifacts, particularly shifts in the center of mass (CoM) of electron beam intensity, which are commonly attributed to local electric fields. However, our findings highlight multiple conditions where CoM shifts may not relate to electric fields but instead arise from defocused STEM probes or slight crystal domain misalignments. This final chapter underscores the importance of a careful interpretation in 4D-STEM, especially in complex TMD nanostructures, before one can establish the underlying physical mechanisms explaining the measurements.

The thesis concludes with a summary of findings from each chapter, emphasizing this work's novel contributions to TMD material science and 4D-STEM characterization. It also outlines the implications of these contributions for future research and potential applications, demonstrating how advanced synthesis and characterization techniques together can contribute to ongoing progress toward the next generation of nanophotonic and electronic devices.

REFERENCES

[1] G. Moore, *Cramming More Components onto Integrated Circuits (1965),* in *Ideas That Created the Future: Classic Papers of Computer Science* (The MIT Press, 2021).

[2] G. E. Moore, *Intel: Memories and the microprocessor,* Daedalus **125**, 55 (1996).

[3] R. W. Keyes, *Physical limits of silicon transistors and circuits,* Reports on Progress in Physics **68**, 2701 (2005).

[4] R. Keyes, *Fundamental limits of silicon technology,* Proceedings of the IEEE **89**, 227 (2001).

[5] S. Wang, X. Liu, and P. Zhou, *The road for 2d semiconductors in the silicon age,* Advanced Materials **34**, 2106886 (2022).

[6] Y. Liu, X. Duan, H.-J. Shin, S. Park, Y. Huang, and X. Duan, *Promises and prospects of two-dimensional transistors,* Nature **591**, 43 (2021).

[7] K. S. Novoselov, A. K. Geim, S. V. Morozov, D. Jiang, Y. Zhang, S. V. Dubonos, I. V. Grigorieva, and A. A. Firsov, *Electric field effect in atomically thin carbon films,* Science **306**, 666 (2004).

[8] V. Singh, D. Joung, L. Zhai, S. Das, S. I. Khondaker, and S. Seal, *Graphene based materials: Past, present and future,* Progress in Materials Science **56**, 1178 (2011).

[9] F. Bonaccorso, Z. Sun, T. Hasan, and A. C. Ferrari, *Graphene photonics and optoelectronics,* Nature Photonics **4**, 611 (2010).

[10] J. H. Gosling, O. Makarovsky, F. Wang, N. D. Cottam, M. T. Greenaway, A. Patanè, R. D. Wildman, C. J. Tuck, L. Turyanska, and T. M. Fromhold, *Universal mobility characteristics of graphene originating from charge scattering by ionised impurities,* Communications Physics **4**, 30 (2021).

[11] K. Kaasbjerg, K. S. Thygesen, and K. W. Jacobsen, *Phonon-limited mobility in n-type single-layer mos$_2$ from first principles,* Phys. Rev. B **85**, 115317 (2012).

[12] M. Amani, D.-H. Lien, D. Kiriya, J. Xiao, A. Azcatl, J. Noh, S. R. Madhvapathy, R. Addou, S. KC, M. Dubey, K. Cho, R. M. Wallace, S.-C. Lee, J.-H. He, J. W. Ager, X. Zhang, E. Yablonovitch, and A. Javey, *Near-unity photoluminescence quantum yield in mos₂,* Science **350**, 1065 (2015).

[13] A. Nourbakhsh, A. Zubair, R. N. Sajjad, A. Tavakkoli K. G., W. Chen, S. Fang, X. Ling, J. Kong, M. S. Dresselhaus, E. Kaxiras, K. K. Berggren, D. Antoniadis, and T. Palacios, *Mos2 field-effect transistor with sub-10 nm channel length,* Nano Letters **16**, 7798 (2016).

[14] J. Kang, W. Liu, and K. Banerjee, *High-performance MoS2 transistors with low-resistance molybdenum contacts,* Applied Physics Letters **104**, 093106 (2014).

[15] Y. Xie, B. Zhang, S. Wang, D. Wang, A. Wang, Z. Wang, H. Yu, H. Zhang, Y. Chen, M. Zhao, B. Huang, L. Mei, and J. Wang, *Ultrabroadband mos2 photodetector with spectral response from 445 to 2717 nm,* Advanced Materials **29**, 1605972 (2017).

[16] Y. Li, Z. Zhou, S. Zhang, and Z. Chen, *Mos2 nanoribbons: High stability and unusual electronic and magnetic properties,* Journal of the American Chemical Society **130**, 16739 (2008).

[17] C. Ataca, H. Şahin, E. Aktürk, and S. Ciraci, *Mechanical and electronic properties of mos2 nanoribbons and their defects,* The Journal of Physical Chemistry C **115**, 3934 (2011).

[18] M. Tinoco, L. Maduro, and S. Conesa-Boj, *Metallic edge states in zig-zag vertically-oriented mos2 nanowalls,* Scientific Reports **9**, 15602 (2019).

[19] X. Yin, Z. Ye, D. A. Chenet, Y. Ye, K. O'Brien, J. C. Hone, and X. Zhang, *Edge nonlinear optics on a MoS2 atomic monolayer,* Science **344**, 488 (2014).

[20] T. F. Jaramillo, K. P. Jørgensen, J. Bonde, J. H. Nielsen, S. Horch, and I. Chorkendorff, *Identification of active edge sites for electrochemical h2 evolution from mos2 nanocatalysts,* Science **317**, 100 (2007).

[21] C. H. Lee, G. H. Lee, A. M. Van Der Zande, W. Chen, Y. Li, M. Han, X. Cui, G. Arefe, C. Nuckolls, T. F. Heinz, J. Guo, J. Hone, and P. Kim, *Atomically thin p–n junctions with van der Waals heterointerfaces,* Nature Nanotechnology 2014 9:9 **9**, 676 (2014).

[22] M. Tinoco, L. Maduro, and S. Conesa-Boj, *Metallic edge states in zig-zag vertically-oriented MoS2 nanowalls,* Scientific Reports **9**, 1 (2019).

[23] S. H. Gong, F. Alpeggiani, B. Sciacca, E. C. Garnett, and L. Kuipers, *Nanoscale chiral valley-photon interface through optical spin-orbit coupling,* Science **359**, 443 (2018).

[24] Z. Sun, A. Martinez, and F. Wang, *Optical modulators with 2D layered materials,* (2016).

[25] M. Bolhuis, J. Hernandez-Rueda, S. E. van Heijst, M. Tinoco Rivas, L. Kuipers, and S. Conesa-Boj, *Vertically-oriented mos2 nanosheets for nonlinear optical devices,* Nanoscale **12**, 10491 (2020).

[26] T. Jakubczyk, V. Delmonte, M. Koperski, K. Nogajewski, C. Faugeras, W. Langbein, M. Potemski, and J. Kasprzak, *Radiatively Limited Dephasing and Exciton Dynamics in MoSe2 Monolayers Revealed with Four-Wave Mixing Microscopy,* Nano Letters **16**, 5333 (2016).

[27] A. Autere, H. Jussila, Y. Dai, Y. Wang, H. Lipsanen, and Z. Sun, *Nonlinear Optics with 2D Layered Materials,* (2018).

[28] X. Zhang, S. Zhang, Y. Xie, J. Huang, L. Wang, Y. Cui, and J. Wang, *Tailoring the nonlinear optical performance of two-dimensional MoS2 nanofilms via defect engineering,* Nanoscale **10**, 17924 (2018).

[29] M. V. Bollinger, J. V. Lauritsen, K. W. Jacobsen, J. K. Nørskov, S. Helveg, and F. Besenbacher, *One-dimensional metallic edge states in MoS2,* Physical Review Letters **87**, 196803 (2001).

[30] Y. Zhan, Z. Liu, S. Najmaei, P. M. Ajayan, and J. Lou, *Large-area vapor-phase growth and characterization of mos2 atomic layers on a sio2 substrate,* Small **8**, 966 (2012).

[31] N. Choudhary, J. Park, J. Y. Hwang, and W. Choi, *Growth of large-scale and thickness-modulated mos2 nanosheets,* ACS Applied Materials & Interfaces **6**, 21215 (2014).

[32] K. Kang, S. Xie, L. Huang, Y. Han, P. Y. Huang, K. F. Mak, C.-J. Kim, D. Muller, and J. Park, *High-mobility three-atom-thick semiconducting films with wafer-scale homogeneity,* Nature **520**, 656 (2015).

[33] L. Maduro, M. Noordam, M. Bolhuis, L. Kuipers, and S. Conesa-Boj, *Position-controlled fabrication of vertically aligned mo/mos2 core–shell nanopillar arrays,* Advanced Functional Materials **32**, 2107880 (2022).

[34] D. Li, W. Xiong, L. Jiang, Z. Xiao, H. Rabiee Golgir, M. Wang, X. Huang, Y. Zhou, Z. Lin, J. Song, S. Ducharme, L. Jiang, J. F. Silvain, and Y. Lu, *Multimodal Nonlinear Optical Imaging of MoS2 and MoS2-Based van der Waals Heterostructures,* ACS Nano **10**, 3766 (2016).

2

Building the Foundations: Synthesis and Potential Applications of Transition Metal Dichalcogenides

Transition metal dichalcogenides (TMDs) represent a class of layered materials that consist of a transition metal layer like molybdenum (Mo) or tungsten (W) sandwiched in between two layers of chalcogen atoms, like sulfur (S). As these materials transition from bulk crystals to monolayers, such as (MoS_2 and WS_2), they undergo a significant shift from an indirect to a direct bandgap. Moreover, depending on the type of edge termination, TMDs can display both metallic and semiconducting behavior. These tunable properties make TMDs a perfect candidate for various nano-electronic and nano-photonics devices. However, precise control over synthesis is essential to maximize the full potential of TMDs. This chapter underscores the crucial role of synthesis control in tailoring the orientation of resulting nanostructures relative to the substrate, as the orientation - whether horizontal or vertical - determines the suitability of TMDs for specific applications. This chapter begins with exploring the unique optical and electronic characteristics of MoS_2, shedding light on its potential applications across various fields. This exploration is followed by exploring various synthesis techniques, with particular emphasis on chemical vapor deposition (CVD). Finally, we detail the specific synthesis methods employed to fabricate the TMD nanostructures detailed in this thesis.

2.1. INTRODUCTION

Researchers have focused their attention on low-dimensional nanostructures in the search for ever-smaller electronic and photonic devices. These structures are so small that they confine the physics to two or even fewer dimensions. Such a dimension reduction gives rise to interesting physical phenomena not present in larger three-dimensional (3D) structures. Furthermore, the most studied example of a low-dimensional material is graphene. Graphene is a true two-dimensional (2D) material consisting of a single layer of carbon atoms arranged in a hexagonal pattern [1]. Like graphite, which is the three-dimensional variant of hexagonal carbon, graphene is a zero-bandgap semiconductor, which gives graphene a metallic behavior [2, 3]. However, graphene has a much higher electrical conductivity than graphite because it has exceptionally high electron mobility [4]. The high electron mobility can be attributed to the fact that the charge carriers in the carbon lattice become Dirac fermions when the lattice is reduced to the monolayer limit. These Dirac fermions effectively behave as if they have no mass or charge [5]. Moreover, graphene is very strong, an excellent heat conductor, and, under certain conditions, superconducting.

However, graphene is missing one vital property that makes it unsuitable for switching applications, like integrated circuits and nano-photonics: a non-zero bandgap. Luckily, there are more low-dimensional materials, each with its unique properties. Some, like graphene, are metallic; others are insulating, like hexa-boron nitride (hBN) [6], and others are semiconducting, like indium selenide (InSe) [7]. All these materials belong to the layered material family. Their common property is the anisotropic bonding between the atoms. The covalent bonds between atoms in the same atomic plane are much stronger than the weak van der Waals (vdW) forces between the atomic layers [8]. Therefore, one can easily separate the atomic layers while keeping individual layers intact. With care, one can continue breaking the vdW-bonds and separate the atomic layers until the single-layer limit [9].

Transition metal dichalcogenides (TMDs) are a special class of layered materials. These materials consist of a single transition metal (M) layer, sandwiched between two chalcogen (X) layers, forming a three-atom thick MX_2 monolayer. Common TMD materials are molybdenum disulfide (MoS_2) and tungsten disulfide (WS_2), but many combinations of M (Mo, W, Ti, Nb) and X (S, Se, Te) exist. While most TMDs are semiconductors, others have been reported as insulators, metals, superconductors, ferroelectrics, and magnetic [10–14]. This wide range of properties makes TMDs an interesting platform for many nano-electronic and nano-photonic applications [15–17]. In this chapter, we discuss the interesting electronic and optical properties of TMDs and MoS_2 in particular. We highlight possible applications and discuss fabrication techniques. Finally, we will focus on the chemical vapor deposition techniques used to synthesize all the unique morphologies discussed throughout this thesis.

2.2. PROPERTIES OF TRANSITION METAL DICHALCOGENIDES

Transition metal dichalcogenides (TMDs) encompass a variety of materials, each with unique properties. This section will focus on the unique properties of one such TMD, MoS_2. MoS_2 is part of the Group 6 (Mo, W) semiconducting TMDs. Similar to graphene, MoS_2 is a layered material with weak van der Waals (vdW) bonds that keep the atomic layers together. The first research efforts on MoS_2 centered on its use in lubrication to reduce friction and wear. The low friction coefficient, provided by the weak vdW interaction between the atomic layer, makes MoS_2 an excellent solid lubricant [18, 19]. MoS_2 is used as a catalyst to remove sulfur (S) from natural gas [20]. Furthermore, it is also a viable alternative for the more expensive Group 10 (Ni, Pd, Pt) metals in the reduction of nitro compound [21]. A MoS_2 catalyst can also be applied in a hydrogen evolution reaction (HER) to produce hydrogen gas ($2\,H_2$) from water (H_2O) [22, 23]. However, the effectiveness of MoS_2 as a catalyst is relatively low. The number of chemically active sites, the dangling bonds, is limited due to the 2D nature of MoS_2 [24, 25]. The atoms in the 2D atomic plane are arranged in a hexagonal pattern, resulting in an atomically flat plane without the dangling bonds on the surface that are typical for 3D materials. Therefore, the chemically active sites of MoS_2 are located at the edges and not at the material's surface. By reducing the dimensionality of MoS_2, one can increase the ratio between the edge and the surface, thereby increasing the effectiveness of MoS_2 as a catalyst [26, 27].

THE CRYSTAL STRUCTURE OF MoS_2

A single layer of MoS_2 consists of an Mo sublayer sandwiched between two S sublayers. Each Mo is bonded to six S atoms in an octahedral or trigonal prismatic geometry. The position of the S atoms with respect to the Mo atom can vary, leading to different geometries and giving rise to several MoS_2 polytypes. The most common polytypes are denoted as 1T, 2H, and 3R, where the number represents the layers in the unit cell, and the letter denotes the symmetry of the entire unit cell (T = Trigonal, H = Hexagonal, and R = Rhombohedral) [28]. A three-dimensional side and top view of the three MoS_2 polytypes are depicted in fig. 2.1a. Both the 2H and 3R polytypes of MoS_2 are stable and found in nature, with the majority of naturally occurring MoS_2 being of the $2\,H-MoS_2$. Selective synthesis of both $2\,H-MoS_2$ and $3\,R-MoS_2$ bulk crystals can be achieved using chemical vapor transport methods [29]. The thickness of a single $2\,H-MoS_2$ layer is 3.15 A, and the distance between adjacent layers is approximately 6.15 A [28].

The lattice parameters of the hexagonal $2\,H-MoS_2$ unit cell, containing two layers, are $a = 3.15$ A and $c = 12.30$ A [30]. The crystal structure of $2\,H-MoS_2$ belongs to the $P_{63/}mmc$ space group and has a hexagonal Brillouin zone. With an even number of MoS_2 layers, the unit cell exhibits inversion symmetry. However, monolayer $1\,H-MoS_2$ lacks inversion symmetry, which plays an important role in several physical phenomena. The crystal structure of $3\,R-MoS_2$ is similar to that of $2\,H-MoS_2$ but with a different stacking order of layers. $2\,H-MoS_2$ has a (AbA)(BaB) stacking, while $3\,R-MoS_2$ has a (AbA)(BcB)(CaC) stacking, where the upper(lower) case letter denotes the position of the S(Mo atom. In this work, we denote $2\,H-MoS_2$ simply as MoS_2 because of its prevalence in nature. However, the synthesis of other polytypes, such as 1T and 3R, as well as mixed polytypes, has been demonstrated [31]. Monolayer MoS_2 is often classified as $1\,H-MoS_2$, preserv-

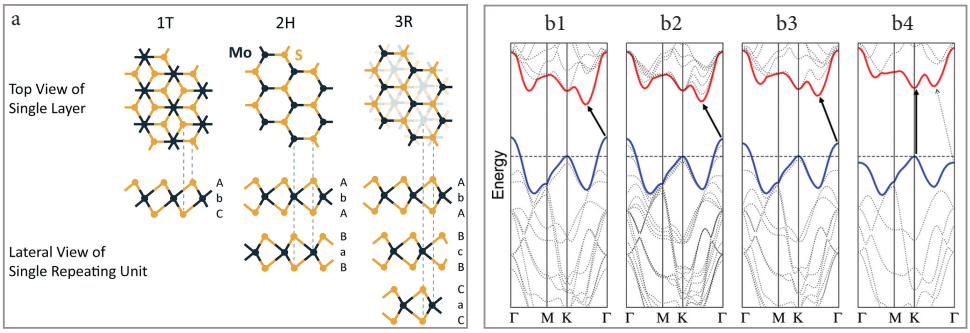

Figure 2.1: **a)** Top and lateral views of the MoS_2 crystal structure for the 1T, 2H, and 3R polytypes, respectively. The lateral view shows the different types of layer stacking, unique to each polytype. Reproduced from Song et al.[28], with permission from the Royal Society of Chemistry. **b1-b4)** The band structure of different MoS_2 configurations, with bulk MoS_2 on the left (b1), quadrilayer (b2) and bilayer (b3) MoS_2 in the middle and monolayer MoS_2 on the rigth (b4). These band structures, calculated using ab inito calculations, show the indirect to direct bandgap transition of MoS_2 in the monolayer limit. Reprinted with permission from Splendiani et al.[32] ©2010 American Chemical Society.

ing the hexagonal symmetry even in the monolayer limit. Other TMDs from Group 6 share similar 2H symmetry and lattice parameters, making them excellent building blocks for creating complex lateral and out-of-plane heterostructures with combined properties.

THE BAND STRUCTURE OF MoS_2

MoS_2 has a non-zero bandgap and is, unlike graphene, a true semiconductor with an indirect bandgap. Moreover, MoS_2 exhibits a very high On/Off ratio of 10^8 and a theoretical electron mobility of approximately 410 $cm^2V_1^-s_1^-$ [33]. The combination of the bandgap and the high On/Off ratio makes MoS_2 a suitable material for switching applications like integrated circuits, although the highest experimentally achieved electron mobility (200 $cm^2V_1^-s_1^-$) falls short of conventional semiconductors like silicon (1400 $cm^2V_1^-s_1^-$) [34]. However, when MoS_2 is reduced to a single layer, the bandgap transitions to a direct bandgap, making MoS_2 suitable for photonic applications. The nature of this bandgap transition becomes evident in first-principle calculations of the MoS_2 bandgap. The bandgaps of bulk, double layer, and single layer MoS_2 are illustrated in fig. 2.1b [32]. The maximum energy value in the valence band (VB_{max}) is centered around the Γ-point in the Brillouin zone, whereas the minimum energy value in the conduction band (CB_{min}) is located in the middle of the Γ-K direction. As the number of MoS_2 layers decreases, the CB_{min} point moves towards the K-point, and its energy increases away from the Fermi level. The VB_{max} point also moves towards the K-point. The band structure of a single layer of MoS_2, as shown in fig. 2.1b, reveals a direct bandgap transition of 1.9 eV. This bandgap transition enhances the photoluminescence (PL) emission. When MoS_2 is reduced to the monolayer limit, the PL yield increases by three orders of magnitude [35].

RAMMAN ACTIVE MODES OF MoS_2

Raman spectroscopy is a common method in solid-state physics for characterizing materials. The method relies on the inelastic scattering between photons in laser light and phonon modes in the crystal. The shift in the energy of the scattered light provides information about the phonon modes inside the material. Hexagonal MoS_2 exhibits four first-order active Raman modes, each with its characteristic wavenumber: $E^2_{2g} = 32\ cm^{-1}$, $E_{1g} = 286\ cm^{-1}$, $E^1_{2g} = 383\ cm^{-1}$, $A_{1g} = 408\ cm^{-1}$ [36]. Only the A_{1g} Raman mode belongs to an out-of-plane vibration; the other Raman modes are all in-plane vibrations. With the dimensionality reduction, the intensity of the out-of-plane Raman mode (A_{1g})is reduced. Therefore, a MoS_2 monolayer has a 1:1 ratio between the E^1_{2g} and A_{1g} Raman modes [37]. An example of a MoS_2 Raman spectrum is shown in figs. 3.1 and A.3.5. However, the intensity ratio is unreliable for identifying the number of MoS_2 layers. A more reliable method of identifying the number of MoS_2 layers is by measuring the spacing between E^1_{2g} and A_{1g} Raman modes. MoS_2 exhibits a thickness-dependent blue (red) shift of the E^1_{2g} (A_{1g}) Raman mode [38, 39]. The spacing for bulk MoS_2 is approximately 25 cm^{-1}, while the spacing reduces to approximately 19 cm^{-1} for monolayer MoS_2. While the frequency shift can be useful for identifying the number of MoS_2 layers, one must be careful because other effects, like strain and doping, can also contribute to the Raman shift. Besides the intensity ratio and frequency spacing, one can identify the orientation of MoS_2 layers from the Raman spectrum. The intensity of the E_{1g} Raman mode drops to zero when the incoming laser light is perpendicular to the basal plane of the MoS_2. This so-called forbidden Raman mode prevents the detection of the E_{1g} Raman mode for horizontally aligned MoS_2 in typically backscattering experiments. However, when MoS_2 is oriented vertically, the E_{1g} Raman mode resurfaces, allowing it to serve as a fingerprint for vertical MoS_2 [40, 41].

OPTICAL PROPERTIES OF MoS_2

The indirect to direct bandgap transition benefits the photoluminescence (PL) emission. When MoS_2 is reduced to the monolayer limit, the PL yield will increase by three orders of magnitude [32, 35]. Not only PL but all optical responses of MoS_2 are dominated by exciton transitions [42]. The 2D nature of MoS_2 provides strong geometrical confinement while reducing the dielectric screening typically provided by neighboring atoms. The strong confinement and the weak dielectric screening result in a strong Coulomb interaction between charged particles within a single MoS_2 layer. The strong Coulomb interaction forms electron-hole pairs (excitons) when MoS_2 is optically excited. The binding energy of these excitons has been measured to be 0.5 eV [43–45], which is an order of magnitude higher than the exciton binding energy of 3D materials [46]. The large binding energy of excitons means they are present at room temperatures. The PL spectrum of monolayer MoS_2 contains two distinct peaks corresponding to the A and B exciton transitions. The valance band for a single layer of MoS_2 is split by the strong spin-orbit coupling and the lack of inversion symmetry, resulting in two distinct exciton transitions. The split valence band also provides an avenue for valley polarization [47, 48]. The split valence band creates two equivalent valleys around the K-point, named K and K'. Using left-handed (right-handed) circularly polarized light, one can selectively couple to the

K' (K) valley, thus opening up the new field of valleytronics [49, 50]. Furthermore, the broken inversion of MoS_2 enhances its non-linear optical (NLO) response. Therefore, the NLO response is highest for a single layer of MoS_2, which naturally lacks inversion symmetry. However, an increase in the NLO response can also be observed at the edges of MoS_2, where there is an inherent lack of local inversion symmetry.

FUNCTIONAL MATERIAL ENGINEERING WITH TMDS

The lack of inversion symmetry at the edge of a MoS_2 crystal enhances the NLO response and results in two distinct edge terminations. The MoS_2 edge can terminate in either a zigzag (ZZ) or an armchair (AC) pattern, as depicted in fig. 2.2. The ZZ edges consist of only Mo and S atoms, while the AC edge consists of alternating Mo and S atoms [51, 52]. Edges that form 60- or 120 angles with neighboring edges exhibit the same termination type, whereas edges at 30- or 90-degree angles switch termination types. Predictions suggest that the ZZ edge termination is the most stable and exhibits metallic behavior, while the AC edge is semiconducting, consistent with bulk MoS_2 properties. The metallic behavior of ZZ edges can induce plasmon formation. A further dimensionality reduction enhances the influence of the edge states relative to the basal plane, such as creating one-dimensional (1D) nanoribbons [53, 54]. Selective creation of 1D nanoribbons with either metallic ZZ edges, or semiconducting AC edges within a single electronic device or application can extend this functionality [55].

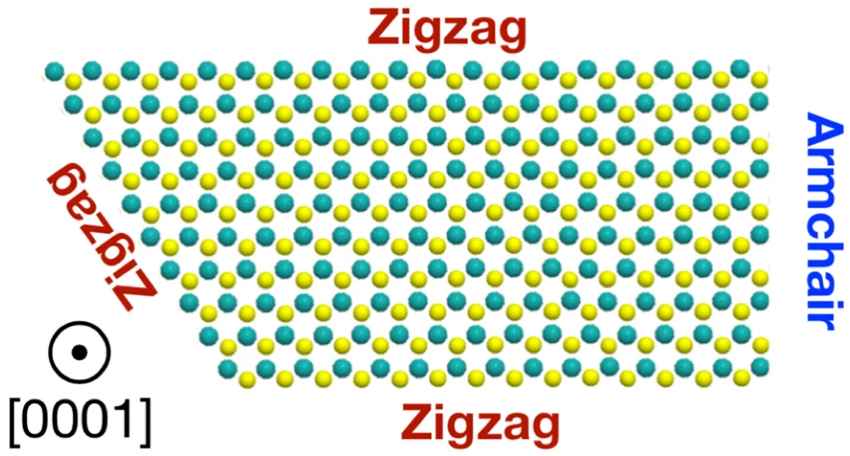

Figure 2.2: Representation of the different edge terminations of MoS_2. The zigzag edge terminates only in Mo or S atoms, whereas the armchair edge terminates in both Mo and S atoms. Notably, a 60° (120°) angle between edges preserves the type of edge termination and preserves (changes) the atom type. A 90° angle between edges changes the edge type. Reprinted from Tinoco et al.[55]. ©2019, Miguel Tinoco et al.

The unique properties of various TMD materials can be combined to create a wide range of functional materials. The 2D nature of TMDs facilitates the stacking of multiple layers, enabling the engineering of the band gaps, the formation of interlayer excitons, and the development of 2D field-effect transistors (FET) [56–58]. Stacking two exfoliated materials on top of each other can lead to the formation of out-of-plane heterostruc-

tures. Additionally, the lateral joining of various TMD materials can create in-plane heterostructures. When two 2D materials are placed on top of each other, an extra degree of freedom emerges. By slightly misaligning the two layers, large Moire superlattices are formed. Unique physical phenomena arise at precise twist angles, such as ultra-flat valence bands or superconductivity [59, 60]. The ability to tune these functional materials using twist angles is explored in the emerging field of twisttronics.

2.3. TMD FABRICATION METHODS

The unique 2D nature of TMD materials lends itself to the fabrication or synthesis of specimens with precise control over the number of layers. The layer-dependent properties of TMDs allow researchers to engineer specimens with tailored characteristics for specific applications. Therefore, the ability to selectively synthesize specimens with the exact number of layers or precise geometry is crucial for integrating TMDs more widely in future applications. After the first isolation of a graphene layer in 2004 [1] using the scotch tape method, the isolation of a single MoS_2 quickly followed in 2005 [61]. The Scotch tape method represents the simplest form of mechanical exfoliation. By delicately applying force in the out-of-plane direction, one can break the weak van der Waals bonds between the layers of bulk TMD material. With precision, a single TMD layer can be isolated without disrupting the in-plane covalent bonds, resulting in a pristine monolayer. Layered heterostructures can be created by isolating monolayers of two different materials and stacking them on top of each other [62]. These heterostructures can consist solely of TMD materials or contain any combination of other layered materials, like hBN or graphene. While effective, the scotch tape method has its limitations. Producing large and pristine specimens with consistent thickness has proven challenging. The manual nature of the process, combined with difficulties in achieving uniform monolayers, renders the scotch tape method unsuitable for mass-producing TMD devices [63].

Using mechanical exfoliation in combination with a wet process like ultrasonication to separate the TMD layers can enhance the rapid production of TMD monolayers [64]. However, the low monolayer yield and the instability of the specimens made liquid-phase exfoliation impractical. Wet processes can be improved by using organic solvents during exfoliation. These solvents improve the interaction between the liquid and the TMD layers, stabilizing the exfoliated monolayers and preventing agglomeration [65]. Electrochemical exfoliation offers another method to separate TMD layers by inducing electrolysis to create small bubbles between the layers [66]. These bubbles serve to intercalate and selectively separate the TMD layers, favoring the formation of monolayers. Alternatively, chemicals containing lithium (Li) can be used to intercalate Li ions into layered materials like MoS_2. The resulting Li-infused MoS_2 can then be dispersed into water and reconstructed or "restacked" using filtration [67]. However, one drawback of this chemical exfoliation method is that the restacked MoS_2 loses its semiconducting properties, transitioning into the metallic $1T-MoS_2$ phase [68]. Both dry and wet exfoliation techniques share a common challenge: reliably fabricating large quantities of single-layer TMDs with consistent uniformity. This limitation makes any form of exfoliation unsuitable for large-scale applications.

A way forward is provided by bottom-up approaches like physical vapor deposition (PVD) or chemical vapor deposition (CVD). Both methods offer the synthesis of TMD materials on various substrates. PVD techniques, like sputtering or evaporation, utilize a bulk crystal as a target, which vaporizes through heating or ion bombardment. The resulting vapor then deposits onto the substrate to form a thin film [69, 70]. In contrast, CVD relies on high temperatures to facilitate chemical reactions and synthesize thin films.

THE KINETICS OF CHEMICAL VAPOR DEPOSITION

Chemical vapor deposition is a technique used to deposit thin layers onto a heated substrate. The process relies on chemical reactions taking place between precursors. These reactions can occur in the gas phase and on the substrate. Increasing the temperature generally stimulates chemical reactions. The most important parameters for CVD are temperature, pressure, and flow rate. Specific layer properties, such as electrical properties, growth directions, and growth modes, can be determined by controlling these parameters. The CVD process is governed by thermodynamics and kinetics [71]. Thermodynamics governs the chemical reactions in the gas phase and on the substrate. The transport of the precursors by the carrier gas and the precursors over the substrate is governed by kinetics. The various CVD synthesis methods can be classified into two groups. The first, the two-step method, relies on directly sulfurizing a pre-deposited transition metal. In this method, chemical reactions only occur at the substrate. The second class uses chemical reactions in the vapor phase to form TMD material deposited as a thin film onto the substrate.

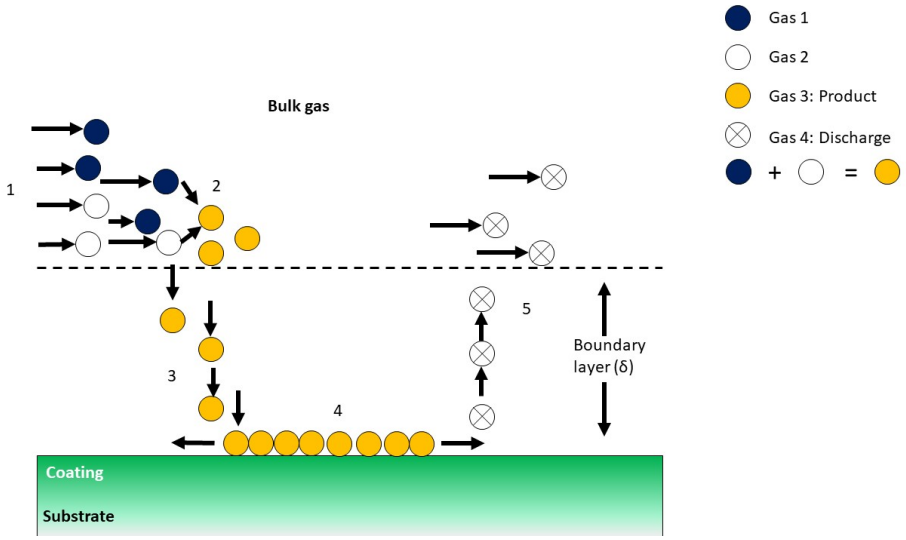

Figure 2.3: Schematic of the kinetic processes in a CVD process. (1) The gaseous precursors are transported by the bulk gas. (2) The first reactions take place and form new gaseous precursors. (3) The precursors diffuse through the boundary layer and deposit on the substrate surface. (4) Reactions take place on the surface. (5) Gaseous reaction products diffuse back through the boundary layer and are transported away. (adapted from Sudarshan 2000 [71])

The schematic in figure 2.3 shows the kinetic processes occurring during CVD. In most CVD processes, flow is assumed to be laminar, forming a boundary layer at the substrate interface where gas velocity is zero. Precursors diffuse through this boundary layer and deposit onto the substrate. Initial chemical reactions between precursors can occur within this boundary layer or the bulk gas, generating new precursors that are subsequently deposited. On the substrate, various single or multi-step reactions occur. Gases produced during substrate reactions diffuse back through the boundary layer before being transported away by the laminar flow [71].

TWO-STEP SYNTHESIS OF MoS_2

The direct sulfurization of transmission metals is usually classified as a two-step process. First, a transition metal thin film, like Mo, is deposited on the substrate. Next, the transition metal is sulfurized by heating the thin film in a sulfur-rich atmosphere. Electron beam evaporation or magnetron sputtering are common techniques for depositing Mo thin films. These bottom-up approaches allow for precise control over the thin film thickness. Mo evaporation leads to the most uniform thin films with a larger grain size but has a low deposition rate [72]. On the other hand, magnetron sputtering has a much faster deposition rate, but grains tend to be smaller. Moreover, magnetron sputtering, especially at room temperature, induces a columnar growth structure containing small grains and voids. These columnar structures become especially prominent for thicker Mo films. The sulfurization of the thin film is commonly done by placing a solid sulfur precursor upstream from the heated thin film in a CVD system. The solid sulfur precursor is heated to its melting point, at which point the evaporated sulfur is transported to the thin film by a carrier gas, creating the sulfur-rich atmosphere needed for direct sulfurization. This process can be performed at atmospheric pressure or using a low-pressure CVD (LPCVD) system.

The thickness of the initial Mo thin film directly influences the thickness of the synthesized MoS_2 and, therefore, the number of MoS_2 layers [73]. Varying the thickness of the Mo thin film between 1-5 nm results in the formation of monolayer, bilayer, and multilayer MoS_2. Because of the column formation during the Mo thin film deposition, it proves to be challenging to synthesize large uniform MoS_2 monolayers. Annealing the Mo thin film before sulfurization or replacing it with a molybdenum oxide MoO_3 thin film can improve the uniformity of the MoS_2 monolayers [74]. The use of thicker ($\geqslant\sim 3$ nm) Mo seed layers leads to the formation of vertical MoS_2 nanosheets (v-MoS_2) [41]. The orientation of the nanosheets during the initial MoS_2 formation is randomly oriented [41, 75], but after a critical depth, the MoS_2 nanosheets favor the vertical orientation. The sulfur diffusion from the substrate surface favors the vdW gaps between the layers, promoting the vertical growth perpendicular to the substrate surface. This process is aided by the columnar structure of the Mo seed layer. In chapter 3, we provide an in-depth discussion on the growth mechanisms of v-MoS2.

VAPOR PHASE SYNTHESIS OF MoS_2

The second type of CVD method revolves around vapor phase reactions. Separate precursors required for MoS_2 synthesis are introduced in the vapor phase and either react in the laminar flow or on an arbitrary substrate to form MoS_2, as depicted in fig. 2.3. Gaseous precursors provide the Mo and S compounds necessary for the vapor reactions. Examples include molybdenum chloride $MoCl_5$ or metal-organic compounds like molybdenum hexacarbonyl $Mo[Co]_6$ together with diethyl sulfide $[C_2H_5]_2S$ [76]. Metal-Organic CVD MOCVD has proven effective in synthesizing large, uniform sheets of monolayer MoS_2 [77]. However, vapor phase processes using only gaseous precursors require specialized and complex CVD systems equipped with multiple gas lines and precise flow controllers. Moreover, certain gaseous compounds like the byproduct hydrochloric acid HCL are highly corrosive.

The most common approach to vapor phase reactions in a CVD system is using solid precursors heated to the appropriate temperature for evaporation. Solid precursors like S and an oxide powder like MoO_3 can produce the vapors necessary for the vapor phase reaction [78, 79]. However, the melting point of S (114 °C) is much lower than that of MoO_3 (795 °C). Although MoO_3 begins to sublimate at a much lower temperature, it is advisable to separate the S and MoO_3 powder into separate heating zones to ensure optimal process control. Typically, S is placed upstream from the target substrate and heated past its boiling point, while the oxide power is placed just before or directly on the substrate. The oxide powder and the substrate are then heated to ensure the sublimation of the oxide powder into volatile oxide compounds (MoO_x). Following the vapor phase reaction, MoS_2 forms on the heated substrate. The advantage of these vapor phase methods lies in the versatility of the substrate. While a crystalline substrate can enhance synthesis, amorphous substrates like Si/SiOx wafers can also serve as suitable synthesis platforms. These vapor phase methods can even extend to synthesizing MoS_2 structures directly on amorphous Si_3N_4 membranes used in TEM inspection grids. This direct synthesis enables high-quality TEM inspection without the need for complex transfer methods that could compromise monolayer integrity. Finally, it is possible to synthesize mixtures by selecting oxide compounds with matching sublimation temperatures. Conversely, selecting two oxides with different sublimation temperatures allows for creating in-plane heterostructures through sequential vapor phase reactions with each oxide.

2.4. TMD SPECIMENS STUDIED IN THIS WORK

The CVD methods we described have served as a basis for the CVD synthesis of the MoS_2 specimens presented in this work. This final section will first discuss the CVD system used to synthesize the specimens. Next, we will detail the conditions used during the two-step synthesis of the v-MoS_2 nanosheets presented in chapter 3. We will also discuss the evolution of the v-MoS_2 approach, the synthesis of vertical MoS_2/WS_2 in-plane heterostructures, and Mo/MoS_2 core-shell nanopillars. Finally, we will discuss the conditions used to synthesize the MoS_2 monolayers, discussed in chapters 6 and 7, and the MoS_2/MoO_3 heterostructure in chapter 6.

THREE-ZONE CVD FURNACE

The CVD system used to synthesize almost every specimen in this work is a three-zone atmospheric hot wall reactor (Carbolite Gero). A schematic of this reactor is displayed in fig. 2.4. The reactor consists of a large quartz tube placed in an electric oven with three separate heating elements. The quartz tube is connected to an argon (Ar) source at one end and a gas bubbler at the other. The middle zone of the reactor is always used as the main reaction zone, while the zone closest to the Ar source is used to heat the S powder. The three zones can be heated separately and are thermally isolated by alumina (Al_2O_3) disks. However, once the temperature gradient between the hottest and coldest zones becomes too large, the coolest zone will slightly heat up even with the AlO_3 disks. The Ar flow rate can be regulated before it enters the reaction tube by a flow meter with a range of 1000 sccm to 100 sccm. Once the CVD reaction is complete, the reaction tube is naturally cooled to 100 C before the reactor can be opened to cool further.

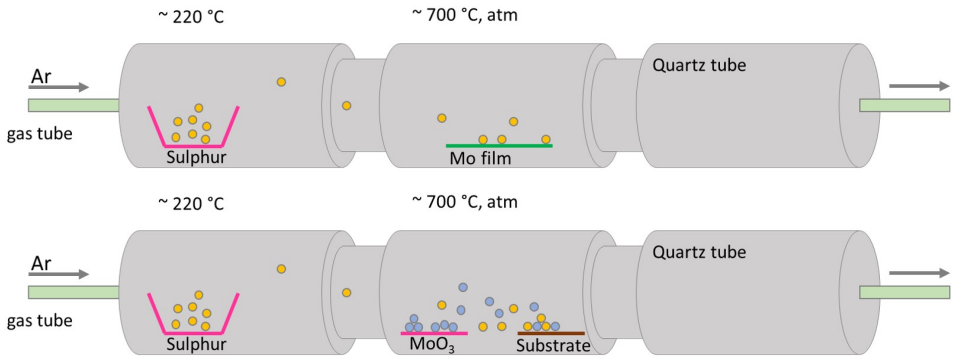

Figure 2.4: A schematic representation of the CVD process in a three-zone atmospheric hot wall reactor (Carbolite Gero). The top schematic represents the two-step synthesis of a pre-deposited Mo thin film. The bottom schematic represents a vapor phase CVD process where the MoOx and S react in the vapor phase to form MoS_2 on a target substrate. n both scenarios, the S is supplied by heating S powder in an alumina crucible upstream from the substrate. Ar gas is used as a carrier gas and to vacate oxygen from the reactor.

SYNTHESIS OF V-MoS_2

To synthesize the vertically oriented MoS_2 nanosheets discussed in chapter 3, we used a two-step CVD process to directly sulfurize thick Mo layers over large areas. First, a 700 nm-thick Mo seed layer was pre-deposited on a Si/SiO_2 wafer ($< 1\ cm^2$) using magnetron sputtering. This target substrate was placed in the middle zone of the CVD reactor. The solid S precursor (400 mg) was placed upstream from the target substrate in zone one.

A schematic illustration of the synthesis protocol adopted for synthesizing the v-MoS_2 nanosheets is provided in fig. 2.5. Before the sulfurization, a pretreatment with Ar flow (500 sccm) was carried out for 30 minutes, followed by a gradual temperature ramp-up at 10 °C /min. The temperature of the reaction zone was increased within the range of 500 °C to 700 °C. Once the reactor zone reached 500 °C, the Ar gas flow was reduced from 500 sccm to 150 sccm. Upon reaching the target temperature, the temperature in the zone

containing the S powder was ramped up to 220 °C at a rate of 10 °C /min. The starting point of the reaction (T=0 s) was defined as the moment when the sulfur temperature reached 220 °C. When the desired reaction time was reached, the heating of both furnace zones was switched off simultaneously. The Ar gas flow was kept at 100 sccm to prevent possible oxidation during the cooldown procedure. This synthesis protocol offers three easily adjustable degrees of freedom: reaction time, temperature, and Ar flow. Each parameter's impact is discussed in detail in chapter 3.

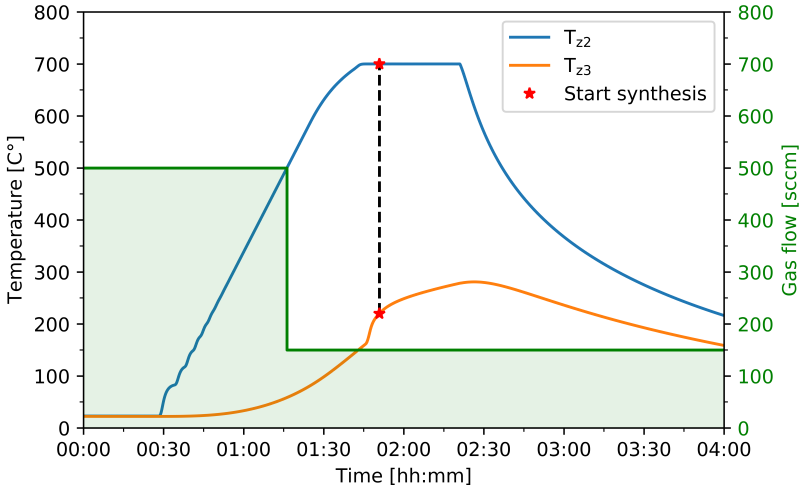

Figure 2.5: A representation of the synthesis protocol used in this work. The oxygen in the reactor is vacated by a 30-minute Ar flush. Next, we increase the temperature of the zone where the substrate is located (T_{z2}) to the target temperature. Once T_{z2} = 500°C, the Ar flow is reduced to 150 sccm. Once T_{z2} reaches the target temperature the S is heated up (T_{z3}). Finally, the synthesis is started the moment T_{z3} = 220°C.

ADVANCEMENTS IN VERTICAL NANOSHEET SYNTHESIS

The synthesis of the vertical TMD nanosheets can be extended to more complex geometries. The two-step method lends itself to the formation of TMD heterostructures. Similar to Mo, magnetron sputtering can be used to deposit tungsten (W). By alternating the Mo and W deposition, one can create a Mo/WS_2 multilayer stack. Next, the multilayer stack can be sulfurized using the same synthesis protocol for the v-MoS_2 nanosheets. When the S diffuses through the stack, it will form alternating MoS_2 and WS_2 layers. The result is an MoS_2/WS_2 multilayer consisting of vertical nanosheets. The vertical nanosheets form in-plane heterostructures at the interface between the MoS_2 and WS_2. The sulfurization depth can be controlled by the reaction time and temperature. The number of layers, the order, and the thickness of the layers are predetermined by the geometry of the magnetron-sputtered Mo/W multilayer stack. In principle, one can create any combination of layers. However, some considerations affect the uniformity of the resulting MoS_2/WS_2 multilayer stack. First, one must ensure that the first transition metal (Mo or W) layer is sufficiently thick. The bottom layer should not be completely sulfurized to ensure the integrity of the multilayer stack. Once the entire seed

layer gets sulfurized, the TMD layers will delaminate from the substrate surface, and the MoS_2/WS_2 multilayer stack will flake off the substrate. Depositing a sufficiently thick first layer can sulfurize the entire multilayer stack while ensuring the bottom transition metal is not completely sulfurized. The second consideration is the thickness of the top layer of the multilayer stack. Cross-sectional analysis has shown that the orientation of the nanosheets in the first 20 nm has random orientations. This layer of random-orientated nanosheet thickness is self-limited and only dependent on the reaction temperature. Please see chapter 3 for more information about this region. Finally, the use of Mo as a top and bottom layer is strongly preferred.

As discussed earlier, magnetron sputtering of TMD materials leads to the formation of columns. This effect is worse for W compared to Mo sputtering. The strong colonization of W leads to an uneven diffusion rate throughout the specimen. The result is an uneven growth rate of WS_2 or even voids in the multilayer stack. Using Mo as a top and bottom layer ensures a uniform growth rate. However, this is a limiting factor in the design of possible quantum wells. Usually, a quantum well is constructed by encapsulating a material with low bandgap energy in between a material with a higher bandgap. That would mean a $WS_2/MoS_2/WS_2$ stack. With a top and bottom WS_2 layer, this stack is more challenging to synthesize reliably. This challenge can be circumvented by designing a multilayer stack with a thin MoS_2 layer (10nm) sandwiched between two thicker WS_2 layers (20 nm) and a thick MoS_2 layer on top and bottom (200-500 nm).

The two-step method also enables shaping the transition metal seed layer before sulfurization, enabling the synthesizing of TMD materials with unique geometries. Using electron beam lithography and cryogenic deep reactive ion etching, one can create Mo nanopillar arrays in several different shapes and with high aspect-ratio (up to 15) [80]. We used the same synthesis protocol as detailed before to synthesize Mo/MoS_2 coreshell nanopillars array [81]. The surface area of the Mo nanopillar is much higher than that of a Mo thin film. Moreover, the high aspect ratio means that the diameter of the Mo nanopillar is much smaller than the height of the nanopillar. Therefore, a short reaction time is needed to ensure that the Mo core is not entirely sulfurized and can act as a scaffold for the nanopillar. High-resolution TEM images of the core-shell nanopillar show the successful synthesis of v-MoS_2 nanosheets. The nanosheets are always vertically aligned with respect to the surface of the nanopillar. This behavior highlights the diffusion of the S through the vdW-gaps, as discussed previously. The high aspect ratio of the nanopillars drastically increases the number of exposed v-MoS_2 edges. Therefore, the Mo/MoS_2 coreshell nanopillars exhibit an enhanced non-linear optical (NLO) response [81]. Combined with the configurable geometry and location of the nanopillars afforded by the lithography step, one can create a localized NLO response. The flexibility of this three-step approach, deposition, lithography, and sulfurization, makes it ideal for fabricating NLO devices.

2

Vapor Phase synthesis of MoS_2 and MoO_3

Synthesis of the MoS_2 and MoO_3 nanostructures

The MoS_2 nanostructure from chapters 6 and 7 was synthesized using chemical vapor deposition on a TEM grid. The Si TEM grid has nine viewing windows with a Si_3N_4 thin film spanning the entire grid. A small amount of MoO_2 was drop-casted onto the TEM grid from a solution of 2.6 mg of MoO_2 suspended in 6 ml of isopropanol. Next, the grid was placed in an alumina crucible at 2 cm from 7.5 mg of MoO_2 powder. The crucible was placed in the middle of the gradient tube furnace, upstream from another alumina crucible containing 400 mg of sulfur. Ar was used as a carrier gas with a flow rate of 100 sccm. The middle zone was heated to 780 °C, and the sulfur reached a maximum temperature of 270 °C. The uniform thickness of the synthesized MoS_2 layer was verified using electron energy loss spectroscopy (EELS) maps. We calculated the thickness map from an EELS spectral map using the `EELSfitter` framework[82, 83]. The `EELSfitter` framework uses machine learning to automatically subtract the zero-loss peak (ZLP) from all the EELS spectra in the spectroscopy map. It does so without any prior assumptions on the shape of the ZLP and provides a confidence interval for the remaining spectra. In turn, this spectrum, without the ZLP, is used to determine the single-scattering distribution (SSD), the local thickness, and the bandgap energy using the Kramers-Kroning relation [83, 84]. The local thickness map of the MoS_2 layer is depicted in fig. 2.6a and the bandgap energy in fig. 2.6b. The thickness map shows that the substrate and the MoS_2 layer together are roughly 15 nm thick. The thickness of the substrate itself is just below 14 nm, indicating that the MoS_2 layer is just over 1 nm thick. Together with the almost uniform bandgap energy map, which shows a bandgap energy of around 1.75 eV, we can conclude that the MoS_2 layer is most likely a monolayer when measurement errors are considered.

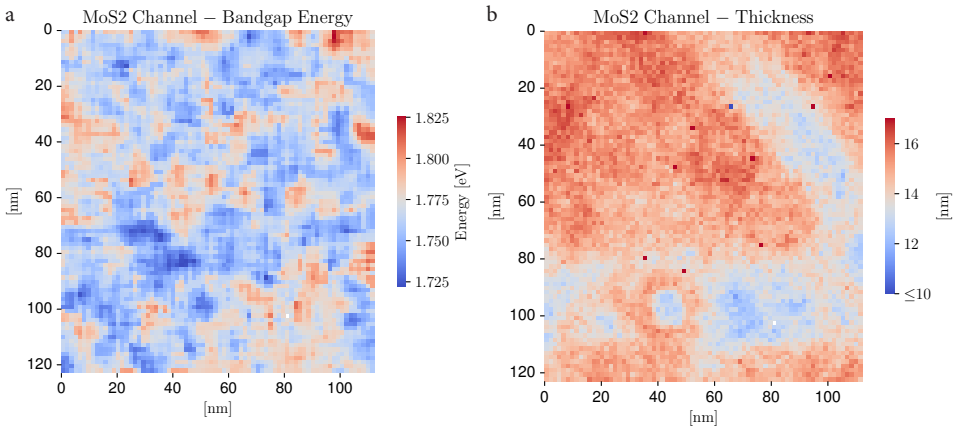

Figure 2.6: **a)** An EELS spectral map displaying the bandgap energy of the MoS_2 nanosheet. The almost uniform bandgap of 1.8 eV demonstrates that this nanosheet consists of a single layer of MoS_2. **b)** An EELS spectral map displaying the thickness of the MoS_2 nanosheet combined with the thickness of the Si_3N_4 substrate.

The MoO_3 nanorod from fig. 6.6 was synthesized using similar conditions to the MoS_2 nanostructure. In this case, the TEM grid was placed at a distance of 1.2 cm from 24.4 mg of MoO_2 powder. Furthermore, 50 mg of WO_3 powder was placed next to the MoO_2 powder. We determined the composition of the MoO_3 nanorod using energy dispersive X-ray (EDX) STEM. An annular darkfield (ADF) image of the MoO_3 nanorod is depicted in fig. 2.7a. An EDX spectral map of the tip of the MoO_3 nanorod is depicted in fig. 2.7b. The linescan in fig. 2.7c shows that the edges of the nanorod are sulfurized and contain MoS_2, whereas the center of the nanorod is still MoO_3. In chapter 6, we investigate the strain and rigid rotation in the MoO_3 nanorod using 4D-STEM.

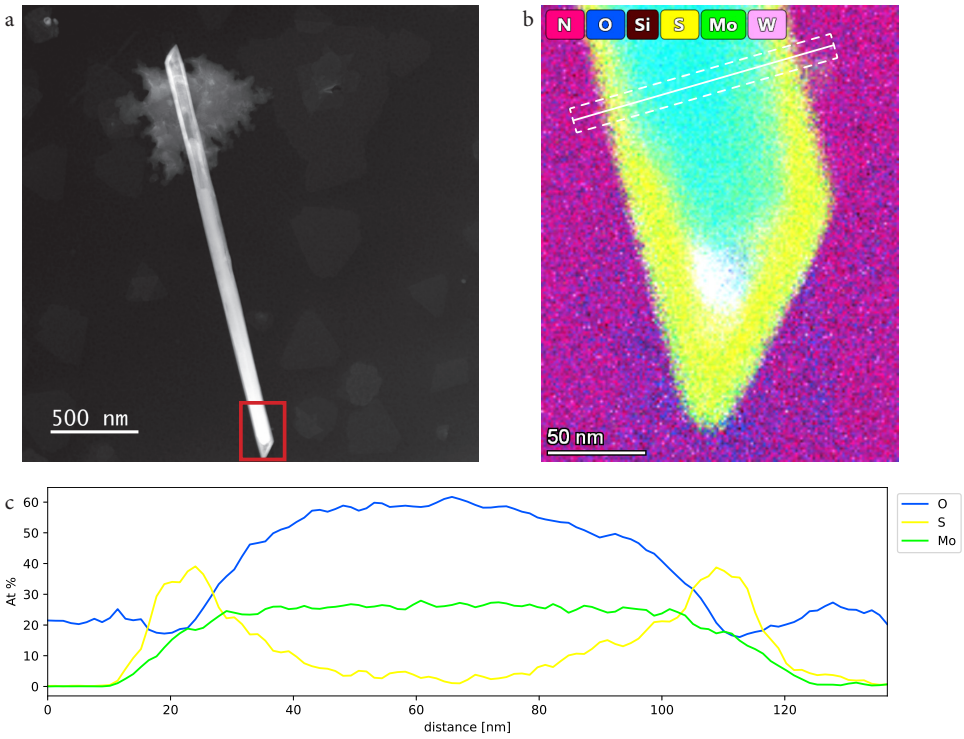

Figure 2.7: **a)** Low magnification high-angle annular diffraction (HAADF) image of a representative MoO_3 nanorod, synthesized using the CVD method detailed above. **b)** A energy dispersive X-ray (EDX) color map of the tip of the MoO_3, indicated by the red box in **a**. **c)** An EDX linescan across the width of the MoO_3 nanorod, indicated by the white line in **b**. The linescan shows the atomic percent (At%) for oxygen (blue), sulfur (yellow), and molybdenum (green). The MoS_2/MoO_3 core-shell nature of the nanorod is clearly visible.

REFERENCES

[1] K. S. Novoselov, A. K. Geim, S. V. Morozov, D. Jiang, Y. Zhang, S. V. Dubonos, I. V. Grigorieva, and A. A. Firsov, *Electric field effect in atomically thin carbon films,* Science **306**, 666 (2004).

[2] V. Singh, D. Joung, L. Zhai, S. Das, S. I. Khondaker, and S. Seal, *Graphene based materials: Past, present and future,* Progress in Materials Science **56**, 1178 (2011).

[3] F. Bonaccorso, Z. Sun, T. Hasan, and A. C. Ferrari, *Graphene photonics and optoelectronics,* Nature Photonics **4**, 611 (2010).

[4] J. H. Gosling, O. Makarovsky, F. Wang, N. D. Cottam, M. T. Greenaway, A. Patanè, R. D. Wildman, C. J. Tuck, L. Turyanska, and T. M. Fromhold, *Universal mobility characteristics of graphene originating from charge scattering by ionised impurities,* Communications Physics **4**, 30 (2021).

[5] K. Bolotin, K. Sikes, Z. Jiang, M. Klima, G. Fudenberg, J. Hone, P. Kim, and H. Stormer, *Ultrahigh electron mobility in suspended graphene,* Solid State Communications **146**, 351 (2008).

[6] L. Song, L. Ci, H. Lu, P. B. Sorokin, C. Jin, J. Ni, A. G. Kvashnin, D. G. Kvashnin, J. Lou, B. I. Yakobson, and P. M. Ajayan, *Large scale growth and characterization of atomic hexagonal boron nitride layers,* Nano Letters **10**, 3209 (2010).

[7] D. A. Bandurin, A. V. Tyurnina, G. L. Yu, A. Mishchenko, V. Zólyomi, S. V. Morozov, R. K. Kumar, R. V. Gorbachev, Z. R. Kudrynskyi, S. Pezzini, Z. D. Kovalyuk, U. Zeitler, K. S. Novoselov, A. Patanè, L. Eaves, I. V. Grigorieva, V. I. Fal'ko, A. K. Geim, and Y. Cao, *High electron mobility, quantum hall effect and anomalous optical response in atomically thin inse,* Nature Nanotechnology **12**, 223 (2017).

[8] T. Björkman, A. Gulans, A. V. Krasheninnikov, and R. M. Nieminen, *van der waals bonding in layered compounds from advanced density-functional first-principles calculations,* Phys. Rev. Lett. **108**, 235502 (2012).

[9] Y. Huang, Y.-H. Pan, R. Yang, L.-H. Bao, L. Meng, H.-L. Luo, Y.-Q. Cai, G.-D. Liu, W.-J. Zhao, Z. Zhou, L.-M. Wu, Z.-L. Zhu, M. Huang, L.-W. Liu, L. Liu, P. Cheng, K.-H. Wu, S.-B. Tian, C.-Z. Gu, Y.-G. Shi, Y.-F. Guo, Z. G. Cheng, J.-P. Hu, L. Zhao, G.-H. Yang, E. Sutter, P. Sutter, Y.-L. Wang, W. Ji, X.-J. Zhou, and H.-J. Gao, *Universal mechanical exfoliation of large-area 2d crystals,* Nature Communications **11**, 2453 (2020).

[10] R. A. Klemm, *Pristine and intercalated transition metal dichalcogenide superconductors,* Physica C: Superconductivity and its Applications **514**, 86 (2015), superconducting Materials: Conventional, Unconventional and Undetermined.

[11] M. S. El-Bana, D. Wolverson, S. Russo, G. Balakrishnan, D. M. Paul, and S. J. Bending, *Superconductivity in two-dimensional nbse2 field effect transistors,* Superconductor Science and Technology **26**, 125020 (2013).

[12] D. Varsano, M. Palummo, E. Molinari, and M. Rontani, *A monolayer transition-metal dichalcogenide as a topological excitonic insulator,* Nature Nanotechnology **15**, 367 (2020).

[13] Y. Guo, H. Deng, X. Sun, X. Li, J. Zhao, J. Wu, W. Chu, S. Zhang, H. Pan, X. Zheng, X. Wu, C. Jin, C. Wu, and Y. Xie, *Modulation of metal and insulator states in 2d ferromagnetic vs2 by van der waals interaction engineering,* Advanced Materials **29**, 1700715 (2017).

[14] C. Cui, F. Xue, W.-J. Hu, and L.-J. Li, *Two-dimensional materials with piezoelectric and ferroelectric functionalities,* npj 2D Materials and Applications **2**, 18 (2018).

[15] A. Nourbakhsh, A. Zubair, R. N. Sajjad, A. Tavakkoli K. G., W. Chen, S. Fang, X. Ling, J. Kong, M. S. Dresselhaus, E. Kaxiras, K. K. Berggren, D. Antoniadis, and T. Palacios, *Mos2 field-effect transistor with sub-10 nm channel length,* Nano Letters **16**, 7798 (2016).

[16] J. Kang, W. Liu, and K. Banerjee, *High-performance MoS2 transistors with low-resistance molybdenum contacts,* Applied Physics Letters **104**, 093106 (2014).

[17] Y. Xie, B. Zhang, S. Wang, D. Wang, A. Wang, Z. Wang, H. Yu, H. Zhang, Y. Chen, M. Zhao, B. Huang, L. Mei, and J. Wang, *Ultrabroadband mos2 photodetector with spectral response from 445 to 2717 nm,* Advanced Materials **29**, 1605972 (2017).

[18] V. R. Johnson and G. W. Vaughn, *Investigation of the Mechanism of MoS2 Lubrication in Vacuum,* Journal of Applied Physics **27**, 1173 (1956).

[19] G. Salomon, A. De Gee, and J. Zaat, *Mechano-chemical factors in mos2-film lubrication,* Wear **7**, 87 (1964).

[20] R. V. Mom, J. N. Louwen, J. W. M. Frenken, and I. M. N. Groot, *In situ observations of an active mos2 model hydrodesulfurization catalyst,* Nature Communications **10**, 2546 (2019).

[21] L. Huang, P. Luo, M. Xiong, R. Chen, Y. Wang, W. Xing, and J. Huang, *Selective reduction of nitroarenes with molybdenum disulfide,* Chinese Journal of Chemistry **31**, 987 (2013).

[22] D. Voiry, M. Salehi, R. Silva, T. Fujita, M. Chen, T. Asefa, V. B. Shenoy, G. Eda, and M. Chhowalla, *Conducting mos2 nanosheets as catalysts for hydrogen evolution reaction,* Nano Letters **13**, 6222 (2013).

[23] Y. Li, H. Wang, L. Xie, Y. Liang, G. Hong, and H. Dai, *Mos2 nanoparticles grown on graphene: An advanced catalyst for the hydrogen evolution reaction,* Journal of the American Chemical Society **133**, 7296 (2011).

[24] J. Zhang, J. Wu, H. Guo, W. Chen, J. Yuan, U. Martinez, G. Gupta, A. Mohite, P. M. Ajayan, and J. Lou, *Unveiling active sites for the hydrogen evolution reaction on monolayer mos2,* Advanced Materials **29**, 1701955 (2017).

[25] Z. Wu, B. Fang, Z. Wang, C. Wang, Z. Liu, F. Liu, W. Wang, A. Alfantazi, D. Wang, and D. P. Wilkinson, *Mos2 nanosheets: A designed structure with high active site density for the hydrogen evolution reaction,* ACS Catalysis **3**, 2101 (2013).

[26] L. Liu, X. Li, L.-C. Xu, R. Liu, and Z. Yang, *Effect of edge structure on the activity for hydrogen evolution reaction in mos2 nanoribbons,* Applied Surface Science **396**, 138 (2017).

[27] D.-R. Chen, J. Muthu, X.-Y. Guo, H.-T. Chin, Y.-C. Lin, G. Haider, C.-C. Ting, M. Kalbáč, M. Hofmann, and Y.-P. Hsieh, *Edge-dominated hydrogen evolution reactions in ultra-narrow mos2 nanoribbon arrays,* J. Mater. Chem. A **11**, 15802 (2023).

[28] I. Song, C. Park, and H. C. Choi, *Synthesis and properties of molybdenum disulphide: from bulk to atomic layers,* RSC Adv. **5**, 7495 (2015).

[29] R. M. A. Lieth, *Preparation and Crystal Growth of Materials with Layered Structures* (Springer Netherlands, 1977).

[30] O. Madelung, U. Rössler, and M. Schulz, *Mos2: crystal structure, physical properties: Datasheet from landolt-börnstein - group iii condensed matter non-tetrahedrally bonded binary compounds ii,* SpringerMaterials **41d** (2000).

[31] S. E. van Heijst, M. Bolhuis, A. Brokkelkamp, J. J. M. Sangers, and S. Conesa-Boj, *Heterostrain-driven bandgap increase in twisted ws2: A nanoscale study,* Advanced Functional Materials **34**, 2307893 (2024).

[32] A. Splendiani, L. Sun, Y. Zhang, T. Li, J. Kim, C.-Y. Chim, G. Galli, and F. Wang, *Emerging photoluminescence in monolayer mos2,* Nano Letters **10**, 1271 (2010).

[33] K. Kaasbjerg, K. S. Thygesen, and K. W. Jacobsen, *Phonon-limited mobility in n-type single-layer mos_2 from first principles,* Phys. Rev. B **85**, 115317 (2012).

[34] B. Radisavljevic, A. Radenovic, J. Brivio, V. Giacometti, and A. Kis, *Single-layer mos2 transistors,* Nature Nanotechnology **6**, 147 (2011).

[35] M. Amani, D.-H. Lien, D. Kiriya, J. Xiao, A. Azcatl, J. Noh, S. R. Madhvapathy, R. Addou, S. KC, M. Dubey, K. Cho, R. M. Wallace, S.-C. Lee, J.-H. He, J. W. Ager, X. Zhang, E. Yablonovitch, and A. Javey, *Near-unity photoluminescence quantum yield in mos₂,* Science **350**, 1065 (2015).

[36] C. Lee, H. Yan, L. E. Brus, T. F. Heinz, J. Hone, and S. Ryu, *Anomalous lattice vibrations of single- and few-layer mos2,* ACS Nano **4**, 2695 (2010).

[37] Y. Jung, J. Shen, Y. Sun, and J. J. Cha, *Chemically synthesized heterostructures of two-dimensional molybdenum/tungsten-based dichalcogenides with vertically aligned layers,* ACS Nano **8**, 9550 (2014).

[38] H. Li, Q. Zhang, C. C. R. Yap, B. K. Tay, T. H. T. Edwin, A. Olivier, and D. Baillargeat, *From bulk to monolayer mos2: Evolution of raman scattering,* Advanced Functional Materials **22**, 1385 (2012).

[39] X. Zhang, X.-F. Qiao, W. Shi, J.-B. Wu, D.-S. Jiang, and P.-H. Tan, *Phonon and raman scattering of two-dimensional transition metal dichalcogenides from monolayer, multilayer to bulk material,* Chem. Soc. Rev. **44**, 2757 (2015).

[40] Y. Jung, J. Shen, Y. Liu, J. M. Woods, Y. Sun, and J. J. Cha, *Metal seed layer thickness-induced transition from vertical to horizontal growth of MoS2 and WS2,* Nano Letters **14**, 6842 (2014).

[41] M. Bolhuis, J. Hernandez-Rueda, S. E. van Heijst, M. Tinoco Rivas, L. Kuipers, and S. Conesa-Boj, *Vertically-oriented mos2 nanosheets for nonlinear optical devices,* Nanoscale **12**, 10491 (2020).

[42] A. Steinhoff, J.-H. Kim, F. Jahnke, M. Rösner, D.-S. Kim, C. Lee, G. H. Han, M. S. Jeong, T. O. Wehling, and C. Gies, *Efficient excitonic photoluminescence in direct and indirect band gap monolayer mos2,* Nano Letters **15**, 6841 (2015).

[43] H.-P. Komsa and A. V. Krasheninnikov, *Effects of confinement and environment on the electronic structure and exciton binding energy of mos_2 from first principles,* Phys. Rev. B **86**, 241201 (2012).

[44] H. M. Hill, A. F. Rigosi, C. Roquelet, A. Chernikov, T. C. Berkelbach, D. R. Reichman, M. S. Hybertsen, L. E. Brus, and T. F. Heinz, *Observation of excitonic rydberg states in monolayer mos2 and ws2 by photoluminescence excitation spectroscopy,* Nano Letters **15**, 2992 (2015).

[45] T. Mueller and E. Malic, *Exciton physics and device application of two-dimensional transition metal dichalcogenide semiconductors,* npj 2D Materials and Applications **2**, 29 (2018).

[46] S. B. Nam, D. C. Reynolds, C. W. Litton, R. J. Almassy, T. C. Collins, and C. M. Wolfe, *Free-exciton energy spectrum in gaas,* Phys. Rev. B **13**, 761 (1976).

[47] D. W. Latzke, W. Zhang, A. Suslu, T.-R. Chang, H. Lin, H.-T. Jeng, S. Tongay, J. Wu, A. Bansil, and A. Lanzara, *Electronic structure, spin-orbit coupling, and interlayer interaction in bulk* mos_2 *and* ws_2*,* Phys. Rev. B **91**, 235202 (2015).

[48] L. Sun, J. Yan, D. Zhan, L. Liu, H. Hu, H. Li, B. K. Tay, J.-L. Kuo, C.-C. Huang, D. W. Hewak, P. S. Lee, and Z. X. Shen, *Spin-orbit splitting in single-layer* mos_2 *revealed by triply resonant raman scattering,* Phys. Rev. Lett. **111**, 126801 (2013).

[49] J. J. Carmiggelt, M. Borst, and T. van der Sar, *Exciton-to-trion conversion as a control mechanism for valley polarization in room-temperature monolayer ws2,* Scientific Reports **10**, 17389 (2020).

[50] C. Mai, A. Barrette, Y. Yu, Y. G. Semenov, K. W. Kim, L. Cao, and K. Gundogdu, *Many-body effects in valleytronics: Direct measurement of valley lifetimes in single-layer mos2,* Nano Letters **14**, 202 (2014).

[51] M. Tinoco, L. Maduro, M. Masaki, E. Okunishi, and S. Conesa-Boj, *Strain-dependent edge structures in mos2 layers,* Nano Letters **17**, 7021 (2017).

[52] H. Rostami, R. Asgari, and F. Guinea, *Edge modes in zigzag and armchair ribbons of monolayer mos2,* Journal of Physics: Condensed Matter **28**, 495001 (2016).

[53] Y. Li, Z. Zhou, S. Zhang, and Z. Chen, *Mos2 nanoribbons: High stability and unusual electronic and magnetic properties,* Journal of the American Chemical Society **130**, 16739 (2008).

[54] C. Ataca, H. Şahin, E. Aktürk, and S. Ciraci, *Mechanical and electronic properties of mos2 nanoribbons and their defects,* The Journal of Physical Chemistry C **115**, 3934 (2011).

[55] M. Tinoco, L. Maduro, and S. Conesa-Boj, *Metallic edge states in zig-zag vertically-oriented mos2 nanowalls,* Scientific Reports **9**, 15602 (2019).

[56] H.-L. Tang, M.-H. Chiu, C.-C. Tseng, S.-H. Yang, K.-J. Hou, S.-Y. Wei, J.-K. Huang, Y.-F. Lin, C.-H. Lien, and L.-J. Li, *Multilayer graphene–wse2 heterostructures for wse2 transistors,* ACS Nano **11**, 12817 (2017).

[57] G.-H. Lee, Y.-J. Yu, X. Cui, N. Petrone, C.-H. Lee, M. S. Choi, D.-Y. Lee, C. Lee, W. J. Yoo, K. Watanabe, T. Taniguchi, C. Nuckolls, P. Kim, and J. Hone, *Flexible and transparent mos2 field-effect transistors on hexagonal boron nitride-graphene heterostructures,* ACS Nano **7**, 7931 (2013).

[58] H. Tian, Z. Tan, C. Wu, X. Wang, M. A. Mohammad, D. Xie, Y. Yang, J. Wang, L.-J. Li, J. Xu, and T.-L. Ren, *Novel field-effect schottky barrier transistors based on graphene-mos2 heterojunctions,* Scientific Reports **4**, 5951 (2014).

[59] Y. Cao, V. Fatemi, S. Fang, K. Watanabe, T. Taniguchi, E. Kaxiras, and P. Jarillo-Herrero, *Unconventional superconductivity in magic-angle graphene superlattices,* Nature **556**, 43 (2018).

[60] H. Guo, X. Zhang, and G. Lu, *Shedding light on moiré excitons: A first-principles perspective,* Science Advances **6**, eabc5638 (2020).

[61] K. S. Novoselov, D. Jiang, F. Schedin, T. J. Booth, V. V. Khotkevich, S. V. Morozov, and A. K. Geim, *Two-dimensional atomic crystals,* Proceedings of the National Academy of Sciences **102**, 10451 (2005).

[62] A. K. Geim and I. V. Grigorieva, *Van der waals heterostructures,* Nature **499**, 419 (2013).

[63] G. Z. Magda, J. Pető, G. Dobrik, C. Hwang, L. P. Biró, and L. Tapasztó, *Exfoliation of large-area transition metal chalcogenide single layers,* Scientific Reports **5**, 14714 (2015).

[64] A. Jawaid, D. Nepal, K. Park, M. Jespersen, A. Qualley, P. Mirau, L. F. Drummy, and R. A. Vaia, *Mechanism for liquid phase exfoliation of mos2,* Chemistry of Materials **28**, 337 (2016).

[65] D. M. Sim, H. J. Han, S. Yim, M.-J. Choi, J. Jeon, and Y. S. Jung, *Long-term stable 2h-mos2 dispersion: Critical role of solvent for simultaneous phase restoration and surface functionalization of liquid-exfoliated mos2,* ACS Omega **2**, 4678 (2017).

[66] N. Liu, P. Kim, J. H. Kim, J. H. Ye, S. Kim, and C. J. Lee, *Large-area atomically thin mos2 nanosheets prepared using electrochemical exfoliation,* ACS Nano **8**, 6902 (2014).

[67] Z. Zeng, Z. Yin, X. Huang, H. Li, Q. He, G. Lu, F. Boey, and H. Zhang, *Single-layer semiconducting nanosheets: High-yield preparation and device fabrication,* Angewandte Chemie International Edition **50**, 11093 (2011).

[68] M. Acerce, D. Voiry, and M. Chhowalla, *Metallic 1t phase mos2 nanosheets as supercapacitor electrode materials,* Nature Nanotechnology **10**, 313 (2015).

[69] C. Muratore, J. J. Hu, B. Wang, M. A. Haque, J. E. Bultman, M. L. Jespersen, P. J. Shamberger, M. E. McConney, R. D. Naguy, and A. A. Voevodin, *Continuous ultra-thin MoS2 films grown by low-temperature physical vapor deposition,* Applied Physics Letters **104**, 261604 (2014).

[70] L. Li, R. Long, and O. V. Prezhdo, *Why chemical vapor deposition grown mos2 samples outperform physical vapor deposition samples: Time-domain ab initio analysis,* Nano Letters **18**, 4008 (2018).

[71] E. Sudarshan, *Surface Engineering Series Volume 2: Chemical Vapor Deposition*, Chemical Vapor Deposition (ASM International, 2000).

[72] Y. Zhan, Z. Liu, S. Najmaei, P. M. Ajayan, and J. Lou, *Large-area vapor-phase growth and characterization of mos2 atomic layers on a sio2 substrate,* Small **8**, 966 (2012).

[73] N. Choudhary, J. Park, J. Y. Hwang, and W. Choi, *Growth of large-scale and thickness-modulated mos2 nanosheets,* ACS Applied Materials & Interfaces **6**, 21215 (2014).

[74] S. Hussain, M. A. Shehzad, D. Vikraman, M. F. Khan, J. Singh, D.-C. Choi, Y. Seo, J. Eom, W.-G. Lee, and J. Jung, *Synthesis and characterization of large-area and continuous mos2 atomic layers by rf magnetron sputtering,* Nanoscale **8**, 4340 (2016).

[75] C. Stern, S. Grinvald, M. Kirshner, O. Sinai, M. Oksman, H. Alon, O. E. Meiron, M. Bar-Sadan, L. Houben, and D. Naveh, *Growth Mechanisms and Electronic Properties of Vertically Aligned MoS2,* Scientific Reports 2018 8:1 **8**, 1 (2018).

[76] Y. Yu, C. Li, Y. Liu, L. Su, Y. Zhang, and L. Cao, *Controlled scalable synthesis of uniform, high-quality monolayer and few-layer mos2 films,* Scientific Reports **3**, 1866 (2013).

[77] K. Kang, S. Xie, L. Huang, Y. Han, P. Y. Huang, K. F. Mak, C.-J. Kim, D. Muller, and J. Park, *High-mobility three-atom-thick semiconducting films with wafer-scale homogeneity,* Nature **520**, 656 (2015).

[78] Y.-C. Lin, W. Zhang, J.-K. Huang, K.-K. Liu, Y.-H. Lee, C.-T. Liang, C.-W. Chu, and L.-J. Li, *Wafer-scale mos2 thin layers prepared by moo3 sulfurization,* Nanoscale **4**, 6637 (2012).

[79] Y.-H. Lee, X.-Q. Zhang, W. Zhang, M.-T. Chang, C.-T. Lin, K.-D. Chang, Y.-C. Yu, J. T.-W. Wang, C.-S. Chang, L.-J. Li, and T.-W. Lin, *Synthesis of large-area mos2 atomic layers with chemical vapor deposition,* Advanced Materials **24**, 2320 (2012).

[80] L. Maduro, C. de Boer, M. Zuiddam, E. Memisevic, and S. Conesa-Boj, *Molybdenum nanopillar arrays: Fabrication and engineering,* Physica E: Low-dimensional Systems and Nanostructures **134**, 114903 (2021).

[81] L. Maduro, M. Noordam, M. Bolhuis, L. Kuipers, and S. Conesa-Boj, *Position-controlled fabrication of vertically aligned mo/mos2 core–shell nanopillar arrays,* Advanced Functional Materials **32**, 2107880 (2022).

[82] L. I. Roest, S. E. van Heijst, L. Maduro, J. Rojo, and S. Conesa-Boj, *Charting the low-loss region in electron energy loss spectroscopy with machine learning,* Ultramicroscopy **222**, 113202 (2021).

[83] A. Brokkelkamp, J. ter Hoeve, I. Postmes, S. E. van Heijst, L. Maduro, A. V. Davydov, S. Krylyuk, J. Rojo, and S. Conesa-Boj, *Spatially Resolved Band Gap and Dielectric Function in Two-Dimensional Materials from Electron Energy Loss Spectroscopy,* The Journal of Physical Chemistry A **126**, 1255 (2022).

[84] R. Egerton, *Limits to the spatial, energy and momentum resolution of electron energy-loss spectroscopy,* Ultramicroscopy **107**, 575 (2007).

3

VERTICALLY-ORIENTED MoS_2 NANOSHEETS FOR NONLINEAR OPTICAL DEVICES

Transition metal dichalcogenides such as MoS_2 represent promising candidates for building blocks of ultra-thin nanophotonic devices. For such applications, vertically-oriented MoS_2 (v-MoS_2) nanosheets could be advantageous as compared to conventional horizontal MoS_2 (h-MoS_2) given that their inherent broken symmetry would favor an enhanced nonlinear response. However, the current lack of a controllable and reproducible fabrication strategy for v-MoS_2 limits the exploration of this potential. Here, we present a systematic study of the growth of v-MoS_2 nanosheets based on the sulfurization of a pre-deposited Mo–metal seed layer. We demonstrate that the sulfurization process at high temperatures is driven by the diffusion of sulfur from the vapor–solid interface to the Mo seed layer. Furthermore, we verify an enhanced nonlinear response in the resulting v-MoS_2 nanostructures as compared to their horizontal counterparts. Our results represent a stepping stone toward the fabrication of low-dimensional TMD-based nanostructures for versatile nonlinear nanophotonic devices.

Parts of this chapter has been published in *Nanoscale* 12, 10491 (2020) by **M. Bolhuis**, J. Hernandez-Rueda, S. E. van Heijst, M. Tinoco Rivas, L. Kuipers, and S. Conesa-Boj.

3.1. INTRODUCTION

Two-dimensional (2 D) materials, such as transition metal dichalcogenides (TMDs), have been extensively studied for a wide range of applications, including optoelectronics devices [1, 2] and catalysis, [3] among others. Specifically, these materials exhibit numerous remarkable electronic and optical properties thanks to their broken inversion symmetry [4–6]. Significant attention has been recently devoted to their nonlinear optical response [7–9], which makes TMDs ideal building blocks for ultra-thin nonlinear photonic devices [10, 11]. Such nonlinear optical effects have been demonstrated in horizontal MoS_2 (h-MoS_2) monolayers, displaying a marked dependence on the specific crystalline symmetry and orientation [12]. For instance, a nonlinear optical response has been reported at the atomic edges of h-MoS_2 crystals, where translation symmetry is broken [13]. These findings suggest that vertically-oriented MoS_2 (v-MoS_2) nanosheets, a configuration that maximizes the number of exposed edge sites, could represent a promising platform to enhance the second-order nonlinear response and realize a novel candidate for the building blocks of high-efficiency nanophotonic devices.

Considerable progress has been achieved in the understanding of the growth dynamics of horizontal MoS_2. Different fabrication methods have been employed, such as chemical vapor deposition (CVD) techniques [10, 14], the direct sulfurization of pre-deposited molybdenum (Mo) seed layer [15, 16], the solvothermal/hydrothermal approach [17], and by using a vapor phase reaction with MoO_3 [18, 19]. On the other hand, the growth mechanism of its vertical counterpart, v-MoS_2, remains poorly understood. Several attempts at explaining the growth of vertically oriented MoS_2 nanostructures have been put forward. For instance, in the context of growth strategies based on the sulfurization of a pre-existing Mo-metal layer [20], it has been shown that a low reaction temperature of 550 °C results in v-MoS_2 with the kinetically-controlled growth being diffusion limited. Furthermore, it has been reported that the orientation of the resulting MoS_2 layers with respect to the substrate is sensitive to the thickness of the Mo-metal layer [21]. Specifically, thicker and more uniform Mo-metal seed layers lead to a higher fraction of v-MoS_2 layers. Additionally, theoretical models have also been constructed aiming to describe the synthesis of vertically-oriented MoS_2 based on the solid-vapor reaction [20–23], though most of these predictions remain to be verified.

Given this state of affairs, achieving further progress toward a controllable and reproducible fabrication strategy for v-MoS_2 requires detailed studies of the associated growth mechanisms. Here, we present a systematic investigation of the growth mechanism of vertical MoS2 nanosheets based on the sulfurization of a pre-deposited Mo-metal seed layer. Thanks to an extensive structural cross-section characterization by means of transmission electron microscopy (TEM), we demonstrate that the sulfurization mechanism for temperatures between 600 and 700 °C proceeds via diffusion. These findings imply that the growth propagates from the vapor-solid interface inwards into the Mo seed layer during the Sulfur reaction. In addition, we investigate the prospects of the resulting v-MoS2 nanostructures for nonlinear optical applications. We verify an enhanced nonlinear response as compared to their h-MoS2 counterparts, confirmed by the observation of second-harmonic generation and sum-frequency generation. Our results provide a stepping stone toward the large-scale fabrication of high-quality v-MoS_2

nanosheets and represent a crucial step in a program aimed at designing and fabricating low-dimensional nanostructures to develop efficient and versatile nonlinear optical devices based on 2D materials.

3.2. INVESTIGATING THE MORPHOLOGY OF THE MoS_2 NANOSHEETS SYNTHESIZED USING CVD

A two-step process was used to synthesize the vertically oriented MoS_2 nanosheets by means of the sulfurization of a pre-deposited Mo-metal layer. A thick Mo seed layer of 700 nm was chosen in order to ascertain the dependence on the reaction time and the sulfurization depth. The sulfurization process was carried out inside a three-zone hot-wall horizontal tube. Before and during the sulfurization, an Argon gas flow was used to prevent any possible oxidation, as well as a carrier to transport the Sulphur vapor phase to the substrate. Further details about the growth process are described in section 2.4. The resulting MoS_2 nanosheet's orientation was investigated as a function of the reaction temperature. For these studies, we considered several growth temperatures in the range between 500 °C and 700 °C. We now highlight the results obtained for the two limiting cases corresponding to 500 °C and 700 °C temperatures. Figures 3.1a and 3.1b display top-view scanning electron microscopy (SEM) images of the sulfurized Mo-metal layer at 500 and 700 °C, respectively. One observes marked differences in the morphology between the results obtained in the two growths. While the vertical nature of the MoS_2 nanosheets grown at a temperature of 500 °C is unambiguous from the SEM image (fig. 3.1a), the same inspection is less conclusive for the sample grown at 700 °C, whose surface exhibits a granular-like aspect (fig. 3.1b).

Figures 3.1c and 3.1d depict Raman spectroscopy measurements taken in the samples grown at 500 and 700°C, respectively. These Raman spectra are dominated by the in-plane E^1_{2g} and the out-of-plane A_{1g} Raman modes. The appearance and position of these peaks are consistent with a trigonal prismatic ($2H-MoS_2$) crystal phase, further confirming the successful MoS_2 growth [24]. Interestingly, we find that for the sample grown at 500 (700) °C, the ratio of intensities between the A_{1g} and E^1_{2g} peaks increases by a factor of 2 (3) as compared to regular MoS_2 flakes, where the two peaks exhibit comparable intensities [21]. Given that the A_{1g} and E^1_{2g} Raman peaks are associated respectively with the out-of-plane and in-plane vibration modes, these results suggest that our specimens exhibit the presence of v-MoS_2 nanosheets in the samples grown at both temperatures, therefore indicating a higher density of exposed edges. Furthermore, in fig. 3.1c (3.1d), a third peak located at 287 (283) cm-1 and associated with the E_{1g} Raman mode is also observed. This mode is forbidden in backscattering experiments [25], which implies that it should not be observed when the incident laser beam is perpendicular to the basal plane, as happens for horizontal MoS_2. The presence of the E_{1g} mode thus indicates that the laser beam is no longer perpendicular to the incident (basal) plane, providing further confirmation of the presence of vertically oriented (with respect to the substrate) MoS_2 nanosheets in both samples.

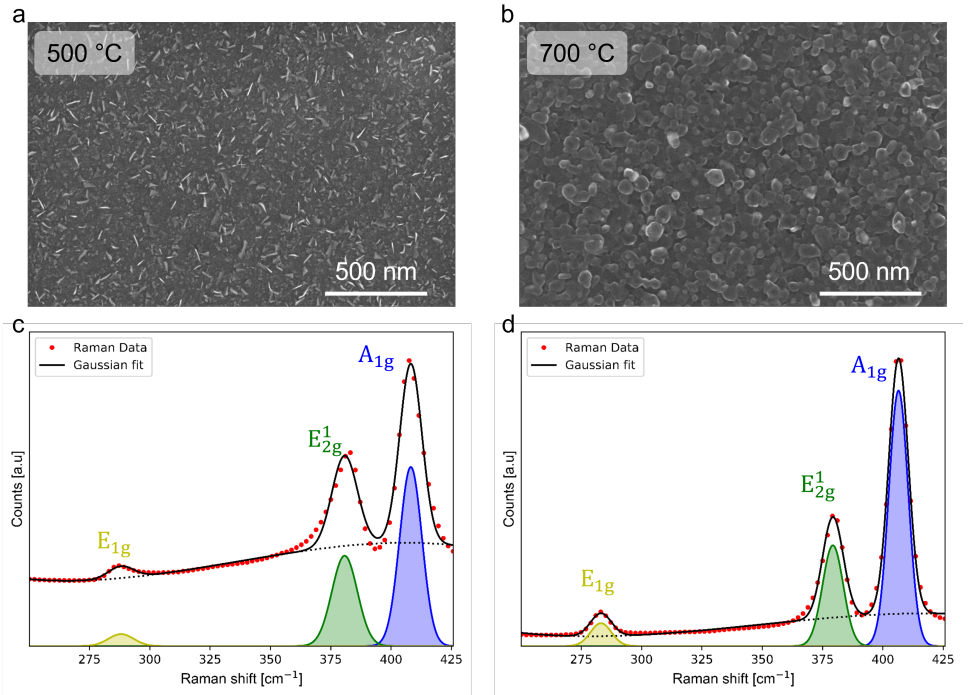

Figure 3.1: **a-b)** Top-view SEM images of the surface of the samples sulfurized at 500 and 700 °C, respectively. **c-d)** The associated Raman spectra, where the two main Raman modes (A_{1g} and E^1_{2g}) are visible along with the smaller E_{1g} mode. The similarities between the two spectra suggest the vertical orientation of the MoS2 nanosheets in the samples grown at both temperatures.

To investigate the orientation of the grown MoS_2, we further complement this surface analysis with a cross-section study performed by focus ion beam (FIB) followed by SEM inspection. For the sample grown at 500 °C (fig. 3.2a), the thickness of the original Mo seed layer (700 nm) remains mostly unaffected after sulfurization. However, for the sample grown at 700 °C (fig. 3.2b), the Mo seed layer is close to being fully sulfurized. From the cross-section SEM image, one observes that the original thickness of the Mo-metal layer has been reduced down to a length of 200 nm, with the rest of the Mo layer sulfurized into MoS_2. In this specific case, the final sulfurized layer has a length of 1.95 µm, representing an increase with a factor of around three compared to the thickness of the initial Mo layer. From these experimental results, one can, therefore, distinguish two distinctive dynamics for the growth of the v-MoS_2 nanosheets. On the one hand, at 500 °C, the sulfur only reacts on the immediate Mo seed layer surface, leading to vertically-standing MoS_2 as can be observed in the top-view SEM image in figure fig. 3.1a. On the other hand, at 700 °C, the sulfur diffuses through the Mo seed layer by consuming it and forming v-MoS_2 layers. To investigate the crystalline quality of the vertical MoS_2 grown at 700 °C, we have produced a cross-section sample using FIB and then analyzed it by means of transmission electron microscopy (TEM). The three different contrasts

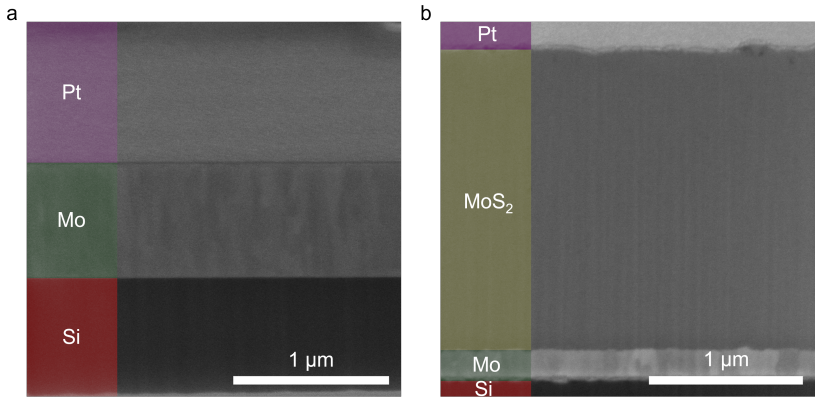

Figure 3.2: **(a)** and **(b)** SEM images of the FIB cross-sections corresponding to the samples shown in figs. 3.1a and 3.1b. In **a**, the sample grown at 500 °C, we observe three distinctive regions with different contrasts associated with the protective Pt layer (magenta), the Mo seed layer (green), and the Si substrate (red). Note that in this case, the presence of MoS2 is restricted to the sample's surface. In **(b)**, grown at 700 °C, the four regions are associated with the protective Pt (magenta), the MoS2 layer with vertical nanosheets (yellow), the Mo seed layer (green), and the Si substrate (red).

observed in fig. 3.3a reveal the sequence MoS_2, Mo-metal layer, and Silicon. The high-resolution TEM (HRTEM) measurements performed at the MoS_2/Mo interface (fig. 3.3b) indicate that the MoS_2 grows vertically with respect to the Mo seed layer. The distance between two neighboring MoS_2 layers was measured to be about 0.65 nm (fig. 3.3c), consistent with previous results in the literature [26]. Energy dispersive X-ray spectroscopy (EDX) measurements along the length of the whole cross-section (fig. 3.3d) provide clear evidence of the sulfur diffusion into the Mo seed layer that results into the growth of the vertically-oriented MoS_2 nanosheets.

3.3. INVESTIGATING SULFUR DIFFUSION THROUGH MOLYBDENUM METAL DURING MoS_2 GROWTH

In order to further elucidate the sulfurization mechanism of the v-MoS_2 at 700 °C, we have sulfurized for different times samples containing each 700 nm of Mo seed layer. Subsequently, we prepared, with FIB, cross-section lamellas for TEM and EDX inspection that allowed us to determine the thicknesses of the MoS_2 layer and of the consumed Mo. We have only considered reaction times equal to and larger than 15 min, in a way that the Mo seed layer will always be completely sulfurized, see fig. A.3.4. In fig. 3.4a, we display the value of the consumed Mo seed layer as a function of the reaction time. These measurements are fitted to a model of the form:

$$z = K\,(t - t_0)^n\,, \tag{3.1}$$

where z and t are the thickness of the consumed Mo seed layer and the reaction time,

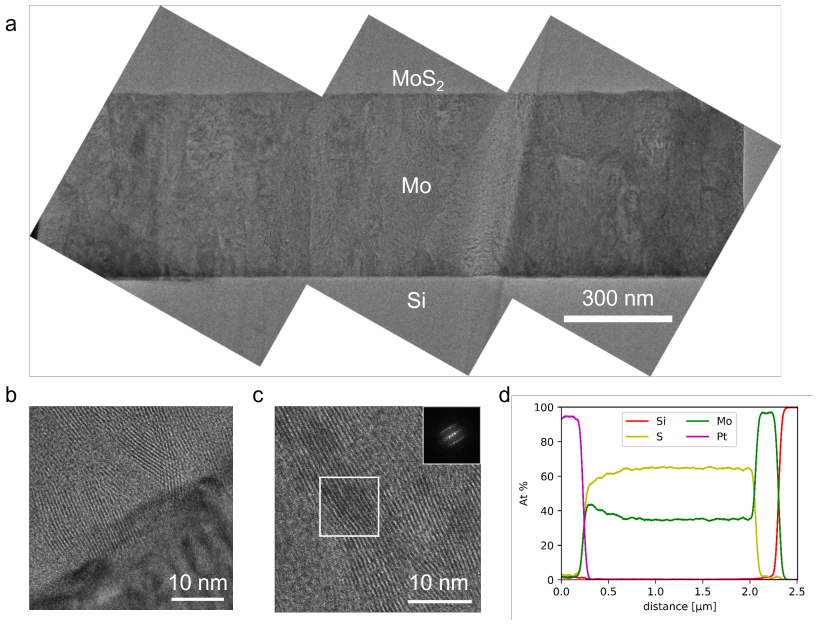

Figure 3.3: **(a)** Reconstructed low-magnification bright-field TEM image of a sample sulfurized at 700 °C, displaying the Mo seed layer sandwiched between v-MoS2 on the top and the Si substrate on the bottom. **(b)** HRTEM image of the interface region showing how the v-MoS2 nanosheets arise from the Mo-metal layer. **(c)** HRTEM image of a region containing only v-MoS2 nanosheets, together with the FFT calculated in the area highlighted with a white square in the inset. **(d)** EDX line scan of a sample sulfurized for 1 hour at 700 °C indicating its elemental composition.

respectively. The best-fit value for the growth exponent n is found to be 0.48. The fact that n is very close to $\frac{1}{2}$ is consistent with a sulfurization process dominated by the diffusion mechanism. Since the growth exponent is essentially 0.5, we can use the following relation:

$$z_{dif} = 2\sqrt{Dt} \tag{3.2}$$

to extract the diffusion coefficient of sulfur within the Mo seed layer from the data. The best-fit value for D is calculated to be 20.7 nm^2/s, similar to the diffusion coefficients measured for sulfur in other metals [27]. Therefore, Our findings confirm that the diffusion of the sulfur drives the reaction and that the consumption of sulfur occurs predominantly at the boundary between the Mo seed layer and the grown v-MoS_2 layers. These results are consistent with theoretical models of the diffusion-reaction growth proposed for synthesizing vertically oriented MoS_2 [22]. From the HR−TEM cross-section lamella analysis (fig. A.3.3), we also found an orientation-disordered region extending from the surface to the first 20 nm, where both vertical and horizontal MoS_2 nanosheets are present. The reaction mechanism in this initial region appears to be self-limited [22], but then from this point onward, the growth front changes into v-MoS_2 being dominated by the

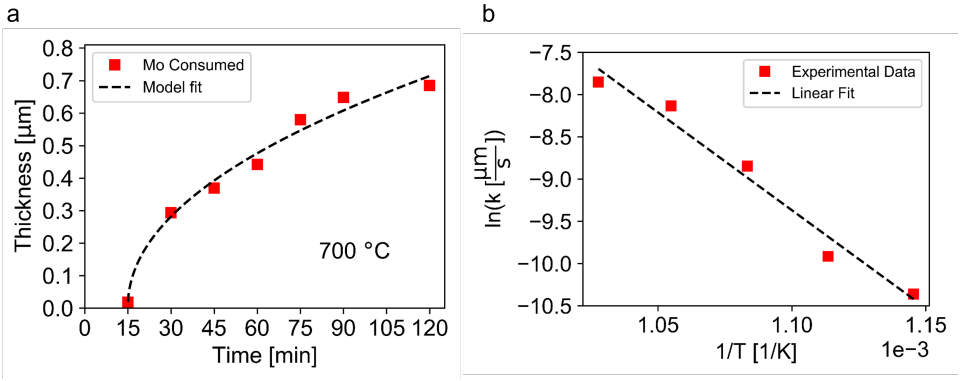

Figure 3.4: **(a)** The thicknesses of the consumed Mo-metal layer as a function of the reaction time for the sample grown at 700°C. The dotted line corresponds to a model fit of the form $z = K(t - t_o)^n$. The best-fit growth exponent is found to be n=0.48, very close to the n=0.5 expected for a diffusion-driven process. **(b)** An Arrhenius diagram where the logarithm of the rate constant k is represented as a function of the inverse of the reaction temperature. The linear fit to the data allows us to determine the activation energy required to sulfurize the Mo seed layer.

diffusion kinetics of sulfur, as discussed above.

The influence of the temperature on the rate of the consumed Mo seed layer was also examined in the range between 600 and 700 °C. The lower range of this interval corresponds to the minimum temperature required to initiate the diffusion of the sulfur within the Mo seed layer [17]. A fixed reaction time of 30 min was adopted in these experiments. Figure 3.4b highlights the effect of the rate of the MoS_2 thickness growth as a function of the reaction temperature. The experimental Arrhenius plot can be fitted very well by a straight line to determine the activation energy, which turns out to be 192.44 kJ/mol. These findings provide additional evidence that the sulfur diffuses in the range between 600 and 700 °C through the Mo seed layer, leading to the phase transformation into vertically-oriented MoS_2 nanosheets.

3.4. NONLINEAR OPTICAL PHENOMENA IN VERTICAL-ORIENTED MoS_2 NANOSHEETS

As mentioned above, TMD materials have generated ample attention because of their nonlinear optical response [7]. In particular, second and third-order nonlinear optical processes have recently been demonstrated in few-layer MoS_2 flakes. Second-harmonic (SHG) and sum-frequency generation (SFG) have been shown to be more efficiently generated in thin MoS_2 flakes with a few atomic layers [28, 29]. The intensity of both processes exponentially increases when decreasing the number of layers, thus revealing MoS_2 monolayers to be the most efficient thickness in order to generate second-order processes. Moreover, due to inversion symmetry breaking, only odd-layered MoS_2 flakes present second-order processes,(i.e. MoS_2 layered semiconductors have vanishing $\chi_V^{(2)}$

due to symmetry when the number of layers is even). In contrast, third-order processes, such as four-wave mixing (FWM), gradually increase their intensity with increasing number of layers (reaching saturation for a certain thickness) irrespective of their parity. It is also worth noting that the study of nondegenerate optical processes in MoS_2 flakes using multi-color multi-phonon spectroscopy is very limited in the literature [7, 12].

Here, we use multi-photon spectroscopy to explore the nonlinear optical response of the synthesized vertical MoS_2 nanosheets reported in this work and compare the results with those of their h-MoS_2 counterparts. Figure 3.5a depicts the spectra of the nonlinear emission when excited with a laser pulse at 776 nm (blue line) and with two synchronized laser pulses at 776 nm and 1210 nm (red line). The labels indicate the nonlinear mechanisms that originate the emission at each spectral peak. The spectra in fig. 3.5a illustrate all the above-mentioned processes. In order to benchmark the response of the v-MoS_2 nanosheets in fig. 3.5a, we also measured the nonlinear emission of the horizontally oriented case.

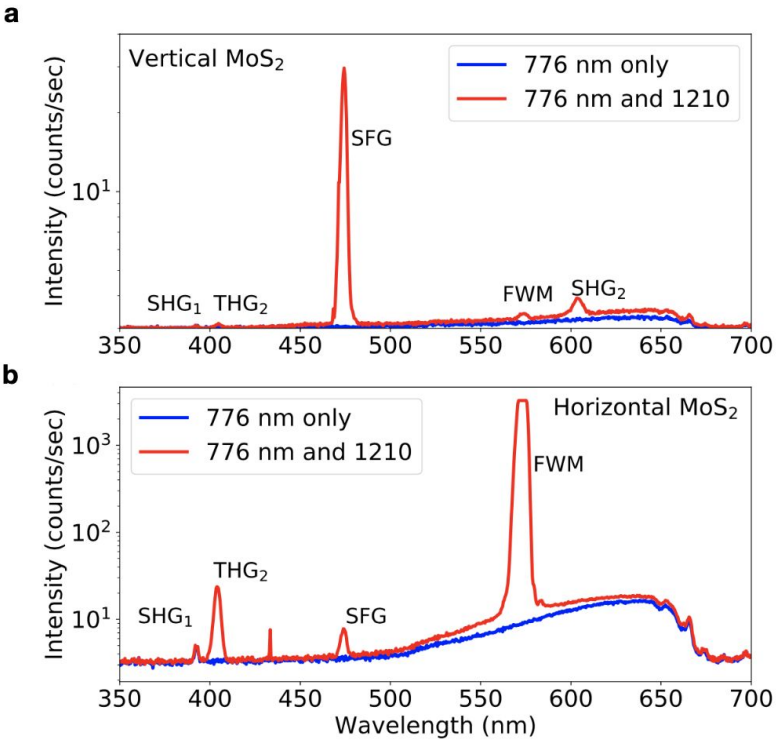

Figure 3.5: Spectra from a vertical **(a)** and horizontal **(b)** MoS_2 nanosheets simultaneously illuminated with ultrashort laser pulses at 776 nm and 1210 nm. The labels next to each peak indicate the corresponding nonlinear mechanisms that mediate each emission. The repletion rate of the laser during the experiments was 80 MHz and the pulse duration 230 fs. The energy of the laser pulses used in **(a)** were 7.5 pJ at 776 nm and 15.4 pJ at 1210 nm in **(b)** 380 pJ at 776 nm and 48 pJ at 1210 nm. Note that we present the spectra in counts per second by using integration times of **(a)** 150 seconds and **(b)** 20 seconds.

Figure 3.5b shows the spectra collected upon laser illumination with a single 776 nm beam (blue line) and both beams at 776 nm and 1210 nm (red line). Although both MoS_2 geometries exhibit the same emission peaks (except SHG_2), it is clear that vertically-oriented MoS_2 nanosheets favor second-order processes (i.e. SFG in fig. 3.5a) over third-order processes (i.e. THG and FWM in fig. 3.5a). In contrast, the horizontal configuration shows the opposite trend where third-order processes dominate, and second-order processes are three orders of magnitude smaller due to inversion symmetry, in agreement with previous results in the literature [12, 30].

By using the intensity of the spectral peaks for SFG and SHG along with the power of the excitation beams, one can estimate the relative ratio of the nonlinear susceptibility [7, 31]. The relevant formulae related to second harmonic generation and sum frequency generation are provided in the SI-G. The second-order susceptibility ratios between the vertical and horizontal geometries extracted from SHG and SFG turn out to be $\chi_V^{(2)}/\chi_H^{(2)}|_{SHG} = 22.9 \pm 1.5$ and $\chi_V^{(2)}/\chi_H^{(2)}|_{SFG} = 24.7 \pm 1.0$, respectively. These results indicate that vertically-oriented MoS_2 nanosheets significantly favor second-order nonlinear processes as compared to their horizontal counterparts. As mentioned above, this enhancement can be traced back to the effects of inversion symmetry breaking at the exposed edges of the nanosheets

3.5. CONCLUSION

In this chapter, we have reported the controllable and reproducible fabrication of vertically-oriented MoS_2 nanosheets. We have demonstrated that the phase transformation from Mo seed layers to vertically-oriented molybdenum disulfide ($2H-MoS_2$) can be achieved by means of reacting the pre-deposited Mo-metal layer with sulfur at relatively high temperatures, in the range between 600 and 700 °C. Following a systematic characterization analysis of these v-MoS_2 nanosheets using TEM and EDX, we have established that in this range of temperatures, the sulfurization mechanism proceeds via diffusion.

Furthermore, we have investigated the nonlinear optical response of the resulting v-MoS_2 nanostructures, including second-harmonic generation, and found an enhanced second-order nonlinear response as compared to the h-MoS_2 case. The latter property could be explained by the effects of inversion symmetry breaking at the exposed edges of the nanosheets. Therefore, our findings represent a stepping stone towards the fabrication of low-dimensional TMD-based nanostructures for versatile nonlinear nanophotonic devices.

A.3. APPENDIX

A.3.1. ARGON FLOW DEPENDENCE

Figure A.3.1 displays the variation of the MoS_2 thickness as the Ar flow rate is increased. We found that as the Ar flow rate increased, the MoS_2 thickness increased as well, until a maximum value of 1um at an Ar flow rate of 75 sccm. From this point onwards, the MoS_2 thickness decreased with further increases of the Ar flow rate. For this reason, in the design of the growth parameters, we only considered Ar flow rates above 75 sccm, for which the expected trend that higher flow rates slow the reaction and lead to thinner MoS_2 was verified. Specifically, for all the experiments presented in chapter 3, we fixed the Ar flow at a value of 150 sccm [20]. It is worth mentioning that the growth of v-MoS_2 nanosheets via sulfurization can be strongly dependent on the Ar flow when the furnace tube is affected by flow instabilities. In fig. A.3.1, we also display two points (red crosses) corresponding to growths affected by such instabilities in the tube furnace. The results of these growths differed significantly from the main trend and thus were not considered further.

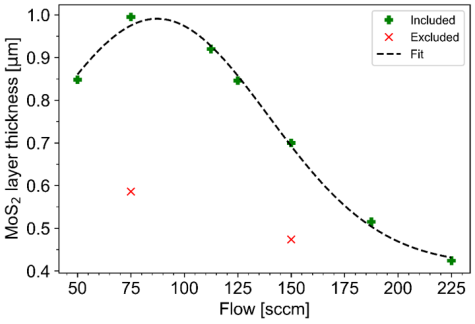

Figure A.3.1: The thickness of the grown MoS_2 layer as a function of the Ar gas flow. The model fit is based on the data points labeled with a green cross. We observe that for Ar flows above 75 sccm, the MoS_2 thickness decreases monotonically as the flow increases.

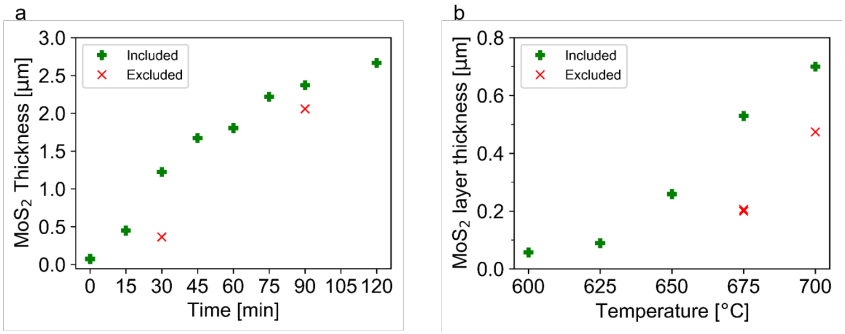

Figure A.3.2: Same as fig. A.3.1 with the resulting MoS_2 thicknesses represented as a function of the reaction time **(a)** and of the reaction temperature **(b)**.

A.3.2. STRUCTURAL CHARACTERIZATION OF V-MoS_2 NANOSHEETS

Figure A.3.3 displays a cross-section HRTEM analysis of one of the representative specimens sulfurized at a temperature of 700 °C. Measurements were taken at different regions of the cross-section lamella: at the Mo seed layer (fig. A.3.3a), at the interface between the Mo seed layer and the v-MoS_2 nanosheets (fig. A.3.3c), and the first nanometers from the surface of the sulfurized lamella (fig. A.3.3d). In the first case, we also include the corresponding FFT indicating that the Mo-metal crystallizes in the BCC structure. In the latter case, the MoS_2 nanosheets were found to exhibit random orientations: in the first 20 nm from the surface (beneath the Pt protective layer), vertical and horizontal nanosheets appear simultaneously, as can be seen from the orientations of lattice fringes in fig. A.3.3d. Afterward, the rest of the grown MoS_2 is restricted to the vertical orientation. Different scenarios have been proposed to explain the appearance of an orientation-disordered region where both horizontal and vertical MoS_2 are present. Our experimental findings are consistent with the theoretical modeling of the diffusion-reaction growth proposed for synthesizing vertically oriented v-MoS_2 [22]. This model describes the v-MoS_2 growth from the co-existence of two different morphologies, the first an orientation-disordered region extending from the surface to the first few nanometers, and the region containing exclusively vertically-oriented MoS_2 nanosheets.

A.3.3. CHEMICAL ANALYSIS OF THE CROSS-SECTION TEM LAMELLAS OF THE V-MoS_2 NANOSHEET

A Python analysis code was developed to process and interpret the EDX line spectra data. In the following, we describe how the S/Mo atomic ratio was calculated at three different locations of the chemical spectra. Figure A.3.4a displays the elemental atomic percentage profile is taken along the cross-section lamella, from the protective layer Pt (violet line) to the Silicon wafer (red line). Figure A.3.4b shows the same raw data after applying a Savitzky-Golay filter to smoothen the stochastic fluctuations. Figure A.3.4c represents the data restricted to the points we defined as the top and bottom of the MoS_2 sulfurized region. We determined the crosspoint between the Pt and S (from the top) and between the S and Mo (in the bottom), and then we chose three different locations to calculate the S/Mo ratio automatically. We selected these three locations at distances of 35% (close to the surface), 50%, and 65%, respectively, as seen in fig. A.3.4d. All the calculated S/Mo ratios were then collected and plotted in fig. A.3.4e. From this figure, we can observe that for times below 15 minutes, the sulfurization is not fully complete. From the same plot, we can also observe that the S/Mo ratio remains stable along the lamella.

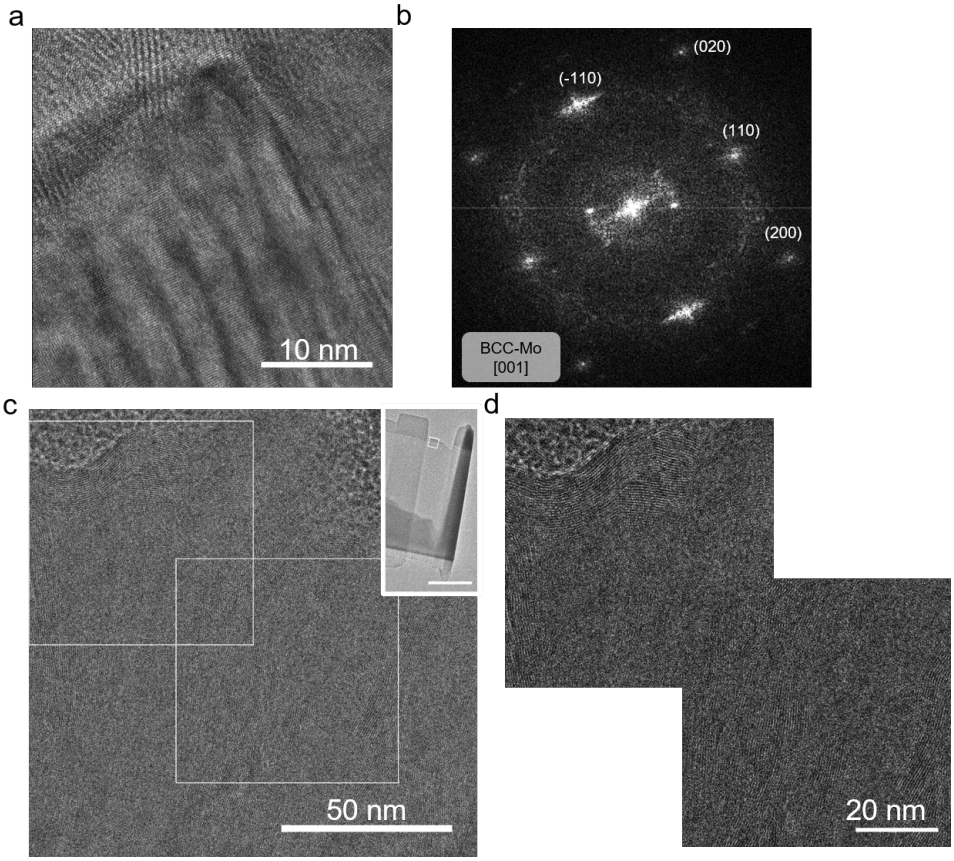

Figure A.3.3: **a)** HRTEM image taken from a representative specimen sulfurized at 700 °C displaying a region of the Mo-metal seed layer. **b)** the FFT of the HRTEM image in **a**, indicating that the Mo is characterized by the BCC crystal phase. **c)** HRTEM image of the upper region of the grown MoS_2 (see inset) immediately below the Pt protective layer. **d)** The inverse FFT is calculated from the two regions marked with white squares in **c**.

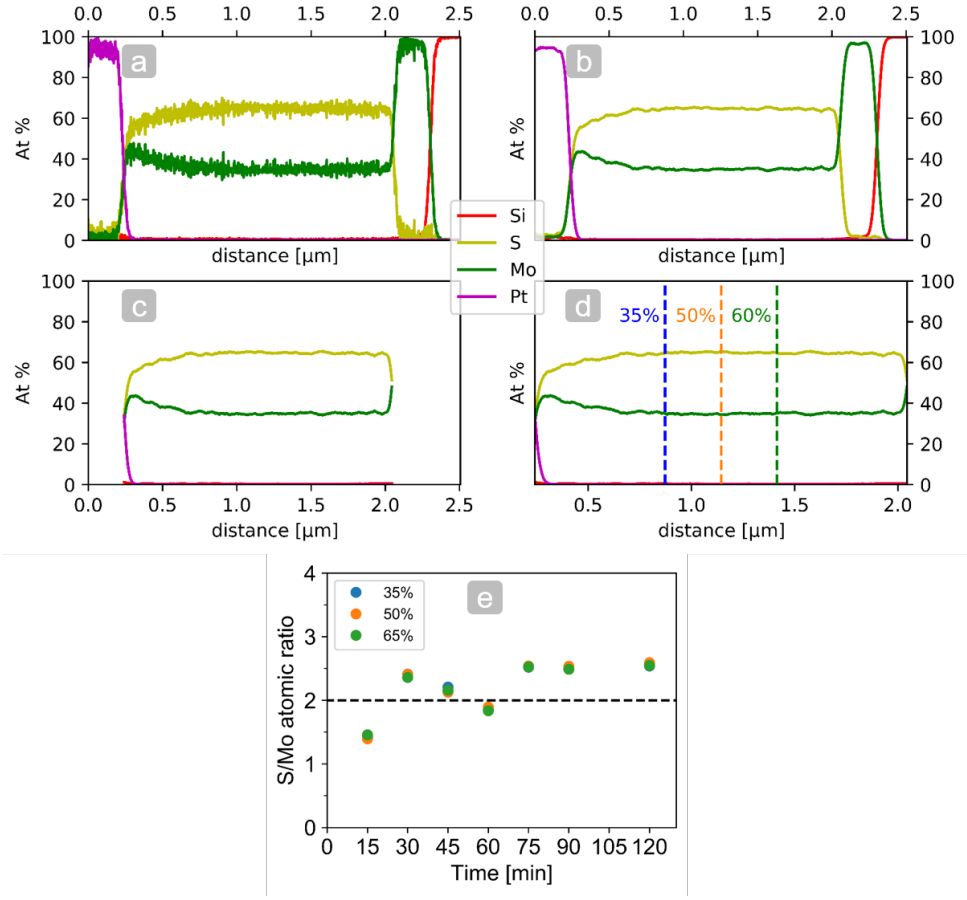

Figure A.3.4: **a)** The elemental atomic percentage profile taken along the cross-section lamella, from the protective layer Pt (violet line) to the Silicon wafer (red line). **b)** The same raw data after applying a Savitzky-Golay filter in order to smoothen the stochastic fluctuations. **c)** The same data is now restricted to the points defined as the top and bottom of the MoS_2 sulfurized region. **d)** The three different locations selected to calculate the S/Mo ratio, see text. **e)** Summary of the calculated S/Mo ratios calculated as a function of the reaction time.

A.3.4. RAMAN SPECTROSCOPY OF EXFOLIATED MoS_2 FLAKES.

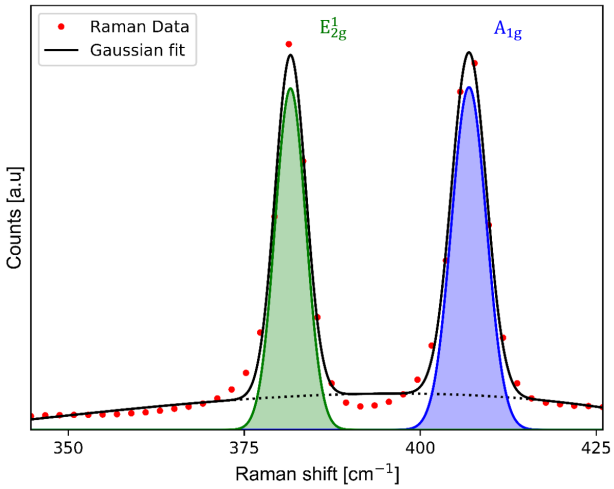

Figure A.3.5: Raman emission spectra taken on a regular exfoliated MoS2 flake using the same experimental set-up as in figs. 3.1c and 3.1d. We observe that the intensity of the two dominating Raman modes, E^1_{2g} and A_{1g}, is very similar, and therefore, the ratio of intensities is close to unity. These two Raman peaks are associated with the in-plane and out-of-plane vibration modes, respectively.

A.3.5. HORIZONTALLY-ORIENTED MoS_2 SAMPLE PREPARATION

The horizontal MoS_2 flakes were directly grown onto a Si3N4 TEM grid. A vapor-solid growth mechanism was used. The Si_3N_4 TEM grid was placed next to a Mo-seed layer in the middle zone of the tube furnace, with the sulfur located upstream from the sample. From this step onwards, the rest of the growth process is the same as the one described in section 2.4. Vertically-oriented MoS_2 sample preparation. On the other hand, the vertical MoS_2 specimen was prepared using the ultramicrotomy technique [32]. This method allows us to prepare the specimen, ensuring that a large area is available for TEM inspection and nonlinear optical measurements.

A.3.6. NONLINEAR RESPONSE OF A MoS_2 SPECIMEN

To calibrate our experimental multi-photon spectroscopy system, we studied the nonlinear response of a MoS_2 specimen and thin nanostructured gold specimens [33]. Figure A.3.6 illustrates several nonlinear signals as a function of the laser energy. The solid lines display fits to monomial functions. The fits to the four-wave mixing signal illustrate a linear and quadratic behavior with the energy of the laser at ω_2 and ω_1 (i.e. $\omega_{FWM} = 2\omega_1 - \omega 2$). The fits to the third harmonic generation signal originated from the interaction of the laser at % and the sample follows a cubic response (i.e. $\omega_{THG} = 3\omega_2$. The laser energy dependencies observed here are consistent with the equations of the polarization vector [31]. In the main text, we discuss the ratio of the second-order nonlinear susceptibilities of the vertical $\chi^{(2)}_V$ and horizontally $\chi^{(2)}_H$ oriented MoS_2 nanosheets. Here, we detail the formulae of the second-order polarization vector (2) for SHG and SFG used

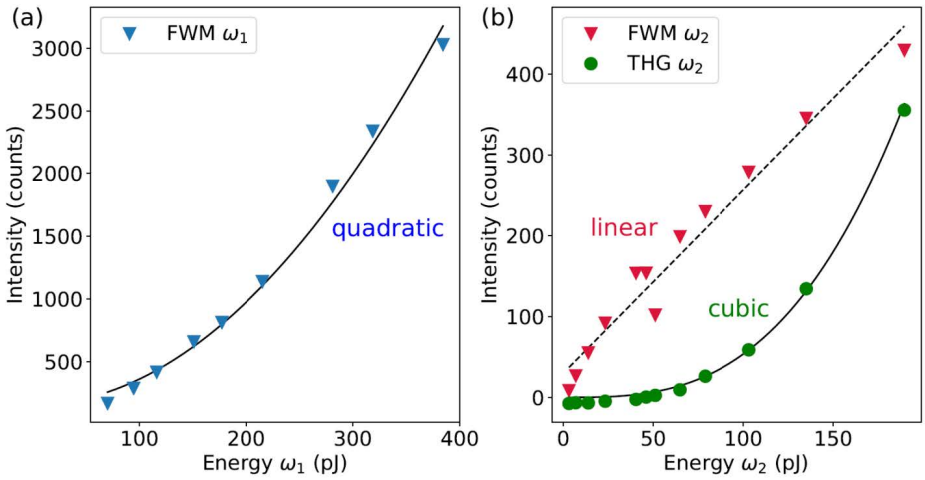

Figure A.3.6: **a)** FWM signal as a function of the laser energy per pulse at ω_1. **b)** FWM and THG signals as a function of the laser energy per pulse at ω_2. The energies of the beams at ω_1 in **b** and ω_2 in **a** correspond to 56 pJ and 51 pJ at a repetition rate of 80 MHz and with a pulse duration of approximately 230 fs. The solid lines are fits to monomial functions of first, second and third order

for the calculation of the ratios. These can also be found in Nonlinear Optics by R. Boyd [31].

$$\begin{aligned} P^{(2)}_{\mathrm{SHG}} \equiv \chi^{(2)} E_2 E_2 \rightarrow \chi^{(2)} \propto \sqrt{I_{\mathrm{SHG}}/I_2 I_2} \\ P^{(2)}_{\mathrm{SFG}} \equiv \chi^{(2)} E_1 E_2 \rightarrow \chi^{(2)} \propto \sqrt{I_{\mathrm{SHG}}/I_1 I_2} \end{aligned} \tag{3.3}$$

where E_1 and E_2 are the electric field strength of the laser at 776 nm and 1210 nm, respectively, and I_1 and I_2 are the intensities of the laser. By using the experimental laser parameters combined with the spectral peaks presented in the spectra, Therefore, we can obtain the ratios of the second-order susceptibilities both using SHG and SFG signals:

$$\begin{aligned} \left.\frac{\chi^{(2)}_V}{\chi^{(2)}_H}\right|_{\mathrm{SHG}} = \frac{\sqrt{I^V_{\mathrm{SHG}}/I^V_2 I^V_2}}{\sqrt{I^H_{\mathrm{SHG}}/I^H_2 I^H_2}} \\ \left.\frac{\chi^{(2)}_V}{\chi^{(2)}_H}\right|_{\mathrm{SFG}} = \frac{\sqrt{I^V_{\mathrm{SFG}}/I^V_2 I^V_2}}{\sqrt{I^H_{\mathrm{SFG}}/I^H_2 I^H_2}} \end{aligned} \tag{3.4}$$

We note that considering that the MoS_2 layer thickness is smaller than the optical penetration depth and the coherence length of the laser, we neglect both absorption and phase matching effects in our estimation of the nonlinear susceptibility [34, 35].

REFERENCES

[1] L. Britnell, R. M. Ribeiro, A. Eckmann, R. Jalil, B. D. Belle, A. Mishchenko, Y. J. Kim, R. V. Gorbachev, T. Georgiou, S. V. Morozov, A. N. Grigorenko, A. K. Geim, C. Casiraghi, A. H. Castro Neto, and K. S. Novoselov, *Strong light-matter interactions in heterostructures of atomically thin films,* Science **340**, 1311 (2013).

[2] C. H. Lee, G. H. Lee, A. M. Van Der Zande, W. Chen, Y. Li, M. Han, X. Cui, G. Arefe, C. Nuckolls, T. F. Heinz, J. Guo, J. Hone, and P. Kim, *Atomically thin p–n junctions with van der Waals heterointerfaces,* Nature Nanotechnology 2014 9:9 **9**, 676 (2014).

[3] T. F. Jaramillo, K. P. Jørgensen, J. Bonde, J. H. Nielsen, S. Horch, and I. Chorkendorff, *Identification of active edge sites for electrochemical h2 evolution from mos2 nanocatalysts,* Science **317**, 100 (2007).

[4] M. Tinoco, L. Maduro, and S. Conesa-Boj, *Metallic edge states in zig-zag vertically-oriented MoS2 nanowalls,* Scientific Reports **9**, 1 (2019).

[5] S. H. Gong, F. Alpeggiani, B. Sciacca, E. C. Garnett, and L. Kuipers, *Nanoscale chiral valley-photon interface through optical spin-orbit coupling,* Science **359**, 443 (2018).

[6] Z. Sun, A. Martinez, and F. Wang, *Optical modulators with 2D layered materials,* (2016).

[7] T. Jakubczyk, V. Delmonte, M. Koperski, K. Nogajewski, C. Faugeras, W. Langbein, M. Potemski, and J. Kasprzak, *Radiatively Limited Dephasing and Exciton Dynamics in MoSe2 Monolayers Revealed with Four-Wave Mixing Microscopy,* Nano Letters **16**, 5333 (2016).

[8] A. Autere, H. Jussila, Y. Dai, Y. Wang, H. Lipsanen, and Z. Sun, *Nonlinear Optics with 2D Layered Materials,* (2018).

[9] X. Zhang, S. Zhang, Y. Xie, J. Huang, L. Wang, Y. Cui, and J. Wang, *Tailoring the nonlinear optical performance of two-dimensional MoS2 nanofilms via defect engineering,* Nanoscale **10**, 17924 (2018).

[10] K. Kang, S. Xie, L. Huang, Y. Han, P. Y. Huang, K. F. Mak, C.-J. Kim, D. Muller, and J. Park, *High-mobility three-atom-thick semiconducting films with wafer-scale homogeneity,* Nature **520**, 656 (2015).

[11] A.-P. Luo, M. Liu, X.-D. Wang, Q.-Y. Ning, W.-C. Xu, and Z.-C. Luo, *Few-layer MoS_2-deposited microfiber as highly nonlinear photonic device for pulse shaping in a fiber laser [Invited],* Photonics Research **3**, A69 (2015).

[12] D. Li, W. Xiong, L. Jiang, Z. Xiao, H. Rabiee Golgir, M. Wang, X. Huang, Y. Zhou, Z. Lin, J. Song, S. Ducharme, L. Jiang, J. F. Silvain, and Y. Lu, *Multimodal Nonlinear Optical Imaging of MoS2 and MoS2-Based van der Waals Heterostructures,* ACS Nano **10**, 3766 (2016).

[13] X. Yin, Z. Ye, D. A. Chenet, Y. Ye, K. O'Brien, J. C. Hone, and X. Zhang, *Edge nonlinear optics on a MoS2 atomic monolayer,* Science **344**, 488 (2014).

[14] Y. Yu, C. Li, Y. Liu, L. Su, Y. Zhang, and L. Cao, *Controlled scalable synthesis of uniform, high-quality monolayer and few-layer MoS2 films,* Scientific Reports **3**, 1 (2013).

[15] Y. Zhan, Z. Liu, S. Najmaei, P. M. Ajayan, and J. Lou, *Large-area vapor-phase growth and characterization of mos2 atomic layers on a sio2 substrate,* Small **8**, 966 (2012).

[16] N. Choudhary, J. Park, J. Y. Hwang, and W. Choi, *Growth of large-scale and thickness-modulated mos2 nanosheets,* ACS Applied Materials & Interfaces **6**, 21215 (2014).

[17] X. Zhang, S. Zhang, B. Chen, H. Wang, K. Wu, Y. Chen, J. Fan, S. Qi, X. Cui, L. Zhang, and J. Wang, *Direct synthesis of large-scale hierarchical MoS2 films nanostructured with orthogonally oriented vertically and horizontally aligned layers,* Nanoscale **8**, 431 (2015).

[18] Y. H. Lee, X. Q. Zhang, W. Zhang, M. T. Chang, C. T. Lin, K. D. Chang, Y. C. Yu, J. T. W. Wang, C. S. Chang, L. J. Li, and T. W. Lin, *Synthesis of large-area MoS 2 atomic layers with chemical vapor deposition,* Advanced Materials **24**, 2320 (2012).

[19] S. Najmaei, Z. Liu, W. Zhou, X. Zou, G. Shi, S. Lei, B. I. Yakobson, J. C. Idrobo, P. M. Ajayan, and J. Lou, *Vapour phase growth and grain boundary structure of molybdenum disulphide atomic layers,* Nature Materials **12**, 754 (2013).

[20] D. Kong, H. Wang, J. J. Cha, M. Pasta, K. J. Koski, J. Yao, and Y. Cui, *Synthesis of MoS2 and MoSe2 films with vertically aligned layers,* Nano Letters **13**, 1341 (2013).

[21] Y. Jung, J. Shen, Y. Liu, J. M. Woods, Y. Sun, and J. J. Cha, *Metal seed layer thickness-induced transition from vertical to horizontal growth of MoS2 and WS2,* Nano Letters **14**, 6842 (2014).

[22] C. Stern, S. Grinvald, M. Kirshner, O. Sinai, M. Oksman, H. Alon, O. E. Meiron, M. Bar-Sadan, L. Houben, and D. Naveh, *Growth Mechanisms and Electronic Properties of Vertically Aligned MoS2,* Scientific Reports 2018 8:1 **8**, 1 (2018).

[23] H. Wang, Z. Lu, S. Xu, D. Kong, J. J. Cha, G. Zheng, P. C. Hsu, K. Yan, D. Bradshaw, F. B. Prinz, and Y. Cui, *Electrochemical tuning of vertically aligned MoS2 nanofilms and its application in improving hydrogen evolution reaction,* Proceedings of the National Academy of Sciences of the United States of America **110**, 19701 (2013).

[24] R. Saito, Y. Tatsumi, S. Huang, X. Ling, and M. S. Dresselhaus, *Raman spectroscopy of transition metal dichalcogenides,* Journal of Physics: Condensed Matter **28**, 353002 (2016).

[25] X. Zhang, X. F. Qiao, W. Shi, J. B. Wu, D. S. Jiang, and P. H. Tan, *Phonon and Raman scattering of two-dimensional transition metal dichalcogenides from monolayer, multilayer to bulk material,* Chemical Society Reviews **44**, 2757 (2015).

[26] H. Li, Q. Zhang, C. C. R. Yap, B. K. Tay, T. H. T. Edwin, A. Olivier, and D. Baillargeat, *From bulk to monolayer MoS 2: Evolution of Raman scattering,* Advanced Functional Materials **22**, 1385 (2012).

[27] F. Moya, G. E. Moya-Gontier, and F. Cabane-Brouty, *Sulphur Diffusion in Copper: Departure from the Arrhenius Plot,* physica status solidi (b) **35**, 893 (1969).

[28] L. M. Malard, T. V. Alencar, A. P. M. Barboza, K. F. Mak, and A. M. De Paula, *Observation of intense second harmonic generation from MoS2 atomic crystals,* Physical Review B - Condensed Matter and Materials Physics **87**, 1 (2013).

[29] A. Säynätjoki, L. Karvonen, H. Rostami, A. Autere, S. Mehravar, A. Lombardo, R. A. Norwood, T. Hasan, N. Peyghambarian, H. Lipsanen, K. Kieu, A. C. Ferrari, M. Polini, and Z. Sun, *Ultra-strong nonlinear optical processes and trigonal warping in MoS2 layers,* Nature Communications 2017 8:1 **8**, 1 (2017).

[30] R. I. Woodward, R. T. Murray, C. F. Phelan, R. E. De Oliveira, T. H. Runcorn, E. J. Kelleher, S. Li, E. C. De Oliveira, G. J. Fechine, G. Eda, and C. J. De Matos, *Characterization of the second- and third-order nonlinear optical susceptibilities of monolayer MoS2 using multiphoton microscopy,* 2D Materials **4**, 011006 (2016).

[31] R. W. Boyd, *Nonlinear Optics,* Nonlinear Optics (2008), 10.1201/9781420004694.ch5.

[32] M. O. Cichocka, M. Bolhuis, S. E. Van Heijst, and S. Conesa-Boj, *Robust Sample Preparation of Large-Area In- And Out-of-Plane Cross Sections of Layered Materials with Ultramicrotomy,* ACS Applied Materials and Interfaces **12**, 15867 (2020).

[33] M. L. Noordam, J. Hernandez-Rueda, L. Y. Talsma, and L. Kuipers, *Plasmon-induced enhancement of nonlinear optical processes in a double-resonant metallic nanostructure grating,* Applied Physics Letters **116**, 101101 (2020).

[34] H. Wang, F. Liu, W. Fu, Z. Fang, W. Zhou, and Z. Liu, *Two-dimensional heterostructures: Fabrication, characterization, and application,* Nanoscale **6**, 12250 (2014).

[35] N. Kumar, S. Najmaei, Q. Cui, F. Ceballos, P. M. Ajayan, J. Lou, and H. Zhao, *Second harmonic microscopy of monolayer mos_2,* Phys. Rev. B **87**, 161403 (2013).

4

4D-STEM: Principles, Methodologies, and Advanced Data Analysis

The flexibility and high spatial resolution of scanning transmission electron microscopy (STEM) have made it an often-used technique for nanomaterial research. In recent years, advances in detector technology have made it possible to record complete convergent beam electron diffraction (CBED) patterns for every scan position, widening the capabilities of STEM systems. Four-dimensional STEM (4D–STEM) is an extension of conventional STEM capable of advanced imaging techniques that superseded conventional STEM. In this chapter, we first formulate a general description of the STEM image-forming process. Next, we discuss image formation in conventional STEM techniques. Finally, we use the center-of-mass (CoM) method to demonstrate the power of 4D–STEM. We break down the direct linear relation between the shift in the CoM of the CBED pattern and local potential fields in the specimen. The theoretical framework laid down in this chapter is crucial for a better understanding of the 4D–STEM techniques that follow in the subsequent chapters.

4.1. INTRODUCTION

The development of four-dimensional (4D) scanning transmission electron microscopy (STEM) has been a milestone in materials science, enabled by advancements in detector technology and computational power. STEM is a technique that combines the principles of transmission electron microscopy (TEM) and scanning electron microscopy (SEM) [1]. In STEM, a focused electron beam is scanned across the sample, and the transmitted electrons are collected by a detector beneath the sample, providing detailed imaging and diffraction patterns. Key to this evolution is the development of pixelated detectors like the Electron Microscope Pixel Array Detector (EMPAD)[2, 3]. These detectors record the intensity and position of transmitted electrons with high precision and enable advanced imaging capabilities. The EMPAD, known for its high dynamic range and fast readout speed, allows for capturing a wide range of electron intensities at each pixel. These features are crucial for detailed image reconstruction and the analysis of complex diffraction patterns from each pixel of the scanned area. Such detailed data collection facilitates reconstructing a sample's three-dimensional structure and properties, offering an unparalleled view of the material at the atomic level. Among these advanced applications, 4D STEM facilitates phase orientation and strain mapping within samples from distortions and shifts in diffraction patterns. This strain mapping is crucial for understanding nanoscale mechanical behavior. Additionally, its phase contrast analysis, which manipulates the electron beam to vary image contrast, is invaluable for revealing subtle variations in composition or thickness. This technique proves helpful in investigating biological samples or materials with inherently low contrast.

With 4D STEM, nano diffraction becomes attainable, enabling the study of crystallographic defects and the determination of crystallographic phases at the nanoscale. Analyzing diffraction patterns acquired at each pixel makes it possible to identify and characterize defects such as dislocations, stacking faults, and grain boundaries [4, 5]. In addition to defect characterization, the derived diffraction data from 4D STEM can provide insights into the atomic arrangement and crystal structure at the nanoscale. This information is of immense value in materials science, as it assists in optimizing and tailoring material properties for specific applications. Furthermore, 4D STEM enables imaging capabilities through ptychography [6, 7]. This advanced technique combines diffraction and scanning microscopy. Conducting precise electron beam scans across the sample and collecting the corresponding diffraction patterns enables the reconstruction of high-resolution images. This method notably improves contrast and spatial resolution, making it particularly effective for examining samples with complex structures or those exhibiting weak scattering contrast.

Advances in 4D STEM methodology have opened up new avenues for characterizing and understanding materials at the nanoscale. This technique stands out by simultaneously capturing diffraction and direct imaging data, empowering researchers to explore the structural, compositional, and electronic properties of materials in unprecedented detail. Integrating high-resolution imaging with comprehensive diffraction data offers an extensive view of the sample, facilitating in-depth analysis and interpretation of material behavior.

This chapter aims to provide a comprehensive overview of the methodology employed in 4D STEM with a focus on the electron microscope pixel array detector (EMPAD). It is structured to cover the fundamentals of 4D STEM, including the core principles of STEM imaging, various detector technologies, and the benefits of employing EMPAD in 4D STEM. Additionally, the chapter will provide a detailed discussion of the experimental setup for 4D STEM, along with strategies for effective data acquisition and analysis.

4.2. BASIC PRINCIPLES OF 4D STEM ELECTRON MICROSCOPY

The image formation process in STEM commences with a crucial component: the scanning electron probe. This probe is generated by a demagnification of the electron wave emitted from a source, a task accomplished by the condenser lens. The condenser lens's role extends past the electron probe's demagnification. It performs a Fourier transformation on the electron wave function. This transformation effectively shifts the wave function from the back focal plane to the image plane. Notably, within the unique setup of an electron microscope, this image plane aligns with the sample plane, as illustrated in fig. 4.1.

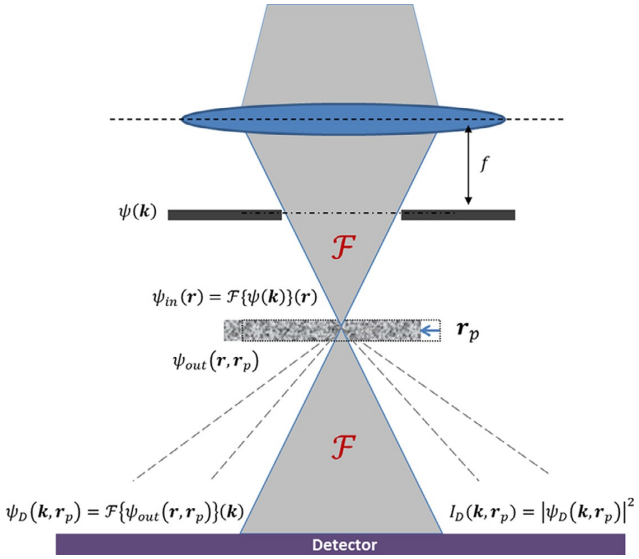

Figure 4.1: Schematic overview of the STEM image forming process. The wavefunction on the detector plane can be described as the Fourier transform of the wavefunction exiting the specimen after interacting with it. Reproduced from Lazić et al. [8], with permission from ©Elsevier (2017).

The wave function at the back focal plane contains any variations in phase and amplitude caused by the aberrations o of the condenser lens and the spatial and temporal incoherences of the electron source. We will denote the wave function at the back focal plane as $\psi(\vec{k})$, where $\vec{k} = (k_x, k_y)$, following the analytical insight provided by Lazić et al. [8]. The position vector $\vec{k}$ corresponds to the position in the reciprocal space of the Fourier transform. In a conventional TEM system, the incoming electron beam is

constrained by a condenser aperture denoted as $A(\vec{k})$. Consequently, the wave function becomes zero at positions where this aperture obstructs the electron beam.

$$\psi(\vec{k}) = 0 \text{ for } |\vec{k}| > k_A \tag{4.1}$$

Now, we possess a comprehensive depiction of the wave function of the electron probe at the sample plane:

$$\psi_{\text{in}}(\vec{r}) = \mathscr{F}\left\{\psi(\vec{k})\right\}(\vec{r}) \text{ for } |\vec{k}| < k_A \tag{4.2}$$

where $\vec{r} = (r_x, r_y)$ is a position vector in the sample plane. The interaction between the electron probe and the sample leads to alterations in the wave function's phase and amplitude. This modification can be described using a transmission function, assuming the sample is non-magnetic and thin.

$$T(\vec{r}) = e^{i\varphi(\vec{r})} \tag{4.3}$$

The imaginary part of the complex value $\phi(\vec{r})$, where $\vec{r}$ represents the position vector, can be decomposed into its real and imaginary parts. The imaginary part reflects variations in the amplitude, while the real part represents variations in the phase. When considering a thin sample, it is assumed to primarily induce changes in the wave function phase. This approximation, known as the phase object approximation (POA), allows for a direct interpretation of the phase shift $\phi(\vec{r})$:

$$\varphi(\vec{r}) = \sigma V(\vec{r}) \tag{4.4}$$

The interaction parameter, denoted as σ, is determined by several factors. It depends on Planck's constant h and the charge e, relativistic mass m, and the electron's wavelength (λ). The relationship between these quantities can be expressed as $\sigma = 2\pi me\lambda/h^2$. Here, the interaction parameter σ encapsulates the interplay between these fundamental properties of the electron, providing insight into the electron's behavior in various physical phenomena. Equation (4.4) demonstrates the direct proportionality between the phase shift $\varphi(\vec{r})$ and the projected electrostatic potential $V(\vec{r})$ of the sample. It is widely accepted that $V(\vec{r})$ remains constant over time, ensuring a time-independent nature. This assumption is crucial for our subsequent analysis.

Now, incorporating the definition of the phase shift $V(\vec{r})$ from eq. (4.4) and the transfer function outlined in eq. (4.3), we can formulate an expression for the wave function of the exit wave at the sample plane:

$$\psi_{\text{out}}(\vec{r}) = \psi_{\text{in}}(\vec{r}) \cdot T(\vec{r}) = \psi_{\text{in}}(\vec{r}) e^{i\varphi(\vec{r})} = \psi_{\text{in}}(\vec{r}) e^{i\sigma V(\vec{r})} \tag{4.5}$$

The exit wave function from the sample plane undergoes projection onto the detector plane by utilizing another lens. This lens, similar to the previous one, effectively performs a Fourier transform on the wave function. As a consequence, a new wave function ψ_D is obtained at the detector plane, and it is expressed as follows:

$$\psi_D(\vec{k}) = \mathscr{F}\left\{\psi_{\text{out}}(\vec{r})\right\}(\vec{k}) = \mathscr{F}\left\{\psi_{\text{in}}(\vec{r})e^{i\sigma V(\vec{r})}\right\}(\vec{k}) \tag{4.6}$$

The detection of the electron wave function is accomplished through the measurement of electron intensity at the detector plane:

$$I_D(\vec{k}) = |\psi_D(\vec{k})|^2 \tag{4.7}$$

The detected electron intensity pattern in a STEM probe at the detector plane is called the convergent beam electron diffraction (CBED) pattern. CBED is a fundamental component of various STEM imaging techniques to generate an image. To better understand the CBED pattern, we can examine the scenario where there is no sample interaction with the electron probe. In this case, we can simplify eq. (4.6) by setting $\psi_{\text{out}}(\vec{r}) = \psi_{\text{in}}(\vec{r})$, resulting in:

$$I_D(\vec{k}) = |F\left\{\psi_{\text{in}}(\vec{r})\right\}(\vec{k})|^2 = |F^2\left\{\psi(\vec{k'})\right\}(\vec{k})|^2 = |\psi(-\vec{k})|^2 \tag{4.8}$$

This implies that the CBED pattern represents the aperture through which the electron beam passes. Typically, the aperture is circular, resulting in a CBED pattern resembling a disk. This disk is commonly referred to as the bright-field (BF) disk. The radius of the BF disk directly relates to the semi-angle (α) of the electron probe, and it can be expressed as $k_{\text{BF}} = \alpha/\lambda$.

When we detect only the electron intensity at the detector, we lose the phase information of the electron wave function at the detector plane. However, the phase of the exit wave at the sample plane is still encoded in the amplitude of the wave function at the detector plane. The phase, including the phase shift $\psi(\vec{k})$, can be extracted from a data set that contains the CBED pattern for each electron probe position at the sample plane. So far, we have focused on forming a CBED pattern for a single electron probe position. However, to construct a complete image of the sample, we must record a data set comprising multiple probe positions. Therefore, scanning the probe across the sample is a fundamental aspect of all STEM techniques. Consequently, we must incorporate the act of scanning the probe over the sample plane into our representation of the wave function during the STEM image formation process. Firstly, we need to define the position of the probe relative to the sample as $\vec{r}_p = (r_x, r_y)$. Secondly, we must consider the forward motion of the probe across the sample:

$$\psi_{\text{in}}(\vec{r}) \rightarrow \psi_{\text{in}}(\vec{r} - \vec{r}_p) \tag{4.9}$$

To facilitate understanding, conceptualizing the sample moving in the reverse direction beneath the probe is often simpler. This perspective allows us to modify eq. (4.5) as follows:

$$\psi_{\text{out}}(\vec{r}, \vec{r}_p) = \psi_{\text{in}}(\vec{r}) \cdot T(\vec{r} + \vec{r}_p) = \psi_{\text{in}}(\vec{r})e^{i\sigma V(\vec{r}+\vec{r}_p)} \tag{4.10}$$

With the provided formulation of the exit wave function, we can derive the wave function at the detector plane for each scanning position of the electron probe, utilizing eq. (4.6). As a result, we can determine the electron intensity at the detector plane using the following equations:

$$\psi_D(\vec{k},\vec{r}_p) = \mathscr{F}\left\{\psi_{\text{out}}(\vec{r},\vec{r}_p)\right\}(\vec{k}) = \mathscr{F}\left\{\psi_{\text{in}}(\vec{r})e^{i\sigma V(\vec{r},\vec{r}_p)}\right\}(\vec{k}) \tag{4.11}$$

$$I_D(\vec{k},\vec{r}_p) = |\psi_D(\vec{r},\vec{r}_p)|^2 \tag{4.12}$$

Having obtained a comprehensive understanding of the CBED formation for each probe position, we can now delve into how various STEM techniques utilize some or all aspects of CBED to generate an image. In the subsequent section, we will explore the usage of central symmetric detectors for forming conventional STEM bright and dark field images. Additionally, in section 4.4, we will discuss determining the center of mass of the CBED for image formation.

4.3. CONVENTIONAL STEM TECHNIQUES

In the preceding section, we derived an expression for the CBED pattern corresponding to each probe position. However, capturing the entire CBED pattern for every probe position poses practical challenges, including recording speed, dynamic range, and file size. While these challenges can be overcome with state-of-the-art detectors (as discussed in chapters 6 and 7), it is also possible to overcome these limitations by selectively using portions of the CBED pattern and employing clever detector designs to form an image efficiently.

The most practical approach to image formation using CBED is achieved by integrating the wave function at the detector plane across a predefined area of interest. This integration involves considering $\psi_D(\vec{k},\vec{r}_p)$ over a range of $\vec{k}$ values determined by the window function $W(\vec{k})$. Mathematically, this integration can be expressed as:

$$I_D(\vec{r}_p) = \int_{-\infty}^{\infty}\int_{-\infty}^{\infty} W(\vec{k})I_D(\vec{k},\vec{r}_p)d^2\vec{k} = \int_{-\infty}^{\infty}\int_{-\infty}^{\infty} W(\vec{k})|\psi_D(\vec{k},\vec{r}_p)|^2 d^2\vec{k} \tag{4.13}$$

By utilizing eq. (4.13), it is possible to demonstrate that the maximum resolution of any STEM technique is inherently limited to spatial frequencies below $2k_{\text{BF}}$.

The most efficient approach to performing the windowed integration described in eq. (4.13) is implementing it at the hardware level. Such an implementation involves designing an electron detector that records and accumulates all the electron counts for each probe position $\vec{r}_p$. The shape of the detector determines the corresponding window function $W(\vec{k})$. The most straightforward detector shape is a disk with dimensions matching the size of the bright field disk. When this detector is placed along the microscope's optical axis, it integrates the wave function over the area of the bright field disk, resulting in what is commonly known as a bright-field STEM image.

By adjusting the detector geometry to a ring shape with an inner diameter close to that of the bright-field disk, the resulting image is referred to as an annular dark field (ADF) image. In ADF imaging, the detector captures electrons scattered at angles beyond the bright field disk. Furthermore, in the case of high-angle ADF (HAADF) imaging, the inner diameter of the ring-shaped detector is substantially larger than the diameter of the bright-field disk, emphasizing electrons scattered at even higher angles.

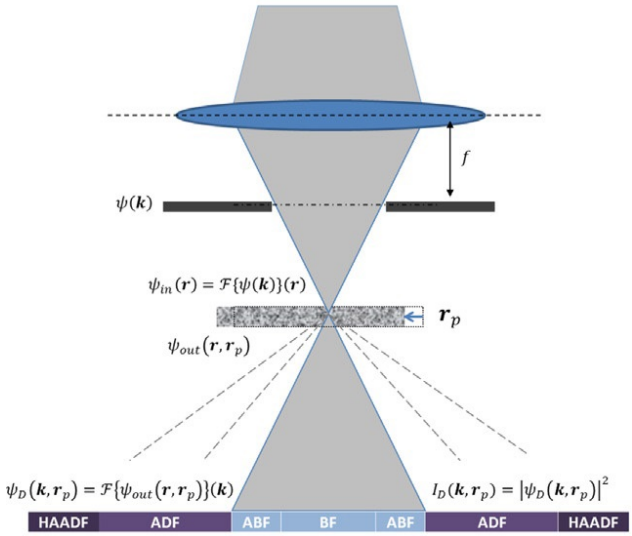

Figure 4.2: A schematic overview of the different classical STEM imaging modes. The different modes are defined by which area of the detector plane is selected by the window function $W(\vec{k})$. Reproduced from Lazić et al. [8], with permission from ©Elsevier (2017).

Equation (4.13) can be reformulated to incorporate the incoming wave function $\psi_{in}(\vec{r})$, the window function $W(\vec{k})$, and the phase shift $\varphi(\vec{r})$. The resulting expression for the integrated electron intensity per probe position, with an arbitrary window function $W(\vec{k})$, can be found in section A.4.2. A comprehensive mathematical derivation of this expression can be found in [8].

The expression for the integrated electron intensity consists of four components. The first component is independent of the probe position $\vec{r}_p$ and, therefore, does not contribute to the image formation process. Furthermore, in the case of a dark-field detector, the first three components of the expression in the section A.4.2 become zero. This is because the first three terms involve the product of the window function $W(\vec{k})$ and the (inverse) Fourier transform of the incoming wave function $\psi_{\text{in}}(\vec{r})$. Given that $\psi_{\text{in}}(\vec{r})$ is limited by the condenser aperture, resulting in $\psi_{\text{in}}(\vec{k}) = 0$ for $\vec{k} > k_{\text{BF}}$, and the window function is constrained by the detector geometry, resulting in $W(\vec{k}) = 0$ for $|\vec{k}| < k_{\text{BF}}$, there is no overlap between the window function $W(\vec{k})$ and the incoming wave function $\psi_{\text{in}}(\vec{r})$. Consequently, only the fourth term remains, which is solely responsible for the formation of the dark-field image:

$$I_D(\vec{r}_p) = \int_{-\infty}^{\infty}\int_{-\infty}^{\infty} (\zeta(\vec{r}+\vec{r}_p)\psi_{\text{in}}(\vec{r}) \otimes \zeta(\vec{r}+\vec{r}_p)\psi_{\text{in}}(\vec{r}))(\vec{r}') \cdot \mathscr{F}\left\{W(\vec{k})\right\}(\vec{r}')d^2\vec{r}' \tag{4.14}$$

where the transmission function is represented by $\zeta(\vec{r}) = 1 - T(\vec{r}) = 1 - e^{i\varphi(\vec{r})}$ and $\otimes$ is the cross-correlation as defined and below ([8]):

$$(f(\vec{r}') \otimes q(\vec{r}'))(\vec{r}') \equiv \int_{-\infty}^{\infty}\int_{-\infty}^{\infty} \overline{f(\vec{r}')}g(\vec{r}+\vec{r}')d^2\vec{r}' \tag{4.15}$$

Equation (4.14) completely describes the ADF image-forming process and is therefore known as the ADF term. Even though this term also plays a role in other STEM imaging techniques. Equation (4.14) can not be efficiently computed for the entire image and needs to be calculated for each probe position $(\vec{r}_p)$. However, for symmetric detectors eq. (4.14) can be approximated by another cross-correlation with the same $1-\cos\phi(r)$ objects, as described by Lazic et al.[8].

4.4. CENTER-OF-MASS IMAGING TECHNIQUES

In the preceding section, we employed a window function $W(\vec{k})$ determined by the detector shape and integrated over the detector itself to generate a STEM image. This approach offers the advantage of requiring only a single integrated electron intensity measurement per probe position $\vec{r}_p$. However, with recent advancements in detector technology, it is now feasible to capture the complete CBED pattern for each probe position $\vec{r}_p$. This development eliminates the need for hardware integration over a predefined window function $W(\vec{k})$. Consequently, we can utilize the momentum transfer between the probing electrons and the sample to construct linear images of the local electric field.

It is beneficial to initially approach the path of the probe electrons from a classical perspective to understand the linear relationship between the momentum transfer of the probe electrons and the local electric field. Let us consider an infinitely thin electron beam traversing through the sample at a specific position $\vec{r}p = (rxp, r_{yp})$. As the electrons interact with the local electric field $E(\vec{r}_p)$ of the sample, their direction will change. Consequently, the deflected electrons will strike the detector at a position offset from the optical axis, denoted as $\vec{r}_D$:

$$\vec{r}_D(\vec{r}_p) = l\alpha(\vec{r}_p) = l\lambda\vec{k}(\vec{r}_p) \tag{4.16}$$

Here, $\vec{r}_D$ represents the position where the electrons hit the detector, α corresponds to the scattering angle of the electrons after interacting with the local electric field, λ denotes the wavelength of the electrons, and l signifies the camera length of the microscope. In this classical scenario, the scattering angle α is determined by the interaction of the probe electrons with the local field. The following equation describes this interaction:

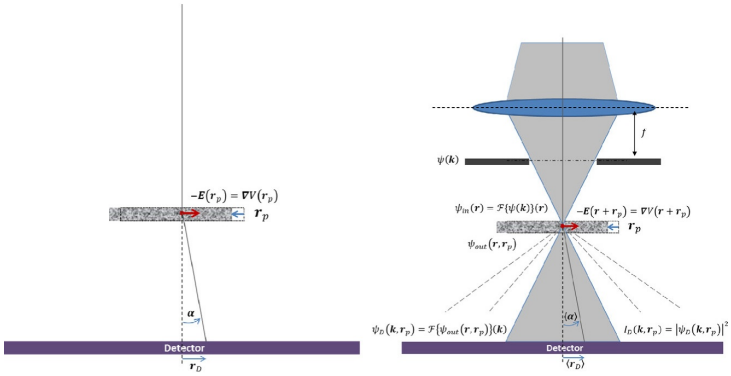

Figure 4.3: A schematic representation of the momentum transfer induced by a potential field in the specimen, perpendicular to the electron beam. The schematic on the left demonstrates the classical perspective, whereas the schematic on the right demonstrates the wave function propagation in the STEM. Reproduced from Lazić et al. [8], with permission from ©Elsevier (2017).

$$\alpha(\vec{r}_p) = \frac{e\Delta z}{2K_o} E(\vec{r}_p) \tag{4.17}$$

In eq. (4.17), Δz represents the thickness of the sample, e is the elementary charge of the electrons, K_0 denotes the kinetic energy of the incoming electrons, and $\vec{E}$ represents the projected electric field of the sample in the z direction, given by:

$$\vec{E}(\vec{r}) = \frac{1}{\Delta z} \int_0^{\Delta z} \vec{E}(\vec{r}, z) dz = -\nabla V(\vec{r}) \tag{4.18}$$

By combining eqs. (4.16) and (4.17), we can derive a linear relation between the position on the detector where the electron strikes and the local electric field in the sample for each probe position:

$$\vec{r}_D(\vec{r}_p) = \frac{el\Delta z}{2K_0} \vec{E}(\vec{r}_p) \tag{4.19}$$

This classical description reveals a linear relationship between the electron deviation and the local electric field. However, the STEM electron probe cannot be described classically. Instead, we must describe the electron probe using the electron wave function, as discussed in section 4.2.

The Center of Mass Concept

The center of mass is the position at which the weighted relative position of a distribution of masses sums to zero. This concept is easiest to visualize in the 1D example of a seesaw.

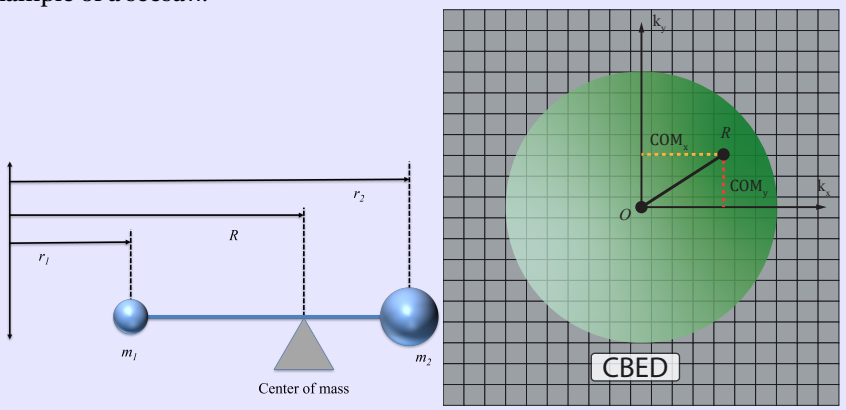

The center of mass of the two spheres in the left image is defined as the position where the two masses are perfectly balanced. This concept can be expressed mathematically by the following equation:

$$R = \frac{1}{M}\sum_{i=1}^{n} m_i r_i \tag{4.20}$$

Similarly, this concept can be extended to two dimensions. The center of mass of the circle in the right image can be defined as:

$$R_x = \frac{1}{I_{sum}}\sum_{i=1}^{n} m_i k_{xi} \tag{4.21}$$

$$R_y = \frac{1}{I_{sum}}\sum_{i=1}^{n} m_i k_{yi} \tag{4.22}$$

Here, R_x and R_y represent the x and y coordinates of the center of mass, respectively. I_{sum} is the sum of all the masses, and k_{xi} and k_{yi} are the x and y coordinates of each mass m_i.

The wave function at the detector plane, denoted as ψ_D, is governed by eq. (4.6). Analogous to the classical description in eq. (4.16), we can derive the location of the electrons at the detector using the expectation value $\langle \vec{r}_D \rangle = l\langle \alpha \rangle = l\lambda \left\langle \vec{k} \right\rangle$. The complete waveform expression for the electron location is given by eqs. (4.23) and (4.24), where $\vec{k} = \alpha/\lambda$, with $\vec{k}$ representing the position on the detector and λ denoting the wavelength of the electrons.

$$\left\langle \vec{k} \right\rangle (\vec{r}_p) = \left\langle \psi_D | \vec{k} | \psi_D \right\rangle (\vec{r}_p) = \int_{-\infty}^{\infty} \int_{-\infty}^{\infty} \psi_D(\vec{k}, \vec{r}_p) \vec{k} \overline{\psi_D}(\vec{k}, \vec{r}_p) d^2\vec{k} \tag{4.23}$$

$$\left\langle \vec{k} \right\rangle (\vec{r}_p) = \int_{-\infty}^{\infty} \int_{-\infty}^{\infty} \vec{k} |\psi_D(\vec{k}, \vec{r}_p)|^2 d^2\vec{k} = \int_{-\infty}^{\infty} \int_{-\infty}^{\infty} \vec{k} \cdot I_D(\vec{k}, \vec{r}_p) d^2\vec{k} \tag{4.24}$$

Equation (4.24) shows that the expectation value for the electron position at the detector plane is given by the momentum shift of the CBED pattern ($I_D(\vec{k}, \vec{r}_p) = |\psi_D(\vec{k}, \vec{r}_p)|$). The explanation of the center of mass (CoM) in the sidebar on the previous page demonstrates how we can relate the expectation value $\left\langle \vec{k} \right\rangle$ to the CBED pattern. The CoM of the CBED pattern is given by:

$$\text{CoM} = \frac{\int_{-\infty}^{\infty} \int_{-\infty}^{\infty} \vec{k} |\psi_D(\vec{k}, \vec{r}_p)|^2 d^2\vec{k}}{\int_{-\infty}^{\infty} \int_{-\infty}^{\infty} |\psi_D(\vec{k}, \vec{r}_p)|^2 d^2\vec{k}} \tag{4.25}$$

Since the wave function ψ_D is normalized, eq. (4.25) reduces to:

$$\text{CoM} = \int_{-\infty}^{\infty} \int_{-\infty}^{\infty} \vec{k} |\psi_D(\vec{k}, \vec{r}_p)|^2 d^2\vec{k} \tag{4.26}$$

which is equivalent to the expectation value $\left\langle \vec{k} \right\rangle$. By scanning the probe over the sample and calculating the CoM for each probe position, we can chart the CoM and CoM shift for the entire sample. This generates two independent images for the CoM in the x-direction and the CoM in the y-direction. Together, these two images form a vector image:

$$\vec{I}^{\text{com}}(\vec{r}_p) = \int_{-\infty}^{\infty} \int_{-\infty}^{\infty} \vec{k} |\psi_D(\vec{k}, \vec{r}_p)|^2 d^2\vec{k} \tag{4.27}$$

where $\vec{I}^{\text{com}} = (I_x^{\text{com}}, I_y^{\text{com}})$. Using eq. (4.11) from section 4.2, it can be proven that the CoM vector image becomes:

$$\vec{I}^{\text{com}}(\vec{r}_p) = \frac{1}{2\pi i} \int_{-\infty}^{\infty} \int_{-\infty}^{\infty} \nabla \psi_{\text{in}}(\vec{r}) \cdot \overline{\psi_{\text{in}}(\vec{r})} d^2\vec{r} + \frac{1}{2\pi} (|\psi_{\text{in}}(\vec{r})|^2 \otimes \nabla \varphi(\vec{r}))(\vec{r}_p) \tag{4.28}$$

The expression for the CoM vector image, as given by eq. (4.28), involves two terms. The first term represents the gradient of the incident wave function ψ_{in} and its complex conjugate $\overline{\psi_{\text{in}}}$ integrated over the sample area. The second term involves the cross-

correlation operation $\otimes$ between the squared magnitude of ψ_{in} and the gradient of the phase shift $\nabla\varphi$ evaluated at the probe position $\vec{r}_p$.

The complete derivation of eq. (4.28) can be found in section A.4.2. It is important to note that the first term in the equation does not depend on the probe position, allowing us to set this offset to zero. As mentioned in eq. (4.4) in section 4.2, for thin samples and when using the phase object approximation, the phase shift directly relates to the electrostatic potential of the sample. Consequently, the CoM is linearly related to the local electric field in the sample.

By further simplifying the equation, we obtain the following expression for the CoM vector image:

$$\vec{I}^{\text{com}}(\vec{r}_p) = -\frac{\sigma}{2\pi}(|\psi_{\text{in}}(\vec{r})|^2 \otimes \vec{E}(\vec{r}))(\vec{r}_p) \tag{4.29}$$

where σ represents a scaling factor. Additionally, the relationship between the gradient of the phase shift $\nabla\varphi$ and the electric field $\vec{E}$ is given by:

$$\nabla\varphi(\vec{r}) = \sigma\nabla V(\vec{r}) = -\sigma\vec{E}(\vec{r}) \tag{4.30}$$

This equation confirms the linear relationship between the CoM vector image and the local electric field in the sample.

4.5. EFFECTS OF LONG AND SHORT-RANGE POTENTIALS ON THE COM

The previous section showed a linear relation between the potential field and the CoM. However, there are multiple ways that the CoM of a CBED can shift, for instance, by a shift of the entire CBED pattern or by a redistribution of electrons within the CBED pattern. This final section discusses two limiting cases to understand better the interaction between a local potential field and the beam electrons [9].

THE PROBE SIZE IS MUCH SMALLER THAN THE FEATURE SIZE

We start with the case where the size of the electron probe is much smaller than the size of the feature or potential field. In this case, we can model the potential field as a linear ramp $V(\vec{r}) = E_0 x(\vec{r})$. Using eq. (4.11), we can describe the electron intensity at the detector as:

$$I_D\left(\vec{k}\right) = \left|F\left\{\psi_{in}(\vec{r})\, e^{i\sigma \mathrm{E}_o x(\vec{r}+\vec{r}_p)}\right\}\left(\vec{k}\right)\right|^2 \tag{4.31}$$

Equation (4.31) shows that the CBED pattern is essentially the original BF disk of the unscattered beam, but it is slightly shifted in a single direction. The only contribution to the CoM is this slight shift. This shift is analogous to the classical shift detailed in section 4.4.

THE PROBE SIZE IS MUCH LARGER THAN THE FEATURE SIZE

The second limiting case is when the size of the electron probe is much larger than the size of the feature or potential field. In this case, we can model the potential field as a delta function. Given that a regular STEM probe is very small, only the smallest potential fields fit this limiting case. For example, consider an atomic-size potential field. A specimen must be very thin to achieve spatial resolutions capable of imaging atomic columns. The phase change induced by such a thin specimen is very small. Therefore, we can extend the POA to form the linear weak phase object approximation (WPOA), where we can describe the transmission function T as $T(r) = 1 + i\sigma V(\vec{r})$. Using eq. (4.10), we can describe the exit wave as:

$$\psi_{out}\left(\vec{r},\vec{r}_p\right) = \psi_{\text{in}}(\vec{r})\left[1 + \sigma V_0 \delta\left(\vec{r}+\vec{r}_p\right)\right] \tag{4.32}$$

Finally, we can describe the CBED pattern on the detector in [9]:

$$I_D\left(\vec{k}\right) = \left|\psi\left(\vec{k}\right)\right|^2 - 4\pi\psi\left(\vec{k}\right)\sigma V_0 k_0 \frac{J_1\left(k_0\left|\vec{r}_p\right|\right)}{\left|\vec{r}_p\right|}\sin\left(\vec{k}\cdot\vec{r}_p\right) + \left|2\pi V_0 k_0 \frac{J_1\left(k_0\left|\vec{r}_p\right|\right)}{\left|r_p\right|}\right|^2 \tag{4.33}$$

The first term in this linear combination is simply the BF disk, similar to Equation 4.7. The final term is a second-order scattering term with a much lower intensity. Moreover, this term is uniform in momentum space (k) for a delta function potential, as described in this limiting case. Therefore, it will produce a uniform offset in the CBED pattern but not influence its CoM. The CoM of the CBED pattern is only affected by the second term in eq. (4.33). The delta-shaped potential causes a redistribution of the electron intensity, which varies depending on the electron probe's position and the position in momentum space $\left(\vec{k}\right)$. Moreover, the single $\psi\left(\vec{k}\right)$ in the second term ensures no intensity redistribution outside the BF disk because, due to the aperture, $\psi\left(\vec{k}\right) = 0$ for $\left|\vec{k}\right| > k_A$. Therefore, when the electron probe is much larger than the potential field, the BF disk itself does not shift; instead, the delta function potential redistributes the electron intensity within the BF disk.

DISENTANGLING LONG- AND SHORT-RANGE POTENTIALS

The shift of the CBED pattern (long-range potentials) and the redistribution of the electron intensity in the BF disk (short-range potentials) result in a shift of the CoM. While it is sometimes possible to approach the limiting cases described earlier in this section, contributions from both the CBED shift and the intensity redistribution might occur on other occasions. Disentangling these contributions is vital in understanding the type of the measured potential field.

The best way to separate the contributions is to measure the position of the BF disk without using the CoM. One can measure the position of the BF disk in multiple ways. The first uses template-matching algorithms similar to those used in strain mapping applications. The second uses contour-finding algorithms to locate the position of the BF

disk [4, 10–12]. Because the BF disk has the highest electron intensity of any region in the CBED pattern, finding the correct contour for it is relatively straightforward. Finally, the cross-correlation between the position-averaged CBED (PACBED) and the measured CBED can be used to determine the shift of the BF disk with respect to its average position. A more detailed explanation of the cross-correlation between the PACBD and the measured CBED can be found in chapter 7, where we use the cross-correlation to cluster slightly misaligned crystal grains using K-Means clustering.

A.4. APPENDIX

A.4.1. CLOSED-FORM EXPRESSION OF STEM IMAGES

In section 4.3, we discussed that the most practical approach to image formation using CBED is achieved by integrating the wave function at the detector plane across a predefined area of interest. This integration involves considering $\psi_D(\vec{k},\vec{r}_p)$ over a range of $\vec{k}$ values determined by the window function $W(\vec{k})$. Mathematically, this integration can be expressed as:

$$I_D(\vec{r}_p) = \int_{-\infty}^{\infty}\int_{-\infty}^{\infty} W(\vec{k}) I_D(\vec{k},\vec{r}_p)\, d^2\vec{k} = \int_{-\infty}^{\infty}\int_{-\infty}^{\infty} W(\vec{k}) |\psi_D(\vec{k},\vec{r}_p)|^2\, d^2\vec{k} \tag{4.34}$$

Equation (4.34) can be reformulated to incorporate the incoming wave function $\psi_{in}(\vec{r})$, the window function $W(\vec{k})$, and the phase shift $\varphi(\vec{r})$ [13].

$$\begin{aligned} I^{\mathrm{STEM}}(\vec{r}_p) = & \int_{-\infty}^{\infty}\int_{-\infty}^{\infty} W\left(\vec{k}\right)\left|F\left\{\psi_{\mathrm{in}}(\vec{r})\right\}\left(\vec{k}\right)\right| d^2k + \\ & \left(i\left(\psi_{\mathrm{in}}(\vec{r})\cdot F\left\{W\left(\vec{k}\right)F^{-1}\left\{\overline{\psi_{\mathrm{in}}(\vec{r}')}\right\}\left(\vec{k}\right)\right\}(\vec{r}) - \overline{\psi_{\mathrm{in}}(\vec{r})}\cdot F^{-1}\left\{W\left(\vec{k}\right)F\left\{\psi(\vec{r}')\right\}\left(\vec{k}\right)\right\}(\vec{r})\right)\otimes \sin\varphi(\vec{r})\right)(\vec{r}_p) + \\ & \left(\left(\psi_{\mathrm{in}}(\vec{r})\cdot F\left\{W\left(\vec{k}\right)F^{-1}\left\{\overline{\psi_{\mathrm{in}}(\vec{r}')}\right\}\left(\vec{k}\right)\right\}(\vec{r}) + \overline{\psi_{\mathrm{in}}(\vec{r})}\cdot F^{-1}\left\{W\left(\vec{k}\right)F\left\{\psi(\vec{r}')\right\}\left(\vec{k}\right)\right\}(\vec{r})\right)\otimes(1-\cos\varphi)(\vec{r})\right)(\vec{r}_p) + \\ & \int_{-\infty}^{\infty}\int_{-\infty}^{\infty}\left(\zeta(\vec{r}+\vec{r}_p)\,\psi_{\mathrm{in}}(\vec{r})\otimes\zeta(\vec{r},\vec{r}_p)\,\psi_{\mathrm{in}}(\vec{r})\right)(\vec{r}')\cdot F\left\{W\left(\vec{k}\right)\right\}(\vec{r}')\, d^2r' \end{aligned} \tag{4.35}$$

where $\otimes$ denotes the cross-correlation and ζ represents the transmission function, as discussed in section 4.3. Equation (4.35) can be considered a closed-form expression for the STEM image-forming process, albeit the fourth term can not be computed directly.

The first term in eq. (4.35) does not depend on the probe position $\vec{r}_p$ and can be considered a DC offset. The following two terms are cross-correlations with a $\sin\phi(r)$ and $1-\cos\phi(r)$ term as the object, respectively. The two non-linear objects in the second and third terms mean that STEM imaging, in general, is non-linear. However, it can be described as a linear combination of the images of two objects. When applied to dark field imaging, eq. (4.35) can be reduced to only the final term. In dark field imaging, the window function $W\left(\vec{k}\right)$ becomes zero for $\vec{k} < \mathrm{BF}$. This function is directly opposite to the function of the aperture, which reduces the incoming wave function to zero for the area outside the aperture, as described in eq. (4.1). The final term in eq. (4.35) can not be computed directly for the entire image but must be computed for each probe position r_p. Only for symmetric detectors can the final term in eq. (4.35) be reduced to another cross-correlation with the same $1-\cos\phi(r)$ object. This simplification makes it easier to simulate the ADF image-forming process efficiently [8].

A.4.2. CENTER-OF-MASS IMAGE FORMATION

In this section, we derive the image-forming process of the CoM and how it relates to the potential local field. This derivation was first detailed by Lazic et al. [8].

The CoM of the CBED pattern, as described in section 4.4, is repeated below

$$I^{\mathrm{CoM}}\left(\vec{r}_p\right) = \int_{-\infty}^{\infty}\int_{-\infty}^{\infty} \vec{k}\cdot I_D\left(\vec{k},\vec{r}_p\right) d^2k = \int_{-\infty}^{\infty}\int_{-\infty}^{\infty} \vec{k}\cdot\left|\psi_D\left(\vec{k},\vec{r}_p\right)\right| d^2k \tag{4.36}$$

The wave function at the detector level ψ_{D} is the exit wave function ψ_{out} that has been Fourier transformed by the image-forming lenses in the STEM. Equation (4.36) can therefore be rewritten as:

$$I^{\mathrm{CoM}}\left(\vec{r}_p\right) = \int_{-\infty}^{\infty}\int_{-\infty}^{\infty} \vec{k}\cdot F\left\{\psi_{\mathrm{out}}\left(\vec{r}',\vec{r}_p\right)\right\}\left(\vec{k}\right)\cdot\overline{F\left\{\psi_{\mathrm{out}}\left(\vec{r}',\vec{r}_p\right)\right\}}\left(\vec{k}\right) d^2k \tag{4.37}$$

By bringing the multiplication with $\vec{k}$ inside the Fourier transform eq. (4.37) can be transformed to:

$$I^{\mathrm{CoM}}\left(\vec{r}_p\right) = \frac{1}{2\pi i}\int_{-\infty}^{\infty}\int_{-\infty}^{\infty} F\left\{\nabla\psi_{\mathrm{out}}\left(\vec{r}',\vec{r}_p\right)\right\}\left(\vec{k}\right)\cdot\overline{F\left\{\psi_{\mathrm{out}}\left(\vec{r}',\vec{r}_p\right)\right\}}\left(\vec{k}\right) d^2k \tag{4.38}$$

With the cross-correlation, described in eq. (4.15), the relation above can be simplified to:

$$I^{\mathrm{CoM}}\left(\vec{r}_p\right) = \frac{1}{2\pi i}\int_{-\infty}^{\infty}\int_{-\infty}^{\infty} F\left\{\left(\psi_{\mathrm{out}}\left(\vec{r},\vec{r}_p\right)\otimes\left(\nabla\psi_{\mathrm{out}}\left(\vec{r},\vec{r}_p\right)\right)\right)\right\}\left(\vec{k}\right) d^2k \tag{4.39}$$

For any function with an existing integral, one can state that:

$$\int_{-\infty}^{\infty}\int_{-\infty}^{\infty} F\left\{f\left(\vec{r}\right)\right\}\left(\vec{k}\right) d^2k = f\left(0\right) \tag{4.40}$$

If we now assume that eq. (4.39) is finite we can rewrite the integral to:

$$I^{\mathrm{CoM}}\left(\vec{r}_p\right) = \frac{1}{2\pi i}\left(\psi_{\mathrm{out}}\left(\vec{r},\vec{r}_p\right)\otimes\left(\nabla\psi_{\mathrm{out}}\left(\vec{r},\vec{r}_p\right)\right)\right)\left(\vec{r}'\right)\Big|_{\vec{r}'=0} \tag{4.41}$$

If we set $r' = 0$ the integral reduces to:

$$I^{\mathrm{CoM}}\left(\vec{r}_p\right) = \frac{1}{2\pi i}\int_{-\infty}^{\infty}\int_{-\infty}^{\infty} \psi_{\mathrm{out}}\left(\vec{r},\vec{r}_p\right)\cdot\nabla\psi_{\mathrm{out}}\left(\vec{r},\vec{r}_p\right) d^2r \tag{4.42}$$

As discussed in section 4.2, for very thin specimens, the exit wave function ψ_{out} can be described as the incoming wave function ψ_{in} times a transmission function.

$$\psi_{\text{out}}\left(\vec{r},\vec{r}_p\right) = \psi_{\text{in}}\left(\vec{r}\right) e^{i\varphi\left(\vec{r}+\vec{r}_p\right)} \tag{4.43}$$

Using the product and chain rule, we can rewrite the final term in eq. (4.42)$\left(\nabla\psi_{\text{out}}\right)$ as:

$$\nabla\psi_{\text{out}}\left(\vec{r},\vec{r}_p\right) = e^{i\varphi\left(\vec{r}+\vec{r}_p\right)}\nabla\psi_{\text{in}}\left(\vec{r}\right) + i\psi_{\text{in}}\left(\vec{r}\right) e^{i\varphi\left(\vec{r}+\vec{r}_p\right)}\nabla\varphi\left(\vec{r}+\vec{r}_p\right) \tag{4.44}$$

If we then multiply eq. (4.44) with:

$$\overline{\psi_{\text{out}}\left(\vec{r},\vec{r}_p\right)} = \overline{\psi_{\text{in}}\left(\vec{r}\right)}\cdot e^{-i\varphi\left(\vec{r}+\vec{r}_p\right)} \tag{4.45}$$

we can rewrite the first term inside the intergral in eq. (4.42) to:

$$\overline{\psi_{\text{out}}\left(\vec{r},\vec{r}_p\right)}\cdot\left(\nabla\psi_{\text{out}}\left(\vec{r},\vec{r}_p\right)\right) = \overline{\psi_{\text{in}}\left(\vec{r}\right)}\cdot\nabla\psi_{\text{in}}\left(\vec{r}\right) + i\left|\psi_{\text{in}}\left(\vec{r}\right)\right|^2\cdot\nabla\varphi\left(\vec{r}+\vec{r}_p\right) \tag{4.46}$$

By placing eq. (4.46) inside eq. (4.42) we end up with the following relation:

$$I_{\text{CoM}}\left(\vec{r}_p\right) = \frac{1}{2\pi i}\int_{-\infty}^{\infty}\int_{-\infty}^{\infty}\nabla\psi_{in}\left(\vec{r}\right)\cdot\overline{\psi_{\text{in}}\left(\vec{r}\right)}\,d^2r + \frac{1}{2\pi i}\int_{-\infty}^{\infty}\int_{-\infty}^{\infty}\left|\psi_{in}\left(\vec{r}\right)\right|^2\nabla\varphi\left(\vec{r}+\vec{r}_p\right)\,d^2r \tag{4.47}$$

The first term in eq. (4.47) does not depend on the probe position r_p and can be seen as a DC offset. The final term can be seen as cross-corelation between $\left|\psi_{in}\left(\vec{r}\right)\right|^2$ and $\nabla\varphi\left(\vec{r}\right)$. Therefore, the final description for the CoM image becomes:

$$I_{\text{CoM}}\left(\vec{r}_p\right) = \frac{1}{2\pi i}\int_{-\infty}^{\infty}\int_{-\infty}^{\infty}\nabla\psi_{in}\left(\vec{r}\right)\cdot\overline{\psi_{\text{in}}\left(\vec{r}\right)}\,d^2r + \frac{1}{2\pi}\left(\left|\nabla\psi_{in}\left(\vec{r}\right)\right|^2\otimes\nabla\varphi\left(\vec{r}\right)\right)\left(\vec{r}_p\right) \tag{4.48}$$

In section 4.4, we show that with further simplifications, eq. (4.48) indicates a linear relation between the CoM image and the local electric field in a specimen.

REFERENCES

[1] R. Egerton and M. Watanabe, *Spatial resolution in transmission electron microscopy,* Micron **160**, 103304 (2022).

[2] M. W. Tate, P. Purohit, D. Chamberlain, K. X. Nguyen, R. Hovden, C. S. Chang, P. Deb, E. Turgut, J. T. Heron, D. G. Schlom, D. C. Ralph, G. D. Fuchs, K. S. Shanks, H. T. Philipp, D. A. Muller, and S. M. Gruner, *High Dynamic Range Pixel Array Detector for Scanning Transmission Electron Microscopy,* Microscopy and Microanalysis **22**, 237 (2016).

[3] M. Nord, R. W. Webster, K. A. Paton, S. McVitie, D. McGrouther, I. Maclaren, and G. W. Paterson, *Fast Pixelated Detectors in Scanning Transmission Electron Microscopy. Part I: Data Acquisition, Live Processing, and Storage,* Microscopy and Microanalysis **26**, 653 (2020).

[4] V. B. Ozdol, C. Gammer, X. G. Jin, P. Ercius, C. Ophus, J. Ciston, and A. M. Minor, *Strain mapping at nanometer resolution using advanced nano-beam electron diffraction,* Applied Physics Letters **106**, 253107 (2015).

[5] T. Grieb, F. F. Krause, M. Schowalter, D. Zillmann, R. Sellin, K. Müller-Caspary, C. Mahr, T. Mehrtens, D. Bimberg, and A. Rosenauer, *Strain analysis from nano-beam electron diffraction: Influence of specimen tilt and beam convergence,* Ultramicroscopy **190**, 45 (2018).

[6] Y. Jiang, Z. Chen, Y. Han, P. Deb, H. Gao, S. Xie, P. Purohit, M. W. Tate, J. Park, S. M. Gruner, V. Elser, and D. A. Muller, *Electron ptychography of 2d materials to deep sub-ångström resolution,* Nature **559**, 343 (2018).

[7] Y. Jiang, Z. Chen, Y. Han, P. Deb, H. Gao, S. Xie, P. Purohit, M. W. Tate, J. Park, S. M. Gruner, V. Elser, and D. A. Muller, *Electron ptychography of 2D materials to deep sub-ångström resolution,* Nature **559**, 343 (2018).

[8] I. Lazić and E. G. Bosch, *Analytical Review of Direct Stem Imaging Techniques for Thin Samples,* Advances in Imaging and Electron Physics **199**, 75 (2017).

[9] M. C. Cao, Y. Han, Z. Chen, Y. Jiang, K. X. Nguyen, E. Turgut, G. D. Fuchs, and D. A. Muller, *Theory and practice of electron diffraction from single atoms and extended objects using an EMPAD,* Microscopy **67**, i150 (2017).

[10] T. C. Pekin, C. Gammer, J. Ciston, A. M. Minor, and C. Ophus, *Optimizing disk registration algorithms for nanobeam electron diffraction strain mapping,* Ultramicroscopy **176**, 170 (2017), 70th Birthday of Robert Sinclair and 65th Birthday of Nestor J. Zaluzec PICO 2017 – Fourth Conference on Frontiers of Aberration Corrected Electron Microscopy.

[11] Y. Han, K. Nguyen, M. Cao, P. Cueva, S. Xie, M. W. Tate, P. Purohit, S. M. Gruner, J. Park, and D. A. Muller, *Strain mapping of two-dimensional heterostructures with subpicometer precision, Nano Letters,* Nano Letters **18**, 3746 (2018).

[12] A. Armigliato, R. Balboni, G. P. Carnevale, G. Pavia, D. Piccolo, S. Frabboni, A. Benedetti, and A. G. Cullis, *Application of convergent beam electron diffraction to two-dimensional strain mapping in silicon devices,* Applied Physics Letters **82**, 2172 (2003).

[13] E. G. Bosch and I. Lazić, *Analysis of HR-STEM theory for thin specimen,* Ultramicroscopy **156**, 59 (2015).

5

STRAIN MAPPING WITH 4D-STEM USING THE EXIT-WAVE POWER CEPSTRUM

Mapping strain in nanomaterials using transmission electron microscopy (TEM) has traditionally been limited to strain maps at the atomic scale. The introduction of four dimensional scanning TEM (4D–STEM) has made it possible to map local strain fields in micrometer-sized crystal structures with nanometer precision. Using nanobeam electron diffraction (NBED) patterns, one can map the variation in the crystal lattice. However, disentangling complex NBED patterns to map the strain in complex nanostructures accurately remains challenging. A way forward is provided by transforming the NBED pattern using the exit-wave power cepstrum (EWPC) to create a representation of the atomic spacing of the crystal directly underneath the STEM probe. This chapter discusses the mathematical relation between the NBED and the EWPC patterns. We demonstrate how to use the EWPC transform to map the strain accurately. Finally, we describe how we use the EWPC transform, peak tracking, and K-Means clustering algorithms to map the local strain fields. The techniques detailed in this chapter are combined in our open-source strain mapping framework, `StrainMAPPER`.

Parts of this chapter has been published in Small Sci, **M. Bolhuis**, S.E. van Heijst, J.J.M. Sangers, and S. Conesa-Boj (2024)

5.1. INTRODUCTION

In the previous chapter, we discussed the principles behind 4D-STEM. Specifically, we explored conventional STEM image formation and the Center-of-Mass (CoM) based momentum resolved imaging technique. Another field that significantly benefits from the introduction of 4D-STEM detectors is TEM strain mapping. 4D-STEM enables strain mapping with nanometer-scale precision over a large field of view. Before the introduction of 4D-STEM, strain measurements in TEM specimens were typically measured using Geometrical Phase Analysis (GPA) [1–3]. This method relies on atomic-resolution images to discern strain deformations in the crystal lattice. GPA's high spatial resolution limited its application to small fields of view, limiting its use to micrometer-sized specimens. In contrast, 4D-STEM offers a much broader field of view, limited only by the number and density of scan positions. Despite the nanometer-sized STEM probe, it can still detect even the slightest deformations in the crystal structure. 4D-STEM strain mapping relies on capturing a diffraction pattern for each scan position and comparing the deformations in each pattern to a diffraction pattern from an unstrained reference region. Typically, deformations are measured by tracking the positions of multiple Bragg diffraction disks in a Nanobeam Electron Diffraction (NBED) pattern [4, 5]. However, these approaches are often restricted to thinner specimens because variations in thickness and orientation affect the intensity distribution within an NBED pattern. Moreover, determining the exact locations of the Bragg disks can be challenging for more complex geometries like heterostructures.

We have addressed these challenges by developing an open-source 4D-STEM strain mapping method called `StrainMAPPER`. In this chapter, we provide an overview of the critical components of the `StrainMAPPER` method. For a more detailed and step-by-step explanation of the processing steps, please refer to chapter 6. In this chapter, we will focus on the mathematical description of the Exit-wave Power Cepstrum (EWPC), the Difference of Gaussian (DoG) Peak track method, and the K-Means clustering algorithm, all of which are essential components of the `StrainMAPPER` method. Subsequently, we will discuss how we map strain and rigid rotation within the specimen using the affine deformation matrix. Finally, we will evaluate the accuracy of the `StrainMAPPER` method and demonstrate its ability to measure strain, rigid rotation, and inter-layer twist angle in a $MoSe_2/WSe_2$ heterostructure.

5.2. THE EXIT-WAVE POWER CEPSTRUM

As the name implies, the exit-wave power cepstrum (EWPC) is a tool for investigating periodic structures in reciprocal space. It is particularly suitable for measuring deviations in diffraction patterns, representing the crystal structure in reciprocal space. The power cepstrum is generated by taking the Fourier transform of the logarithm of the nanobeam electron diffraction pattern (NBED). The NBED pattern is a specialized form of convergent beam electron diffraction (CBED) pattern discussed, as discussed in section 4.2. Under NBED conditions, the Bragg disks within the zero-order Laue zone (ZOLZ) are entirely separated. This separation allows for indexing the diffraction pattern without overlapping the Bragg disks, with each disk representing a specific crystal plane [6].

The NBED patterns will be identical for a perfectly unstrained specimen for every scan position. However, when the local crystal lattice beneath the electron probe experiences slight strain or rotation, the NBED pattern deforms. Consequently, local strain within a specimen can be mapped by assessing the deformation of the NBED pattern.

One can use the ideal crystal lattice from literature or, more commonly, define an NBED pattern from an unstrained region as the reference. Deformation in an NBED pattern is typically measured by determining the position of two or more Bragg diffraction disks. The ideal conditions for this approach involve a convergence angle smaller than the size of the condenser aperture $\left[\alpha = A\left(\vec{k}\right)\right]$ and a large camera length ($L \geqslant 700$ mm). A large camera length maximizes precision when measuring the positions of the Bragg disks. Measuring the position of the Bragg disks is commonly accomplished using template-matching algorithms. These algorithms rely on cross-correlation between the NBED pattern and an image of the BF disk to locate the positions of the Bragg disks. However, template-matching techniques work well when the Bragg disks are clearly visible but may encounter difficulties under challenging conditions [7, 8]. For instance, limited diffraction contrast in thin layered materials, especially when combined with thicker amorphous substrates like Si_3N_4 TEM grids, can make it challenging to determine the locations of the Bragg disks.

Factors such as dynamical scattering and misalignment on thicker specimens can lead to intensity variations in the NBED pattern, further complicating the strain mapping process. Attempts have been made to improve template matching techniques using machine learning and intensity fitting algorithms. The `StrainMAPPER` method uses a different approach. We utilize the Exit-Wave Power Cepstrum to reduce the influence of specimen thickness and misalignment.

MATHEMATICAL FORMULATION OF THE EWPC

The Exit-Wave Power Cepstrum (EWPC), developed by Padget et al. [9], transforms the electron wave that exits the specimen into a real-space representation of the atomic spacing in the crystal. We can mathematically describe the EWPC transform as follows:

$$I_{\mathrm{EWPC}}(\vec{r},\vec{r}_p) = \left|\mathscr{F}\left(\ln\left|\mathscr{F}\left(\psi_{\mathrm{out}}\left(\vec{k},\vec{r}_p\right)\right)\right|^2\right)\right|^2 \tag{5.1}$$

In section 4.2, we showed that the projection lens system in the TEM performs a Fourier transform, resulting in the following description of the electron intensity on the detector:

$$I_D(\vec{k},\vec{r}_p) = |\psi_D(\vec{k},\vec{r}_p)|^2 = \left|\mathscr{F}\left\{\psi_{\mathrm{out}}(\vec{r},\vec{r}_p)\right\}(\vec{k})\right|^2 \tag{5.2}$$

The equation above shows that the microscope's lens system automatically performs the first Fourier transform in the EWPC transform, forming the aforementioned NBED pattern. This Fourier transformation converts convoluted signals within the wavefunction into a multiplication of signals.

$$\mathscr{F}(u(t) * v(t)) = U(\omega)\cdot V(\omega) \tag{5.3}$$

The next step in generating the EWPC involves taking the logarithm of the wave function. The logarithm isolates the contributions of the convoluted signals within the wave function, which makes them easier to separate.

$$\ln(|U(\omega)\cdot V(\omega)|^2) = \ln(|U(\omega)|^2) + \ln(|V(\omega)|^2) \tag{5.4}$$

Lastly, the EWPC is obtained by performing the Fourier transform on eq. (5.4).

$$\text{EWPC} = \mathscr{F}(\ln(|U(\omega)|^2) + \ln(|V(\omega)|^2)) = \mathscr{F}(\ln(|U(\omega)|^2)) + \mathscr{F}(\ln(|V(\omega)|^2)) \tag{5.5}$$

Equation (5.5) shows how the EWPC can be used to separate convoluted contributions within the wave function. Similar to section 4.2, we assume that the specimen can be approximated as a strong phase object. Therefore, the exit wave can be described as $\psi_{\text{out}}(\vec{r},\vec{r}_p) = \psi_{\text{in}}(\vec{r},\vec{r}_p)e^{i\sigma V(\vec{r},\vec{r}_p)}$. Using eq. (5.2) we can describe the NBED pattern as:

$$\begin{aligned} I_D(\vec{k},\vec{r}_p) &= \left|\mathscr{F}\left\{\psi_{\text{out}}(\vec{r},\vec{r}_p)\right\}(\vec{k})\right|^2 = \left|\mathscr{F}\left\{\psi_{\text{in}}(\vec{r},\vec{r}_p)\right\}(\vec{k}) * \mathscr{F}\left\{e^{i\sigma V(\vec{r},\vec{r}_p)}\right\}(\vec{k})\right|^2 \\ I_D(\vec{k},\vec{r}_p) &= \left|\psi_{\text{in}}\left(\vec{k},\vec{r}_p\right) * \phi\left(\vec{k},\vec{r}_p\right)\right|^2 \end{aligned} \tag{5.6}$$

where $\psi_{\text{in}}(\vec{k},\vec{r}_p)$ is the reciprocal space representation of the electron probe and $\phi(\vec{k},\vec{r}_p)$ is the Fourier transform of the transmission function. Under NBED conditions, ϕ represents the Bragg diffraction disks. We can extend the description of the NBED pattern by including kinematical scattering effects induced by variations in the specimen tilt and thickness. The effect of specimen tilt on the NBED pattern can be described by the excitation error $s(\vec{k},\vec{r}_p)$, which denotes the distance between the Ewald sphere and the reciprocal lattice point. See section A.7.4 for more information about the excitation error. The sample thickness effectively broadens the reciprocal lattice points by a convolution with the Fourier transform of a top-hat function[9]. The effects of the specimen tilt and thickness combined attenuate the NBED intensity.

$$\begin{aligned} I_{\text{EWPC}}(\vec{r},\vec{r}_p) &= \left|\mathscr{F}\left(\ln\left|\mathscr{F}\left(\psi_{\text{out}}\left(\vec{k},\vec{r}_p\right)\right)\right|^2\right)\right|^2 \\ \mu(\vec{k},\vec{r}_P) &= \text{sinc}\left(\frac{s(\vec{k},\vec{r}_p)T}{2}\right) \end{aligned} \tag{5.7}$$

Here, T is the thickness of the specimen, and $\mu(\vec{k},\vec{r}_P)$ is the attenuation envelope, which we will call the tilt envelope. The tilt and thickness variations usually vary relatively slowly over the entire specimen. Therefore, we can simplify eq. (5.7) to:

$$I_D(\vec{k},\vec{r}_p) = \left|\mu(\vec{k},\vec{r})\cdot\left(\psi_{\text{in}}(\vec{k},\vec{r}_p) * \phi(\vec{k},\vec{r}_p)\right)\right|^2 = \left|\mu(\vec{k},\vec{r})\right|^2 \cdot \left|\psi_{\text{in}}(\vec{k},\vec{r}_p) * \phi(\vec{k},\vec{r}_p)\right|^2. \tag{5.8}$$

Using the properties of the EWPC from eqs. (5.4) and (5.5), we can separate the tilt envelope from the rest of the signal.

$$I_{\mathrm{EWPC}}(\vec{r},\vec{r}_p) \approx \left|\mathscr{F}\left(\ln\left(\left|\mu(\vec{k},\vec{r})\right|^2\right)\right)\right|^2 + \left|\mathscr{F}\left(\ln\left(\left|\psi_{\mathrm{in}}(\vec{k},\vec{r}_p) * \phi(\vec{k},\vec{r}_p)\right|^2\right)\right)\right|^2 \tag{5.9}$$

Effectively isolating the effects of the tilt envelope and the contributions of the crystal in the NBED pattern. The result is an EWPC pattern where the reciprocal lattice points condense in small peaks while the slowly varying tilt envelope is located around the pattern's center. The peaks in the EWPC pattern are a real space representation of the atomic distances in the crystal lattice [9, 10].

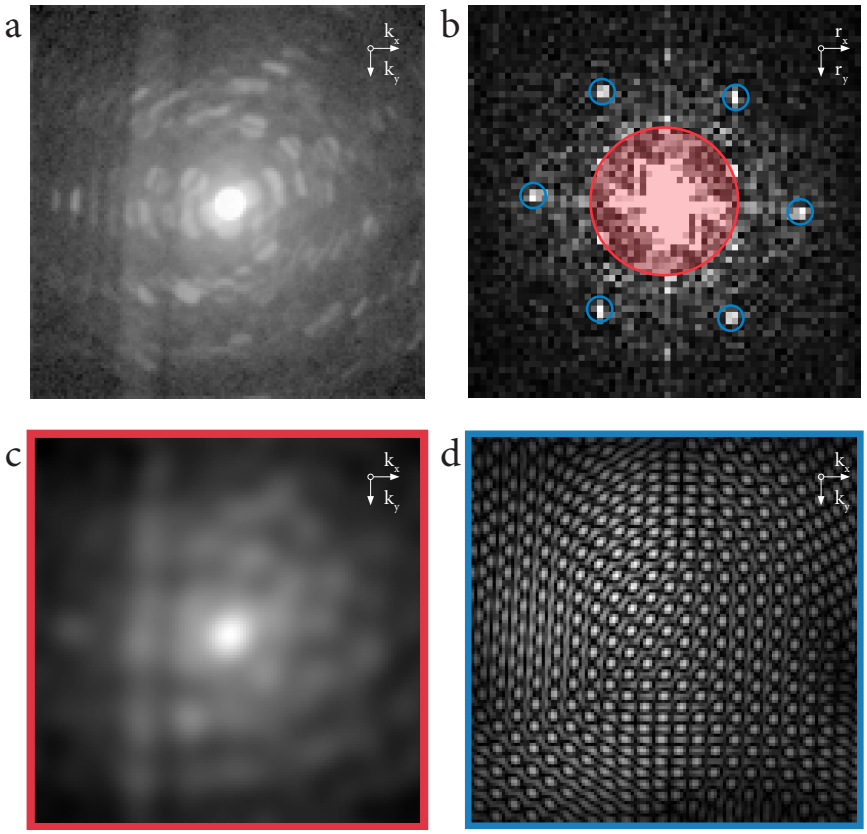

Figure 5.1: **a)** A NBED pattern of a typical TMD material. Similarly to Fig.1**c**, the intensity of the NBED pattern is normalized using a logarithm. **b)** The exit-wave power cepstrum (EWPC) of the NBED pattern in **a**. The long-range contributions to the intensity coming from the non-ideal sample tilt are located in the red circle. The sharp peaks, indicated by the blue circles, represent the contributions of the TMD crystal lattice. **c)** The inverse EWPC of the red area in **b**. This NBED contains contributions from the non-ideal two-dimensional sample, like sample thickness and tilt. **d)** The inverse EWPC of the blue areas in **b**. This NBED contains only the contributions of the TMD crystal lattice.

EWPC BAND-PASS FILTERING

In the previous section, we mathematically showed that the tilt envelope and crystal diffraction can be separated using the EWPC. When we use the proper conditions, band-pass filtering can perform this separation. Because of the final Fourier transform in eq. (5.9), we need to ensure that the distance between the lattice information and the center of the NBED is as small as possible by reducing the camera length (CL $\leqslant$ 285 mm). The small camera length ensures that the peaks in the EWPC are far from the center and nicely separated. This separation of the peaks contrasts the tilt envelope, which typically varies slowly in reciprocal space and will concentrate around the EWPC's center. An example of separating the tilt envelope and the lattice contributions is shown in fig. 5.1.

The NBED pattern in figure fig. 5.1a is from a typical TMD material thick enough to induce dynamical scattering effects. While the lattice contributions in the NBED pattern are hard to classify, they are easily identifiable in the corresponding EWPC pattern in figure fig. 5.1b. The long-range contributions of the tilt envelope are located in the center, indicated by the red circle. In contrast, the short-range contributions of the crystal lattice are located in the EWPC peaks, indicated by the blue circles. Using a band-pass filter, we can illustrate the separate contributions to the EWPC pattern. The contribution from the tilt envelope to the NBED pattern is shown in fig. 5.1c, and the contribution from the crystal lattice is shown in fig. 5.1d. The clear separation of the peaks in the EWPC pattern also facilitates their automatic tracking, making the EWPC transform a great tool for 4D-STEM strain mapping.

5.3. PEAK TRACKING WITH SUBPIXEL PRECISION

The peaks in an EWPC pattern are a real-space representation of the atomic distances in the crystal. Tracking the position of these EWPC peaks allows us to measure the local strain that causes minor deviations in the atomic distances. In this section, we will discuss the three steps that the `StrainMAPPER` method uses to measure the position of two non-parallel EWPC peaks with subpixel accuracy. First, we determine the position of the EWPC peaks with an integer pixel precision using a blob detection method, like the Difference-of-Gaussian (DoG) algorithm, for every scan position in the 4D dataset [11, 12]. Next, we reduce the dataset to a 2D point cloud that contains the coordinates of all the EWPC peaks found by the DoG algorithm. We employ K-Means clustering to group the point cloud and assign the correct label to each EWPC peak [13, 14]. Finally, we use the coordinates of every peak from two non-parallel clusters as the center position of a small mask. Then, we determine the center of the EWPC peak by performing a Center-of-Mass (CoM) calculation within the mask [15]. The CoM calculation provides the EWPC peak center with subpixel accuracy, which can then be used to measure local strain deformations accurately.

DIFFERENCE OF GAUSSIAN

The first step in the `StrainMAPPER` method is detecting the location of every EWPC peak in the 4D dataset. We determine the location of the peaks using a blob detection method like the Difference-of-Gaussian (DoG) algorithm. Blob detection methods are commonly used in computer vision to identify regions with significant contrast rela-

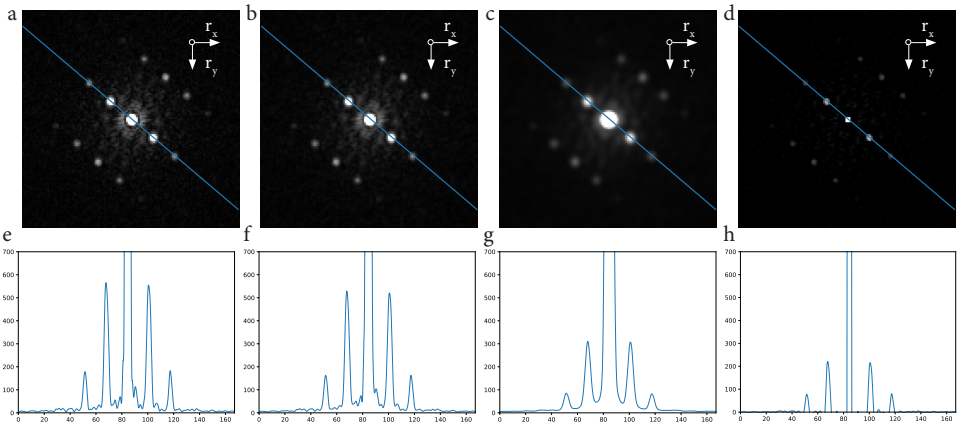

Figure 5.2: **a-d)** The EWPC pattern of the MoO_3 nanorod from fig. 6.6a. **a** is unfiltered and **b-d** are blurred with successively stronger Gaussian kernels. **e-h)** The linescan of the EWPC patterns indicated in **a-d.**

tive to the background. Consequently, the bright peaks against a dark background in an EWPC pattern are ideally suited for blob detection techniques. Here, we will focus on the DoG algorithm, although alternative methods like the Laplacian of Gaussian (LoG) or the Determinant of Hessian (DoH) can also be used. The DoG algorithm's working principle involves subtracting a Gaussian-blurred image from the same image with less blurring applied. These blurred images are obtained from the same original image but employ Gaussian kernels with different standard deviations. A single Gaussian kernel would only suppress high-frequency information and function as a low-pass filter. However, by subtracting two Gaussian-blurred images with different standard deviations, we effectively create a frequency band-pass filter, preserving information within the frequency range of both filters.

In fig. 5.2, we show how the DoG method is used to accurately improve the EWPC pattern to detect peaks in an EWPC pattern. The top row of images represents EWPC patterns of a MoO_3 nanorod. For more information on the nanorod, see section 2.4. The EWPC in fig. 5.2a is the unfiltered EWPC with the intensity profile along the blue linescan in fig. 5.2f. The EWPC in fig. 5.2b has a small Gaussian filter applied to it. In the corresponding lines in fig. 5.2f, we can see that this small Gaussian filter hardly changes the EWPC pattern, as we can still see small variations in intensity. Figure 5.2c shows the same EWPC pattern with a large Gaussian filter applied to it. In the corresponding linescan, we can see that all the small intensity variations are filtered out. However, this increases the risk of filtering out small features. The EWPC in fig. 5.2d is computed by taking the difference between fig. 5.2b and fig. 5.2c. This EWPC pattern, with the DoG applied, only has sharp points remaining and almost no noise around the center beam. The corresponding linescan in fig. 5.2h shows five distinct peaks and a much lower noise floor. The DoG algorithm is used in peak detection. It applies a range of Gaussian kernels with successfully larger standard deviations to the image and stacks the difference between

each blurred image in a cube. Finding the local maxima in this cube locates the peaks. A threshold can be applied to detect only local maxima with a high enough intensity. In `StrainMAPPER`, one can set the minimum and maximum standard deviations used for the Gaussian kernels and the ratio of the standard deviations between the Gaussian kernels used in the difference calculation. Combined with an annular mask to apply a spatial band-pass filter, as described in section 5.2, one can accurately track the position of all the EWPC peaks while minimizing the detection of false positives caused by local maxima in the noise.

K-MEANS CLUSTERING

The next step in the peak tracking process is classifying every EWPC peak in the 4D dataset. We achieve this by flattening the dataset and placing every EWPC in a 2D point cloud. An example of a point cloud is shown in fig. 5.6, where each point represents a unique EWPC peak position in the 4D dataset. The point's color weight determines the frequency of the same peak position in the 4D dataset. Before clustering the weighted point cloud, we can apply a threshold and remove any point that does not meet the threshold. Next, we use K-Means clustering to cluster the weighted point cloud. The K-Means algorithm partitions the weighted point cloud into a pre-determined number of clusters and assigns each point to the nearest cluster centroid while minimizing inertia [13]. The logical choice for the number of clusters is typically the number of atomic positions in the crystal unit cell. However, for certain complex geometries like a heterostructure, choose to increase the number of clusters. Once all EWPC peaks in the 4D dataset are assigned to their correct cluster, we assume that every point within a single cluster represents the same EWPC peak position, only translated. Furthermore, we assume that each cluster has only one EWPC peak per EWPC pattern. With every EWPC assigned to the correct cluster, we can then find the subpixel maximum of all the EWPC peaks from two non-parallel clusters.

SUBPIXEL PRECISION LOCALIZATION OF EWPC PEAKS USING COM

The DoG peak track method provides the center of the EWPC peaks with integer pixel precision. While this precision is sufficient for the K-Means clustering algorithm, it is insufficient for accurately creating a strain map. Therefore, `StrainMAPPER` uses the position determined by the DoG method as the center of a small circular mask. This mask is then used in a CoM calculation to pinpoint the EWPC center with subpixel precision. The choice for this approach primarily aims to ensure quick computation times. A typical 4D dataset may consist of over 16,000 frames, necessitating determining the center of two EWPC peaks per frame for an accurate strain map. While the CoM calculation can introduce some systematic errors due to background noise, we will demonstrate in section 5.5 how these errors can be mitigated with an appropriate CoM mask radius. The result of the CoM measurement is two EWPC peak locations with subpixel resolution.

5.4. AFFINE DEFORMATION MATRIX

The EWPC peak positions serve as the end position of two vectors originating from the center of the EWPC pattern. To establish a reference, we define an EWPC pattern from an unstrained region. This reference provides the basis for comparing all the other vectors in the 4D dataset. It is often more accurate to average vector positions over multiple EWPC patterns to mitigate small errors in the peak positions. Next, we use the affine deformation matrix and polar decomposition to compute the strain and rigid rotation between an EWPC pattern and the reference area. This section covers the affine deformation matrix and the choice between the Cartesian and vector reference frames.

This section covers the affine deformation matrix and the choice between the Cartesian and vector reference frames. We define $\vec{v}_1$ and $\vec{v}_2$ as the basis vectors that span the object's initial reference configuration, and let $\vec{v}'_1$ and $\vec{v}'_2$ be the basis vectors that span the object's deformed configuration. The deformation matrix $\mathbf{D}$ describes the transformation that maps the reference matrix $\mathbf{A_0}$ onto the measured matrix $\mathbf{A}$. Where:

$$\mathbf{A_0} = \begin{bmatrix} v_{1x} & v_{2x} \\ v_{1y} & v_{2y} \end{bmatrix} \tag{5.10}$$

$$\mathbf{A} = \begin{bmatrix} v'_{1x} & v'_{1x} \\ v'_{1y} & v'_{1y} \end{bmatrix} \tag{5.11}$$

One can evaluate the deformation matrix $\mathbf{D}$ using the following two equations:

$$\mathbf{D_{car}} = \mathbf{A}\mathbf{A_0^{-1}} \rightarrow \mathbf{A} = \mathbf{D_{car}} \cdot \mathbf{A_0} \tag{5.12}$$

$$\mathbf{D_{vec}} = \mathbf{A_0^{-1}}\mathbf{A} \rightarrow \mathbf{A} = \mathbf{A_0} \cdot \mathbf{D_{vec}} \tag{5.13}$$

The subscripts "**car**" and "**vec**" in $\mathbf{D_{car}}$ and $\mathbf{D_{vec}}$ indicate the method used to calculate the deformation matrix. $\mathbf{D_{car}}$ involves inverting the reference matrix and multiplying it by the measured matrix, while $\mathbf{D_{vec}}$ involves multiplying the reference matrix by the inverted measured matrix. Both equations can be used to obtain a deformation matrix $\mathbf{D}$, and both $\mathbf{D_{car}}$ and $\mathbf{D_{vec}}$ fully describe the affine transformation between the reference matrix $\mathbf{A_0}$ and the measured matrix $\mathbf{A}$. However, $\mathbf{D_{car}}$ and $\mathbf{D_{vec}}$ describe the deformation in different reference frames.

Here, we discuss the difference between eqs. (5.12) and (5.13). We begin by considering the definition of the strain matrix $\mathbf{E}$:

$$\mathbf{E} = \begin{bmatrix} \varepsilon_{xx} & \varepsilon_{xy} \\ \varepsilon_{yx} & \varepsilon_{yy} \end{bmatrix}, \tag{5.14}$$

which is given by:

$$\mathbf{E} = \mathbf{U} - \mathbf{I} \text{ or } \mathbf{E} = \mathbf{V} - \mathbf{I}, \tag{5.15}$$

where the identity matrix represented as $\mathbf{I}$ is given by:

$$\mathbf{I} = \begin{bmatrix} 1 & 0 \\ 0 & 1 \end{bmatrix}$$

and **U** and **V** are the strain deformation matrices. These matrices represent the deformation of the specimen under strain and can be extracted from the general deformation matrix using a polar decomposition:

$$\mathbf{D} = \mathbf{R} \cdot \mathbf{U} = \mathbf{V} \cdot \mathbf{R} \tag{5.16}$$

where **R** is the ridged rotation matrix described by:

$$\mathbf{R} = \begin{bmatrix} \cos\theta & -\sin\theta \\ \sin\theta & \cos\theta \end{bmatrix}. \tag{5.17}$$

The polar decomposition indicates that any specimen deformation can be decomposed into a rigid-body rotation and a strain. Here, **U** and **V** represent the strain part of the deformation, while **R** represents the rigid-body rotation part of the deformation. In order to highlight the differences between eqs. (5.12) and (5.13), we assume a deformation with a vanishing rotation $\theta = 0$, resulting in $\mathbf{R} = \mathbf{I}$. Therefore eq. (5.16) can be reduced to **D=U=V**, which means that the strain matrix **E** can be expressed as:

$$\mathbf{E} = \mathbf{D} - \mathbf{I}, \tag{5.18}$$

which in turn can be rewritten as:

$$\mathbf{D} = \mathbf{E} + \mathbf{I}. \tag{5.19}$$

For example, let us assume a compressive strain of 25 % along the x-axis and a tensile strain of 50 % along the y-axis. In this case, the deformation matrix is given by:

$$\mathbf{D} = \begin{bmatrix} 0.75 & 0 \\ 0 & 1.50 \end{bmatrix}. \tag{5.20}$$

Note that the strain values of 25 and 50 % are not realistic, but they serve an illustrative purpose here. If now we apply this deformation matrix to eq. (5.12) ($\mathbf{A} = \mathbf{D_{car}} \cdot \mathbf{A_0}$), we get:

$$\mathbf{A} = \begin{bmatrix} 0.75 & 0 \\ 0 & 1.50 \end{bmatrix} \cdot \begin{bmatrix} v_{1x} & v_{2x} \\ v_{1y} & v_{2y} \end{bmatrix} \cdot = \begin{bmatrix} 0.75 \cdot v_{1x} & 0.75 \cdot v_{2x} \\ 1.50 \cdot v_{1y} & 1.50 \cdot v_{2y} \end{bmatrix} \tag{5.21}$$

Equation (5.21) shows that the vectors $\vec{v}_1$ and $\vec{v}_2$ are deformed along the Cartesian coordinates (x, y) by the deformation matrix $\mathbf{D_{car}}$. Every point x is compressed 0.75 times, while every point y is stretched 1.50 times. The green vectors in fig. 5.3 schematically represent this deformation.

Now, if we apply the same deformation matrix to eq. (5.13) ($\mathbf{A} = \mathbf{A_0} \cdot \mathbf{D_v}$), we get the result:

$$\mathbf{A} = \begin{bmatrix} v_{1x} & v_{2x} \\ v_{1y} & v_{2y} \end{bmatrix} \cdot \begin{bmatrix} 0.75 & 0 \\ 0 & 1.50 \end{bmatrix} = \begin{bmatrix} 0.75 \cdot v_{1x} & 1.50 \cdot v_{2x} \\ 0.75 \cdot v_{1y} & 1.50 \cdot v_{2y} \end{bmatrix} \tag{5.22}$$

As we can see from eq. (5.22), the vectors $\vec{v}_1'$ and $\vec{v}_2'$ are now deformed along the direction of the original vectors. The new vector $\vec{v}_1'$ is compressed by 0.75 times along the direction of the original vector $\vec{v}_1$, while the new vector $\vec{v}_2'$ is stretched by 1.50 times along

the direction of $\vec{v}_2$. This deformation effectively creates a new coordinate system (x', y') with vectors $\vec{v}_1$ and $\vec{v}_2$ as a basis. The red vectors in fig. 5.3 schematically represent this deformation.

In summary, eqs. (5.12) and (5.13) describe two different ways of representing the deformation of the specimen. Equation (5.12) describes the deformation of the specimen with respect to the Cartesian coordinate system (x, y). In the `StrainMAPPER` method, the Cartesian basis is defined as the pixelated detector's x and y coordinates. Whereas eq. (5.13) describes the deformation with respect to the vector basis of $\vec{v}_1$ and $\vec{v}_2$. In the `StrainMAPPER` method, this basis is formed by the two EWPC peaks selected for the strain calculations. Using the vector basis, one can determine the strain along the two lattice planes represented by the EWPC peaks. The choice of which basis to use ultimately depends on the analysis's specific needs.

5.5. STUDY ON THE SYSTEMATIC ERRORS IN THE STRAINMAPPER METHOD

To validate the systematic error in the `StrainMAPPER` method, one needs a well-known reference sample or a dummy dataset in which the expected strain values are known in advance. To facilitate the benchmarking of the systematic error in our method, we have included the ability to generate dummy datasets in the `StrainMAPPER` package. This section discusses various dummy datasets that demonstrate our method's systematic error. Furthermore, we demonstrate that our method achieves greater accuracy than the difference of the Gaussian (DoG) method for real-world measurements by combining the DoG peak track with the center-of-mass (CoM) method to determine the center of EWPC with sub-pixel precision.

The dummy dataset used for validation consists of the same EWPC pattern for each frame and a total of a 128x128 frames. The resulting strain and rotation across the entire "specimen" should be zero when there are no systematic errors. As a result, any deviation from zero strain is attributed to systematic errors in tracking the EWPC peaks. First, we track the EWPC peak positions for an ideal pattern, in which the peaks are precisely located at the center of a detector pixel and no noise is present. The DoG peak tracking method accurately identifies the EWPC peak locations for each frame, as evidenced by the peak cluster shown in fig. 5.4a. This figure illustrates the flawless EWPC pattern and six identical EWPC peak clusters, each containing 16,384 counts (128x128). The resulting strain map will display zero strain across the entire "specimen" due to the uniformity of the EWPC pixel location within each cluster. It's worth noting that the increased precision offered by the CoM method does not provide any advantage in this scenario, as the centers of the EWPC peaks are already precisely positioned on individual detector pixels.

Subsequently, we introduce a 30-degree rotation to the EWPC pattern, causing the center of the EWPC peaks to no longer align perfectly with a single detector pixel. This rotation makes interpolation of pixel intensities necessary because it introduces a misalignment between the EWPC peak center and the pixel center. This scenario more closely resembles a real-world EWPC pattern. Due to the limited pixel density of 4D-STEM detectors, such as the Electron Microscope Pixel Array Detector (EMPAD), the center of an EWPC

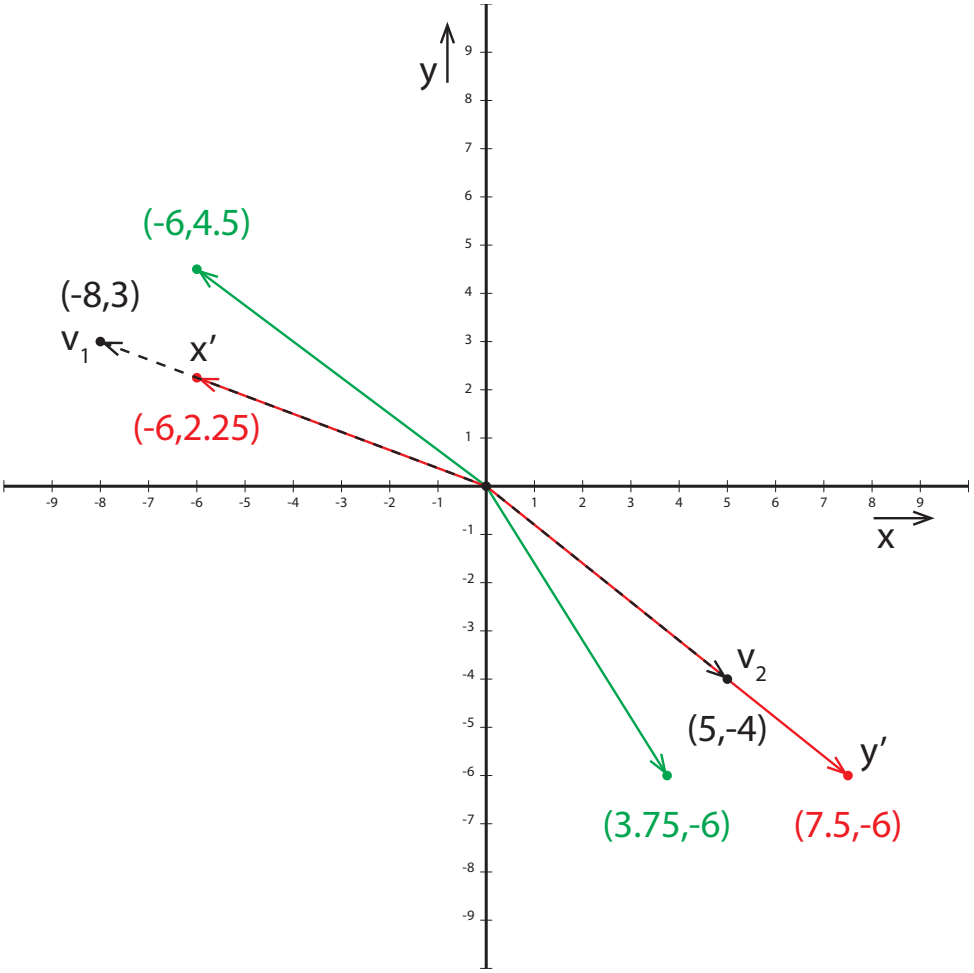

Figure 5.3: A schematic representation of a deformation applied along the Cartesian basis and along the vector basis. The two reference vectors $\vec{v}_1$ and $\vec{v}_2$ are denoted in black. A compressive strain of 25 % along the x-axis and a tensile strain of 50 % along the y-axis is applied. The green vectors represent the deformation applied in the Cartesian basis (x, y), while the red vectors represent the deformation applied in the vector basis (x', y').

peak likely spans more than one pixel. Furthermore, we introduce random noise to each EWPC pattern, creating a unique EWPC pattern for each frame in the 4D dataset.

To match the noise level of the dummy dataset with the noise level of an actual 4D-STEM measurement, we calculate the mean and maximum intensity, standard deviation, and noise quality (NQ) for each EWPC pattern and then average these values over the entire 4D dataset. The 4D-STEM data is taken from the MoS_2 nanostructure from chapter 4.

Table 5.1: This table presents the statistical analysis results, including mean intensity, maximum intensity, standard deviation, and noise quality, for each EWPC pattern within the 4D dataset. The values are computed over the entire dataset, providing insights into the noise characteristics of the patterns, which closely resemble real-world scenarios.

	4D-STEM Data	Dummy Data
Mean	37.75	34.42
Max	372.4	375.0
StDev	28.27	27.83
NQ	9.054E-2	9.12E-2

Here, the noise quality is given by the following equation:

$$\mathrm{NQ} = \frac{\sqrt{Mdn(\epsilon_{xy}^2)}}{\max(\epsilon_{xy})} \tag{5.23}$$

Figure 5.4b shows a three-dimensional (3D) plot of one of the EWPC patterns in the 4D dataset of the MoS_2 nanostructure, and fig. 5.4c presents a 3D plot of one of the generated EWPC patterns from the dummy dataset. This dummy dataset's mean and maximum intensity, standard deviation, and noise quality are listed in table 5.1. Comparing fig. 5.4b and fig. 5.4c alongside the values in table 5.1, one can observe that we can introduce a similar noise level to the dummy dataset as the one present in the actual dataset.

The results of the DoG peak track on the dummy dataset are displayed in fig. 5.4d. One can observe 15 unique peak locations. The pixel interpolation, introduced by the 30-degree rotation, combined with the random noise, causes the DoG method to identify the center or the EWPC peaks in several locations. One can observe this effect most clearly in the map of the x component of the vector belonging to cluster 1 ($V1_x$) in fig. 5.4e. This figure shows that the EWPC peak position, as determined by the DoG method, can vary by 1 pixel. This integer pixel precision adversely affects the accuracy of the strain measurement, resulting in strain values ranging from +0.8% to -8.1%, with a standard deviation (σ) of +2.7%, as depicted in fig. 5.4f.

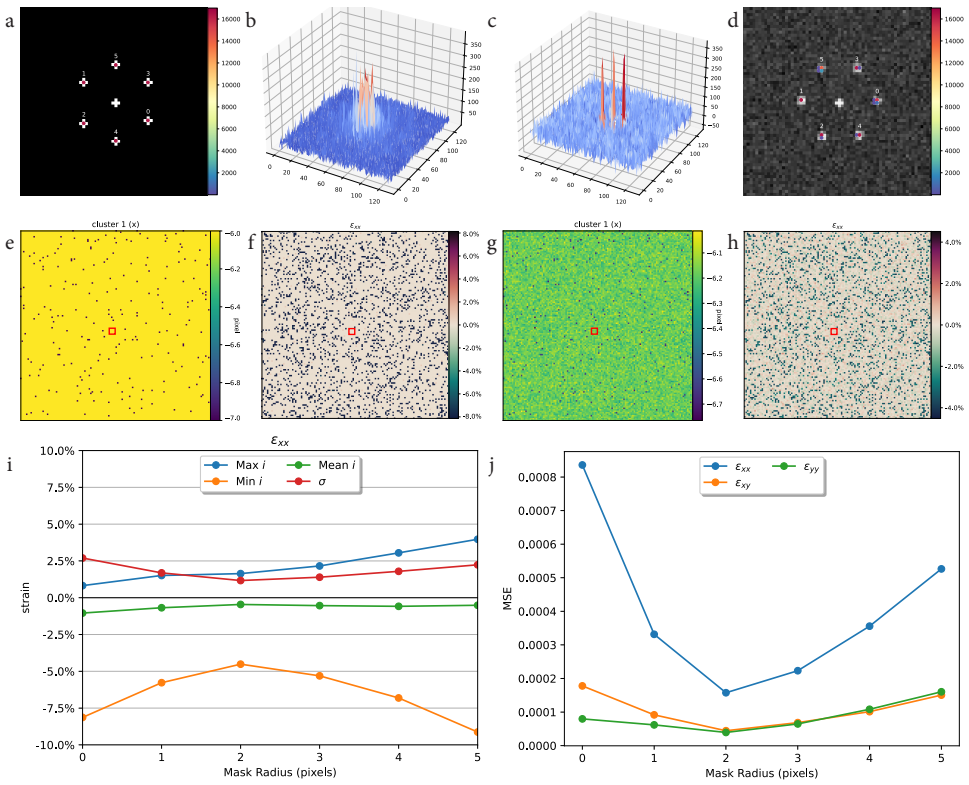

Figure 5.4: This figure illustrates the steps taken to quantify the accuracy in `StrainMAPPER` strain measurements. **a)** Shows the peak cluster for a perfect 4D dataset without noise. **b-c)** Show 3D plots of a single EWPC pattern from a real-world and dummy dataset, respectively. **d)** Displays the peak cluster of the dummy dataset with noise. **e-f)** The results of the DoG peak tracking method on ($V1_x$) and the corresponding strain map (ϵ_{xx}). The strain values exhibit variations from +0.8% to -8.1% with σ = +2.7%. **g-h)** A vector map showcasing the finer granularity achieved by the CoM method in determining the EWPC peak center and the corresponding strain map. The strain values range from +1.6% to -4.5%, with σ = 1.2%. **i)** Shows the $Max, Min,$ and $Mean$ strain values and the standard deviation in ϵ_{xx} for different mask radii. **j)** Shows the MSE for different mask radii. Both **i** and **j** show an optimum at a mask size of 2 pixels.

SUBPIXEL ACCURACY USING THE CENTER-OF-MASS

Enhancing the accuracy of the EWPC peak center location can significantly improve and clarify the precision of the strain measurements. In `StrainMAPPER`, the CoM method utilizes the DoG peak tracking result as the center of a small mask. The CoM is calculated from the weighted intensity within this masked area, providing the EWPC peak center with sub-pixel accuracy. The vector map in fig. 5.4g demonstrates subpixel accuracy and is generated using the CoM calculation. This map exhibits finer granularity in the x coordinate of the EWPC peak position compared to the binary vector map in fig. 5.4f. The sub-pixel precision in the EWPC location results in a more accurate strain map (ϵ_{xx}) with values ranging from +1.6% to -4.5% and σ = 1.2%, as shown in fig. 5.4h.

The accuracy of strain measurements depends on the size of the CoM mask. If the mask is too small, the CoM method does not offer a significant benefit. Conversely, if the mask is too large, noise in the EWPC pattern can affect the CoM position of the EWPC peak. Figure 5.4i illustrates the maximum and minimum strain values (ϵ_{xx}) and the standard deviation for various CoM mask radii (r), where $r = 0$ represents using only the DoG method. This graph reveals that this dataset's optimal choice is a CoM mask radius of 2 pixels. Figure 5.4j shows the mean squared error between different strain maps ($\epsilon_{xx}, \epsilon_{yy}$, and ϵ_{xy}) and expected maps with no strain ($\epsilon = 0$) for different CoM mask radii. Once again, a CoM mask with a radius of 2 pixels proves to be the most accurate.

IMPROVE ACCURACY USING A GAUSSIAN FILTER

The 4D-STEM detector's low pixel density can lead to significant shifts in the perceived center of the EWPC peak from one frame to the next. These shifts introduce pixelated noise into the strain map, as seen in fig. 5.4h. To mitigate this noise, `StrainMAPPER` employs a Gaussian blur on the final strain map. The Gaussian filter functions as two sequential 1D-convolution filters [16], where it maps the pixel intensity to a weighted average of the surrounding pixels, with the original pixel receiving the highest weight. The Gaussian filter reduces noise in the strain map at the cost of spatial resolution and sharpness. Given that `StrainMAPPER's` primary goal is mapping strain over large micrometer-sized structures, a slight reduction in spatial resolution in exchange for a less noisy strain map is a favorable trade-off. The complete set of strain maps, with a Gaussian filter (σ_G = 0.65) applied, are presented in figs. 5.5a to 5.5d, with a maximum strain value for ϵ_{xx} of +0.6% and a minimum value of -3.1% with σ = 0.5%. The average σ over ϵ_{xx}, ϵ_{yy}, and ϵ_{xy} is 0.36%, resulting in a 3σ confidence value of 1.1%. Therefore, it can be stated that the strain measurements of the MoS_2 nanostructure in chapter 6 have an uncertainty of ±1.1%. The same process can be applied to the rotation map in fig. 5.5d, resulting in a standard deviation of $\sigma = 0.16^\circ$ and an uncertainty of $\pm 0.47^\circ$.

Finally, we explore an alternative approach to enhance the accuracy of the `StrainMAPPER` method. Ensuring that the EWPC pattern spans more pixels reduces the impact of a one-pixel shift in the peak location on the strain calculation. This reduction can be achieved by either increasing the 4D-STEM detector's pixel density or ensuring that the EWPC pattern spans more pixels. The first option is constrained by hardware design, while the second option can be achieved by decreasing the camera length of the TEM [9]. For example, when we create a dummy sample, the EWPC peaks are separated from the

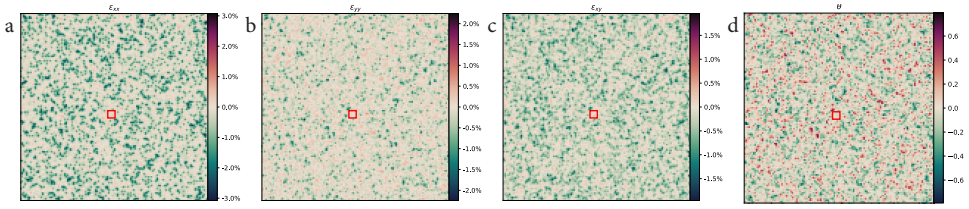

Figure 5.5: **a-d)** Showcase the complete set of strain maps after applying a Gaussian filter with a standard deviation (σ_G) of 0.65. This post-processing step effectively reduces pixelated noise in the strain maps, improving visual clarity and accuracy. The strain map (ϵ_{xx}) exhibits variations from +0.6% to -3.1% with σ = 0.5%

center by three times as many pixels as in the previous dummy sample. The average standard deviation over ϵ_{xx}, ϵ_{yy}, and ϵ_{xy} decreased to σ = 0.26%. When applying the Gaussian blur to the strain map, the average standard deviation decreased even further to σ = 0.116%. Therefore, when the measurement conditions allow for a well-separated EWPC pattern, the accuracy of the `StrainMAPPER` method can increase to ±0.35% (3σ).

5.6. CASE STUDY: TWISTED $MoSe_2$/WSe_2 HETEROSTRUCTURE

In the previous sections, we discussed the `StrainMAPPER` method and its accuracy. This final section presents a case study using the `StrainMAPPER` method to measure the local strain fields in a transition metal dichalcogenide (TMD) heterostructure. Due to their unique electronic and optical properties, heterostructures formed by stacking two-dimensional (2D) crystals have gained attention [17, 18]. One of the most intriguing phenomena in such materials is the emergence of Moiré patterns, which arise from the relative misalignment or "twist" between adjacent layers. These patterns, in turn, are closely tied to local strain fields within individual layers [19, 20]. In this section, we not only delve into the detailed strain maps of the heterostructure but also elucidate the underlying mechanisms that differentiate the Moiré twist angle (α) between adjacent layers from the rigid rotation deformation within the crystal lattice of a single layer. For this purpose, we use a multilayer stack of $MoSe_2$ and WSe_2 flakes misaligned by approximately 15 degrees.

Figure 5.6a presents an Annular Dark-Field (ADF) image obtained from a 4D-STEM dataset of the multilayered stack. This image reveals the overall morphology of the stack, highlighting the presence of multiple layers. Figure 5.6b showcases a high-resolution TEM (HR-TEM) image of the Moiré lattice, emphasizing the fine details within the crystal structure. In fig. 5.6c, we display the Fast Fourier Transform (FFT) of the Moiré lattice, demonstrating the two sets of the characteristic hexagonal diffraction pattern of $MoSe_2$ and WSe_2, which indicates the presence of a Moiré superlattice. Figure 5.6d presents an EWPC pattern extracted from the 4D dataset at the location marked by the blue dot in fig. 5.6a. This EWPC pattern also exhibits the same hexagonal Moiré pattern observed in the FFT, affirming that we can probe the Moiré lattice with nanometer precision even when imaging a micrometer-sized structure, as depicted in fig. 5.6a. Figure 5.6e illus-

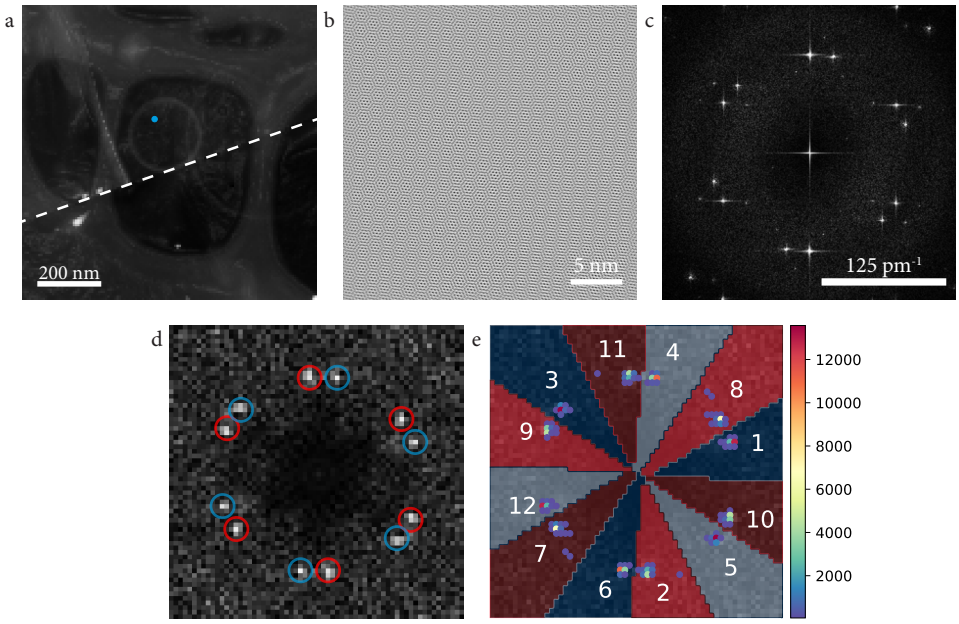

Figure 5.6: **a)** An ADF image from the $MoSe_2$/WSe_2 multilayer. The white line indicates the border between the single-layer and double-layered area. **b)** A filtered High-Resolution TEM image of the Moiré lattice. **c)** The fast Fourier transform (FFT) of the HR-TEM image in **b**. **d)** The EWPC taken from the position marked by the blue dot in **a**. Similar to the FFT in **c**, the EWPC contains two hexagonal patterns, showcasing the Moiré lattice. **e)** The cluster plot showcases the position of all the EWPC peaks appearing at least 50 times. The 12 clusters represent the different layers within the multilayer stack, each denoted by either blue or red clusters.

trates a cluster plot of all the EWPC peak positions, revealing 12 distinct clusters.

These clusters correspond to the different layers within the multilayer stack, with each layer's peaks denoted by either blue or red clusters. By selecting two clusters that belong to the same layer, we can map the local strain fields and the rigid rotation (θ) within a single layer. In figs. 5.7a to 5.7d, we display strain and rotation maps for one of the layers in the multilayer stack, generated using clusters 1 and 4 from the cluster plot in fig. 5.6e. These maps reveal considerable tensile strain at areas where the multilayer hangs over the holes in the lacy-carbon TEM grid. In contrast, figs. 5.7e to 5.7h present strain and rotation maps for the second layer in the multilayer stack, utilizing clusters 8 and 11 from the cluster plot in fig. 5.6e. The rotation map (fig. 5.7f) highlights a slight, clockwise rotation with respect to the reference area (indicated by the red box). This rotation arises from the ripple within this layer and represents an excellent example of strain-induced rigid rotation deformation within a single layer.

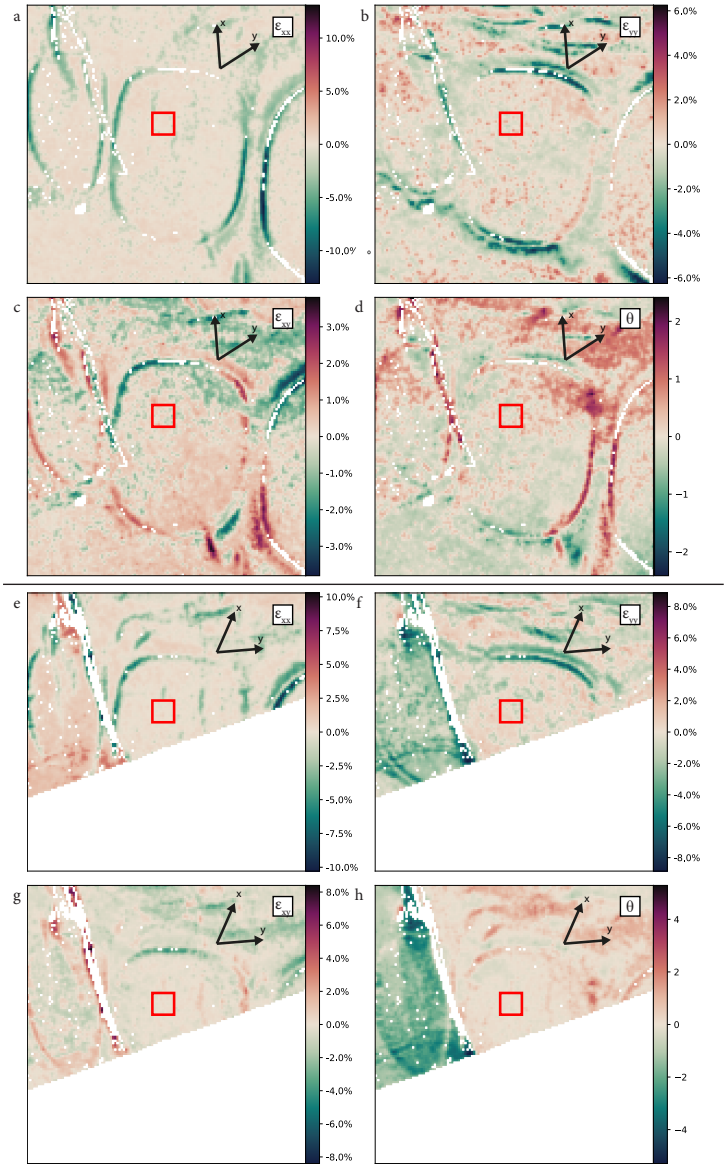

Figure 5.7: **a-d)** strain and rigid rotation deformation maps of one of the layers in the multilayer stack. The red box indicates the reference area. One can observe considerable compressive strain at the edges of holes in the lacy-carbon TEM grid. **e-f)** The strain and rigid rotation deformation maps of the second layer in the multilayer stack. This second layer is visible only in the top half of the map. Analogous to **a-d**, there is noticeable compressive strain around the edges of the holes in the lacy-carbon TEM grid and around the fold spanning the width of this layer. Additionally, there is a relative rigid rotation deformation ($\theta = 2°$) between the area on the left side of the fold and the reference area, which is located on the right side of the fold.

The schematic in fig. 5.8a introduces the concept of a twist angle (α) between two separate layers within a multilayer stack. This twist angle arises from the relative rotation of the crystal lattices in adjacent layers, contributing to the formation of Moiré patterns. On the other hand, fig. 5.8b illustrates the concept of rigid rotation deformation within a single layer. The rotation angle (θ) denotes the rotation of the crystal lattice between the measured location and a reference area. We illustrate this concept with the rotation of the EWPC pattern in this figure. Local variations in strain or defects can drive such rotations within individual layers.

Finally, in fig. 5.8c, we present a map showing the twist angle (α) between two layers within the multilayer stack. One can determine the twist angle by measuring the angle between the EWPC peaks from two neighboring clusters: one from a red cluster and one from a blue cluster. The twist angle in fig. 5.8c denotes the angle between the EWPC peaks in clusters 11 and 4. Notably, the twist angle varies across the stack. On the right side of the fold, the twist angle is approximately 15 degrees, consistent with the measurement from the FFT in fig. 5.6c. However, a smaller twist angle is observed on the left side of the fold due to a slight clockwise rotation in one of the layers, as demonstrated in fig. 5.7f. In summary, our method enables us to map strain within multilayered materials and distinguish between the twist (α) in Moiré lattices and strain-induced rigid rotation deformations (θ).

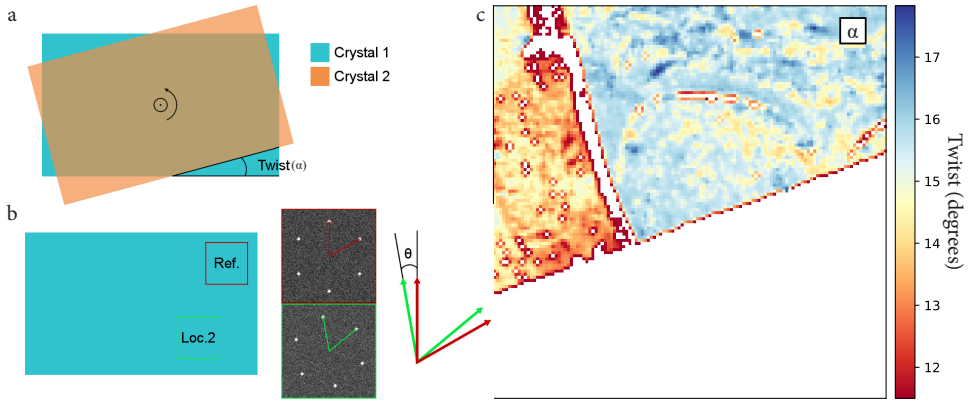

Figure 5.8: **a)** A schematic illustrating the Moiré twist angle (α) between two layers in a multilayer stack. **b)** A representation of the rigid rotation deformation (θ) within the crystal lattice of a single layer. This deformation is defined as the relative rotation of the lattice in the measured location compared to that in a reference area, as depicted by the rotation of the EWPC patterns. **c)** A map highlighting the Moiré twist angle (α) between the two layers in the stack. A slight variation in the twist angle is observed between the left side ($\alpha \simeq 13°$) and the right side ($\alpha \simeq 15°$) of the multilayer

REFERENCES

[1] M. Hÿtch, E. Snoeck, and R. Kilaas, *Quantitative measurement of displacement and strain fields from hrem micrographs,* Ultramicroscopy **74**, 131 (1998).

[2] M. Tinoco, L. Maduro, M. Masaki, E. Okunishi, and S. Conesa-Boj, *Strain-dependent edge structures in mos2 layers,* Nano Letters **17**, 7021 (2017).

[3] M. de la Mata, C. Magén, P. Caroff, and J. Arbiol, *Atomic scale strain relaxation in axial semiconductor iii–v nanowire heterostructures,* Nano Letters **14**, 6614 (2014).

[4] V. B. Ozdol, C. Gammer, X. G. Jin, P. Ercius, C. Ophus, J. Ciston, and A. M. Minor, *Strain mapping at nanometer resolution using advanced nano-beam electron diffraction,* Applied Physics Letters **106**, 253107 (2015).

[5] Y. Han, K. Nguyen, M. Cao, P. Cueva, S. Xie, M. W. Tate, P. Purohit, S. M. Gruner, J. Park, and D. A. Muller, *Strain mapping of two-dimensional heterostructures with subpicometer precision, Nano Letters,* Nano Letters **18**, 3746 (2018).

[6] D. B. Williams and C. B. Carter, *Transmission Electron Microscopy: A Textbook for Materials Science*, 2nd ed. (Springer, 2009) pp. 1–760.

[7] N. Cautaerts, P. Crout, H. W. Ånes, E. Prestat, J. Jeong, G. Dehm, and C. H. Liebscher, *Free, flexible and fast: Orientation mapping using the multi-core and gpu-accelerated template matching capabilities in the python-based open source 4d-stem analysis toolbox pyxem,* Ultramicroscopy , 113517 (2022).

[8] J. Munshi, A. Rakowski, B. H. Savitzky, S. E. Zeltmann, J. Ciston, M. Henderson, S. Cholia, A. M. Minor, M. K. Y. Chan, and C. Ophus, *Disentangling multiple scattering with deep learning: application to strain mapping from electron diffraction patterns,* npj Computational Materials **8**, 254 (2022).

[9] E. Padgett, M. E. Holtz, P. Cueva, Y.-T. Shao, E. Langenberg, D. G. Schlom, and D. A. Muller, *The exit-wave power-cepstrum transform for scanning nanobeam electron diffraction: robust strain mapping at subnanometer resolution and subpicometer precision,* Ultramicroscopy **214**, 112994 (2020).

[10] A. L. Patterson, *A fourier series method for the determination of the components of interatomic distances in crystals,* Phys. Rev. **46**, 372 (1934).

[11] S. van der Walt, J. L. Schönberger, J. Nunez-Iglesias, F. Boulogne, J. D. Warner, N. Yager, E. Gouillart, T. Yu, and the scikit-image contributors, *scikit-image: image processing in Python,* PeerJ **2**, e453 (2014).

[12] D. G. Lowe, *Distinctive image features from scale-invariant keypoints,* International Journal of Computer Vision **60**, 91 (2004).

[13] F. Pedregosa, G. Varoquaux, A. Gramfort, V. Michel, B. Thirion, O. Grisel, M. Blondel, P. Prettenhofer, R. Weiss, V. Dubourg, J. Vanderplas, A. Passos, D. Cournapeau, M. Brucher, M. Perrot, and E. Duchesnay, *Scikit-learn: Machine learning in Python,* Journal of Machine Learning Research **12**, 2825 (2011).

[14] D. Arthur and S. Vassilvitskii, *How slow is the k-means method?* in *Proceedings of the Twenty-Second Annual Symposium on Computational Geometry*, SCG '06 (Association for Computing Machinery, New York, NY, USA, 2006) p. 144–153.

[15] M. Nord, R. W. H. Webster, K. A. Paton, S. McVitie, D. McGrouther, I. MacLaren, and G. W. Paterson, *Fast pixelated detectors in scanning transmission electron microscopy. part i: Data acquisition, live processing, and storage,* Microscopy and Microanalysis **26**, 653 (2020).

[16] P. Virtanen, R. Gommers, T. E. Oliphant, M. Haberland, T. Reddy, D. Cournapeau, E. Burovski, P. Peterson, W. Weckesser, J. Bright, S. J. van der Walt, M. Brett, J. Wilson, K. J. Millman, N. Mayorov, A. R. J. Nelson, E. Jones, R. Kern, E. Larson, C. J. Carey, İ. Polat, Y. Feng, E. W. Moore, J. VanderPlas, D. Laxalde, J. Perktold, R. Cimrman, I. Henriksen, E. A. Quintero, C. R. Harris, A. M. Archibald, A. H. Ribeiro, F. Pedregosa, P. van Mulbregt, and SciPy 1.0 Contributors, *SciPy 1.0: Fundamental Algorithms for Scientific Computing in Python,* Nature Methods **17**, 261 (2020).

[17] K. S. Novoselov, D. Jiang, F. Schedin, T. J. Booth, V. V. Khotkevich, S. V. Morozov, and A. K. Geim, *Two-dimensional atomic crystals,* Proceedings of the National Academy of Sciences **102**, 10451 (2005).

[18] A. K. Geim and I. V. Grigorieva, *Van der waals heterostructures,* Nature **499**, 419 (2013).

[19] N. P. Kazmierczak, M. Van Winkle, C. Ophus, K. C. Bustillo, S. Carr, H. G. Brown, J. Ciston, T. Taniguchi, K. Watanabe, and D. K. Bediako, *Strain fields in twisted bilayer graphene,* Nature Materials **20**, 956 (2021).

[20] Y. Cao, V. Fatemi, S. Fang, K. Watanabe, T. Taniguchi, E. Kaxiras, and P. Jarillo-Herrero, *Unconventional superconductivity in magic-angle graphene superlattices,* Nature **556**, 43 (2018).

6

Automated Strain Mapping with 4D-STEM for 2D Materials Beyond the Planar Configuration

Achieving nanoscale strain field mapping in intricate van der Waals (vdW) nanostructures, like twisted flakes and nanorods, presents several challenges due to their complex geometry, small size, and sensitivity limitations. Understanding these strain fields is pivotal as they significantly influence the optoelectronic properties of vdW materials, playing a crucial role in a plethora of applications ranging from nanoelectronics to nanophotonics. Here, we present a novel approach for achieving a nanoscale-resolved mapping of strain fields across entire micron-sized vdW nanostructures using four-dimensional (4D) Scanning Transmission Electron Microscopy (STEM) imaging equipped with an Electron Microscope Pixel Array Detector (EMPAD). Our technique extends the capabilities of STEM-based strain mapping by means of the exit-wave power cepstrum method, which incorporates automated peak tracking and K-means clustering algorithms. We validate our approach on two representative vdW nanostructures: a 2D MoS_2 thin twisted flakes and a 1D MoO_3/MoS_2 nanorod heterostructure. Beyond just vdW materials, our versatile methodology offers broader applicability for strain-field analysis in various low-dimensional nanostructured materials. This advances our understanding of the intricate relationship between nanoscale strain patterns and their consequent optoelectronic properties.

Parts of this chapter has been published in Small Sci, **M. Bolhuis**, S.E. van Heijst, J.J.M. Sangers, and S. Conesa-Boj (2024)

6.1. INTRODUCTION

The unique mechanical and electronic properties of two-dimensional (2D) van der Waals (vdW) materials have made them increasingly relevant in a wide range of fields, from nanoelectronics to nanophotonics. The presence of local strain fields provides a key handle on the functionalities of vdW materials, which is known to affect the resulting optical, electrical, magnetic, and mechanical properties. [1–6] Consequently, understanding the quantitative implications of local strain fields for the optoelectronic properties of vdW materials is essential for their practical applications.

Transmission Electron Microscopy (TEM) represents a powerful tool for studying crystal structures with high spatial resolution and benefits from the capability of accessing the underlying strain fields by means of electron diffraction methods. Commonly used methods are selected area diffraction (SAD) [7, 8], convergent beam electron diffraction (CBED) [9, 10], and geometric phase analysis (GPA) [11–14]. However, implementing these techniques for 2D vdW materials is challenging because they rely on diffraction contrast. The thin layers in a 2D vdW material often produce a weak diffraction signal, making it difficult to accurately quantify the strain fields with the sought-for nanometer-scale resolution without the use of specialized patterned probes [15, 16]. Furthermore, GPA and related methods are fundamentally limited to a small field of view, which prevents comprehensive inspection of large specimens.

In recent years, four-dimensional (4D) Scanning Transmission Electron Microscopy (STEM) has emerged as a promising complementary technique for strain mapping in nanomaterials. 4D-STEM strain mapping relies on capturing a nanobeam electron diffraction (NBED) [17, 18] pattern for each electron probe position while scanning the entire specimen, which one can accomplish using specialized detectors like the Electron Microscope Pixel Array Detector (EMPAD) [19]. This STEM-based approach enables the mapping of strain fields across complete, micron-sized specimens without sacrificing nanoscale resolution by tracking the position of the NBED diffraction disk [18, 20–23]. However, achieving nanometer spatial resolution in strain mapping remains challenging for 2D vdW materials configurations beyond the traditional regular flakes. The main difficulty in STEM-based strain mapping arises for complex nanostructures, such as twisted 2D layers or 1D heterostructures. The diffraction patterns from these geometries are challenging to classify, as they contain contributions from different crystal structures, crystal orientations, and materials.

In this context, various machine learning methods have been employed to analyze materials at the atomic scale, including deep learning [24] and unsupervised clustering algorithms [25]. While unsupervised clustering algorithms can classify different deformations in nanomaterials based on similarities in their diffraction patterns, they might fall short in accurately isolating strain deformation in the crystal lattice, especially when strain and deformation intricacies are closely intertwined. Indeed, extracting local strain in complex nanostructures requires disentangling the individual contributions of the different crystal structures and materials in the recorded diffraction pattern. This includes accounting for the contributions from non-ideal sample tilt. Advanced techniques like Precession Electron Diffraction (PED) can counteract the contributions from

non-ideal sample orientations but require specialized equipment and increase acquisition time [26, 27]. Additionally, these 2D vdW configurations often exhibit Moiré patterns, further complicating the interpretation of the acquired diffraction patterns regarding strain fields. While recent advances in Bragg interferometry have made it possible to probe strain deformations in twisted graphene and TMD bilayers [28–30], it is still limited to very thin specimens because Bragg interferometry relies on the weak phase approximation to be applicable. The aforementioned limitations highlight the need for general, precise, and accurate methods in analyzing 2D vdW materials beyond the planar configuration, especially in cases where the strain and deformation are intertwined.

Here, we tackle all these challenges by extending STEM-based strain mapping methods by means of the exit-wave power cepstrum (EWPC) approach [31]. The EWPC method has recently been instrumental in strain and grain mapping for a variety of applications, from core-shell nanoparticles to superconducting materials [32–36]. Building upon the EWPC approach, we implement automated peak tracking and K-means clustering algorithms to efficiently calculate interatomic distances at various positions across micron-sized specimens. To demonstrate the reliability of our approach, we apply it to two distinct vdW nanostructures, namely a thin 2D molybdenum disulfide (MoS_2) twisted flake and a 1D MoO_3/MoS_2 nanorod heterostructure. In both cases, we can successfully identify the contributions to the diffraction pattern from individual crystal structures and materials using the EWPC and evaluate the associated strain fields corresponding to well-separated structures, layers, or materials.

Although our focus is on vdW materials, specifically the transition metal dichalcogenide (TMD) MoS_2, our method is highly versatile and can be applied to strain-field characterization in other low-dimensional nanostructured materials. Furthermore, while we developed our method for 4D-STEM datasets captured with the EMPAD, it generally applies to any 4D-STEM dataset captured by one of the many types of 4D-STEM detectors currently available. Our approach offers a new avenue for investigating the intricate relationship between non-trivial nanoscale strain patterns and nanostructured materials' resulting optical, electronic, magnetic, and mechanical properties.

6.2. NANOBEAM ELECTRON DIFFRACTION AND THE EXIT-WAVE POWER CEPSTRUM

Obtaining accurate lattice parameters is crucial for strain measurements in thin nanomaterials such as the vdW materials considered here. One way to determine the lattice parameters is by analyzing the diffraction pattern generated by the electron beam as it passes through the specimen. Classical diffraction techniques, like selected area diffraction (SAD), sample a large crystalline area, which averages the diffraction pattern and reduces precision. Converging the electron beam into a nanometer-sized probe, a technique known as convergent beam electron diffraction (CBED), provides a way forward. To determine lattice parameters using CBED, one can analyze the disk spacings in the zero-order Laue zone (ZOLZ) pattern [18] or measure the radius of the higher-order Laue zone (HOLZ) rings [37, 38]. However, the latter is usually only possible for thicker specimens or specific tilt angles [39, 40]. Therefore, the disk spacing in the ZOLZ pattern is

commonly used to determine the lattice parameters. However, it is only visible under specific electron beam conditions known as nanobeam electron diffraction (NBED).

Within an NBED pattern, the radius of the diffraction disks is smaller than the distance between the center points, which means that the convergent angle (α) of the electron beam is smaller than the Bragg angle (θ_B) for the lattice planes, causing the disks to separate. To achieve NBED conditions, a small condenser aperture (between 10 and 50 μm) can be used [41]. Thus, by combining NBED conditions in STEM imaging with a pixelated detector, the ZOLZ pattern can be recorded for each location on the specimen, allowing for accurate determination of the lattice parameters with excellent spatial resolution.

Figure 6.1a displays a schematic representation of the STEM imaging system, complete with a pixelated detector. The system operates by directing an electron probe towards a thin 2D material specimen, leading to the formation of diffracted beams that form an NBED pattern on the pixelated detector. In such a configuration, the electron beam probes the specimen at position $\mathbf{r}_p = (x, y)$. The projection lenses, not depicted in fig. 6.1a, transmit the corresponding exiting electron wavefunction, $\psi_{\text{out}}(\mathbf{k}, \mathbf{r}_p)$, onto the pixelated detector. These lenses perform an effective Fourier transformation on the electron wave such that the electron wave at the detector plane can be expressed[42] as:

$$\psi_D(\mathbf{k}, \mathbf{r}_p) = \mathcal{F}\{\psi_{\text{out}}(\mathbf{r}, \mathbf{r}_p)\}(\mathbf{k}), \qquad \mathbf{k} = (k_x, k_y). \tag{6.1}$$

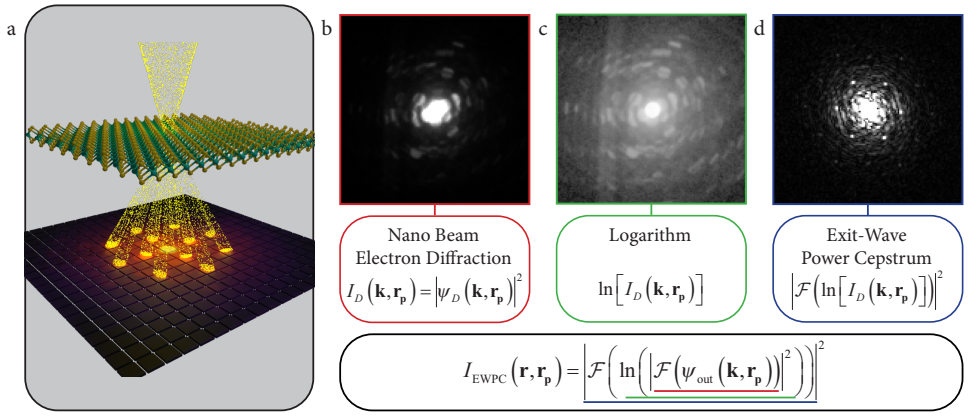

Figure 6.1: **Determination of the exit-wave power cepstrum. a)** Schematic representation of the STEM imaging system, including the pixelated detector, where the electron beam probes a 2D material specimen, and the diffracted beams form an NBED pattern onto the pixelated detector. **b)** A full nanobeam electron diffraction pattern of internally twisted WS_2, which provides the starting point for generating the EWPC. **c)** The logarithm of the NBED pattern displayed in **c**, the second step in generating the EWPC. **d)** The resulting EWPC is generated by taking the fast Fourier transform of **c**.

The electron wave intensity as measured at the detector plane is then given by $I_D\left(\mathbf{k},\mathbf{r}_p\right) = \left|\psi_D\left(\mathbf{k},\mathbf{r}_p\right)\right|^2$. Figure 6.1b shows an example of a captured electron wave intensity pattern, which corresponds to an NBED pattern in this case. This NBED pattern is taken from a internally twisted WS_2 bulk crystal[43]. The intensity distribution in such an NBED pattern directly relates to the crystal lattice parameters. However, this pattern is also susceptible to variations in the specimen thickness and to the tilt or orientation of the specimen, as can be seen in fig. 6.1c.

Indexing an NBED pattern works best when the specimen is precisely oriented in zone-axis (ZA)[44]. However, since the goal is to measure local variations in the lattice parameters of micrometer-sized specimens with many grain boundaries, aligning the entire specimen in ZA is impossible. To overcome this challenge, we apply the exit-wave power cepstrum (EWPC) approach, developed by Padget et al.[31, 45], which enables us to isolate the intensity contributions of the crystal lattice in the NBED pattern and filter out any contributions from non-ideal sample orientation. The EWPC pattern contains sharp peaks representing the crystal's inter-atomic spacing, which is ideal for measuring small variations in the specimen's crystal lattice parameters.

An EWPC can be generated from an NBED pattern using the following relation:

$$I_{\mathrm{EWPC}}\left(\mathbf{r},\mathbf{r}_p\right) = \left|\mathscr{F}\left(\ln\left|\mathscr{F}\left(\psi_{\mathrm{out}}\left(\mathbf{k},\mathbf{r}_p\right)\right)\right|^2\right)\right|^2. \tag{6.2}$$

The initial step in eq. (6.2) involves taking the Fourier transform of the electron wavefunction as it exits the specimen. The microscope lenses automatically perform this transformation, resulting in the NBED pattern depicted in fig. 6.1b. This Fourier transformation translates any convoluted signals into a multiplication of signals.

Next, we construct the EWPC from the NBED pattern in fig. 6.1b by taking the logarithm of the intensity, as shown in fig. 6.1c. The intensity range within the NBED image is effectively flattened by applying a logarithmic transformation, revealing additional Bragg reflections. Furthermore, the logarithm isolates the contributions of the convoluted signals within the wavefunction (additional details can be found in section 5.2).

Finally, a Fast Fourier Transform (FFT) is employed to convert the logarithmic NBED pattern into a real-space representation of the inter-atomic distance. The EWPC pattern in fig. 6.1d reveals six peaks arranged in a hexagonal pattern, characteristic of transition metal dichalcogenide (TMD) materials. Even though the NBED pattern in fig. 6.1c was not oriented along the zone axis or any high-symmetry direction, the hexagonal atomic arrangement can still be clearly identified in the EWPC. The short-range contributions of the non-ideal sample tilt center around the middle of the EWPC, and the sharp peaks in the EWPC represent the contributions of the TMD crystal lattice. By applying band-pass filtering, one can display the individual contributions of the tilt and the crystal lattice in the NBED. See section 5.2 for more details.

6.3. STRAIN FIELDS IN TMD NANOSTRUCTURES

While our method is applicable to and can be utilized for the strain-field characterization of a broad range of crystalline materials [46–48], here we showcase its potential for the specific case of the transition metal dichalcogenide (TMD) materials MoS_2. In particular, we investigate two unique morphologies of the vdW material MoS_2: a two-dimensional (2D) MoS_2 thin film and a one-dimensional (1D) MoS_3/MoS_2 nanorod heterostructure. All these morphologies were synthesized directly on a Si_3N_4 TEM grid using chemical vapor deposition (CVD) [49–51]. For more information about the synthesis of the MoS_2 specimens, please refer to section 2.4.

The first nanostructure consists of single-layer MoS_2 with a layer thickness of 0.65 nm [52, 53], significantly thinner than the 5 nm thick Si_3N_4 membrane that spans the TEM grid. This thin MoS_2 layer produces a sizable NBED pattern suitable for strain measurements. However, in the thinnest regions of the MoS_2 specimen, the NBED diffraction pattern is barely distinguishable from the background signal of the amorphous Si_3N_4 substrate. Section A.6.2 illustrates the variation in NBED pattern intensity between the thinnest and thickest parts of the MoS_2 specimen. Due to this limited diffraction contrast, conventional strain mapping techniques, which rely on detecting slight perturbations in the NBED diffraction pattern using disk detection, face challenges in accurately determining diffraction disk positions. Fortunately, even in the thinnest regions of the MoS_2 specimen, the EWPC method generates sufficient contrast to accurately measure small perturbations. Despite the initial limitations, this quality makes the MoS_2 specimen an ideal candidate for demonstrating the efficacy of the approach presented in this work.

In section 6.4 we examen a MoO_3 nanorod covered with a MoS_2 shell, once again directly grown on a Si_3N_4 TEM grid using CVD [54, 55]. The dimensions of the nanorods present a challenge in aligning the entire specimen along the zone axis, which is typically required for strain field measurements based on NBED. Utilizing the EWPC, our method eliminates this requirement, making it particularly suitable for measuring strain in the MoO_3 nanorod. Additionally, horizontal MoS_2 films can be found in the vicinity of the MoO_3 nanorod on the substrate. This presents an opportunity to showcase the effectiveness of our method in selectively measuring strain in multiple nanostructures simultaneously.

PEAK TRACKING AND CLUSTERING

A single EWPC provides information on the inter-atomic spacing of the crystal lattice directly beneath the electron probe. By scanning the electron probe across the entire specimen in a 2D grid, a two-dimensional EWPC can be generated for each probe position $\mathbf{r}_p$. The resulting 4D dataset contains all the information necessary to determine the inter-atomic spacing for each probe position on the entire specimen.

In our approach, the local strain variations are evaluated by comparing the measured atomic spacing across the specimen with respect to a reference area. These strain fields are calculated through a four-step process. First, we identify the approximate position of the sharp peaks for each EWPC in the acquired dataset. Next, we superimpose all the peak positions from every EWPC to form a weighted point cloud. We cluster the points in this point cloud into groups that match the inter-atomic spacing of the crystal lattice.

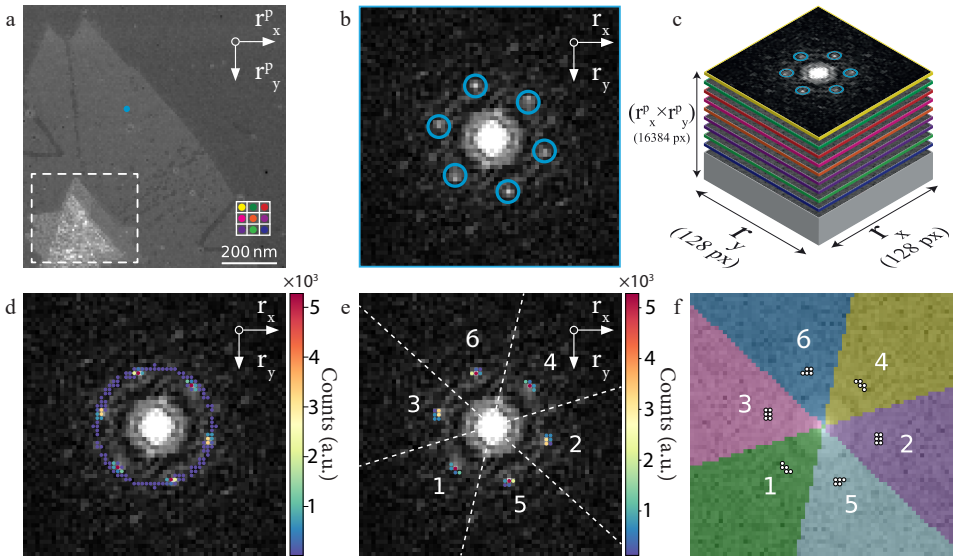

Figure 6.2: **Tracking and clustering of EWPC peaks. a)** ADF image of the MoS_2 thin film studied in this work. The center of the nanostructure, contained in the white box, is composed of multiple overlapping, twisted MoS_2 layers. Each pixel in this ADF image represents a **b)** The EWPC corresponding to the blue dot in **a**, displaying the characteristic hexagonal atomic arrangement of MoS_2. **c)** Representation of the stacking of EWPC patterns into a 2D data array with the r_x and r_y coordinates of every EWPC peak in the 4D dataset. **d)** A weighted point cloud, where each spot represents a unique peak location in the stacked dataset. The spot's color indicates the number of times a unique peak location occurs. **e)** A filtered point cloud, where only the peak locations that appear 53 times or more are displayed. The remaining points can be clustered into six groups. **f)** The resulting six clusters are generated by the K-means clustering algorithm, where each identified peak position is assigned to one of the clusters.

Subsequently, we determine the exact sub-pixel location of the peaks within two non-parallel clusters by calculating the center-of-mass (CoM) of the intensity in the EWPC. Finally, we evaluate the strain across the specimen by measuring the shift in the crystal spacing, represented by the sub-pixel location of the EWPC peaks, with respect to the crystal spacing in the reference region.

Figure 6.2 illustrates the process of identifying the peak locations and the subsequent clustering of the point cloud. The reconstructed Annular Dark-Field (ADF) image in fig. 6.2a showcases the MoS_2 thin film over an Si_3N_4 substrate, as described earlier. Each pixel in this ADF image represents the integrated intensity of a single NBED pattern at a distinct probe position while using an annular mask (see section A.6.1 for additional details). An EWPC can be generated for each probe position using eq. (6.2). The EWPC for the probe location marked by the blue dot in fig. 6.2a is displayed in fig. 6.2b. This EWPC exhibits the characteristic hexagonal atomic arrangement of MoS_2. To assess variations in the atomic arrangement (crystal lattice constants), the location of these six peaks for every probe position must be automatically determined.

Due to noise in the original NBED pattern, which is transferred to the EWPC, accurately detecting the peaks by identifying local maxima in fig. 6.2b is not feasible. Instead, we apply a difference of Gaussian (DoG) detection algorithm that blurs the EWPC with increasing standard deviations. [56] This approach allows the peaks to be detected by identifying the local maxima in the difference between two successively blurred EWPCs (see section 5.3 for more details). Masking can be implemented to ensure that the detected peaks all fall within a specified annular region. Utilizing the annular mask ensures that the short-range contributions of the sample tilt are entirely disregarded during the detection scheme. The DoG detection scheme is then repeated for each EWPC corresponding to every recorded probe position. By utilizing `Dask` arrays instead of the more commonly used `Numpy` arrays, the detection scheme can be executed for multiple EWPCs in parallel, significantly accelerating the entire process.

Upon detecting the peaks in every EWPC within the 4D dataset, an array is obtained that lists the r_x and r_y coordinates of the EWPC peaks for each electron probe position. Subsequently, we combine the arrays for each probe position to form a single two-dimensional array listing all the r_x and r_y coordinates for every EWPC peak throughout the entire 4D dataset, as illustrated schematically in fig. 6.2c. We identify the unique peak positions in the list and determine the number of occurrences to create a weighted point cloud, as displayed in fig. 6.2d. The spots within the point cloud correspond to a unique peak location, with the color of each spot indicating how often this peak location is detected. Hotspots within the point cloud are expected, given that strain effects represent a perturbation rather than a drastic shift in the atomic arrangement of the MoS_2 nanostructure. The remaining spots in the point cloud only appear a few times and can be attributed to incorrectly tracked peaks originating from local maxima in the EWPC noise. Figure 6.2e shows a point cloud with every spot that appears less than 53 times filtered out, revealing a six-fold symmetry that corresponds to the hexagonal atomic arrangement observed in the single EWPC from fig. 6.2b. By applying a K-means clustering algorithm to the filtered point cloud, the spots can be grouped into six clusters, with each peak position assigned to one of the clusters, as shown in fig. 6.2f. All peaks with coordinates in the same cluster are assumed to be a shifted or rotated version of the same peak.

DETERMINATION OF STRAIN FIELD MAPS

The DoG peak identification algorithm determines the peak positions with single-pixel accuracy. However, to achieve the best accuracy in the strain map, the center of the peaks must be determined with sub-pixel accuracy. To do this, we use the peak position found by the DoG scheme as the center of a small circular mask, with a radius R_m of two pixels, that surrounds the peak. The discussion in section 5.5 motivates the need for sub-pixel accuracy and the choice of $R_m = 2$ to achieve the most accurate strain maps. Subsequently, the sub-pixel maximum can be determined by calculating the CoM of the EWPC intensity within this circular mask. Tracking the changes in the peak position of two peaks that are not parallel is sufficient to calculate the local strain variations in the specimen. Thus, calculating the sub-pixel position requires only the peaks from two non-parallel clusters as input, which reduces the computation time.

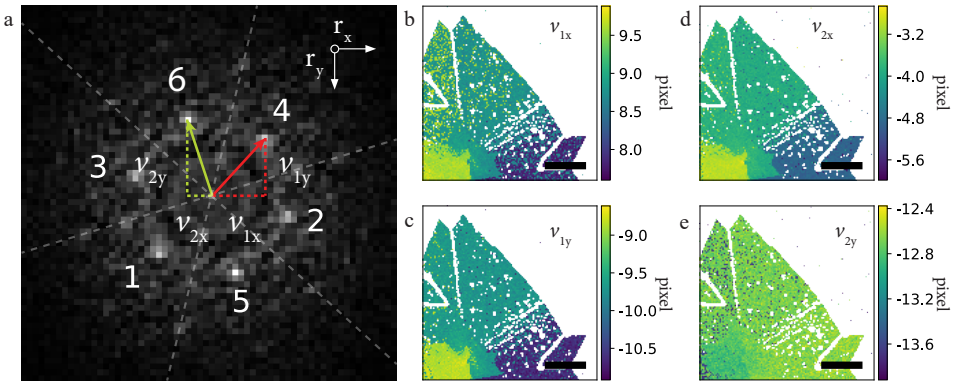

Figure 6.3: **EWPC peak position maps with sub-pixel accuracy. a)** The same EWPC as in fig. 6.2b, now with the vectors $\mathbf{v}_1$ and $\mathbf{v}_2$ indicating the positions of the peaks in clusters 4 and 6 for this specific EWPC. **b-e)** Maps displaying the x and y coordinates, in pixels, for the same $\mathbf{v}_1$ and $\mathbf{v}_2$ vectors for each probe position. The coordinate origin, O(0,0), is the center of the EWPC, and the scale bars in figures **b-e** are 200 nm.

Figure 6.3 illustrates how the r_x and r_y coordinates of two peaks in the EWPC can be mapped for every probe position. Firstly, we select only the peaks corresponding to clusters 4 and 6 from fig. 6.2f. Subsequently, we calculate the sub-pixel maxima of the two non-parallel peaks to determine the r_x and r_y coordinates. The resulting vectors, denoted by $\mathbf{v}_1$ and $\mathbf{v}_2$, represent the location of the two EWPC peaks. The r_x and r_y coordinates of the vectors are given in pixels, and the center of the EWPC image serves as the origin, as depicted in fig. 6.3a. The maps in figs. 6.3b to 6.3e depict the r_x and r_y coordinates for $\mathbf{v}_1$ and $\mathbf{v}_2$, for every probe position.

Using the information in these two vectors, one can calculate the relative strain with respect to the specimen's reference area for each probe position. To calculate the strain fields, we adopt the method commonly used in GPA for finite displacements [57] and construct a deformation matrix $\mathbf{D}$. Depending on the preferred coordinate basis, the deformation matrix can be calculated using:

$$\mathbf{D_{car}} = \mathbf{A}\mathbf{A_0^{-1}} \quad \text{or} \quad \mathbf{D_{vec}} = \mathbf{A_0^{-1}}\mathbf{A} \tag{6.3}$$

Here, matrix $\mathbf{A}$ comprises the measured vectors $\mathbf{v'}_1$ and $\mathbf{v'}_2$, while matrix $\mathbf{A_0}^{-1}$ contains the reference vectors $\mathbf{v}_1$ and $\mathbf{v}_2$. The subscripts "**car**" and "**vec**" in $\mathbf{D_{car}}$ and $\mathbf{D_{vec}}$ indicate which basis determines the deformation. $\mathbf{D_{car}}$ describes the deformation using the Cartesian coordinates system as a basis. In contrast, $\mathbf{D_{vec}}$ characterizes the deformation with respect to the basis formed by vectors $\mathbf{v_1}$ and $\mathbf{v_2}$. Consequently, $\mathbf{D_{vec}}$ describes the deformation perpendicular to the lattice planes represented by the selected EWPC peaks. The choice of basis depends on the specific requirements of the analysis. In this work, we solely demonstrate the deformation concerning the vector basis ($\mathbf{D_{vec}}$). The 2×2 matrix $\mathbf{D_{vec}}$ entirely describes the affine transformation between the vectors $\mathbf{v'}_1$

and $\mathbf{v'}_2$ in the measured region and the vectors $\mathbf{v}_1$ and $\mathbf{v}_2$ in the reference region of the specimen as shown below:

$$\begin{bmatrix} v'_{1x} & v'_{2x} \\ v'_{1y} & v'_{2y} \end{bmatrix} = \mathbf{D_{vec}} \cdot \begin{bmatrix} v_{1x} & v_{2x} \\ v_{1y} & v_{2y} \end{bmatrix}. \tag{6.4}$$

The deformation matrix $\mathbf{D_{vec}}$ contains information about the angular rigid rotation of the specimen and strain deformations within the specimen. By performing a polar decomposition, one can separate the rotation from the strain components in the matrix $\mathbf{D_{vec}}$. Refer to section 5.4 for further details on the definition of $\mathbf{D_{car}}$ and $\mathbf{D_{vec}}$, the different coordinate bases, and the polar decomposition.

We generate the strain and rotation maps displayed in fig. 6.4 by calculating the deformation matrix and executing a polar decomposition for each probe position. Specifically, figs. 6.4a and 6.4b provide the strain components, with ϵ_{xx} representing the strain in the xx direction, which is oriented along the direction of cluster 4 $\langle 10\bar{1}0 \rangle$ in fig. 6.3a, and ϵ_{yy} representing the strain in the yy direction, which is oriented along the direction of cluster 6 $\langle 11\bar{2}0 \rangle$ in fig. 6.3a. Figure 6.4c corresponds to the shear strain (ϵ_{xy}), and fig. 6.4d displays the map of rigid rotation θ within the specimen. All strain and rotation maps have a small Gaussian filter applied to smooth out the pixelated nature of our method. This leads to a more realistic strain field by eliminating point outliers. Further details on the Gaussian filter's effects can be found in section 5.5, while unfiltered strain maps are available in section A.6.3. The red box in each panel indicates the reference region employed for the strain calculations.

The rotation map in fig. 6.4d reveals a rigid clockwise rotation of the MoS_2 nanostructure relative to the reference region. In contrast, figs. 6.4a and 6.4b (representing the ϵ_{xx} and ϵ_{yy} components) indicate substantial strain in the xx and yy directions, respectively. In particular, relative to the reference area, the nanostructure exhibits tensile strain in the xx direction on the left side ($\epsilon_{xx} \simeq 3\%$) and compressive strain on the right side ($\epsilon_{xx} \simeq -4\%$). Conversely, for the strain in the yy direction and in relation to the same reference area, we observe compressive strain on the left side $(\epsilon_{yy} \simeq -3\%)$ and tensile strain on the right $(\epsilon_{yy} \simeq 4\%)$. Additionally, on both the left and right sides of the nanostructure, the tensile strain is observed to be perpendicular to the crack present within the nanostructure. Consistently, the magnitude of strain we observed perpendicular to the direction of the crack in the MoS_2 layer and the rotation across the entire nanostructure align with previously reported behaviors in MoS_2 monolayers, which have been attributed to the emergence of crack structures due to point defects [58, 59]. Furthermore, in the xx direction, distinct regions displaying tensile strain, approximately ($\epsilon_{xx} \simeq 2\%$), are evident. These strained regions can be predominantly linked to the vicinity of point defects and holes present in the MoS_2 layer, a visualization of which is provided in fig. 6.4a. We have estimated the accuracy of the strain and rigid rotation maps to be around $\pm 1.1\%$ and $\pm 0.47^\circ$, respectively, as detailed in section 5.5. It is worth noting that the precision in strain map readings might be further enhanced by increasing the spatial separation between the EWPC peaks and the central position of the EWPC pattern. The strain maps in fig. 6.4 demonstrate that our method is able to accurately

determine the strain in thin TMD materials with weak diffraction contrast. Our method achieves this without the need to filter out the strong contributions of the amorphous Si_3N_4 background, which can influence the accuracy of other strain mapping methods, as discussed in the comparison between different strain mapping methods in section A.6.2.

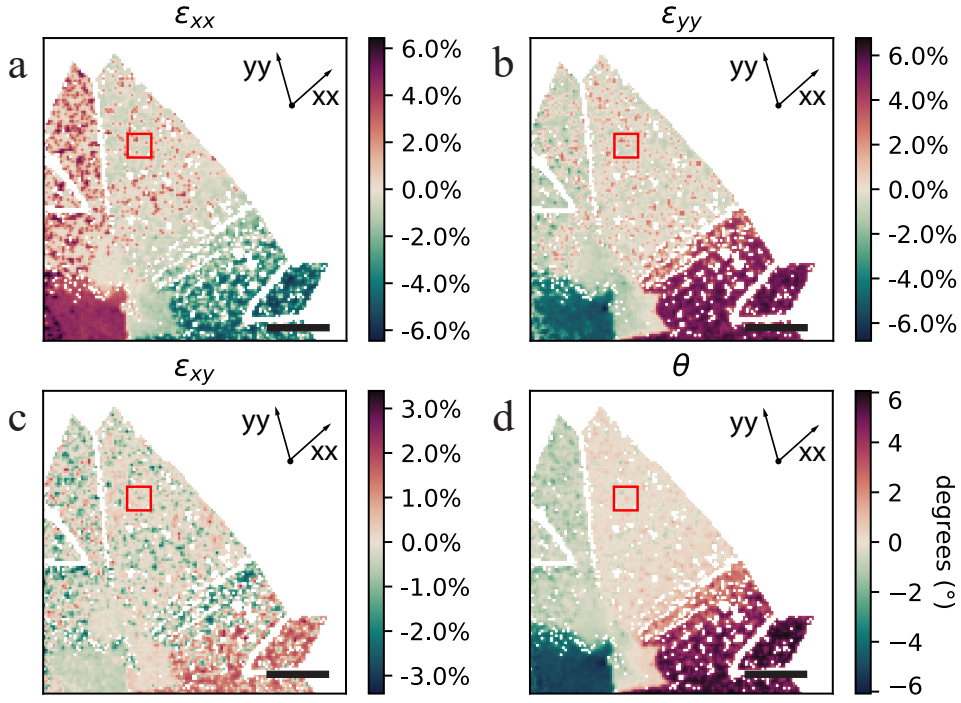

Figure 6.4: **Strain and rotation maps of a MoS_2 thin film nanostructure.** These maps correspond to the nanostructure analyzed in figs. 6.2 and 6.3, with the reference area marked by a red box in each panel. **a)** Strain along the xx-direction, featuring tensile strain ($\epsilon_{xx} \simeq 3\%$) on the left side of the MoS_2 nanostructure and compressive strain ($\epsilon_{xx} \simeq -3\%$) on the right side. **b)** Strain along the yy-direction, displaying compressive strain ($\epsilon_{yy} \simeq -3\%$) on the left side of the MoS_2 nanostructure and tensile strain ($\epsilon_{yy} \simeq 4\%$) on the right side. Note that the tensile strain is consistently perpendicular to the direction of the crack in the MoS_2 nanostructure. **c)** Minimal shear strain ($\epsilon_{xy} \leq 1\%$). **d)** The rigid rotation map illustrates a clockwise rotation of the entire MoS_2 nanostructure. Scale bars in all figures represent 200 nm.

6.4. Strain in Twisted MoS_2 Flakes and 1D MoS_2/MoO_3 Heterostructures

The preceding discussion highlights the capabilities of our approach, which relies on tracking all EWPC peaks using a difference of Gaussians (DoG) scheme, clustering the identified peaks, and calculating the sub-pixel maxima for two non-parallel clusters in determining local strain fields in MoS_2 monolayers. A key aspect of this approach, which makes it applicable to a broad class of nanomaterials and geometries, lies in the clustering of the EWPC peaks. Indeed, by selecting two different clusters, the strain calculation can be performed for two distinct EWPC peaks without tracking the complete set of EWPC peaks again, significantly reducing processing time. Furthermore, this flexibility also renders our method suitable for measuring strain fields in nanostructures with geometries different from the thin film configuration discussed earlier. For instance, in multilayer materials with stacked twisted layers, Moiré patterns can form. These Moiré patterns represent the atomic arrangement of two atomic layers of the same material that are slightly rotated with respect to each other. In such a configuration, the atomic arrangements of the different twisted layers appear as separate peaks in the EWPC.

To demonstrate the applicability of our method in identifying Moiré patterns in van der Waals materials, we observe that the MoS_2 nanostructure examined in figs. 6.2 to 6.4 also includes a small region comprising multiple stacked atomic layers. This region is located at the center of the nanostructure and is highlighted by the white box in fig. 6.2a. Additionally, we extend our study to twisted heterostructures $MoSe_2/WSe_2$, the results of which can be found in section 5.6. In the following, we primarily focus on Moire patterns arising from the same material. Figure 6.5c presents an EWPC obtained from a multilayer region containing two sets of six peaks, with each set belonging to a separate stacked layer. By tracking the 12 peaks simultaneously, a single point cloud can be generated (fig. 6.5b), representing all the peaks associated with both layers. Two peaks from the same layer can then be chosen to isolate the strain fields and the rigid rotation angle associated with each layer. For instance, selecting clusters 4 and 2 in fig. 6.5b isolates the same MoS_2 layer as in fig. 6.4, yielding a strain map that, as expected, is comparable to the previous results (see section A.6.3). Conversely, selecting clusters 9 and 5 isolates the second MoS_2 layer, which is only present in the region of the specimen highlighted by the white box in fig. 6.2a. Figure 6.5b displays the resulting rotation map for this second layer, demonstrating how our method can also be used to independently measure the rigid rotation deformation arising in the crystal lattice of each layer in the stacked vdW multilayer. The corresponding strain maps of the second layer can be found in section A.6.3.

Our method can also be applied to heterostructures composed of different materials with non-trivial geometrical configurations, as demonstrated in the following example. Figure 6.6a displays an ADF image of a MoO_3 nanorod surrounded by a thin MoS_2 shell, resulting in a one-dimensional (1D) MoO_2/MoO_3 heterostructure. In the vicinity of the nanorod on the substrate, we also observe the horizontal growth of MoS_2. In the ADF image, the contrast is quite low, making it challenging to discern the details of the structure. fig. 6.6b depicts the EWPC corresponding to the region displaying horizontal MoS_2

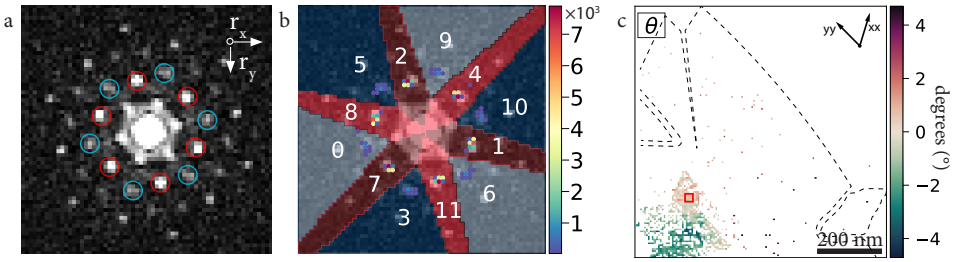

Figure 6.5: **Moiré pattern analysis of twisted multilayer MoS_2 films. a)** EWPC for the same MoS_2 specimen studied in figs. 6.2 to 6.4, corresponding to the area displaying a twisted multilayer structure and indicated by the white box in fig. 6.2a. The resulting Moiré pattern consists of two sets of six peaks, each set belonging to an individual atomic layer. **b)** The resulting weighted point cloud is obtained from the DoG peak detection algorithm, where all unique peak positions with at least 35 occurrences are included. This point cloud is divided into twelve clusters, with the red clusters belonging to the first layer and the blue clusters belonging to the second layer. **c)** The rotation map of the second layer, generated by selecting only the peaks in clusters 9 and 5, with the reference area indicated by the red box.

growth, located at the bottom left corner and marked by a blue dot in fig. 6.6a. The EWPC highlights the characteristic hexagonal peak distribution associated with horizontally oriented MoS_2. Figure 6.6c showcases the EWPC captured at a point in the center of the nanorod, revealing a total of 14 peaks. Four of these peaks, labeled with Roman numerals (III to VI), exhibit low intensity, making their detection challenging. Thus, we exclude them before implementing the automated DoG detection scheme. Additionally, the peaks labeled as I and II are located in close proximity to the center of the EWPC and to the peaks corresponding to the horizontal MoS_2 film. To prevent them from clustering together with the peaks related to the horizontal growth during the DoG detection, we exclude these peaks as well. As a result, we limit the maximum number of peaks the DoG detection scheme needs to identify to eight peaks. This approach enables us to detect all peaks associated with the region of horizontal MoS_2 film (indicated by a blue circle in fig. 6.6b) and the peaks associated with the MoO_3 nanorod (indicated by a ref circle in fig. 6.6c).

Figure 6.6d presents the resulting point cloud, showcasing all peaks detected more than 150 times after applying the DoG detection scheme. We can identify fourteen clusters, where the blue clusters represent the hexagonal pattern of the horizontal MoS_2 film, and the red clusters correspond to the MoO_3 nanorod. Clustering both strain and rigid rotation information offers a significant advantage, as it isolates the individual contributions of the MoO_3 nanorod and the MoS_2 horizontal film. For example, by selecting two clusters that are part of the same pattern, our method can effectively distinguish between the strain fields present in the MoO_3 nanorod and those associated with the MoS_2 horizontal film. Figures 6.6e and 6.6f provide an illustration of this concept. Figure 6.6e showcases the shear strain map (ϵ_{xy}) of the MoO_3 nanorod, calculated by selecting clusters 4 and 9. The map highlights that the nanorod has a region of tensile strain ($\epsilon_{xx} = 0.52$) at the top of the nanorod. This observation is consistent with the change in intensity in the ADF image in fig. 6.6a, which indicates a sharp change in the thickness of the MoO_3 nanorod.

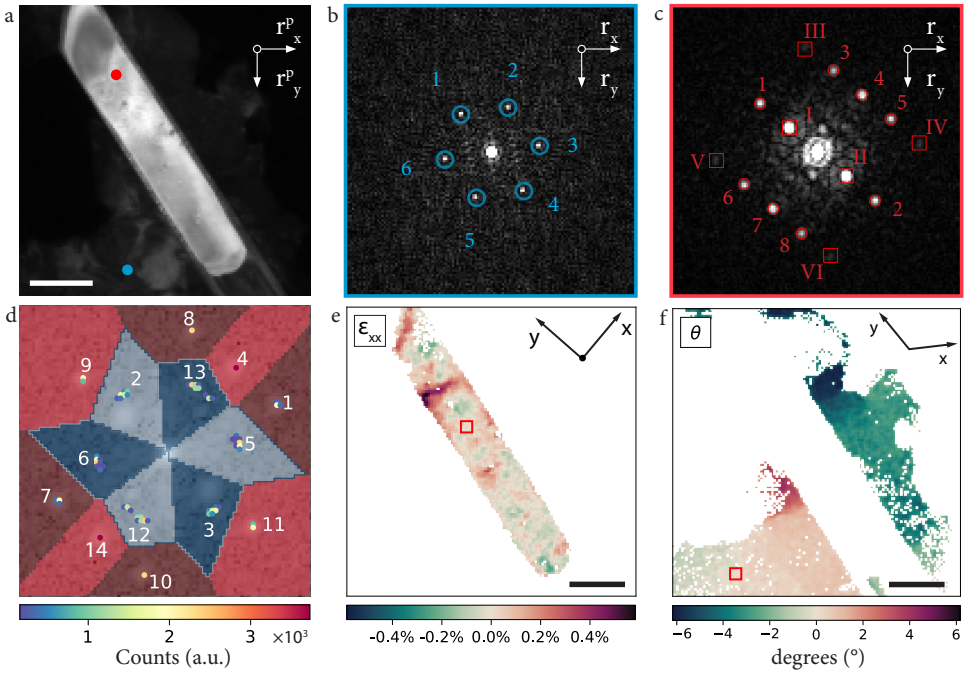

Figure 6.6: **Advanced clustering analysis with DoG for non-planar 2D materials.** **a)** ADF image of a 1D MoO_3/MoS_2 nanorod with horizontal growth of MoS_2 observed on the substrate. The low contrast in the image makes it difficult to discern the details of the structure. **b)** The EWPC obtained from a probe position on the MoS_2 film, indicated by the blue dot in **a**. **c)** The EWPC obtained from a probe position on the MoO_3 nanorod, marked by a red dot in **a**. **d)** The weighted point cloud of all unique peak positions (occurring at least 150 times) identified by the DoG detection algorithm can be classified into 14 clusters. The blue clusters correspond to peaks from the MoS_2 film and exhibit the same six-fold symmetry as in **b**, while the red clusters correspond to the peaks from the MoO_3 nanorod and display mirror symmetry as in **c**. **e)** Shear Strain map, ϵ_{xy}, calculated from clusters 4 and 9 and representing the region within the MoO_3 nanorod. **f)** The rotation map, θ, of the MoS_2 thin film was determined by using the information in clusters 13 and 2. The scale bars in Figs. **a, e** and **f** correspond to 50 nm.

In contrast, fig. 6.6f illustrates the rigid rotation angle (θ) in the MoS_2 thin film, obtained by selecting clusters 13 and 2. The map unveils the presence of two separate MoS_2 films in proximity to the nanorod. Notably, the MoS_2 film located to the right of the nanorod manifests a pronounced rigid rotation compared to the film on its left. This differential rotation suggests that the MoS_2 films were grown independently and are not intrinsically linked to the MoO_3 structure. Building on these findings, our results showcase the ability of our method to measure strain fields independently across diverse materials encapsulated within intricate heterostructures and geometries. This ability is currently beyond the scope of other 4D-STEM strain mapping techniques[23, 31]. See section A.6.4 for the complete set of strain and rotation maps for both the MoO_3 nanorod and the MoS_2 film.

6.5. SUMMARY AND OUTLOOK

In this work, we present a novel approach based on 4D STEM imaging with a pixelated detector (EMPAD) for determining local strain fields in 2D van der Waals materials with nanoscale resolution over complete micron-sized specimens. This method accurately characterizes strain fields and rotation angles, complementing and extending the capabilities of existing strain measurement techniques. A notable advantage is its ability to differentiate between adjacent layers' strain contributions or distinct materials within a heterostructure. As such, it emerges as an indispensable tool for automating the detection of Moiré patterns, in addition to measuring strain fields and rigid rotations in layered vdW nanomaterials.

While our investigation focus centered on MoS_2 in varied configurations, the strategy is fully general and suitable for strain-field characterization in other complex nanomaterials beyond the 2D van der Waals family. The application of this approach can revolutionize our understanding of the nexus between nanoscale strain and the consequent electronic and magnetic attributes of a wide range of nanomaterials. Especially when coupled with spatially-resolved measurements like the band gap and the dielectric function procured from Electron Energy Loss Spectroscopy (EELS) on the same specimen, as showcased in our recent work on internally twisted WS_2 nanostructures [43, 60, 61]. The corresponding software framework, dubbed STRAINMAPPER, is now available to the global community via its GITLAB repository, complemented with comprehensive documentation and illustrative examples. We anticipate that this method will become a valuable resource for scientists aiming to understand the implications of nanoscale strain fields on the properties of the materials under study, a key step in bridging the gap between fundamental vdW material science and their implementation in technological applications.

6.6. METHODS

TRANSMISSION ELECTRON MICROSCOPE EXPERIMENTS

All 4D STEM measurements were conducted using a Titan Cube microscope operated at 300 kV, combined with an Electron Microscope Pixel Array Detector optimized for 4D-STEM. The dwell time for all measurements was set at 1 ms. The resolution of all the 4D-STEM images was 128x128, resulting in a 128x128x128x128 dataset. A 10-μm C2 aperture was used for all measurements, yielding a convergence angle of 0.53 $mrad$. The camera length used for the measurements on the MoS_2 nanostructure from fig. 6.2a was 460 mm, while the camera length used for the measurements on the MoO_3 nanorod from fig. 6.6 was 285 mm. See section A.6.5 an overview.

PEAK TRACKING AND CLUSTERING ALGORITHMS

The proposed approach involves multiple steps, including EWPC peak tracking with a DoG detection scheme, K-means clustering of unique peak positions, calculating the sub-pixel maximum using the CoM, and affine transformation determination relative to a reference area. The method is built on the `Pixstem` Python package [62], which loads and processes 4D datasets into memory-optimized `Dask` arrays [63]. Using `Dask`

arrays enables parallel CPU computing to significantly accelerate all operations in our approach [64]. This makes it possible to use our method efficiently on a personal computer with just 8GB of system memory and four multi-threading CPU cores. The generation of the EWPCs from the NBED patterns and basic operations on the EWPCs is accomplished by combining custom code and using existing Python packages. The DoG detection scheme and the K-means clustering are provided by the `scikit image` [65] and `learn` [66] Python packages, respectively. The sub-pixel maximum is calculated using a CoM algorithm provided by `Pixstem` along with a modified mask generation algorithm optimized for 4D masks. We determine the final affine transformation and strain maps using our custom code, which can calculate the deformation with respect to the Cartesian or vector basis. The polar decomposition is performed using `SciPy`[67].

Additionally, we have conducted a comparison analysis of our proposed approach with alternative strain mapping methods, including `py4DSTEM`[23] and `PC-STEM`[31]. This comparison was performed using two distinct datasets, and the detailed results can be found in section A.6.2. The code used to produce the results of this study, including detailed documentation and instructions for each process step, is available in the `StrainMAPPER` repository[1]. The open-source code is available under the GNU GPL v3 license. Our package functions contain all the necessary steps to go from a 4D NBED dataset to strain maps.

[1] https://gitlab.tudelft.nl/conesabojlab/strainmapper

A.6. APPENDIX

A.6.1. VIRTUAL ANNULAR DARK FIELD IMAGE

Figure A.6.1 highlights how a virtual ADF detector is created by applying an annular mask to each NBED pattern (pixel). This computational method generates an ADF image, similar to the conventional STEM techniques discussed in section 4.3. The mask acts as a window function (W) in eq. (4.13) in the same way as a physical annular detector would in conventional STEM. The advantage of the 4D-STEM method is that the mask size and position can be chosen after the completion of the dataset rather than relying on a fixed set of detector geometries. This flexibility allows one to create BF, ADF, and HAADF images from one single dataset.

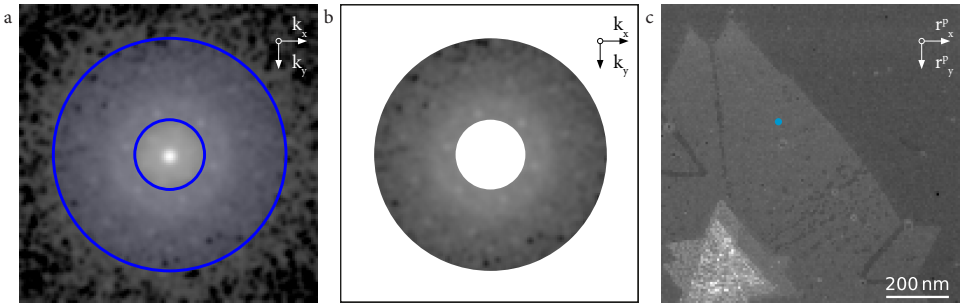

Figure A.6.1: **a)** A virtual ADF detector is created by applying an annular mask to each NBED pattern (pixel). **b)** The electron intensity is integrated over the annular mask giving a total electron count for each pixel. **c)** The process in **a** and **b** is repeated with the same annular mask for each NBED pattern in the 4D dataset, resulting in the virtual ADF image. The blue dot in the ADF image indicates the location of the NBED pattern in **a**.

A.6.2. COMPARISON BETWEEN 4D-STEM STRAIN MAPPING METHODS

In this section, we compare the results of the StrainMAPPER method to other methods aimed at measuring strain fields using 4D-STEM. Directly comparing StrainMAPPER with different methods, such as py4DSTEM [68], pyxem [69], and PC-STEM [31], is not straightforward because each method is developed and optimized for different types of 4D-STEM datasets. Specifically, the py4DSTEM and pyxem methods determine the position of Bragg disks to assess the specimen's strain, while the PC-STEM and StrainMAPPER methods use the position of EWPC peaks to determine the specimen's strain. The optimal TEM acquisition conditions for obtaining clear Bragg disks and distinct EWPC patterns can vary significantly. Therefore, using the same dataset with each method is sometimes unfeasible.

In this section, we will compare the strain maps of two specimens using the py4DSTEM (CBED), PC-STEM (EWPC), and StrainMAPPER (EWPC) methods. The first specimen we examined is a MoS_2 nanostructure. Figure A.6.2a displays an ADF image of the MoS_2 nanostructure generated by the py4DSTEM method. For the py4DSTEM method, we utilized a dataset with a large camera length, $L = 910mm$, to clearly visualize the Bragg disks. Figure A.6.2b shows a CBED pattern taken in the multilayer region of the MoS_2 nanostructure, as indicated by the orange dot in fig. A.6.2a. The py4DSTEM method

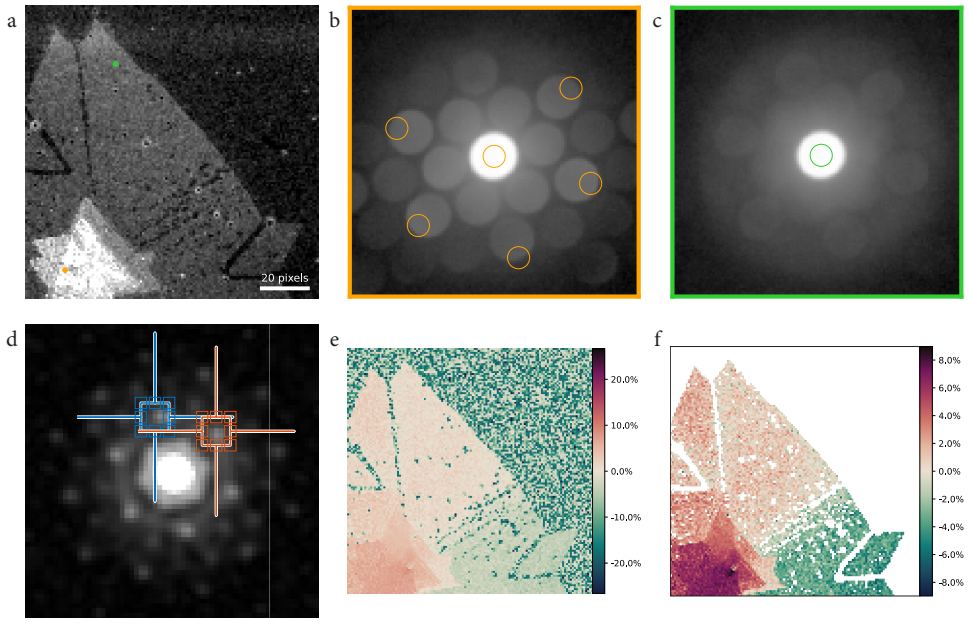

Figure A.6.2: **a)** An ADF image of the MoS_2 nanostructure generated by the py4DSTEM method. **b)** The CBED pattern corresponding to multilayer MoS_2, indicated by the orange dot in **a**. **c)** The CBED pattern corresponding to monolayer MoS_2, indicated by the green dot in **a**. The orange and green circles in **b** and **c** indicate the Bragg disks identified by the py4DSTEM method. **d)** An EWPC pattern generated by the PC-STEM method. The blue and orange search windows indicate the selected EWPC peaks for the strain measurements. **e)** The ϵ_{xx} strain map generated by the PC-STEM method. Due to the amorphous background signal, the method yields large strain values in the substrate. **f)** The same strain map as in **e**, but with a mask applied to filter out the large "strain" values in the substrate. This strain map is comparable to the one generated by the StrainMAPPER method (see Figure 4 in the main manuscript).

accurately determines the positions of multiple Bragg disks in this CBED pattern. However, the diffraction contrast significantly reduces for the thinnest part of the MoS_2 specimen. The CBED pattern in fig. A.6.2c corresponds to a region marked by the green dot in fig. A.6.2a. The very low diffraction contrast of the monolayer MoS_2, combined with the signal from the amorphous Si_3N_4 substrate, leads to the py4DSTEM method losing track of the position of most Bragg disks. For specimens like those presented here, characterized by low diffraction contrast and a strong background signal, CBED-based methods for determining strain are less suitable.

The EWPC-based methods provide a way forward for these challenging specimens. For both the PC-STEM and StrainMAPPER methods, we utilized a dataset with a small camera length, ($L = 460mm$), which is optimal for EWPC applications [31]. Figure A.6.2d shows an EWPC generated using the PC-STEM method, along with the search windows for two EWPC peaks. We selected the same two EWPC peaks as mentioned earlier. The resulting strain map (ϵ_{xx}) from the PC-STEM method is presented in fig. A.6.2e.

The PC-STEM method identifies the local maximum inside the search window to determine the EWPC location with sub-pixel accuracy. However, this approach encounters challenges with specimens like the one under examination here, where only specific areas of the 4D dataset contain crystalline material. In such cases, the PC-STEM method may interpret background signals from the amorphous Si_3N_4 as EWPC peak, leading to strain maps with significant strain values, even in regions lacking a crystalline specimen.

In contrast, the StrainMAPPER method employs a two-step approach that circumvents this issue. First, the DoG peak track method accurately distinguishes between the EWPC peaks from the crystalline specimen and those arising from the amorphous background. Subsequently, the CoM method precisely determines the EWPC peak positions with sub-pixel accuracy only for locations containing crystalline material. However, the PC-STEM method accurately measures the strain in the MoS_2 specimen; it faces difficulties in distinguishing between crystalline and amorphous regions. To address this, a post-process mask can be applied to the substrate region, effectively highlighting the strain in the MoS_2 specimen, as shown in fig. A.6.2f. It is worth noting that the `PC-STEM` method does not currently support the use of such a mask. Instead, we utilized the StrainMAPPER method's results as a mask template. The final strain map (ϵ_{xx}) generated by `PC-STEM` method closely resembles the strain map produced by the StrainMAPPER method, as depicted in fig. 6.4.

For comparison with the py4DSTEM, PC-STEM, and StrainMAPPER methods, we utilized a second specimen obtained from the py4DSTEM tutorials GitHub page. This specimen consists of alternating $Si/Si_{0.82}Ge_{0.18}$ multilayers stacked on top of a Si substrate. The py4DSTEM tutorial includes the experimental 4D-STEM dataset alongside the tutorial materials. The acquisition conditions used for this dataset are well-suited for generating an EWPC pattern, allowing us to apply all three methods to the same dataset. In fig. A.6.3a, you can observe the strain map (ϵ_{xx}) as presented in the py4DSTEM tutorial. To highlight the strain at the SiGe interface, we manually adjusted the maximum and minimum values on the scale bar. Figure A.6.3b displays the same strain map without any adjustments to the scale bar. In this representation, the strain at the SiGe interfaces is no longer discernible due to the large patch on the left. It is important to note that, as indicated in the py4DSTEM tutorial, the accuracy of the obtained strain may be limited due to the specimen's thickness and the downsampling of the dataset provided alongside the tutorial.

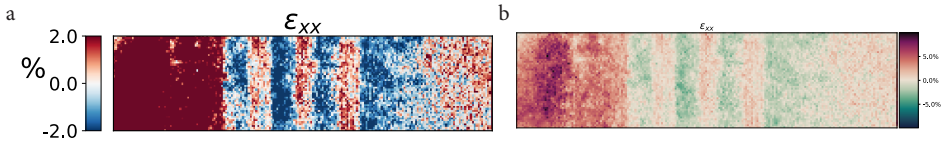

Figure A.6.3: **a)** The ϵ_{xx} strain map of the $Si/Si_{0.82}Ge_{0.18}$ multilayer, as represented by the py4DSTEM method, with manually specified minimum and maximum values. **b)** The same strain map as in **a** but now represented in the same style as the StrainMAPPER strain maps, without manually specified minimum and maximum values. The py4DSTEM method is less accurate in resolving the 5 $Si/Si_{0.82}Ge_{0.18}$ multilayers.

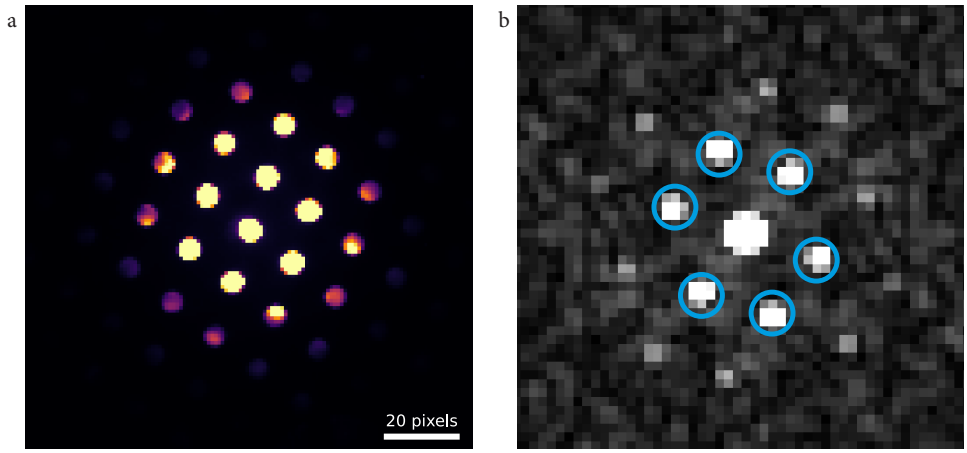

Figure A.6.4: **a)** A (mean) CBED pattern of the Si/$Si_{0.82}Ge_{0.18}$ multilayer generated by the py4DSTEM method. **b)** A single EWPC pattern of the multilayer generated by the StrainMAPPER method.

The dataset from the py4DSTEM tutorial is well-suited for the EWPC strain mapping techniques used in the StrainMAPPER and PC-STEM methods. In fig. A.6.4a, we display the CBED pattern generated using py4DSTEM, representing the Si substrate. Figure A.6.4b shows the corresponding EWPC pattern generated by StrainMAPPER. It's worth noting that the EWPC peaks are located only a few pixels from the center, which may not be ideal for achieving the highest accuracy with the EWPC methods, as discussed in section 5.5. Nevertheless, it is still possible to track the EWPC peak location along the specimen. Figures A.6.5a and A.6.5b display the strain maps generated by the StrainMAPPER and PC-STEM methods, respectively. These maps represent the strain in the x direction (ϵ_{xx}), with the x and y directions denoted by the Cartesian coordinate system. Both EWPC methods yield similar results and offer improved resolution compared to the py4DSTEM CBED-based method when mapping the 5 Si/$Si_{0.82}Ge_{0.18}$ multilayers.

The enhanced accuracy of the StrainMAPPER method is highlighted in figs. A.6.5c and A.6.5d. Using the py4DSTEM tutorial [68], we can map the average strain along the length of the multilayer and compare it with the estimated strain as calculated using Vengard's law. The StrainMAPPER method can resolve all 5 of the multilayers, and the obtained strain values are closer to the expected ones.

In conclusion, the EWPC-based StrainMAPPER method accurately maps strain, even in specimens with limited diffraction contrast. It effectively distinguishes EWPC peaks from crystalline specimens and background signals generated by thick amorphous layers. Moreover, StrainMAPPER can map strain within SiGe multilayers, even when dealing with thick specimens and downsampled 4D datasets.

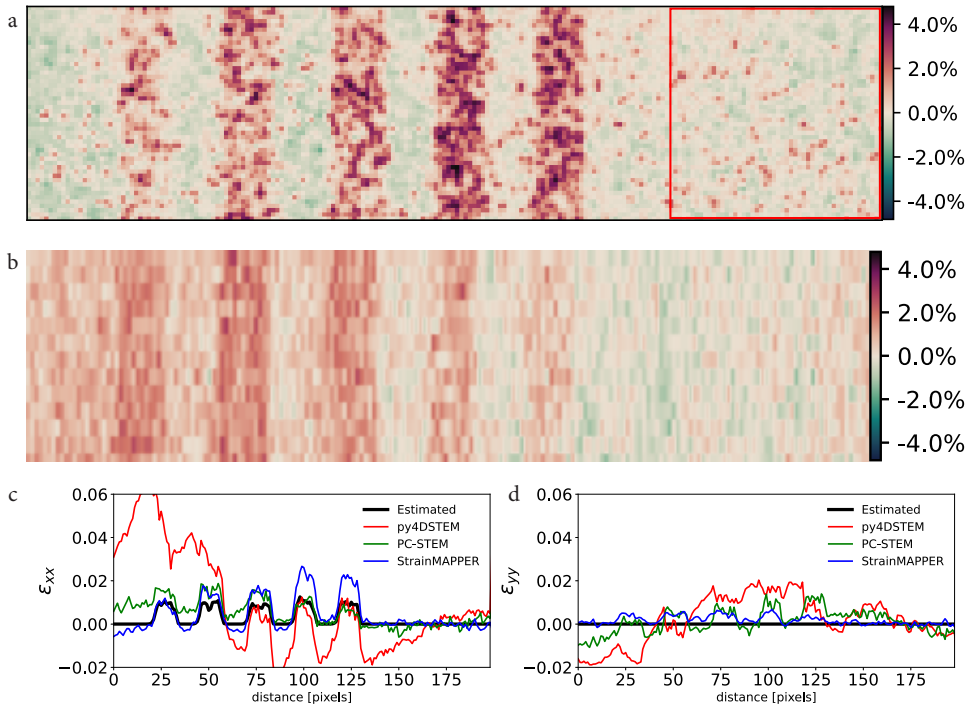

Figure A.6.5: **a-b)** The ϵ_{xx} strain maps, as generated by the StrainMAPPER and PC-STEM methods, respectively. Both methods can resolve all 5 of the $Si/Si_{0.82}Ge_{0.18}$ multilayers. **c-d)** The mean ϵ_{xx} and ϵ_{yy} strain values for all three methods, compared to the estimated strain values by Vengard's law. The strain values of the StrainMAPPER method resemble the estimated strain values the closest.

A.6.3. STRAIN AND ROTATION MAPS OF THE MoS_2 MOIRÉ MULTILAYER

Figure A.6.6 displays the complete set of train and rotation maps of the MoS_2 Moiré multilayer specimen discussed in section 6.4. Figures A.6.6a to A.6.6d depict the strain and ridged rotation in the the bottom MoS_2 layer of the Moiré structure. Figures A.6.6e to A.6.6h depict the strain and ridged rotation in the top MoS_2 layer. Within the field of view of the measurement, there is only a small region that contains the second layer. Therefore, we have indicated the border of the bottom layer with the black dashed line.

A.6.4. STRAIN AND ROTATION MAPS OF THE MoS_2/MoO_3 HETEROSTRUCTURE

Figure A.6.7 displays the full set of strain and rotation maps of the MoO_3 nanorod, and fig. A.6.8 displays the full set of strain and rotation maps of the MoS_2 thin film.

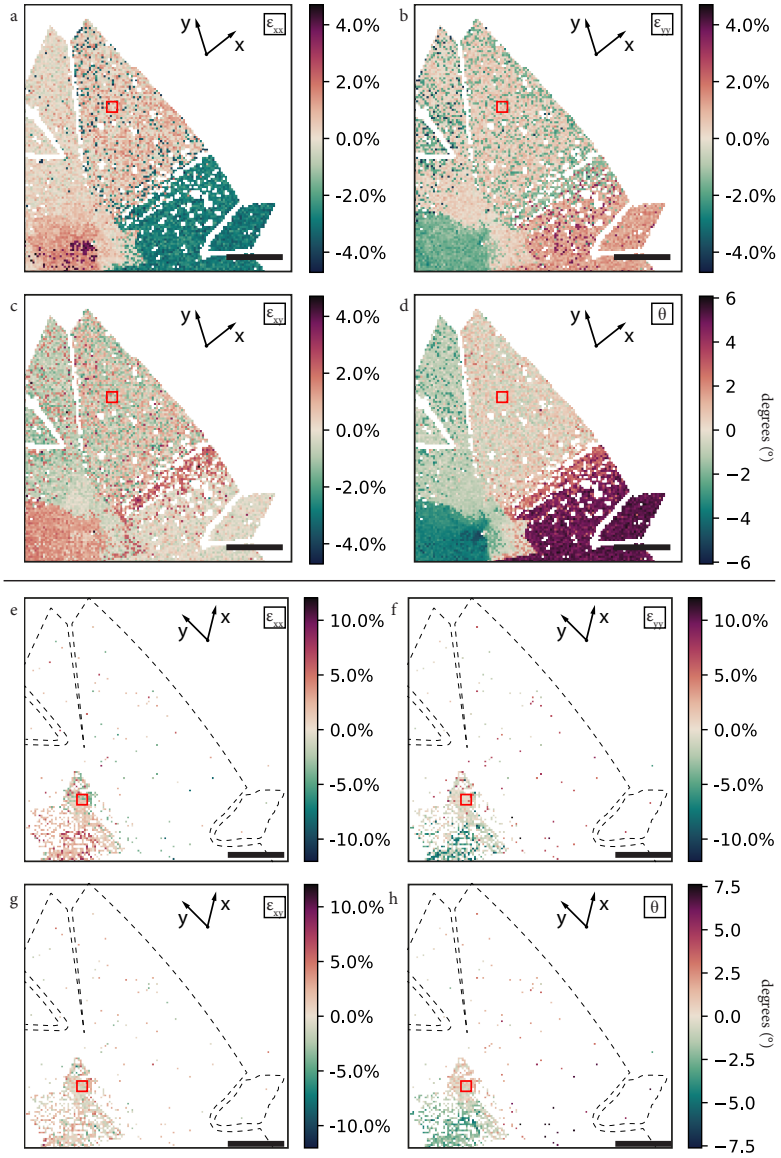

Figure A.6.6: **a-d)** The strain and rotation maps of the first MoS_2 layer in the Moiré point cloud in fig. 6.5b. These maps were calculated using the EWPC peaks from cluster 4 and cluster 2. The region used as a reference is denoted by the red box. These strain maps are almost identical to the strain and rotation maps in fig. 6.4, indicating the flexibility of our approach. It doesn't matter whether we track the EWPC peaks of the Moiré pattern separately or all at once. We can determine the strain in both layers with similar accuracy. **e-h)** The strain and rotation maps of the second MoS_2 layer in the Moiré point cloud in fig. 6.5b. These maps were calculated using the EWPC peaks from cluster 9 and cluster 5. The reference point is denoted by the red box. The scale bars in all figures are 200 nm.

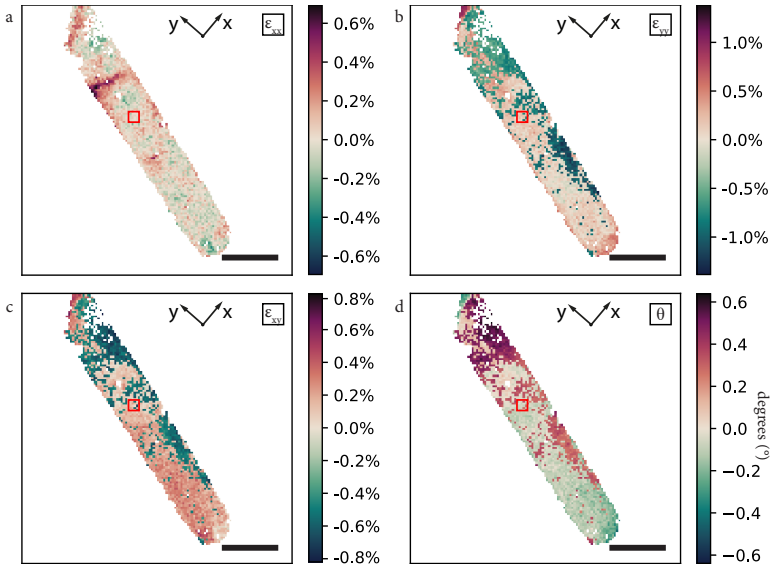

Figure A.6.7: **a-d)** The complete strain and rotation maps of the MoO_3 nanorod. These maps were calculated using the EWPC peaks from cluster 4 and cluster 9 in the point cloud from fig. 6.6d. The region used as a reference is denoted by the red box. The scale bars in all figures are 50 nm.

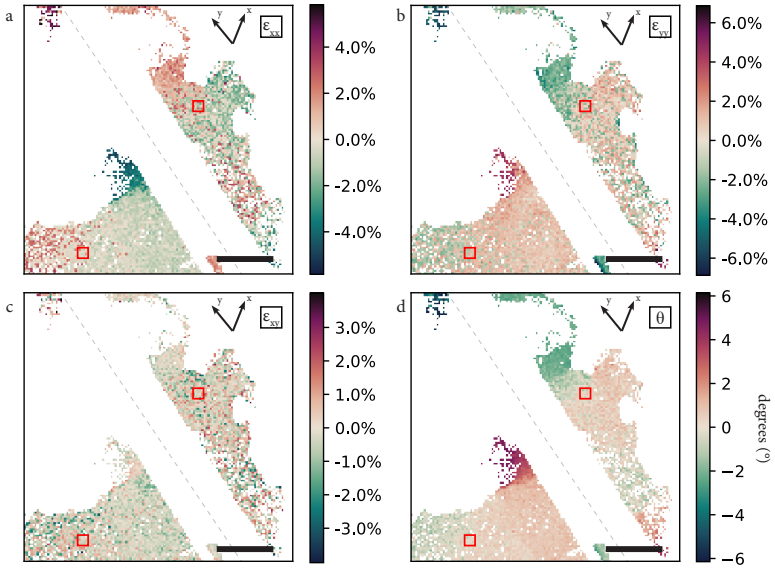

Figure A.6.8: **a-b)** The strain and rotation maps of the MoS_2 thin film. These maps were calculated using the EWPC peaks from cluster 5 and cluster 2 in the point cloud from fig. 6.6d. The rotation map in fig. 6.6e shows that the MoS_2 thin films on the left and the right are separated by the MoO_3 nanorod. Therefore, two reference areas (indicated by the red boxes) were selected for the strain and rotation maps of the MoS_2 thin films. One for the left and one for the right MoS_2 thin film. The scale bars in all figures are 50 nm.

A.6.5. 4D-STEM ACQUISITION DETAILS

Table 6.1 contains the acquisition parameters used in each of the figures shown in chapter 6.

	Figure 6.1	Figures 6.2 to 6.5	Figure 6.6
Accelerating voltage	300 kV	300 kV	300 kV
Convergence semi-angle (mrad)	2.63	0.53	0.53
Camera length (mm)	285	460	285
Dwell time (ms)	1	1	1
Magnification	40K	40K	160K

Table 6.1: 4D-STEM acquisition parameters are used in each of the figures shown in the main manuscript.

REFERENCES

[1] Y. He, Y. Yang, Z. Zhang, Y. Gong, W. Zhou, Z. Hu, G. Ye, X. Zhang, E. Bianco, S. Lei, Z. Jin, X. Zou, Y. Yang, Y. Zhang, E. Xie, J. Lou, B. Yakobson, R. Vajtai, B. Li, and P. Ajayan, *Strain-induced electronic structure changes in stacked van der waals heterostructures,* Nano Letters **16**, 3314 (2016).

[2] S. Huang, G. Zhang, F. Fan, C. Song, F. Wang, Q. Xing, C. Wang, H. Wu, and H. Yan, *Strain-tunable van der waals interactions in few-layer black phosphorus,* Nature Communications **10**, 2447 (2019).

[3] T. M. G. Mohiuddin, A. Lombardo, R. R. Nair, A. Bonetti, G. Savini, R. Jalil, N. Bonini, D. M. Basko, C. Galiotis, N. Marzari, K. S. Novoselov, A. K. Geim, and A. C. Ferrari, *Uniaxial strain in graphene by raman spectroscopy: g peak splitting, grüneisen parameters, and sample orientation,* Phys. Rev. B **79**, 205433 (2009).

[4] V. M. Pereira, A. H. Castro Neto, and N. M. R. Peres, *Tight-binding approach to uniaxial strain in graphene,* Phys. Rev. B **80**, 045401 (2009).

[5] M. Huang, H. Yan, C. Chen, D. Song, T. F. Heinz, and J. Hone, *Phonon softening and crystallographic orientation of strained graphene studied by raman spectroscopy,* Proceedings of the National Academy of Sciences **106**, 7304–7308 (2009).

[6] P. A. Vermeulen, J. Mulder, J. Momand, and B. J. Kooi, *Strain engineering of van der waals heterostructures,* Nanoscale **10**, 1474 (2018).

[7] H. J. Kim, H. Kim, S. Yang, and J. Y. Kwon, *Grains in Selectively Grown MoS2 Thin Films,* Small **13**, 1 (2017).

[8] F. Uesugi, *Strain mapping in selected area electron diffraction method combining a cs-corrected tem with a stage scanning system,* Ultramicroscopy **135**, 80 (2013).

[9] P. M. Jones, G. M. Rackham, J. W. Steeds, and F. C. Frank, *Higher order laue zone effects in electron diffraction and their use in lattice parameter determination,* Proceedings of the Royal Society of London. A. Mathematical and Physical Sciences **354**, 197 (1977).

[10] S. Rozeveld and J. Howe, *Determination of multiple lattice parameters from convergent-beam electron diffraction patterns,* Ultramicroscopy **50**, 41 (1993).

[11] M. Hÿtch, E. Snoeck, and R. Kilaas, *Quantitative measurement of displacement and strain fields from hrem micrographs,* Ultramicroscopy **74**, 131 (1998).

[12] M. Tinoco, L. Maduro, M. Masaki, E. Okunishi, and S. Conesa-Boj, *Strain-dependent edge structures in mos2 layers,* Nano Letters **17**, 7021 (2017).

[13] M. de la Mata, C. Magén, P. Caroff, and J. Arbiol, *Atomic scale strain relaxation in axial semiconductor iii–v nanowire heterostructures,* Nano Letters **14**, 6614 (2014).

[14] R. Bierwolf, M. Hohenstein, F. Phillipp, O. Brandt, G. Crook, and K. Ploog, *Direct measurement of local lattice distortions in strained layer structures by hrem,* Ultramicroscopy **49**, 273 (1993).

[15] S. E. Zeltmann, A. Müller, K. C. Bustillo, B. Savitzky, L. Hughes, A. M. Minor, and C. Ophus, *Patterned probes for high precision 4d-stem bragg measurements,* Ultramicroscopy **209**, 112890 (2020).

[16] A. Londoño-Calderon, R. Dhall, C. Ophus, M. Schneider, Y. Wang, E. Dervishi, H. S. Kang, C.-H. Lee, J. Yoo, and M. T. Pettes, *Visualizing grain statistics in mocvd wse2 through four-dimensional scanning transmission electron microscopy,* Nano Letters **22**, 2578 (2022).

[17] V. B. Ozdol, C. Gammer, X. G. Jin, P. Ercius, C. Ophus, J. Ciston, and A. M. Minor, *Strain mapping at nanometer resolution using advanced nano-beam electron diffraction,* Applied Physics Letters **106**, 253107 (2015).

[18] Y. Han, K. Nguyen, M. Cao, P. Cueva, S. Xie, M. W. Tate, P. Purohit, S. M. Gruner, J. Park, and D. A. Muller, *Strain mapping of two-dimensional heterostructures with subpicometer precision, Nano Letters,* Nano Letters **18**, 3746 (2018).

[19] M. W. Tate, P. Purohit, D. Chamberlain, K. X. Nguyen, R. Hovden, C. S. Chang, P. Deb, E. Turgut, J. T. Heron, D. G. Schlom, D. C. Ralph, G. D. Fuchs, K. S. Shanks, H. T. Philipp, D. A. Muller, and S. M. Gruner, *High Dynamic Range Pixel Array Detector for Scanning Transmission Electron Microscopy,* Microscopy and Microanalysis **22**, 237 (2016).

[20] Y. Jiang, Z. Chen, Y. Han, P. Deb, H. Gao, S. Xie, P. Purohit, M. W. Tate, J. Park, S. M. Gruner, V. Elser, and D. A. Muller, *Electron ptychography of 2d materials to deep sub-ångström resolution,* Nature **559**, 343 (2018).

[21] T. C. Pekin, C. Gammer, J. Ciston, A. M. Minor, and C. Ophus, *Optimizing disk registration algorithms for nanobeam electron diffraction strain mapping,* Ultramicroscopy **176**, 170 (2017), 70th Birthday of Robert Sinclair and 65th Birthday of Nestor J. Zaluzec PICO 2017 – Fourth Conference on Frontiers of Aberration Corrected Electron Microscopy.

[22] D. Johnstone, P. Crout, M. Nord, C. Francis, J. Laulainen, S. Høgås, E. Opheim, B. Martineau, T. Bergh, E. Prestat, N. Cautaerts, S. Smeets, H. W. Ånes, A. Ross, J. Broussard, S. Collins, T. Furnival, D. Jannis, I. Hjorth, S. Huang, E. Jacobsen, M. Danaie, A. Herzing, T. Poon, S. Dagenborg, T. Doherty, J. Morzy, A. Iqbal, T. Ostasevicius, T. I. Thorsen, M. von Lany, and R. Tovey, *pyxem/pyxem: pyxem 0.15.1,* (2023).

[23] B. H. Savitzky, S. E. Zeltmann, L. A. Hughes, H. G. Brown, S. Zhao, P. M. Pelz, T. C. Pekin, E. S. Barnard, J. Donohue, L. Rangel DaCosta, E. Kennedy, Y. Xie, M. T. Janish, M. M. Schneider, P. Herring, C. Gopal, A. Anapolsky, R. Dhall, K. C. Bustillo, P. Ercius, M. C. Scott, J. Ciston, A. M. Minor, and C. Ophus, *py4DSTEM: A Software Package for*

Four-Dimensional Scanning Transmission Electron Microscopy Data Analysis, Microscopy and Microanalysis **27**, 712 (2021).

[24] J. Munshi, A. Rakowski, B. H. Savitzky, S. E. Zeltmann, J. Ciston, M. Henderson, S. Cholia, A. M. Minor, M. K. Y. Chan, and C. Ophus, *Disentangling multiple scattering with deep learning: application to strain mapping from electron diffraction patterns,* npj Computational Materials **8**, 254 (2022).

[25] C. Shi, M. C. Cao, S. M. Rehn, S.-H. Bae, J. Kim, M. R. Jones, D. A. Muller, and Y. Han, *Uncovering material deformations via machine learning combined with four-dimensional scanning transmission electron microscopy,* npj Computational Materials **8**, 114 (2022).

[26] E. Rauch and M. Véron, *Automated crystal orientation and phase mapping in tem,* Materials Characterization **98**, 1 (2014).

[27] J. Jeong, N. Cautaerts, G. Dehm, and C. H. Liebscher, *Automated crystal orientation mapping by precession electron diffraction-assisted four-dimensional scanning transmission electron microscopy using a scintillator-based cmos detector,* Microscopy and Microanalysis **27**, 1102–1112 (2021).

[28] M. J. Zachman, J. Madsen, X. Zhang, P. M. Ajayan, T. Susi, and M. Chi, *Interferometric 4d-stem for lattice distortion and interlayer spacing measurements of bilayer and trilayer 2d materials,* Small **17**, 2100388 (2021).

[29] N. P. Kazmierczak, M. Van Winkle, C. Ophus, K. C. Bustillo, S. Carr, H. G. Brown, J. Ciston, T. Taniguchi, K. Watanabe, and D. K. Bediako, *Strain fields in twisted bilayer graphene,* Nature Materials **20**, 956 (2021).

[30] M. Van Winkle, I. M. Craig, S. Carr, M. Dandu, K. C. Bustillo, J. Ciston, C. Ophus, T. Taniguchi, K. Watanabe, A. Raja, S. M. Griffin, and D. K. Bediako, *Rotational and dilational reconstruction in transition metal dichalcogenide moiré bilayers,* Nature Communications **14**, 2989 (2023).

[31] E. Padgett, M. E. Holtz, P. Cueva, Y.-T. Shao, E. Langenberg, D. G. Schlom, and D. A. Muller, *The exit-wave power-cepstrum transform for scanning nanobeam electron diffraction: robust strain mapping at subnanometer resolution and subpicometer precision,* Ultramicroscopy **214**, 112994 (2020).

[32] E. Padgett, M. E. Holtz, A. Kongkanand, and D. A. Muller, *Strain relaxation in core-shell pt-co catalyst nanoparticles,* (2023).

[33] Z. Sun, Z. Baraissov, R. D. Porter, L. Shpani, Y.-T. Shao, T. Oseroff, M. O. Thompson, D. A. Muller, and M. U. Liepe, *Smooth, homogeneous, high-purity nb3sn superconducting rf resonant cavity by seed-free electrochemical synthesis,* Superconductor Science and Technology **36**, 115003 (2023).

[34] T. Zhang, A. T. Eaton, D. K. Mukherjee, M. Cao, A. L. Coughlin, T. Ruch, X. Zhan, H. Zhu, Y. Han, H. A. Fertig, and S. Zhang, *Experimental observation of geometric*

effect on the electron diffraction of quasi-one-dimensional nanostructures, Materials Today Physics **33**, 101048 (2023).

[35] M. E. Holtz, E. Padgett, A. C. Johnston-Peck, I. Levin, D. A. Muller, and A. A. Herzing, *Mapping Polar Distortions using Nanobeam Electron Diffraction and a Cepstral Approach,* Microscopy and Microanalysis **29**, 1422 (2023).

[36] Y.-T. Shao, R. Yuan, H.-W. Hsiao, Q. Yang, Y. Hu, and J.-M. Zuo, *Cepstral scanning transmission electron microscopy imaging of severe lattice distortions,* Ultramicroscopy **231**, 113252 (2021), 80th Birthdays of Colin Humphreys and Knut Urban, 75th Birthdays of Wolfgang Baumeister and John Spence - PICO 2021 – Sixth Conference on Frontiers of Aberration Corrected Electron Microscopy.

[37] A. Béché, J. L. Rouvière, L. Clément, and J. M. Hartmann, *Improved precision in strain measurement using nanobeam electron diffraction,* Applied Physics Letters **95**, 123114 (2009).

[38] J. Zuo, *Automated lattice parameter measurement from holz lines and their use for the measurement of oxygen content in yba2cu3o7 from nanometer-sized region,* Ultramicroscopy **41**, 211 (1992).

[39] A. Armigliato, R. Balboni, G. P. Carnevale, G. Pavia, D. Piccolo, S. Frabboni, A. Benedetti, and A. G. Cullis, *Application of convergent beam electron diffraction to two-dimensional strain mapping in silicon devices,* Applied Physics Letters **82**, 2172 (2003).

[40] D. DIERCKS, M. KAUFMAN, R. IRWIN, A. JAIN, L. ROBERTSON, J. WEIJTMANS, and R. WISE, *Using a <670> zone axis for convergent beam electron diffraction measurements of lattice strain in strained silicon,* Journal of Microscopy **239**, 154 (2010).

[41] A. Armigliato, S. Frabboni, and G. C. Gazzadi, *Electron diffraction with ten nanometer beam size for strain analysis of nanodevices,* Applied Physics Letters **93**, 161906 (2008).

[42] I. Lazić, E. G. Bosch, and S. Lazar, *Phase contrast STEM for thin samples: Integrated differential phase contrast,* Ultramicroscopy **160**, 265 (2016).

[43] S. E. van Heijst, M. Bolhuis, A. Brokkelkamp, J. J. M. Sangers, and S. Conesa-Boj, *Heterostrain-driven bandgap increase in twisted ws2: A nanoscale study,* Advanced Functional Materials **34**, 2307893 (2024).

[44] T. Grieb, F. F. Krause, M. Schowalter, D. Zillmann, R. Sellin, K. Müller-Caspary, C. Mahr, T. Mehrtens, D. Bimberg, and A. Rosenauer, *Strain analysis from nanobeam electron diffraction: Influence of specimen tilt and beam convergence,* Ultramicroscopy **190**, 45 (2018).

[45] A. M. Noll, *Cepstrum pitch determination,* The Journal of the Acoustical Society of America **41**, 293 (1967).

[46] S. Sharan and J. Narayan, *Strain relief mechanisms and the nature of dislocations in gaas/si heterostructures,* Journal of Applied Physics **66**, 2376 (1989).

[47] Q. Xie, P. Chen, and A. Madhukar, *Inas island-induced-strain driven adatom migration during gaas overlayer growth,* Applied Physics Letters **65**, 2051 (1994).

[48] Z. Yu, D. A. Muller, and J. Silcox, *Study of strain fields at a-si/c-si interface,* Journal of Applied Physics **95**, 3362 (2004).

[49] M. Bolhuis, J. Hernandez-Rueda, S. E. van Heijst, M. Tinoco Rivas, L. Kuipers, and S. Conesa-Boj, *Vertically-oriented mos2 nanosheets for nonlinear optical devices,* Nanoscale **12**, 10491 (2020).

[50] S. E. van Heijst, M. Mukai, E. Okunishi, H. Hashiguchi, L. I. Roest, L. Maduro, J. Rojo, and S. Conesa-Boj, *Illuminating the electronic properties of ws2 polytypism with electron microscopy,* Annalen der Physik **533**, 2000499 (2021).

[51] J. Lee, S. Pak, P. Giraud, Y. W. Lee, Y. Cho, J. Hong, A. R. Jang, H. S. Chung, W. K. Hong, H. Y. Jeong, H. S. Shin, L. G. Occhipinti, S. M. Morris, S. N. Cha, J. I. Sohn, and J. M. Kim, *Thermodynamically Stable Synthesis of Large-Scale and Highly Crystalline Transition Metal Dichalcogenide Monolayers and their Unipolar n–n Heterojunction Devices,* Advanced Materials **29**, 1702206 (2017).

[52] X. Li and H. Zhu, *Two-dimensional mos2: Properties, preparation, and applications,* Journal of Materiomics **1**, 33 (2015).

[53] P. Yang, S. Zhang, S. Pan, B. Tang, Y. Liang, X. Zhao, Z. Zhang, J. Shi, Y. Huan, Y. Shi, S. J. Pennycook, Z. Ren, G. Zhang, Q. Chen, X. Zou, Z. Liu, and Y. Zhang, *Epitaxial growth of centimeter-scale single-crystal mos2 monolayer on au(111),* ACS Nano **14**, 5036 (2020).

[54] J. D. Cain, F. Shi, J. Wu, and V. P. Dravid, *Growth Mechanism of Transition Metal Dichalcogenide Monolayers: The Role of Self-Seeding Fullerene Nuclei,* ACS Nano **10**, 5440 (2016).

[55] C.-M. Hyun, J.-H. Choi, S. W. Lee, J. H. Park, K.-T. Lee, and J.-H. Ahn, *Synthesis mechanism of mos2 layered crystals by chemical vapor deposition using moo3 and sulfur powders,* Journal of Alloys and Compounds **765**, 380 (2018).

[56] D. G. Lowe, *Distinctive image features from scale-invariant keypoints,* International Journal of Computer Vision **60**, 91 (2004).

[57] J. Rouvière and E. Sarigiannidou, *Theoretical discussions on the geometrical phase analysis,* Ultramicroscopy **106**, 1 (2005).

[58] T. H. Ly, J. Zhao, M. O. Cichocka, L.-J. Li, and Y. H. Lee, *Dynamical observations on the crack tip zone and stress corrosion of two-dimensional mos2,* Nature Communications **8**, 14116 (2017).

[59] G. Wang, Y.-P. Wang, S. Li, Q. Yang, D. Li, S. T. Pantelides, and J. Lin, *Engineering the crack structure and fracture behavior in monolayer mos2 by selective creation of point defects,* Advanced Science **9**, 2200700 (2022).

[60] A. Brokkelkamp, J. ter Hoeve, I. Postmes, S. E. van Heijst, L. Maduro, A. V. Davydov, S. Krylyuk, J. Rojo, and S. Conesa-Boj, *Spatially Resolved Band Gap and Dielectric Function in Two-Dimensional Materials from Electron Energy Loss Spectroscopy,* The Journal of Physical Chemistry A **126**, 1255 (2022).

[61] L. I. Roest, S. E. van Heijst, L. Maduro, J. Rojo, and S. Conesa-Boj, *Charting the low-loss region in electron energy loss spectroscopy with machine learning,* Ultramicroscopy **222**, 113202 (2021).

[62] M. Nord, R. W. H. Webster, K. A. Paton, S. McVitie, D. McGrouther, I. MacLaren, and G. W. Paterson, *Fast pixelated detectors in scanning transmission electron microscopy. part i: Data acquisition, live processing, and storage,* Microscopy and Microanalysis **26**, 653 (2020).

[63] Dask Development Team, *Dask: Library for dynamic task scheduling* (2016).

[64] M. Rocklin, *Dask: Parallel computation with blocked algorithms and task scheduling,* in *Proceedings of the 14th Python in Science Conference,* edited by K. Huff and J. Bergstra (2015) pp. 130 – 136.

[65] S. van der Walt, J. L. Schönberger, J. Nunez-Iglesias, F. Boulogne, J. D. Warner, N. Yager, E. Gouillart, T. Yu, and the scikit-image contributors, *scikit-image: image processing in Python,* PeerJ **2**, e453 (2014).

[66] F. Pedregosa, G. Varoquaux, A. Gramfort, V. Michel, B. Thirion, O. Grisel, M. Blondel, P. Prettenhofer, R. Weiss, V. Dubourg, J. Vanderplas, A. Passos, D. Cournapeau, M. Brucher, M. Perrot, and E. Duchesnay, *Scikit-learn: Machine learning in Python,* Journal of Machine Learning Research **12**, 2825 (2011).

[67] P. Virtanen, R. Gommers, T. E. Oliphant, M. Haberland, T. Reddy, D. Cournapeau, E. Burovski, P. Peterson, W. Weckesser, J. Bright, S. J. van der Walt, M. Brett, J. Wilson, K. J. Millman, N. Mayorov, A. R. J. Nelson, E. Jones, R. Kern, E. Larson, C. J. Carey, İ. Polat, Y. Feng, E. W. Moore, J. VanderPlas, D. Laxalde, J. Perktold, R. Cimrman, I. Henriksen, E. A. Quintero, C. R. Harris, A. M. Archibald, A. H. Ribeiro, F. Pedregosa, P. van Mulbregt, and SciPy 1.0 Contributors, *SciPy 1.0: Fundamental Algorithms for Scientific Computing in Python,* Nature Methods **17**, 261 (2020).

[68] B. H. Savitzky, S. E. Zeltmann, L. A. Hughes, H. G. Brown, S. Zhao, P. M. Pelz, T. C. Pekin, E. S. Barnard, J. Donohue, L. Rangel DaCosta, E. Kennedy, Y. Xie, M. T. Janish, M. M. Schneider, P. Herring, C. Gopal, A. Anapolsky, R. Dhall, K. C. Bustillo, P. Ercius, M. C. Scott, J. Ciston, A. M. Minor, and C. Ophus, *py4DSTEM: A Software Package for Four-Dimensional Scanning Transmission Electron Microscopy Data Analysis,* Microscopy and Microanalysis **27**, 712 (2021).

[69] N. Cautaerts, P. Crout, H. W. Ånes, E. Prestat, J. Jeong, G. Dehm, and C. H. Liebscher, *Free, flexible and fast: Orientation mapping using the multi-core and gpu-accelerated template matching capabilities in the python-based open source 4d-stem analysis toolbox pyxem,* Ultramicroscopy , 113517 (2022).

7

Investigating the Effects of CBED Intensity Distribution Patterns Beyond Electric Field Measurements in 2D Materials

The emergence of four-dimensional (4D) Scanning Transmission Electron Microscopy (STEM), enabled by fast pixelated detectors, has revolutionized the study of van der Waals (vdW) materials, allowing unprecedented insights into their structural and electronic properties. However, the interpretation of 4D-STEM data is often complicated by artifacts arising from probe defocus, substrate effects, and crystal misalignments, particularly in low-dimensional systems. This chapter addresses key challenges in interpreting 4D-STEM measurements by using MoS_2 and InSe as model systems. We demonstrate that CoM shifts near MoS_2 edges, previously attributed to intrinsic electric fields, are artifacts caused by defocus-induced shadow imaging. In ultra-thin MoS_2, we reveal how substrate-induced backgrounds reduce diffraction contrast. Additionally, we map grain boundary orientations in bulk InSe and account for artifacts introduced by excitation errors and dynamical scattering. By resolving these challenges, we establish a robust framework for accurately interpreting 4D-STEM data. These findings improve the reliability of nanoscale analyses and offer a pathway for more precise structural and electronic characterization of low-dimensional materials.

7.1. INTRODUCTION

Nanostructured van der Waals (vdW) materials are highly sensitive to atomic-scale structural variations, significantly influencing their electronic and photonic properties [1–3]. Features such as edge structures, polarity, and grain boundaries play critical roles in defining the functionality of transition metal dichalcogenides (TMDs) and other vdW systems. Understanding these structural variations and their impact on material properties requires advanced characterization techniques capable of probing atomic-scale features with high precision. Scanning Transmission Electron Microscopy (STEM) provides exceptional spatial resolution for studying low-dimensional materials by generating convergent beam electron diffraction (CBED) patterns. By employing a condensed electron probe, STEM generates convergent beam electron diffraction (CBED) patterns, which provide a two-dimensional representation of the interaction between the probe and the specimen. These patterns enable the nanoscale characterization of structural properties, such as strain, polarity, and lattice distortions.

The emergence of four-dimensional STEM (4D-STEM), enabled by fast pixelated detectors, such as the high dynamic range Electron Microscope Pixel Array Detector (EMPAD), has significantly advanced the analytical capabilities of STEM [4–6]. By recording CBED patterns at each probe position, 4D-STEM produces datasets that allow for mapping momentum shifts, quantified as center-of-mass (CoM) shifts, across the specimen [7–9]. This approach provides critical insights into local potential fields [7–9], strain [10–13], and crystal polarity [14–16]. The use of Kossel-Möllenstedt (K-M) CBED patterns in 4D-STEM offers advantages for analyzing strain and polarity by minimizing diffraction overlap under specific conditions. CoM analysis, which links CoM shifts to projected local electric fields under the phase object approximation (POA) [17], enables the generation of spatial maps of local fields and strain distributions. However, artifacts caused by probe defocus, substrate effects, and crystal misalignments often complicate data interpretation, particularly in vdW materials[18, 19]. Addressing these challenges is critical to unlocking the full potential of 4D-STEM for nanoscale characterization.

This chapter systematically tackles key challenges in interpreting 4D-STEM data using monolayer MoS_2 and bulk InSe as model systems. First, we identify artefactual CoM shifts near MoS_2 edges, revealing that these shifts, commonly attributed to intrinsic electric fields, arise from defocus-induced shadow imaging. Second, we explore the limitations of polarity imaging in ultra-thin MoS_2, demonstrating how substrate-induced backgrounds and reduced diffraction contrast obscure polarity detection. Lastly, we use CoM analysis to map grain boundary orientations in bulk InSe, addressing artifacts from crystal misalignments and dynamical scattering. By addressing these challenges, this work establishes a robust framework for 4D-STEM data interpretation in vdW materials. Our findings enhance the reliability of CoM-based analysis and demonstrate its potential for uncovering structural and electronic insights in low-dimensional systems. This work paves the way for more accurate characterization of vdW materials and broader applications in nanoscale science and technology.

7.2. CONVERGENT BEAM ELECTRON DIFFRACTION AND THE CENTER-OF-MASS

Scanning transmission electron microscopy (STEM) is an all-encompassing term for various TEM techniques that utilize a scanning electron probe to gather the desired information from the specimen. The unifying property of all STEM techniques is their utilization of a condensed electron probe [20]. This condensed probe is formed by the condenser lenses, which project the defocused electron source from the lens system onto the specimen plane. The electron wavefunction at the back focal plane can be described as $\psi(\vec{k})$, where $\vec{k} = (k_x, k_y)$ is a position vector in reciprocal space. After interacting with the specimen, the exiting electron wavefunction can be described as:

$$\psi_{\text{out}}(\vec{r}, \vec{r}^{\,p}) = \psi_{in}(\vec{r}) \cdot T(\vec{r}, \vec{r}^{\,p}) \tag{7.1}$$

Here, $T(\vec{r}, \vec{r}^{\,p})$ is the transmission function that describes the interaction of the electron wave function with the specimen. This transmission function is specimen-specific and depends on the position of the electron probe on the specimen plane, $\vec{r}^{\,p} = (r_x^p, r_y^p)$.

A second lens system projects the exit wave function onto the detector plane. These lenses Fourier transform ψ_{out}, resulting in the following relation:

$$\psi_D(\vec{k}, \vec{r}^{\,p}) = \mathscr{F}\{\psi_{out}(\vec{r}, \vec{r}^{\,p})\}(\vec{k}) = \mathscr{F}\{\psi_{in}(\vec{r}) \cdot T(\vec{r}, \vec{r}^{\,p})\}(\vec{k}) \tag{7.2}$$

The wave function amplitude is recorded at the detector plane by measuring the electron intensity:

$$I_D(\vec{k}, \vec{r}^{\,p}) = |\psi_D(\vec{k}, \vec{r}^{\,p})|^2 = |\mathscr{F}\{\psi_{out}(\vec{r}, \vec{r}^{\,p})\}(\vec{k})|^2 \tag{7.3}$$

$$I_D(\vec{k}, \vec{r}^{\,p}) = |\mathscr{F}\{\psi_{in}(\vec{r}) \cdot T(\vec{r}, \vec{r}^{\,p})\}(\vec{k})|^2 \tag{7.4}$$

The two-dimensional electron intensity pattern at the detector plane is also known as the convergent beam electron diffraction (CBED) pattern.

The CBED pattern in electron microscopy can exhibit various shapes and forms depending on the specific microscope conditions used during data acquisition. The simplest form of a CBED pattern arises when no specimen is present. In this case, the transmission function $T(\vec{r}, \vec{r}^{\,p})$ becomes equal to one, resulting in the following simplified CBED description: $I_D = |F\{\psi_{in}(\vec{r})\}(\vec{k})|^2$. The CBED pattern directly represents $\psi_{in}(\vec{r})$, which, in conventional TEM systems, is only limited by the size of the condenser aperture. The direct image of the condenser aperture is known as the bright-field (BF) disk.

Broadly speaking, CBED patterns can be classified into two categories. When the individual diffraction disks within the pattern can be resolved, it is classified as a Kossel-Möllenstedt pattern (K-M). Otherwise, the CBED pattern is classified as a Kossel pattern [21]. The separation of diffraction disks occurs when the convergent semi-angle (α) is

smaller than the Bragg angle (θ_B) of the specimen. In cases where $\alpha \ll \theta_B$, the term "nanobeam electron diffraction" (NBED) is commonly used instead of CBED. The choice of specific conditions depends on the desired information to be obtained. For example, CBED Kossel patterns have been utilized to measure the electrostatic potential for thin specimens that satisfy the phase object approximation [22]. On the other hand, NBED patterns have been employed for strain measurements in nanomaterials [10, 12, 13].

This chapter focuses on CBED K-M patterns, where the diffraction disks are slightly smaller than the Bragg angle. These conditions enable us to isolate the contributions of the crystal structure to the CBED pattern from all other factors. CBED is a fundamental concept in every STEM technique. We comprehensively overview how the various STEM techniques utilize the CBED pattern to form unique images in 4.2.

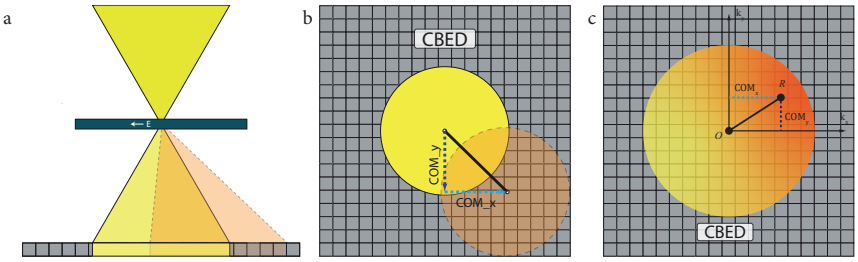

Figure 7.1: **Schematic of 4D-STEM. a)** An illustration of a pixelated detector capturing a CBED pattern with uneven intensity distribution. The CoM indicates the point with the highest weighted intensity. **b)** CoM shift due to a deflected BF disk caused by long-range potential fields (orange). **c)** CoM shift due to intensity redistribution within the BF disk, representing short-range potential fields.

7

CENTER-OF-MASS

Recording the intensity distribution in CBED patterns allows one to measure the momentum shift of the probe electrons induced by the interaction with the specimen. The position of an electron in the detector plane is determined by the expectation value of the reciprocal position vector $\vec{k}$. Using the wavefunction at the sector plane (ψ_D), we can define $\langle\vec{k}\rangle$ as:

$$\langle\vec{k}\rangle(\vec{r}^{\,p}) = \langle\psi_D|\vec{k}|\psi_D\rangle(\vec{r}^{\,p}) = \int_{-\infty}^{\infty}\int_{-\infty}^{\infty} \psi_D(\vec{k},\vec{r}^{\,p})\cdot\vec{k}\cdot\bar{\psi}_D(\vec{k},\vec{r}^{\,p})d^2\vec{k} \tag{7.5}$$

Here we identify $|\psi_D(\vec{k},\vec{r}^{\,p})|$ as the CBED pattern measured directly by the pixelated detector, and $\vec{k}$ is the position vector in momentum space. Because Ψ_D is a normalized wavefunction, we can rewrite eq. (7.5) to:

$$\langle\vec{k}\rangle(\vec{r}^{\,p}) = \frac{\int_{-\infty}^{\infty}\int_{-\infty}^{\infty}\vec{k}|\psi_D(\vec{k},\vec{r}^{\,p})|d^2\vec{k}}{\int_{-\infty}^{\infty}\int_{-\infty}^{\infty}|\psi_D(\vec{k},\vec{r}^{\,p})|d^2\vec{k}} = \text{CoM} \tag{7.6}$$

This is a continuous analog to the discretized definition of the center of mass (CoM) calculation for a two-dimensional signal like the CBED pattern.

$$\mathrm{CoM}(\vec{r}^{\,p}) = \frac{1}{I_{\mathrm{sum}}} \sum_{j=0}^{n} I_j \vec{k}_j \tag{7.7}$$

Here, I and I_{sum} represent the electron intensity of a single pixel and the summed intensity, respectively. Furthermore, the individual components of the vector CoM can be expressed as CoM_x and CoM_y. Equation (7.7) shows how to determine the CoM in a CBED pattern for a single probe position. By performing this calculation for each probe position, one can map the CoM shifts for the entire specimen. Various specimen properties can cause a shift in the CoM. Lazic et al. [17] show that the CoM shift is linearly related to the projected local electric field for thin specimens. However, this only holds when the phase object approximation (POA) can be applied. This approximation states that the specimen is thin enough that only the phase of the electron wavefunction is modified when interacting with the specimen. The POA mostly holds for thin specimens. However, as we will show later, interaction with thicker substrates or a change in defocus conditions can break this approximation, even for thin specimens. Finally, for thicker specimens, the POA does not hold. However, in the final section of this work, we will show that there is still a benefit to measuring the CoM shift using 4D-STEM for thicker specimens.

QUANTITATIVE ANALYSIS OF CBED PATTERNS

Recent advancements in detector technology have provided pixelated detectors with a high dynamic range capable of capturing the entire CBED pattern without over-saturating the detector [4, 6]. Furthermore, these pixelated detectors, like the Electron Microscope Pixel Array Detector (EMPAD), are fast enough to record the two-dimensional CBED pattern for each STEM probe position in the two-dimensional specimen plane ($\vec{r}^{\,p}$). Quantitative analysis techniques applied to the intensity distribution in CBED patterns are essential for extracting valuable structural information from the data obtained through CBED analysis from 4D-STEM EMPAD. The use of four-dimensional scanning transmission electron microscopy (4D-STEM) combined with the electron microscope pixelated detectors (EMPAD) has opened up new possibilities for studying the intensity distribution in CBED patterns. 4D-STEM EMPAD allows for collecting large amounts of diffraction data, enabling the reconstruction of CBED patterns with high spatial resolution and sensitivity to local variations in the sample.

The intensity distribution of the CBED disk of patterns can be measured using various techniques, including center of mass (CoM) calculations, intensity mapping, and other methods based on the energy-filtered CBED pattern intensity profiles [23]. In terms of the CoM measurements of the intensity distribution of CBED disks, the process can be quite intricate due to the complexity of the patterns that often emerge. However, extracting valuable information about crystal structures, strain fields, and crystal symmetry is vital.

For instance, by recording a CBED pattern at each pixel in a STEM image and then determining each diffraction disk's center of mass (CoM), one can create a map of how the CoM shifts across the image. This approach has been used in studies of semiconductor nanostructures, like quantum dots and nanowires, where the strain induced by the mismatch in lattice parameters plays a crucial role in the electronic properties of the device [24, 25].

Furthermore, the diffraction intensity distribution encapsulates data about the Coulomb interaction between the probe and sample, thereby enabling the computation of the local electric field. However, calculating the local electric field from 4D-STEM EMPAD data is not a straightforward task, as it relies heavily on the thickness of the specimen. For the 4D STEM data, the CoM shift is converted to moment transfer, and based on Ehrenfest's theorem, the measured electric field is given by a specific equation,

$$E_{\perp} = -\langle p_{\perp} \rangle_{\perp} \frac{v}{ez}. \tag{7.8}$$

where h is Planck's constant, λ is wavelength, e is the elementary charge, v is the velocity, and z is the thickness [26]. For thin samples, the phase object approximation limit can be applied, and the measure of the CoM shift is associated with the electric field. However, for thicker samples, these CoM variations may be due to additional factors such as sample thickness, dynamic scattering, and the depth of focus of the electron beam [26].

7.3. MoS_2 AND InSe SPECIMENS USED IN THE QUANTITATIVE ANALYSIS

Preparing 2D materials for TEM inspection presents significant challenges. The conventional approach involves fabricating the specimen on a carrier substrate and subsequently transferring it to a delicate TEM grid. The initial fabrication of the specimen typically employs exfoliation techniques or chemical vapor deposition (CVD). Among these techniques, CVD stands out for its ability to provide precise control over the thickness, size, and overall morphology of the 2D material. In this chapter, we investigate two semiconductor layered materials, namely MoS_2 and InSe. The InSe nanostructure is obtained through exfoliation techniques and subsequently deposited on a carbon holey film. For MoS_2, we employ a vapor phase CVD technique to directly synthesize a monolayer of MoS_2 on an amorphous Si_3N_4 TEM grid, eliminating the need for transfer and minimizing the potential damage to the monolayer. However, the 5 nm thick S_3iN_4 substrate introduces a notable background during TEM experiments, which is an order of magnitude greater than the thickness of a MoS_2 monolayer. As we will demonstrate later, this background adversely affects the efficacy of various STEM techniques.

To ensure successful MoS_2 synthesis, we begin by conducting Raman spectroscopy (section A.7.1). The Raman spectrum reveals two distinct peaks associated with MoS_2. The A_{1g} and E^1_{2g} Raman modes demonstrate an intensity ratio close to 1 : 1, indicating the presence of horizontal MoS_2 (h-MoS_2). Furthermore, the difference of approximately 20 cm^{-1} between these modes confirms that the synthesized MoS_2 is nearing the monolayer limit.

7.4. DEFOCUSED-INDUCED COM SHIFTS AT MoS_2 EDGES

CoM shifts in very thin specimens are commonly attributed to in-plane internal electric fields [17]. These fields are particularly significant at edge structures in vdW materials, where broken inversion symmetry and dangling bonds at edge sites play a crucial role. Such edge states have been shown to induce phenomena like metallic edge behavior, which significantly influence local electric fields and the electric properties of the material [27–29]. While pixelated detectors in atomic resolution STEM have enabled precise measurement of these fields [15, 30], small deviations, such as probe defocus, can introduce artifacts that mimic genuine signals in 4D-STEM measurements [18]. Simulation studies by Addiego *et al.* [18] demonstrated that over-focused probes can induce momentum transfer inversions, while under-focused conditions lead to distinctly different CoM behavior. These findings underscore the critical role of probe focus in interpreting CoM shifts accurately. However, the majority of these studies focus on atomic-resolution imaging, leaving a gap in understanding how defocus artifacts manifest in 4D-STEM measurements at lower magnifications or in materials with extended features, such as thin-layer vdW materials.

To address this gap, we investigate the impact of probe defocus on thin-layer materials using 4D-STEM. A monolayer of MoS_2 was analyzed at an acceleration voltage of 300 kV with a semi-convergence angle of 2.63 mrad. Supplementary fig. A.7.3 a shows a low-magnification high-angle annular dark field (HAADF) STEM image of the monolayer, highlighting structural characteristics such as stress-induced cracks. These cracks are likely caused by the interaction of the thin MoS_2 layer with the substrate, as the growth occurs directly on the TEM grid's SiN membrane. The mismatch in thermal expansion coefficients and the inherent strain introduced during growth and cooling can lead to localized stress accumulation, ultimately resulting in crack formation. These cracks form as a natural mechanism to release strain energy. These cracks, abundant with dangling free bonds, represent ideal sites for exploring edge effects. Raman spectroscopy (fig. A.7.2) confirms successful synthesis and monolayer thickness, revealing characteristic vibrational modes consistent with MoS_2.

Imaging was performed using a defocused probe to minimize specimen damage during STEM measurements. While this approach introduces slight blurring in the virtual Annular Dark Field (ADF) image (fig. 7.2a), it effectively reduces the risk of damage to the sample. Despite this blurring, the resulting CBED pattern appears largely unaltered upon initial inspection. To further examine local diffraction characteristics, an individual K-M CBED pattern from the location marked by the red dot in fig. 7.2a is provided in Supplementary fig. A.7.4a. The K-M CBED pattern for the same MoS_2 monolayer, averaged over all probe positions, is displayed in fig. 7.2b, shown on a logarithmic scale to enhance visibility and reduce noise. Using this CBED dataset, the CoM calculation, as described in eq. (7.7) in section 7.2, was applied to each individual CBED pattern. A mask, represented by a red circle in fig. 7.2b, was applied to a higher-order diffraction disk to isolate the diffraction pattern of the MoS_2 monolayer from the interference of the high-intensity background caused by the amorphous substrate. The derived vector field, shown in fig. 7.2c, maps the CoM shifts (CoM_x and CoM_y), represented by the white arrows, superimposed on a color-enhanced version of the virtual ADF image from

fig. 7.2a. An alternative representation is provided in fig. 7.2d, where CoM shifts are encoded using a color map: the hue indicates the shift magnitude, while the color denotes its direction. Both representations of the CoM calculation reveal pronounced edge effects in the MoS_2 specimen, with CoM shifts consistently directed inwards towards the monolayer at every edge. Notably, these edge effects were observed only when using a defocused electron probe. No edge effects were detected when the CoM calculation was performed with a focused probe (see fig. A.7.4b).

The CoM measurements were repeated using a different diffraction disk, indicated by the blue mask in fig. 7.2b), to confirm that these edge effects arise solely from defocus and are not intrinsic to the MoS_2 crystal. The resulting CoM shifts, displayed in fig. A.7.5b, were consistent with those depicted in fig. 7.2d, demonstrating that the effect is independent of the specific diffraction disk chosen. Furthermore, we performed the CoM calculation on a Kossel CBED pattern, characterized by overlapping diffraction disks, from the same MoS_2 specimen and on an empty holey carbon TEM grid. Switching to a Kossel CBED pattern allowed us to assess whether the same defocus-induced edge effects were observable in overlapping diffraction disk patterns, which are more sensitive intensity gradient changes caused by experimental conditions. Figure A.7.6a shows a Kossel position-averaged CBED pattern of the MoS_2 monolayer, where all diffraction information is centered around the BF disk. Due to limited diffraction contrast, only the BF disk is prominently visible. A mask was applied around the BF disk for CoM shift measurements. The resulting CoM shifts (fig. A.7.6b) confirmed that edge-induced CoM shifts remain detectable even with overlapping diffraction disks in such a Kossel pattern. This observation further supports the conclusion that these shifts are artifacts of the probe defocus and are unrelated to the intrinsic crystal properties of MoS_2. Finally, CoM calculations conducted on the holey carbon TEM grid (fig. A.7.7a) provided additional validation for the defocus artifact hypothesis. The experiment was performed under defocused conditions using a thin, standard holey carbon membrane (less than 5 nm in thickness). Regions near the grid holes were analyzed, and consistent CoM shifts toward the specimen edges were observed.

In summary, the consistent observation of CoM shifts toward specimen edges across all the analyses, including various diffraction disks, a Kossel CBED pattern, and a holey carbon TEM grid, confirms that these edge effects are solely artifacts of probe defocus and are entirely unrelated to the specimen's intrinsic crystal structure or properties. The unique behavior of a probe further supports this conclusion. Under defocused conditions, the illuminated area beneath the electron beam is significantly larger than in the focused case. This extended interaction volume forms shadow images within the diffraction disks, particularly in specimens with edges and thickness variations. Shadow images represent real-space projections of the specimen within the diffraction pattern. In these images, the BF disk contains a bright-field projection of the specimen, while high-order diffraction disks encode dark-field representations, as depicted in fig. 7.2a. The formation of such shadow images is a well-established principle in crystallography. It is often used in a technique called Convergent Beam Imaging (CBIM), commonly used to measure structure factors and strain at grain boundaries [31, 32].

Therefore, the observed CoM shift in fig. 7.2c,d can be attributed to the real-space rep-

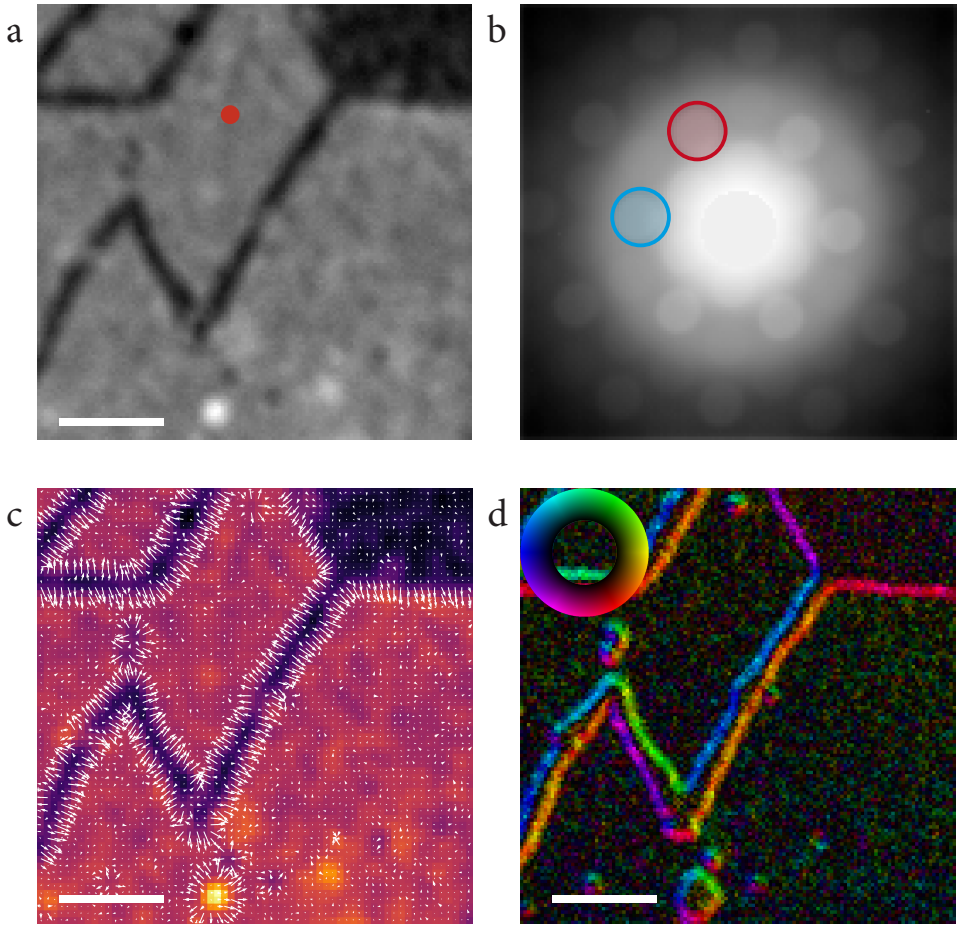

Figure 7.2: **CoM shifts at MoS_2 edges. a)** Virtual ADF image of the MoS_2 monolayer specimen. **b)** The corresponding CBED pattern was obtained as an average of all STEM probe positions to reduce noise. **c)** A vector plot showing the normalized CoM shift due to interaction with the MoS_2 specimen for each STEM probe position. The CoM shifts inward toward the specimen at every edge. **d)** Color map representation of the CoM shifts in **c**, where the color indicates the direction of the shift and the hue represents its magnitude. The scale bars in **a**, **c**, and **d** are 80 nm.

resentation of the local MoS_2 edge within the diffraction pattern, a phenomenon inherently associated with the defocused probe and unrelated to the intrinsic crystal properties. This study establishes a critical framework for accurately interpreting CoM shifts in 4D-STEM analyses of edge-sensitive materials by systematically disentangling these defocus-induced artifacts, highlighting the importance of probe focus alignment for reliable data interpretation.

7.5. EFFECT OF THE AMORPHOUS SUBSTRATE ON THE CBED INTENSITY

Building on the insights from CoM analyses, we now address another challenge in 4D-STEM characterization: understanding the impact of substrate interactions and monolayer thickness on imaging in MoS_2. Substrate effects often overshadow subtle asymmetries in the first-order Bragg disk intensities for ultra-thin specimens, significantly limiting imaging capabilities. Using monolayer MoS_2 as a benchmark, we highlight how substrate-induced artifacts and low Z contrast constrain 4D-STEM imaging.

The MoS_2 monolayer analyzed in this study was synthesized directly onto an amorphous Si_3N_4 film substrate (see Methods for details). This substrate introduces a substantial background signal in the electron intensity distribution, which is comparable in magnitude to the first-order diffraction disks of the MoS_2 monolayer. To illustrate this effect, fig. 7.3a shows the average K-M CBED pattern of the MoS_2 specimen, with a color scale highlighting the intensity distribution. Concentric ring-shaped features, likely resulting from scattering by the amorphous substrate, are visible around the bright-field (BF) disk. The innermost and brightest ring partially overlaps with the first-order diffraction disks, while the outer rings become progressively fainter with increasing distance.

A 3D representation of this CBED pattern (fig. 7.3b) reveals Gaussian-like intensity profiles for both the central beam and the amorphous background. This overlap significantly reduces contrast, complicating the identification of subtle structural features in the diffraction pattern. To address this issue, the CBED pattern and its background can be modeled as a superposition of Gaussian profiles, as detailed in the Supporting Information in section A.7.3. For example, the CBED pattern shown in fig. 7.3a,b can be represented by one Gaussian describing the central beam and another accounting for the background. However, the aperture's Point Spread Function (PSF), described by the Airy function, contains additional smaller local maxima that contribute approximately $\sim 16\%$ of the total STEM probe intensity. These maxima complicate the background subtraction process, introducing ripples in the signal that lead to systematic uncertainties in CoM calculations, as illustrated in fig. 7.3c,d. Further details on the Airy function and its role in background modeling are provided in Supporting Information section A.7.3.

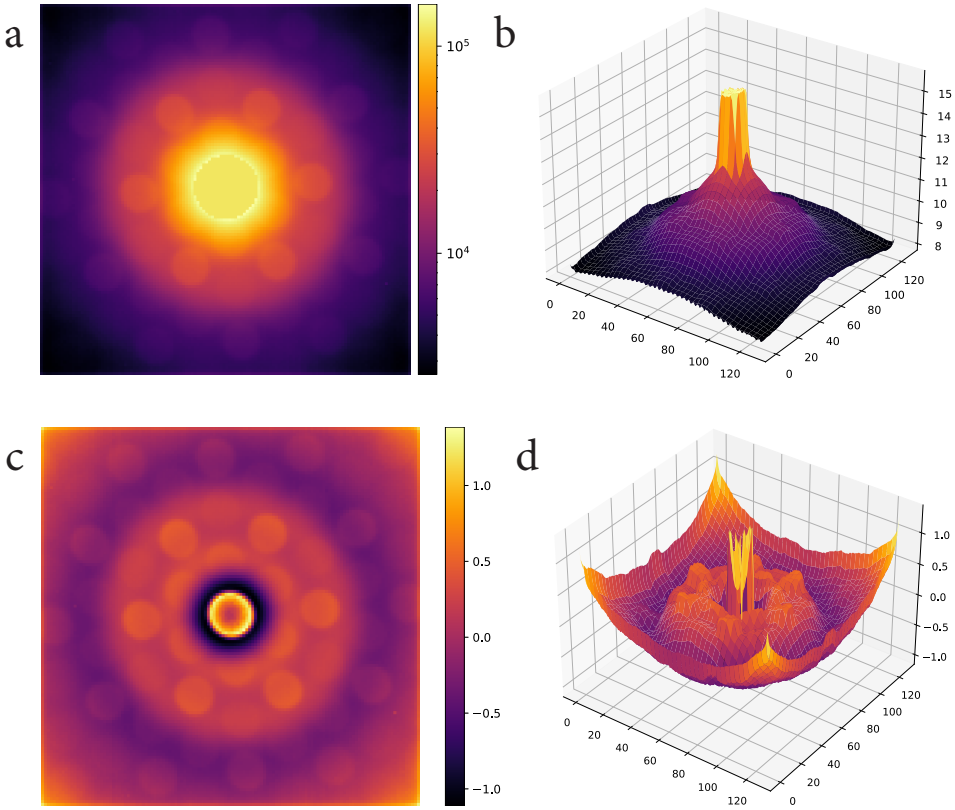

Figure 7.3: **Substrate Background Analysis in CBED Patterns. a)** Averaged CBED pattern, as shown in fig. 7.2b, visualized with a colormap. The pattern reveals three distinct intensity plateaus. **b)** Three-dimensional representation of the CBED pattern in **a**, showing a Gaussian-like background shape. **c)** Background-subtracted CBED pattern from **a**, achieved by fitting a double Gaussian. **d)** Three-dimensional representation of the background-subtracted CBED pattern in **c**, highlighting inaccuracies in the subtraction. Negative intensities are observed in a narrow ring around the central beam and in another ring farther from the center.

7.6. Grain Boundary Identification in Bulk InSe using the Center of Mass

Building on the previous analysis of MoS_2, we extend our investigation to examine CoM shifts into bulk materials. Specifically, we analyze CoM shifts in a bulk InSe crystal to investigate grain boundary features and orientation-related shifts. Grain boundaries, another critical structural feature, introduce significant variations in vdW material properties, enhancing chemical sensor sensitivity in graphene [33], altering bandgap energies, thermal transport, and conductivity in TMDs [34], and enabling phenomena like one-dimensional metallic states in monolayer $MoSe_2$ [35]. Advanced characterization techniques are crucial to distinguish intrinsic behaviors from artifacts. As discussed earlier, a shift in the CoM of a CBED pattern reflects momentum transfer between the specimen and the beam electrons. This shift can arise from physical factors, such as long- and short-range potential fields and dynamical scattering, or from instrumental sources, including probe defocus and substrate-induced backgrounds.

To analyze CoM shifts in bulk materials, we employ a larger STEM probe, which automatically averages the momentum transfer when its size exceeds the dimensions of the unit cell. By reducing the convergence angle ($\alpha = 2.5$ mrad), the Bragg disks are further separated, forming a nanobeam electron diffraction (NBED) pattern. In this configuration, the BF disk and diffracted Bragg disks are well-separated, enabling independent analysis of BF disk shifts and intensity distributions to isolate long- and short-range potentials in CoM calculations.

The well-isolated BF disk in an NBED pattern simplifies the determination of its precise position. For instance, a contour-finding algorithm, such as the marching squares method, can identify the BF disk's contour, which is then fitted to a circle to determine its center[36]. This method is effective because the BF disk is typically the brightest feature in an NBED pattern. Additional steps, such as applying a binary threshold and watershed segmentation, can further improve the separation of the BF disk from neighboring Bragg disks [37]. Alternatively, cross-correlation between a reference image and the measured NBED pattern provides another robust method for locating the BF disk. This approach is the underlying principle of various template-matching techniques commonly used in 4D-STEM strain mapping [38–41].

In this study, we adopt a similar strategy based on determining the phase correlation between the measured and averaged NBED patterns. The resulting phase correlation map is then fitted with a two-component Gaussian to locate the BF disk's center precisely. Figure 7.4a displays the ADF image of the InSe bulk crystal specimen, see the Methods for more details. This image was generated by integrating the intensity of each NBED pattern in the 4D dataset using a virtual annular mask, effectively capturing the structural contrast across the scanned region. The position-averaged NBED (PANBED) pattern obtained from this specimen is shown in fig. 7.4b. The PANBED combines all individual NBED patterns into a single averaged representation, highlighting the overall diffraction features and mitigating noise from individual variations. A camera length (CL) of 1150 mm and a convergence angle of $\alpha = 2.63$ mrad were used for these measurements. Under these conditions, the Bragg disks are well-separated, and the BF disk is cleanly

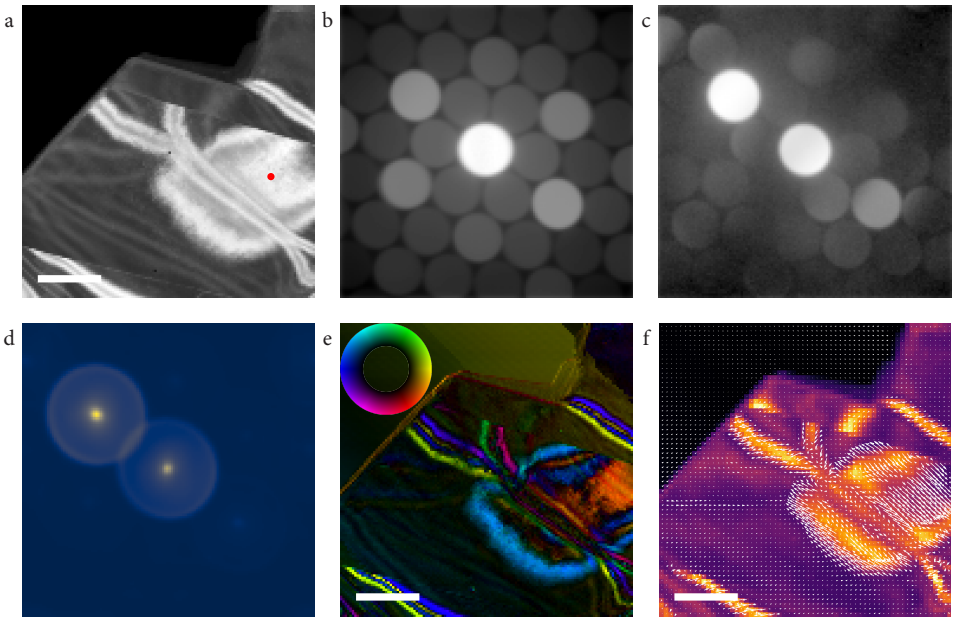

Figure 7.4: **NBED Analysis of the InSe Specimen**. **a)** ADF image of the InSe bulk crystal specimen. **b)** The corresponding position-averaged NBED from **a**. **c)** A single NBED pattern taken from the area indicated by the red dot in **a**. **d)** The phase correlation between the position-averaged NBED in **b** and the single NBED in **c**. **e)** The shift of the BF disk with respect to the center is depicted with a color plot, where the color denotes the direction of the shift and the hue of its magnitude. **f)** Same as **e** now using vector fields. Scale bars in **a**, **e**, and **f** are 100 nm.

isolated, enabling precise measurement of the BF disk shift relative to its position in the PANBED.

To illustrate how we measure the local features contributing to the phase correlation, we analyze an individual NBED pattern from the region marked by the red dot in fig. 7.4a, which is displayed in fig. 7.4c. Before calculating the phase correlation, a Sobel filter is applied to the NBED patterns to enhance edge contrast and mitigate any dynamical scattering effects. The resulting phase correlation map, presented in fig. 7.4d, compares the PANBED (fig. 7.4b) and the individual NBED pattern (fig. 7.4c). The map reveals two prominent locations of high correlation: the central location corresponds to the actual BF disk. In contrast, the secondary location aligns with a diffraction Bragg disk of comparable brightness. This secondary correlation is caused by an excitation error arising from slight misalignments between the crystal and the electron beam. These misalignments result in unintended diffraction intensity at specific higher-order diffraction disk locations. Further details on excitation errors and their relationship with tilted crystal alignments are provided in Supplementary fig. A.7.8.

While this example demonstrates the diffraction effects at a single position, the same analysis must be extended to all pixels across the scanned region to generate a com-

prehensive map of the BF disk shifts. To ensure accuracy, the BF shift was corrected for any displacement caused by the STEM probe's scanning motion (see Section section A.7.5, for further details). The BF disk shift relative to the center is depicted in fig. 7.4e (color representation) and fig. 7.4f (vector representation), following the same format as fig. 7.2c,d. The most pronounced BF shifts occur along three horizontal bands located at the bottom, middle, and top of the InSe specimen and within a large patch at the center. These regions exhibit a clear alternating pattern in which adjacent regions exhibit shifts of equal magnitude but opposing directions. Furthermore, the regions exhibiting the largest BF shifts align with the brightest areas in the ADF image (fig. 7.4a), highlighting a correlation between local structural features and electron scattering intensity.

The increase in intensity of higher-order Bragg disks when the specimen is misaligned highlights the benefit of using information on excitation errors to characterize regions' relative orientations and alignment deviations within the InSe specimen. To identify misalignments, we first analyze the brightest higher-order Bragg disks in an NBED pattern using the same phase correlation analysis as in fig. 7.4. However, now we don't determine the center of the BF disk but calculate the phase correlation's CoM. Using the CoM calculation from eq. (7.7), we capture the location of the higher-order Bragg disks that have a higher intensity due to excitation errors.

Next, the resulting CoM vector field of these excitation errors represents the direction and magnitude of the misalignment. The $\mathrm{CoM_x}$ and The $\mathrm{CoM_y}$ values are arranged in a 2D point cloud in fig. 7.5a, where each point corresponds to a specific scan position within the dataset. Using the K-means clustering algorithm, the 2D point cloud is divided into seven clusters, as shown in fig. 7.5b. Six clusters correspond to higher-order Bragg diffraction disks, while one cluster represents the BF disk at the center. This clustering enables the identification of regions with distinct misalignment characteristics.

To mitigate the effects of dynamical scattering, the NBED patterns within each cluster are averaged to produce PANBEDs, displayed in figs. 7.5c to 7.5h. These PANBEDs clearly illustrate the effect of slight misalignments between the crystal regions and the electron beam. Excitation errors are evident as significant increases in the brightness of certain Bragg disks while their opposing disks remain unaffected, leading to an asymmetric brightness distribution. Using eq. (7.9), the severity of the excitation error for each scan position is quantified.

$$P = \left[I(hkl) - I\left(\overline{hkl}\right) \right] \Big/ \left[I(hkl) + I\left(\overline{hkl}\right) \right], \tag{7.9}$$

The excitation errors for the $\left[\bar{2}110\right], \left[\bar{1}2\bar{1}0\right], \left[11\bar{2}0\right]$ directions are shown in figs. 7.5i to 7.5k. Notably, the areas with the largest excitation errors correspond to those exhibiting the most significant BF shifts in fig. 7.4e. Interestingly, one finds that the areas with the largest excitation errors correspond to those with the largest BF shifts in fig. 7.4e. This correlation underscores the need for caution when interpreting BF shifts and CoM values from NBED patterns. While these shifts might be attributed to physical effects such as potential fields, they can also arise from small misalignments within the crystal structure.

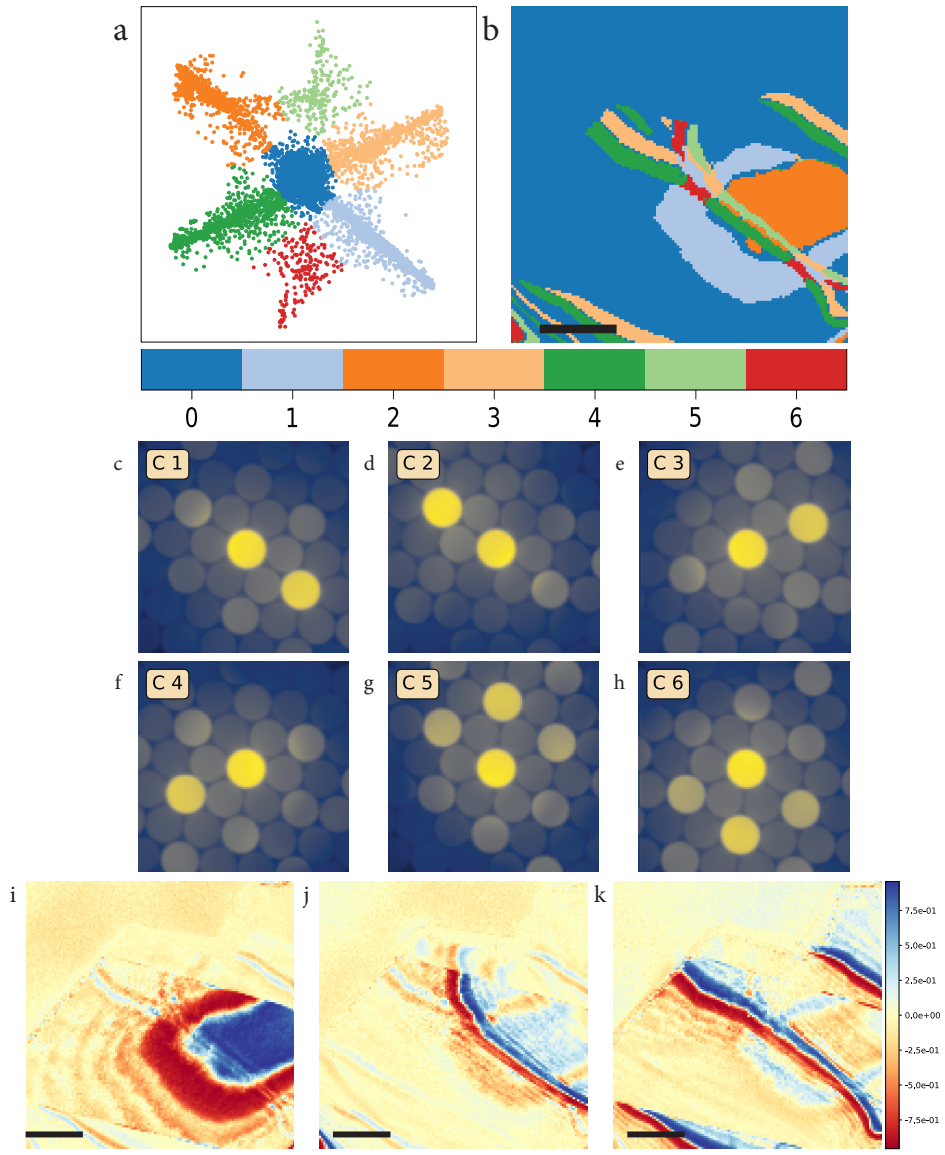

Figure 7.5: **Grain Boundary Determination in the InSe Specimen a)** Point cloud representing the CoM of the phase correlation for each scan position. The points are grouped into seven clusters using the K-means algorithm. **b)** Mapping of the seven clusters back onto the InSe specimen, revealing the locations of the different crystal grains. Refer to fig. 7.4a for the associated ADF image. **c-h)** PANBEDs for each of the six outside clusters, illustrating the averaged NBED patterns for the different grain orientations. **i-k)** Maps of the excitation errors for the $[\bar{2}110]$, $[\bar{1}2\bar{1}0]$, $[11\bar{2}0]$ planes and their opposites. The maps show that the regions with the largest excitation errors correspond to those with the most significant BF shifts in fig. 7.4e. The scale bars in **b**, **i**, **j**, and **k** are 100 nm.

A.7. APPENDIX

A.7.1. MoS_2 MORPHOLOGY AND RAMAN SPECTROSCOPY

Figure A.7.3a displays a low-magnification High-Angle Annular Dark Field (HAADF) STEM image of the MoS_2 monolayer specimen considered in section 7.4. One can observe the presence of stress-induced cracks across the specimen. These cracks are attributed to stress with the Si_3N_4 membrane substrate during the synthesis process. Raman spectroscopy was performed on the MoS_2 specimen to confirm its successful synthesis. The measurements were conducted using a Renishaw InVia Reflex™ confocal Raman microscope, employing a 514 nm excitation laser and a 1800 l/mm grating, which provided a spectral resolution of approximately 1 cm^{-1}.

The Raman spectrum (see fig. A.7.2) exhibits two distinct peaks corresponding to the E^1_{2g} and A_{1g} Raman modes of MoS_2, located at 383 cm^{-1} and 403 cm^{-1}, respectively. These modes are well-documented in the literature for MoS_2, with the E^1_{2g} mode representing in-plane vibrations and the A_{1g} mode corresponding to out-of-plane vibrations [42]. The intensity ratio of these modes is approximately 1:1, indicating the presence of horizontal MoS_2 (h-MoS_2). Furthermore, the observed 20 cm^{-1} separation between the two modes confirms that the synthesized MoS_2 is near the monolayer limit.

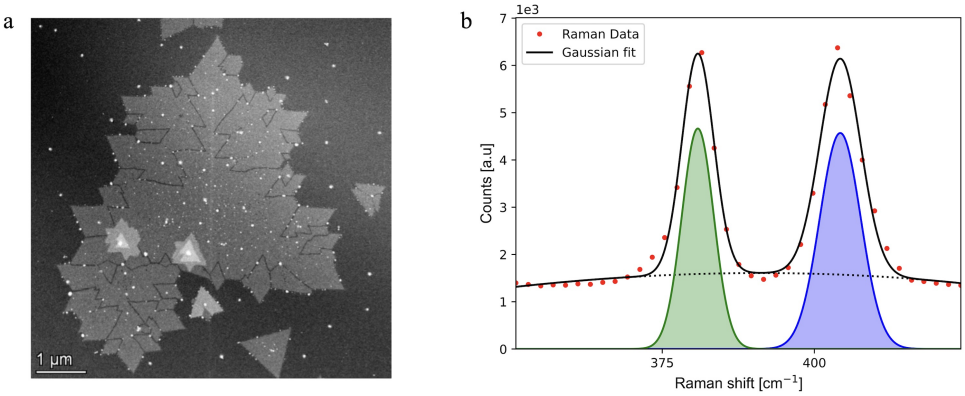

Figure A.7.3: **Raman Spectroscopy of monolayer MoS_2.** **a)** Low-magnification HAADF-STEM image of the MoS_2 monolayer, showing irregularly shaped domains with sharp edges and visible cracks. These cracks are attributed to stress with the Si_3N_4 membrane substrate during the synthesis process. **b)** Raman spectrum of the MoS_2 monolayer, highlighting the E^1_{2g} vibrational mode (green shaded region) at 383 cm^{-1} and the A_{1g} vibrational mode (blue shaded region) at 403 cm^{-1}. The Gaussian fit (solid black line) of the experimental data (red dots) confirms the 20 cm^{-1} separation between the two peaks, consistent with monolayer MoS_2.

A.7.2. CoM SHIFT OF FOCUSED AND DEFOCUSED STEM PROBES

As discussed in chapter 7, a defocused STEM probe may lead to a shift in the CoM in the vicinity of edge structures in the specimen. On the other hand, the same shift is not observed when the STEM probe is correctly focused. To further investigate this point, first, we show in fig. A.7.4a a single CBED pattern from the same MoS_2 monolayer specimen considered in the section 7.4. This CBED pattern is taken from the location indicated by the red dot in fig. 7.2a in section 7.4. The diffraction disks are harder to distinguish compared to the PACBED in fig. 7.2b in section 7.4 due to the low diffraction contrast and the noise in the image. The CoM of each CBED pattern in the 4D dataset is calculated to form the color plot in fig. A.7.4b. When the STEM probe is defocused, the color plot shows a shift of the CoM towards the edge, as seen in fig. 7.2d. However, when the STEM probe is correctly focused, the CoM shift at the edges disappears completely, as seen in fig. A.7.4b. Furthermore, the direction of the CoM shift at the edges is not dependent on the choice of location from the CoM mask.

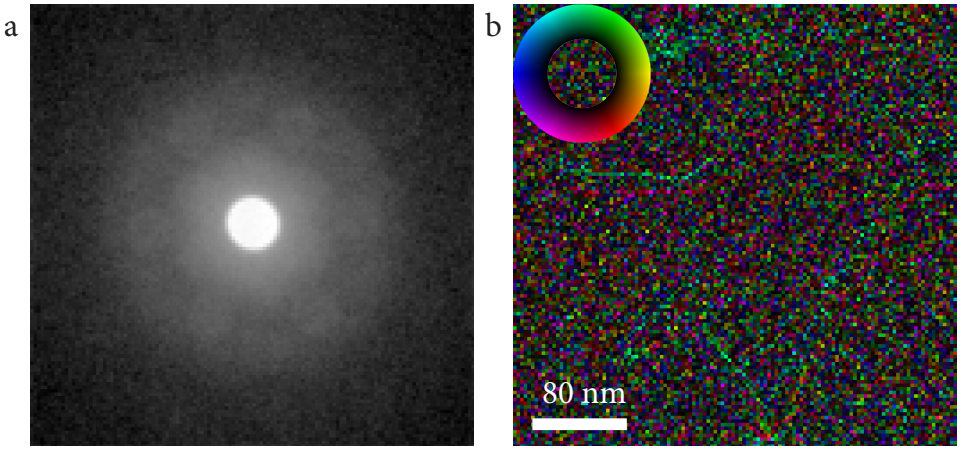

Figure A.7.4: **a)** A single CBED pattern taken from the location indicated with the red dot in fig. 7.2a in section 7.4. **b)** A color plot of the CoM shift in the MoS_2 monolayer with a focused probe. Under these conditions, there is no perceivable CoM shift.

The CoM shift in the color plot in fig. A.7.5b is identical to the color plot in fig. 7.2d, even though a different location (Bragg disk) was selected for the CoM mask. The CoM shift at the edges introduced by a defocused probe is still present when the diffraction conditions are adjusted to form Kossel CBED patterns, like the PACBED pattern displayed in fig. A.7.6a. All the diffraction information in this Kossel pattern is centered around the BF disk. Due to low diffraction contrast, only the BF disk is visible here. However, when using an annular CoM mask right around the BF disk, one can still see the CoM shift at the edges of the MoS_2 monolayer, as seen in fig. A.7.6b.

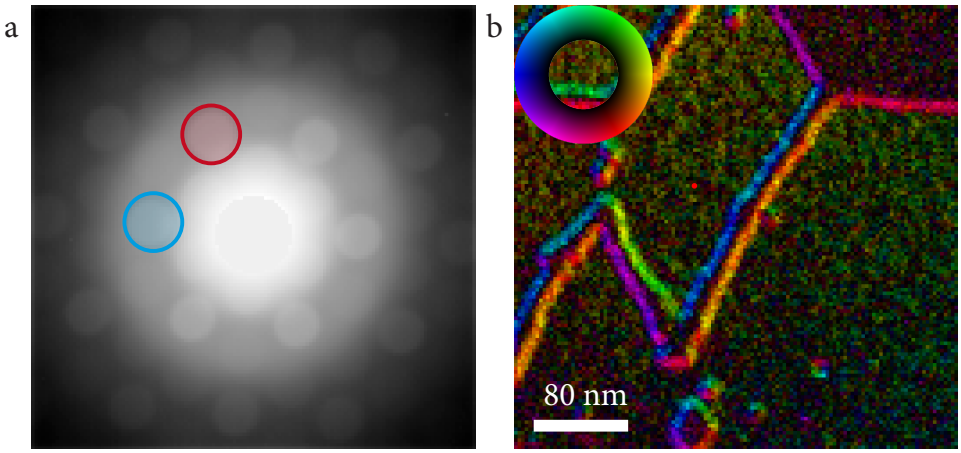

Figure A.7.5: **a)** The averaged CBED pattern from fig. 7.2 from section 7.4. **b)** A color plot of the CoM shift with a defocused STEM probe and a circular CoM mask indicated by the blue circle in **a**

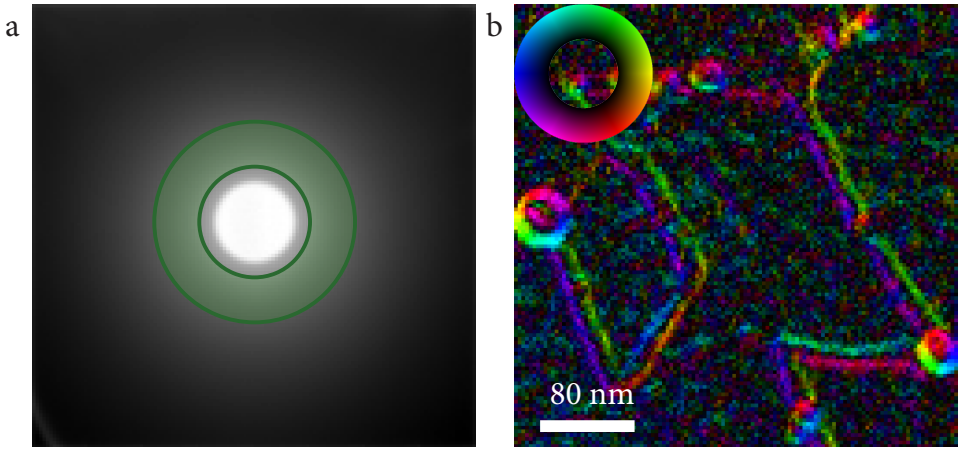

Figure A.7.6: **a)** A Kossel position-averaged CBED pattern of the MoS_2 monolayer. Here, all diffraction information is centered around the BF disk. Due to limited diffraction contrast, only the BF disk is visible. **b)** A color plot showing the CoM shift, constructed from the Kossel CBED patterns.

Finally, we show a color plot of the CoM shift at the edge of an amorphous carbon substrate in fig. A.7.7a. The uniform CoM shift on the edge of the circular hole in the amorphous substrate is a clear indication that a defocused STEM probe always induces a CoM shift towards the normal of the edge, regardless of the crystal orientation, and hence is an effect which is important to take into account when interpreting the 4D-STEM measurements.

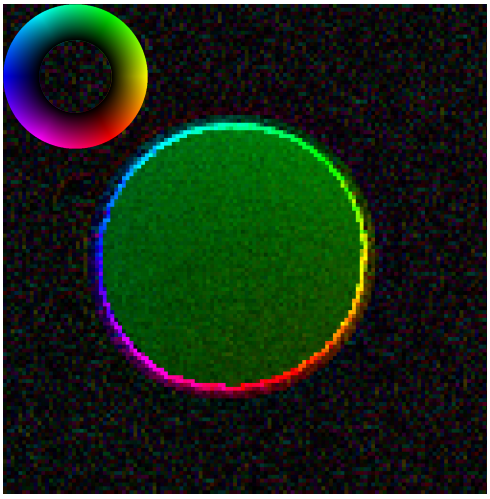

Figure A.7.7: A color plot of the CoM shift at the edge of an amorphous carbon substrate taken with a defocused probe.

A.7.3. Point Spread Function and Airy Disc Modelling

The imaging process in STEM is governed by the cross-correlation between the imaged object and the Point Spread Function (PSF) of the imaging system [20].

Under ideal conditions, the PSF is determined by the convolution of the aperture's PSF and the PSF associated with lens aberrations, commonly referred to as the disc of confusion [43]. The aperture's PSF is mathematically represented by an Airy disc:

$$P_a = (2J_1(\rho)/\rho)^2,, \tag{7.10}$$

where $\rho = (2\pi/\lambda)\alpha r$, and $J_1(\rho)$ is a Bessel function of the first order. The Airy disc's central peak resembles a Gaussian function, which is often used to approximate the CBED pattern's intensity distribution. However, the Airy disc also exhibits smaller local maxima, collectively contributing approximately ~ 16% of the total STEM probe intensity. These features complicate background modeling and subtraction, as detailed in the main text.

A.7.4. Excitation errors in STEM

STEM diffraction patterns provide a representation of the reciprocal crystal lattice. The atoms in the crystal lattice elastically scattered incoming electron waves. When the Bragg conditions are met, the diffracted waves constructively interfere, forming a regular pattern in the reciprocal space. The points in this pattern represent wavevectors that each have the same magnitude. Therefore, the diffraction pattern is a 2D representation of the intersection between the reciprocal lattice points and the Ewald sphere. The diffraction points only appear when the Bragg conditions are met in the diffraction pattern. In practice, many diffraction points are present in a TEM diffraction pattern, even when the Bragg conditions are not exactly matched. The reciprocal lattice points in thin films are not exactly 0D points but elongated ellipses known as relrods. The thinner the crystalline material, the more elongated these relrods are. The elongated oval shape of a relrod means that more reciprocal lattice points intersect with the Ewald sphere, creating more diffraction points in a TEM diffraction pattern. The distance between the center of the relrod and the Ewald sphere is known as the excitation error.

This principle holds for a parallel beam in conventional TEM and convergent beam electron diffraction (CBED). However, in the case of a convergent electron beam, the concept of the Ewald sphere needs to be extended to account for the many different incident angles in a convergent electron probe. The probe effectively creates many Ewald spheres, each with the same radius but slightly rotated, with the bottom of the sphere as a pivot point. The outermost Ewald spheres rotate $\pm\alpha$, where α is the convergent semi-angle. The Ewald spheres of a convergent beam are depicted in fig. A.7.8a, where the solid line represents the central beam and the dotted lines represent the two maxima. Therefore, the resulting Bragg spot in a CBED pattern is not a 0D point but a disk with a radius equal to the convergent semi-angle. The integrated intersection of the Ewald spheres and the relrods determines the intensity distribution within a Bragg disk, as directed in fig. A.7.8b.

When the electron beam and the crystal plane are perfectly aligned (perpendicular), the intensity distribution in the CBED pattern is symmetrical. This symmetry is illustrated by the green and red records in fig. A.7.8a. Here, the green railroads meet the Bragg condition, and the red records do not. The green relrods will appear as individual Bragg disks in the CBED pattern. The intensity of the Bragg disk will vary according to the severity of the excitation error. However, according to Fresnel's Law, the intensity of symmetrically opposed Bragg disks will be identical. This symmetry only holds for a STEM probe aligned with the crystal. The Ewald sphere is effectively rotated along the center relrod when the STEM probe interacts with the crystal lattice. A slight misalignment will lead to a different intersection between the Ewald sphere and the relrods. The interaction between a tilted beam and a reciprocal lattice is depicted in fig. A.7.8c. Due to the tilt, the green relrods are no longer symmetrically distributed around the central point. Therefore, the misalignment will result in a non-symmetric intensity distribution in the CBED pattern. In this situation, the symmetrically opposed Bragg disks in the CBED pattern do not have the same intensity. This non-symmetric intensity distribution is used in fig. 7.5 in section 7.6 to find misaligned crystal domains in the InSe specimen.

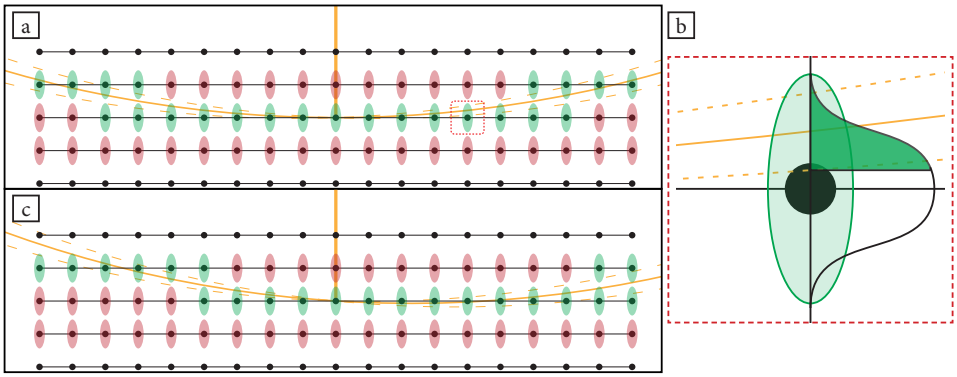

Figure A.7.8: **Excitation errors in STEM. a)** Schematic illustrating the intersection of the Ewald sphere with the relrods. Relrods intersecting the Ewald sphere are shown in green, corresponding to diffraction disks with intensity in the CBED pattern. **b)** The intensity of a diffraction disk in the CBED pattern is determined by the integrated intersection of the tilted Ewald sphere with the relrod, as indicated by the shaded green area. **c)** When the STEM probe and the crystal plane are misaligned, the intersection between the Ewald sphere and the relrods changes, resulting in excitation errors. This misalignment shifts the intensity in the CBED pattern, as shown by the displacement of the green relrods compared to **a**.

A.7.5. Correcting probe movement in 4D-STEM (De-Scan)

When a STEM probe is scanned over a wide area, it can drift off the optical axis, which can have an enormous impact on the calculated CoM. The deflection from the optical axis is most significant for lower-resolution images, like the ones discussed in the main text, because the STEM probe has to be deflected over large real-space distances. Correcting this behavior is, therefore, critical to making accurate CoM measurements. Correcting this behavior using a hardware implementation is known as de-scan. However, the versatility of a 4D-STEM detector allows one to correct the STEM probe's scan motion after data acquisition. Figure A.7.9a shows a CoM color map of a MoS_2 layer, similar to fig. 7.2a. Over the entire image, there is a shift towards the bottom right corner. Figure A.7.9c shows a 3D-plot, with the CoM_y intensity in the Z-direction. One can clearly see a linear slope in this 3D-plot. This slope represents the BF-disk's uniform motion due to the STEM probe's scanning motion. By fitting a 2D plane to this slope, we can isolate the probe movement from the CoM_y value, as indicated by fig. A.7.9c. We effectively perform a De-Scan by subtracting the x and y slope from the CoM measurement using post-processing. The results are shown in fig. A.7.9d and fig. A.7.9e. Both the color and the 3D plot eliminate the scan motion; only the CoM shifts induced by the specimen remain.

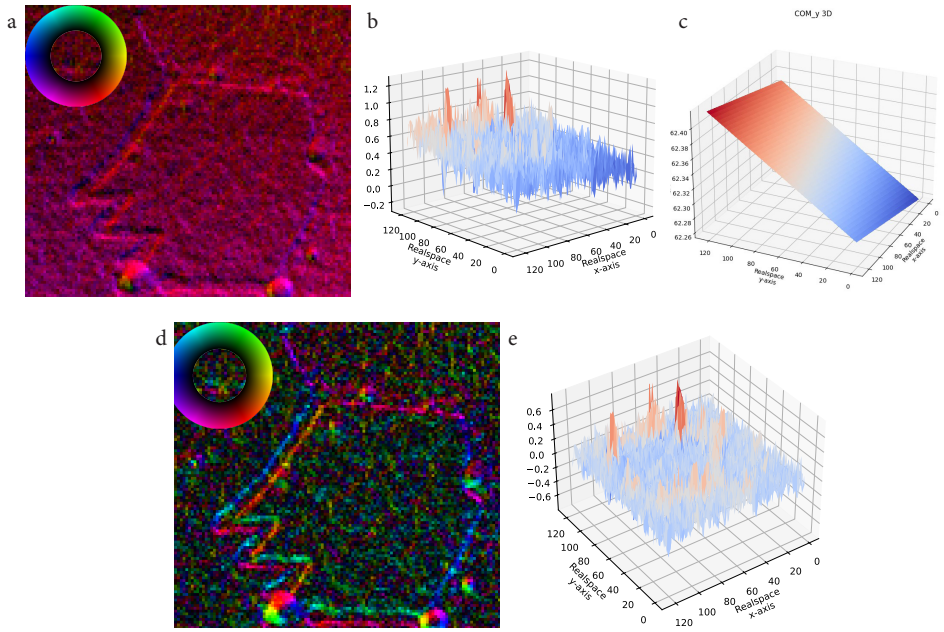

Figure A.7.9: **De-Scan in 4D-STEM. a)** A CoM color plot of a MoS_2 sample. **b)** 3D-plot of the CoM_y showing a slope due to the probe movement. **c)** The 2D plane fitted on the slope from **b.** **d)** A CoM color plot with the post-processing de-scan applied. **e)** The 3D-plot of the CoM_y with the post-processing de-scan applied

REFERENCES

[1] S. T. Ciocys, Q. Marsal, P. Corbae, D. Varjas, E. Kennedy, M. Scott, F. Hellman, A. G. Grushin, and A. Lanzara, *Establishing coherent momentum-space electronic states in locally ordered materials,* Nature Communications **15**, 8141 (2024).

[2] F. Xiang, L. Huberich, P. A. Vargas, R. Torsi, J. Allerbeck, A. M. Z. Tan, C. Dong, P. Ruffieux, R. Fasel, O. Gröning, Y.-C. Lin, R. G. Hennig, J. A. Robinson, and B. Schuler, *Charge state-dependent symmetry breaking of atomic defects in transition metal dichalcogenides,* Nature Communications **15**, 2738 (2024).

[3] G. Moore, *Cramming More Components onto Integrated Circuits (1965),* in *Ideas That Created the Future: Classic Papers of Computer Science* (The MIT Press, 2021).

[4] M. W. Tate, P. Purohit, D. Chamberlain, K. X. Nguyen, R. Hovden, C. S. Chang, P. Deb, E. Turgut, J. T. Heron, D. G. Schlom, D. C. Ralph, G. D. Fuchs, K. S. Shanks, H. T. Philipp, D. A. Muller, and S. M. Gruner, *High Dynamic Range Pixel Array Detector for Scanning Transmission Electron Microscopy,* Microscopy and Microanalysis **22**, 237 (2016).

[5] C. Ophus, *Four-dimensional scanning transmission electron microscopy (4d-stem): From scanning nanodiffraction to ptychography and beyond,* Microscopy and Microanalysis **25**, 563–582 (2019).

[6] M. Nord, R. W. Webster, K. A. Paton, S. McVitie, D. McGrouther, I. Maclaren, and G. W. Paterson, *Fast Pixelated Detectors in Scanning Transmission Electron Microscopy. Part I: Data Acquisition, Live Processing, and Storage,* Microscopy and Microanalysis **26**, 653 (2020).

[7] A. Lubk and J. Zweck, *Differential phase contrast: An integral perspective,* Phys. Rev. A **91**, 023805 (2015).

[8] T. J. Pennycook, A. R. Lupini, H. Yang, M. F. Murfitt, L. Jones, and P. D. Nellist, *Efficient phase contrast imaging in stem using a pixelated detector. part 1: Experimental demonstration at atomic resolution,* Ultramicroscopy **151**, 160 (2015), special Issue: 80th Birthday of Harald Rose; PICO 2015 – Third Conference on Frontiers of Aberration Corrected Electron Microscopy.

[9] K. X. Nguyen, J. Huang, M. H. Karigerasi, K. Kang, D. G. Cahill, J.-M. Zuo, A. Schleife, D. P. Shoemaker, and P. Y. Huang, *Angstrom-scale imaging of magnetization in antiferromagnetic fe2as via 4d-stem,* Ultramicroscopy **247**, 113696 (2023).

[10] M. Bolhuis, S. E. van Heijst, J. J. M. Sangers, and S. Conesa-Boj, *4d-stem nanoscale strain analysis in van der waals materials: Advancing beyond planar configurations,* Small Science **4**, 2300249 (2024).

[11] S. E. van Heijst, M. Bolhuis, A. Brokkelkamp, J. J. M. Sangers, and S. Conesa-Boj, *Heterostrain-driven bandgap increase in twisted ws2: A nanoscale study,* Advanced Functional Materials **34**, 2307893 (2024).

[12] T. Grieb, F. F. Krause, K. Müller-Caspary, R. Ritz, M. Simson, J. Schörmann, C. Mahr, J. Müßener, M. Schowalter, H. Soltau, M. Eickhoff, and A. Rosenauer, *4d-stem at interfaces to gan: Centre-of-mass approach & nbed-disc detection,* Ultramicroscopy **228**, 113321 (2021).

[13] Y. Han, K. Nguyen, M. Cao, P. Cueva, S. Xie, M. W. Tate, P. Purohit, S. M. Gruner, J. Park, and D. A. Muller, *Strain mapping of two-dimensional heterostructures with subpicometer precision, Nano Letters,* Nano Letters **18**, 3746 (2018).

[14] Y. Wen, S. Fang, M. Coupin, Y. Lu, C. Ophus, E. Kaxiras, and J. H. Warner, *Mapping 1d confined electromagnetic edge states in 2d monolayer semiconducting mos2 using 4d-stem, ACS Nano,* ACS Nano **16**, 6657 (2022).

[15] K. Müller-Caspary, F. F. Krause, T. Grieb, S. Löffler, M. Schowalter, A. Béché, V. Galioit, D. Marquardt, J. Zweck, P. Schattschneider, J. Verbeeck, and A. Rosenauer, *Measurement of atomic electric fields and charge densities from average momentum transfers using scanning transmission electron microscopy,* Ultramicroscopy **178**, 62 (2017), fEMMS 2015.

[16] P. Deb, M. C. Cao, Y. Han, M. E. Holtz, S. Xie, J. Park, R. Hovden, and D. A. Muller, *Imaging polarity in two dimensional materials by breaking friedel's law,* Ultramicroscopy **215**, 113019 (2020).

[17] I. Lazić, E. G. Bosch, and S. Lazar, *Phase contrast STEM for thin samples: Integrated differential phase contrast,* Ultramicroscopy **160**, 265 (2016).

[18] C. Addiego, W. Gao, and X. Pan, *Thickness and defocus dependence of inter-atomic electric fields measured by scanning diffraction,* Ultramicroscopy **208**, 112850 (2020).

[19] M. C. Cao, Y. Han, Z. Chen, Y. Jiang, K. X. Nguyen, E. Turgut, G. D. Fuchs, and D. A. Muller, *Theory and practice of electron diffraction from single atoms and extended objects using an EMPAD,* Microscopy **67**, i150 (2017).

[20] R. Egerton and M. Watanabe, *Spatial resolution in transmission electron microscopy,* Micron **160**, 103304 (2022).

[21] D. B. Williams and C. B. Carter, *Transmission Electron Microscopy: A Textbook for Materials Science*, 2nd ed. (Springer, 2009) pp. 1–760.

[22] J. A. Hachtel, J. C. Idrobo, and M. Chi, *Sub-ångstrom electric field measurements on a universal detector in a scanning transmission electron microscope,* Advanced Structural and Chemical Imaging **4**, 10 (2018).

[23] D. Delille, R. Pantel, and E. Van Cappellen, *Crystal thickness and extinction distance determination using energy filtered cbed pattern intensity measurement and dynamical diffraction theory fitting,* Ultramicroscopy **87**, 5 (2001).

[24] Y. He, Y. Yang, Z. Zhang, Y. Gong, W. Zhou, Z. Hu, G. Ye, X. Zhang, E. Bianco, S. Lei, Z. Jin, X. Zou, Y. Yang, Y. Zhang, E. Xie, J. Lou, B. Yakobson, R. Vajtai, B. Li, and P. Ajayan, *Strain-induced electronic structure changes in stacked van der waals heterostructures,* Nano Letters **16**, 3314 (2016).

[25] M. Huang, H. Yan, C. Chen, D. Song, T. F. Heinz, and J. Hone, *Phonon softening and crystallographic orientation of strained graphene studied by raman spectroscopy,* Proceedings of the National Academy of Sciences **106**, 7304–7308 (2009).

[26] S. Fang, Y. Wen, C. S. Allen, C. Ophus, G. G. D. Han, A. I. Kirkland, E. Kaxiras, and J. H. Warner, *Atomic electrostatic maps of 1d channels in 2d semiconductors using 4d scanning transmission electron microscopy,* Nature Communications **10**, 1127 (2019).

[27] M. Tinoco, L. Maduro, and S. Conesa-Boj, *Metallic edge states in zig-zag vertically-oriented mos2 nanowalls,* Scientific Reports **9**, 15602 (2019).

[28] J. Zhang, H. Yu, W. Chen, X. Tian, D. Liu, M. Cheng, G. Xie, W. Yang, R. Yang, X. Bai, D. Shi, and G. Zhang, *Scalable growth of high-quality polycrystalline mos2 monolayers on sio2 with tunable grain sizes,* ACS Nano **8**, 6024 (2014).

[29] M. V. Bollinger, J. V. Lauritsen, K. W. Jacobsen, J. K. Nørskov, S. Helveg, and F. Besenbacher, *One-dimensional metallic edge states in* mos_2, Phys. Rev. Lett. **87**, 196803 (2001).

[30] J. A. Hachtel, J. C. Idrobo, and M. Chi, *Sub-Ångstrom electric field measurements on a universal detector in a scanning transmission electron microscope,* Advanced Structural and Chemical Imaging **4** (2018), 10.1186/s40679-018-0059-4.

[31] J. Taftø, Y. Zhu, and L. Wu, *A New Approach Towards Measuring Structure Factors and Valence-Electron Distribution in Crystals with Large Unit Cells,* Acta Crystallographica Section A **54**, 532 (1998).

[32] Morniroli, Jean-Paul, Cordier, Patrick, Van Cappellen, Éric, Jin Min Zuo, and Spence, John, *Application of the convergent beam imaging (cbim) technique to the analysis of crystal defects,* Microsc. Microanal. Microstruct. **8**, 187 (1997).

[33] P. Yasaei, B. Kumar, R. Hantehzadeh, M. Kayyalha, A. Baskin, N. Repnin, C. Wang, R. F. Klie, Y. P. Chen, P. Král, and A. Salehi-Khojin, *Chemical sensing with switchable transport channels in graphene grain boundaries,* Nature Communications **5**, 4911 (2014).

[34] K. Xu, T. Liang, Z. Zhang, X. Cao, M. Han, N. Wei, and J. Wu, *Grain boundary and misorientation angle-dependent thermal transport in single-layer mos2,* Nanoscale **14**, 1241 (2022).

[35] Y. Ma, H. C. Diaz, J. Avila, C. Chen, V. Kalappattil, R. Das, M.-H. Phan, T. Čadež, J. P. Carmelo, M. C. Asensio, and M. Batzill, *Angle resolved photoemission spectroscopy reveals spin charge separation in metallic mose2 grain boundary,* Nature Communications **8**, 14231 (2017).

[36] L. Wu, M.-G. Han, and Y. Zhu, *Toward accurate measurement of electromagnetic field by retrieving and refining the center position of non-uniform diffraction disks in lorentz 4d-stem,* Ultramicroscopy **250**, 113745 (2023).

[37] S. van der Walt, J. L. Schönberger, J. Nunez-Iglesias, F. Boulogne, J. D. Warner, N. Yager, E. Gouillart, T. Yu, and the scikit-image contributors, *scikit-image: image processing in Python,* PeerJ **2**, e453 (2014).

[38] V. B. Ozdol, C. Gammer, X. G. Jin, P. Ercius, C. Ophus, J. Ciston, and A. M. Minor, *Strain mapping at nanometer resolution using advanced nano-beam electron diffraction,* Applied Physics Letters **106**, 253107 (2015).

[39] G. Wang, Y.-P. Wang, S. Li, Q. Yang, D. Li, S. T. Pantelides, and J. Lin, *Engineering the crack structure and fracture behavior in monolayer mos2 by selective creation of point defects,* Advanced Science **9**, 2200700 (2022).

[40] T. C. Pekin, C. Gammer, J. Ciston, A. M. Minor, and C. Ophus, *Optimizing disk registration algorithms for nanobeam electron diffraction strain mapping,* Ultramicroscopy **176**, 170 (2017), 70th Birthday of Robert Sinclair and 65th Birthday of Nestor J. Zaluzec PICO 2017 – Fourth Conference on Frontiers of Aberration Corrected Electron Microscopy.

[41] D. Johnstone, P. Crout, C. Francis, M. Nord, J. Laulainen, S. Høgås, E. Opheim, E. Prestat, B. Martineau, T. Bergh, N. Cautaerts, H. W. Ånes, S. Smeets, V. J. Femoen, A. Ross, J. Broussard, S. Huang, S. Collins, T. Furnival, D. Jannis, I. Hjorth, E. Jacobsen, M. Danaie, A. Herzing, T. Poon, S. Dagenborg, R. Bjørge, A. Iqbal, J. Morzy, T. Doherty, T. Ostasevicius, T. I. Thorsen, M. von Lany, R. Tovey, and P. Vacek, *pyxem/pyxem: v0.19.1,* (2024).

[42] K. Gołasa, M. Grzeszczyk, R. Bożek, P. Leszczyński, A. Wysmołek, M. Potemski, and A. Babiński, *Resonant raman scattering in mos2—from bulk to monolayer,* Solid State Communications **197**, 53 (2014).

[43] R. Egerton and P. Crozier, *The effect of lens aberrations on the spatial resolution of an energy-filtered tem image,* Micron **28**, 117 (1997).

8

Conclusion & Outlook

In this thesis, we have presented an extensive investigation of the fascinating properties of TMD nanomaterials, focusing on MoS_2 nanostructures with non-trivial morphologies beyond the planar configuration. We have demonstrated the feasibility of novel approaches for fabricating and subsequently characterizing TMD materials in non-standard morphologies that host phenomena absent from the conventional flat 2D geometry. This foray into TMD nanomaterials in complex, three-dimensional configurations significantly broadens the scope of TMD material science, enriching our toolkit for tailoring their physical properties and leading to novel strategies to enhance their functionalities.

Our systematic exploration of the growth mechanisms of v-MoS_2 contributes to the improved understanding of the dynamics underlying the synthesis MoS_2 in non-standard configurations. In chapter 3, we demonstrate the suitability of a two-step chemical vapor deposition (CVD) process that consistently produces v-MoS_2 over large areas and with excellent thickness control by directly sulfurizing a thick pre-deposited layer of the transition metal molybdenum (Mo). The resulting nanosheets propagate downwards from beneath the top surface of the Mo seed layer. We confirm the vertical nature of the nanosheets through Raman spectroscopy combined with a cross-sectional analysis using TEM. This TEM-based cross-sectional inspection provides insights into the diffusion-limited formation of the vertical nanosheets. It enables the determination of the activation energy required for the sulfur diffusion process at temperatures above 600 °C.

These v-MoS_2 nanosheets are characterized by a much higher density of exposed edge sites than the planar 2D configuration. In chapter 3, we show that these exposed edges contribute to a marked increase in the non-linear optical (NLO) response of these v-MoS_2 nanosheets. Specifically, we demonstrate an order of magnitude stronger NLO response than a horizontally oriented MoS_2 nanosheet taken as a reference. This enhanced NLO response underscores the potential of v-MoS_2 nanosheets for nanophotonic device applications.

The insights provided by our study of the growth dynamics of v-MoS_2 nanosheets were also crucial for the fabrication of MoS_2 nanopillars with precise control over the location and the pitch of the nanopillars [1]. Also, for this material configuration, a significantly enhanced NLO response is obtained, which, thanks to the nanopillar geometry, becomes highly localized at the wafer scale. Therefore, this represents a significant step towards developing scalable and efficient nanophotonic devices. Indeed, the ability to localize the strong NLO response precisely opens up new avenues for applying these materials in various optical technologies, including lasers, modulators, and sensors, thereby expanding the functional capabilities of TMD-based devices.

The enhancement in the intensity of the NLO response, together with the ability to spatially localize this response, highlights the excellent optical properties of v-MoS_2. Several potential use cases can be considered for the v-MoS_2 nanosheets. In particular, the semiconducting properties of MoS_2 make it an excellent candidate to replace silicon in field-effect transistors. The two-step synthesis of the v-MoS_2 nanosheets always results in a small amount of the Mo seed layer un-sulfurized. This layer can serve as the metallic back contact, with an improved contact resistance [2–4]. When combined with standard

lithography techniques, one can also prevent the sulfurization of certain regions at the top of the Mo seed layer, which can serve as the top contact. Therefore, provided with top and bottom contacts, the v-MoS_2 nanosheets could be deployed as a back-gated FET.

As discussed in chapter 3, the v-MoS_2 nanosheets fabricated in this thesis possess a high density of exposed edge sites. These edge sites are chemically active and the main contributor to, for instance, hydrogen evolution reactions (HER). The two-step synthesis of v-MoS_2 nanosheets on the wafer scale presented in this work could represent a low-cost and environmentally-friendly alternative to the platinum anodes commonly used in HER [5, 6].

A cornerstone of the results presented in this thesis the application of STEM analyses to characterize TMD materials. More specifically, we utilize four-dimensional STEM (4D-STEM) to obtain precise information on the properties of intricately engineered TMDs, which were previously inaccessible by conventional STEM imaging techniques. In chapter 4, we lay the theoretical groundwork needed for the analysis of TMD nanomaterials through 4D-STEM measurements to achieve atomic-scale spatial resolution over micrometer-sized specimens.

Building upon this foundation, as demonstrated in chapters 5 and 6, our strategy realizes a novel approach suitable to reveal strain patterns in complex TMD nanostructures using 4D-STEM. In particular, mapping strain with nanometer precision over micrometer-sized nanostructures is a task that traditional methods have struggled to accomplish. By addressing these challenges, this thesis introduces a comprehensive methodology that enhances our ability to decode the intricate details of strain within nanostructured TMD materials. This further contributes to our understanding of the critical relationship between nanostructure, strain, and material functionality.

As a proof of concept, we extended in chapter 6 our strain characterization methodology to include heterostructured materials and twisted layers configurations, demonstrating the versatility of our approach. This expansion elucidates the complex characterization challenges posed by these advanced structures. By leveraging 4D-STEM, we have refined the accuracy of strain mapping at the nanoscale and enhanced our understanding of the structural dynamics within complex 2D nanostructures. Given that strain within nanostructures is known to dramatically influence material properties, including electronic, optical, and mechanical behaviors, the progress achieved in his thesis regarding robust strain mapping using 4D-STEM is crucial for strain engineering in TMD materials.

Further expanding the `StrainMAPPER` analysis framework, we investigated the possible effects responsible for shifts in the intensity distribution of convergent beam electron diffraction (CBED) patterns in chapter 7. This study's goal was to determine whether 4D-STEM measurements can be deployed to access electric field measurements in TMD materials. We highlight how progress in charting the phenomena underlying variations in the measured CBED patterns, thoroughly investigated in chapter 7, opens new pathways for characterizing this type of materials. By disentangling the contributions of local electric fields from crystal misalignments, our results contribute to ongoing efforts toward understanding the effects of crystal defects and local heterogeneity on TMD material properties. In particular, these investigations have been instrumental in identifying

grain boundaries in bulk InSe using the Center of Mass method. Such insights are invaluable for developing materials with optimized performance, such as defect-engineered semiconductors for quantum computing and novel catalysts for chemical synthesis.

In addition to the scientific advancements discussed so far, the results presented in chapters 6 and 7 have been possible by developing an open-source Python framework available to the broader scientific community. This framework is composed of two tools: `StrainMAPPER`, which encompasses the techniques necessary for the 4D-STEM strain mapping technique detailed in chapters 5 and 6, and the `EMPAD GUI` (Graphical User Interface). The latter is the tool that we used to visualize the 4D-STEM data collected in this work. Both tools, designed to facilitate the advanced characterization techniques explored in this thesis, are released with comprehensive documentation to ensure their accessibility and ease of use for other researchers.

The `StrainMAPPER` and `EMPAD GUI` tools are under active development, and several improvements are underway. Currently, `StrainMAPPER` cannot distinguish crystal planes with relative twist angles smaller than a minimum value. This limitation arises due to the limited pixel density of currently available 4D-STEM detectors. However, this bottleneck could be circumvented by applying advanced upscaling techniques to the 4D-STEM dataset. Once this improvement is implemented, `StrainMAPPER` will be able to map the twist angle between two single layers of a 2D heterostructure, thus contributing to the emerging field of twisttronics [7, 8]. Similarly, the `EMPAD GUI` functionality can be extended to the ptychography imaging technique. Using 4D-STEM ptychography combined with the `EMPAD GUI` will make it possible to acquire reconstructed images with subatomic resolution, advancing the capabilities of probe-corrected and regular STEM alike [9, 10].

In the future, the continued development of these characterization techniques and the insights they provide will be crucial for designing next-generation materials. The ability to manipulate and understand new quantum materials, such as TMDs, at the atomic scale will pave the way for innovations in numerous fields, including sustainable energy solutions, information technology, energy-efficient electronics, and healthcare.

REFERENCES

[1] L. Maduro, M. Noordam, M. Bolhuis, L. Kuipers, and S. Conesa-Boj, *Position-controlled fabrication of vertically aligned mo/mos2 core–shell nanopillar arrays,* Advanced Functional Materials **32**, 2107880 (2022).

[2] J. Kang, W. Liu, and K. Banerjee, *High-performance MoS2 transistors with low-resistance molybdenum contacts,* Applied Physics Letters **104**, 093106 (2014).

[3] J.-H. Lee, J. Song, D. H. Shin, S. Park, H. R. Kim, S.-P. Cho, and B. H. Hong, *Gradual edge contact between mo and mos2 formed by graphene-masked sulfurization for high-performance field-effect transistors,* ACS Applied Materials & Interfaces **13**, 54536 (2021).

[4] J. Kwon, C. J. Delker, D. B. Janes, C. T. Harris, and S. R. Das, *Molybdenum contacts to mos2 field-effect transistors: Schottky barrier extraction, electrical transport, and low-frequency noise,* physica status solidi (a) **217**, 1900880 (2020).

[5] J. Zhang, H. Yu, W. Chen, X. Tian, D. Liu, M. Cheng, G. Xie, W. Yang, R. Yang, X. Bai, D. Shi, and G. Zhang, *Scalable growth of high-quality polycrystalline mos2 monolayers on sio2 with tunable grain sizes,* ACS Nano **8**, 6024 (2014).

[6] D. Voiry, M. Salehi, R. Silva, T. Fujita, M. Chen, T. Asefa, V. B. Shenoy, G. Eda, and M. Chhowalla, *Conducting mos2 nanosheets as catalysts for hydrogen evolution reaction,* Nano Letters **13**, 6222 (2013).

[7] N. P. Kazmierczak, M. Van Winkle, C. Ophus, K. C. Bustillo, S. Carr, H. G. Brown, J. Ciston, T. Taniguchi, K. Watanabe, and D. K. Bediako, *Strain fields in twisted bilayer graphene,* Nature Materials **20**, 956 (2021).

[8] Y. Cao, V. Fatemi, S. Fang, K. Watanabe, T. Taniguchi, E. Kaxiras, and P. Jarillo-Herrero, *Unconventional superconductivity in magic-angle graphene superlattices,* Nature **556**, 43 (2018).

[9] Y. Jiang, Z. Chen, Y. Han, P. Deb, H. Gao, S. Xie, P. Purohit, M. W. Tate, J. Park, S. M. Gruner, V. Elser, and D. A. Muller, *Electron ptychography of 2D materials to deep sub-ångström resolution,* Nature **559**, 343 (2018).

[10] Z. Chen, Y. Jiang, Y. T. Shao, M. E. Holtz, M. Odstrčil, M. Guizar-Sicairos, I. Hanke, S. Ganschow, D. G. Schlom, and D. A. Muller, *Electron ptychography achieves atomic-resolution limits set by lattice vibrations,* Science **372**, 826 (2021).

CURRICULUM VITÆ

Maarten BOLHUIS

11-10-1990	Born in Utrecht, The Netherlands

EDUCATION

2003–2009	**Voortgezet Wetenschappelijk Onderwijs** St. Bonifatiuscollege, Utrecht, The Netherlands
2010–2013	**Bachelor of Engineering Physics** The Hague University of Applied Sciences, Delft, The Netherlands *Thesis:* Analysing structural changes in multilayer mirrors after thermal loading with grazing incidence x-ray reflectometry *Supervisor:* Dr. Ir. R.W.E. van de Kruijs
2015–2019	**Master of Science in Applied Physics** Delft University of Technology, Delft, The Netherlands *Thesis:* Synthesis of horizontal and vertical molybdenum disulfide nanosheets using chemical vapor deposition *Supervisor:* Dr. S. Conesa-Boj
2019–2024	**Ph.D. in Physics** Delft University of Technology, Delft, The Netherlands *Thesis:* Exploring Van der Waals Materials: from Nanofabrication to Strain Mapping using Transmission Electron Microscopy *Promotors:* Dr. S. Conesa-Boj and Prof. dr. L. Kuipers

LIST OF PUBLICATIONS

8. **M. Bolhuis**, J.J.M. Sangers, A. Brokkelkamp, S. Conesa-Boj, *From Artefactual Edge Effects to Grain Boundaries Identification in van der Waals Materials with Pixelated Detectors*, in preparation (2025).

7. **M. Bolhuis**, S.E. van Heijst, J.J.M. Sangers, S. Conesa-Boj*4D-STEM Nanoscale Strain Analysis in van der Waals Materials: Advancing beyond Planar Configurations* Small Sci., 4: 2300249 (2024).

6. S. E. van Heijst, **M. Bolhuis**, A. Brokkelkamp, J. J. M. Sangers, S. Conesa-Boj, *Heterostrain-Driven Bandgap Increase in Twisted WS2: A Nanoscale Study.* Adv. Funct. Mater. 34, 2307893 (2024).

5. **M. Bolhuis**[†], K. Prateek[†], A. Ben Hamida, D. Scholma, S. Conesa Boj, J. Aarts,*Magnetotransport properties of CrO2 nanowires fabricated by selective area growth* Journal of Physics and Chemistry of Solids, Volume 178 (2023).

4. L. Maduro, M. Noordam, **M. Bolhuis**, L. Kuipers, S. Conesa-Boj, *Position-Controlled Fabrication of Vertically Aligned Mo/MoS2 Core–Shell Nanopillar Arrays* Adv. Funct. Mater. 32, 2107880 (2022).

3. M. W. H. Garming, **M. Bolhuis**, S. Conesa-Boj, P. Kruit, and J. P. Hoogenboom, *Lock-in Ultrafast Electron Microscopy Simultaneously Visualizes Carrier Recombination and Interface-Mediated Trapping* J. Phys. Chem. Lett., 11, 20, 8880–8886 (2020).

2. **M. Bolhuis**, J. Hernandez-Rueda, S. E. van Heijst, M. Tinoco Rivas, L. Kuipers and S. Conesa-Boj, *Vertically-oriented MoS2 nanosheets for nonlinear optical devices*, Nanoscale, 12, 10491-10497 (2020).

1. M.O. Cichocka, **M. Bolhuis**, S.E. van Heijst, and S. Conesa-Boj, *Robust Sample Preparation of Large-Area In- and Out-of-Plane Cross Sections of Layered Materials with Ultramicrotomy*, CS Appl. Mater. Interfaces, 12, 13, 15867–15874 (2020).

[†]Equally contributing

ACKNOWLEDGEMENTS

I want to start by acknowledging all the support and help that **Sonia Conesa-Boj** has given me during PhD career. **Sonia**, as my promotor, you assisted me during every moment. Your door was always open for us to discuss a challenging problem, find support in challenging times, or just for some fun and relaxation. But what you did for me goes beyond your significant contributions to my PhD trajectory. Getting my Master of Applied Physics degree was long and bumpy. Admittedly, I could have made better, or at least different, choices along the way. However, after struggling to find my footing during the master's courses, I started to wonder if I had made the right choice to pursue a master's degree in physics altogether. I already knew I most likely would not pursue a career in academia. In fact, with my track record, I would not get the opportunity anyway. While my interest in physics, specifically nanoscale physics, never waivered, I started to doubt if I had enough affinity for the subject. Maybe I should have listened to the advice I received after my first year and quit Physics.

You, however, played a significant role in restoring my faith in myself. First, during the Master's course, when you graded my final report and you mentioned to me that it was actually of the level you would have expected of me. This trust gave me a well-needed confidence boost at the time. This trust was extended when you agreed to supervise my graduation project. The project only lasted 8 months, but in that time, you and the rest of the, back then, very small Conesa-Boj Lab made me feel like an integral part of the team. The real shocker came when you called me into your office and offered me a PhD position in your Lab. I never contemplated doing a PhD before because I thought no one would ever offer me the opportunity. It took me a long time to decide if doing a PhD was right for me, and I know I kept you waiting for a long time. But the fact that you convinced me to grab this opportunity with both hands shows what a good teacher and motivator you are. I will be forever grateful to you for giving me this opportunity and for you to be a true mentor during the early stages of my career. Even though we both knew that a long-lasting academic career was not in the cards for me, you still tried to develop me into a well-rounded researcher. I will carry those skills with me for the rest of my life. Thank you!

Choosing the PhD life was not an easy decision for me. But **Miguel**, you were definitely part of my decision to go for it. You were a fantastic daily supervisor during my graduation project. I learned a lot from you; you always supported me, even when I made mistakes. I was mortified when I accidentally dropped an entire case of TEM grids, scrambling specimens of different projects together. But you saw it as a learning opportunity to train me on using the Titan sample holder. You showed me the importance of paying attention to others by always asking how I was doing or how my weekend went. Ever since I have tried to mimic this simple act of kindness with others. I was sad to see you

go, but you should know that your parting words of wisdom played a significant role in my decision to accept the PhD position. Finally, I'm truly honored to have you as one of my committee members, as this is a full-circle moment after all these years.

I would also like to thank the rest of my doctoral committee: **Prof. Dr. P.G. Steeneken**, **Prof. Dr. Y.M. Blanter**, **Dr. A. Castellanos-Gómez**, and **Dr. A.A.F.M. Artaud** who were kind enough to accept the invitation to be part of this special moment. In particular, I would like to thank my promotor **Kobus**. As head of the department, you were always very busy, but you always made time for me when needed. You used the mandatory PhD cycle meetings not to grill me on my progress but rather to teach me how to deal with the ever-changing complexities of research. You and **Sonia** made a great tag team! I will never forget how you passionately explained the necessity of keeping the big-money companies out of the Kavli NanoLab to ensure that independent research can thrive with unrestricted access to a top-notch facility.

A big thank you to all the CBL team members I enjoyed working with over the past years. First and foremost, there is my partner in crime. **Sabrya**, you joined the CBL team right after me as the third-ever Master's student in the group. Even though we had not met each other before, it seemed like we had worked together for ages. I had never met somebody I could work together with so well. Taking over critical experiments in a crunch or filling in for each other in group projects seemed like second nature. This dynamic continued till the very end, even during the tough times at the end of the PhD trajectory. Thank you for all your support over the years. I'm truly grateful that you will support me one last time as my Paranymph. The same goes for my second Paranymph, **Abel**. Your calming presence in the group was a welcome contrast to the sometimes more hotheaded group members. You never let your emotions get too high or too low. This quality made you a joy to work with and an outstanding student during the many hours we spent together at the FIB and the Titan. At the end of my tenure, we shared an experience that we will most likely never forget. Stuck in the airport in Madrid, without a passport, and only a bit of Spanish between us. It was a challenging situation, but by sticking our heads together, we arrived home safe and sound. Thank you for accepting to be my Paranymph, and good luck with the end of your PhD career.

Thank you to **Chris** and **Jeroen**, the newer members of the CBL team. You both endeavored to take on topics near and dear to my heart. **Chris**, you have become the new expert on the Kavli Nanolab cleanroom and our humble CVD setup. I hope **Sabrya** and I have made it easy for you to pick up where we left off. I have enjoyed mentoring and working with you. I have complete faith in your ability to carry our work forward to the next level. **Jeroen**, you joined the group for a second time at the end of my PhD career. As a Master's student, you made an immediate impact by adapting the existing EMPAD framework that I mainly had developed to suit your specific needs. The ideas you brought forward were simple and elegant. Exactly what we needed to take the next step in the group's understanding of the EMPAD. I'm very happy you decided to join the CBL group as a PhD student. I hope you will carry the EMPAD framework forward. Thank you as well to all other CBL members I had the pleasure working with: **Stef**, **Magdalena**, **Assunta**,**Steven**, **Philip**, **Stijn**, **Ruben**, **Yashoda**, **Isabel**, **Laurien**, **Rose**, and **Helena**. Thank you as well to **Erika**, who was always ready to support us with any needs we may have had.

For almost five years, I spent my time at the TU Delft in one of the more unique offices in our department. Room F190 always felt a bit different compared to the rest. As a master's student, I had the pleasure of being located in that office instead of the isolated Master's office on the 3rd floor. At least until **Joris** and **Brecht** arrived, and I was relegated back to the 3rd floor. Luckily, I was welcomed back to the same room as a PhD student mere months later. With six people from three different groups in one room, it was bound to be one of the more vibrant offices in the department. **Joris**, **Brecht**, **Dima**, **Jorrit**, **Ulderico**, **Thijs**, **Gesa**, and **Lugi**; it was a pleasure to share the many high and some low lights with you. It was always fun and interesting to engage with each other and learn about each other's research. The one thing I never understood was why you were all so set on the incomprehensible desk setup. Even the university-wide COVID protocols were no match for the illogical placement of our desks! In fact, just before I left the TU Delft, I discovered that **Luigi** had been sitting on the wrong side of his desk all this time.

Speaking of **Luigi**, you were the only PhD student who had joined the group before me. You have forged the path that we all still walk on. Seeing you transition from your simulation work to a true cleanroom warrior was amazing. By the end, you were the expert on all matters of fabrication. Your infamous nanopillars still dawn the halls of QN. We had a lot of fun over the years, but our trip to Upsala I will always remember. It was not the most vibrant city, but we found a place with relatively cheap beer and made due. To this day, I have never met anyone else with the same sleeping habits as you. Just so you know, a cushion is to sleep on, not under. Oh, and don't forget; you are 7 days older than me, Grandpa.

I want to thank all members of the Quantum Nanoscience department with whom I had the pleasure of interacting over the years. There are too many to mention here, but I want to highlight one group in particular. The members of the Kuipers lab always felt like an extension of our own. You probably get that when the two group leads work so well together. Thank you, **Thijs**, **Irina**, **Sonakshi**, **Marc**, and **Daniel**, for all the fun interactions along the way. I also want to thank the support staff of the Kavli Nanolab and, in particular, **Hozanna**, who always supported us when the FIB was acting up. The same goes for **Frans**, who was always ready to solve any issue we faced with the Titan microscope.

I want to thank everyone who stood by me during the long and sometimes difficult road toward completing my PhD. My friends from **Club Mach** always showed tremendous interest in my work while also making fun of my simple PhD life. My teammates at **Groen-Geel**, that wondered if I ever stopped being a student at the TU Delft. And my fellow board members at Groen-Geel, who always believed in my success.

Finally, I want to thank my entire family. First and foremost, my parents. **Pap**, **Mam**, thank you for always believing in me. You supported me when I had to switch to HBO and again when I switched back to the university. Even though it took me more than nine years to complete my Masters degree, you were again really supportive when I accepted the PhD position. You have always allowed me to do what I enjoyed most. I'm forever grateful that you allowed me to develop into a responsible adult at my own pace and never put too much pressure on me to develop faster.

Thank you to the rest of my family and extended family for always showing an interest in what I did. Thanks to my sister **Isabelle** and my nephew **Bram** for always asking about my progress and ensuring that I still enjoyed my work. Thank you to **Tom** and **Pascal** for keeping those two in check. Thank you to my uncle **SiedsJan**; I will hold you to our promise that we share one of our first unassisted walks in each other's homes. Thank you, **Reinette**, **Marcel**, **Paul**, **Mariëlle**, **Fleur**, and **Niels**, for welcoming me into your family and being supportive during my entire PhD trajectory. And thank you to those family members we lost during my PhD. **Marianne**, we will forever miss you, and I wish I could have shared this day with you. **Koos**, even in your final months, you showed a genuine interest in my work, and you could not hide how proud you were of me. I made you a promise to share my thesis with you once it was finished. Unfortunately, I could not keep my promise due to all the delays. But I'm sure you would still be proud of me if you had had the chance to read it.

To my dear **Isabelle**, a simple thank you is not enough to express my gratitude for all your support over the years. You have been with me from the beginning. You have seen all the struggles of the PhD life from close by and were there to catch me when needed. You also had to give up a lot for me to finally complete the PhD. Especially during my last year, I had very little time for you and for us. Long days and weeks made sure to limit what we enjoyed most: being together. I'm so ready to close this chapter and start a new one with you, together, in our new home in Utrecht!

A big thank you to you all!

Maarten Bolhuis,
March 2025

ACRONYMS

- **ABF**: Annular Bright-Field
- **AC**: Armchair
- **ADF**: Annular Dark-Field
- **BCC**: Body-Centered Cubic
- **BF**: Bright-Field
- **CBED**: Convergent Beam Electron Diffraction
- **CBIM**: Convergent Beam Imaging
- **CL**: Camera Length
- **CoM**: Center of Mass
- **CVD**: Chemical Vapor Deposition
- **CPU**: Central Processing Unit
- **EDX**: Energy Dispersive X-ray Spectroscopy
- **EELS**: Electron Energy Loss Spectroscopy
- **EMPAD**: Electron Microscope Pixel Array Detector
- **EWPC**: Exit-Wave Power-Cepstrum
- **FET**: Field Effect Transistor
- **FFT**: Fast Fourier Transform
- **FIB**: Focused Ion Beam
- **FWM**: Four-Wave Mixing
- **GPA**: Geometric Phase Analysis
- **GUI**: Graphical User Interface
- **HAADF**: High-Angle Annular Dark-Field
- **HCL**: Hydrochloric Acid
- **HER**: Hydrogen Evolution Reaction
- **HOLZ**: Higher Order Laue Zone
- **HR**: High-Resolution
- **HRTEM**: High-Resolution Transmission Electron Microscopy
- **LPCVD**: Low-Pressure Chemical Vapor Deposition
- **MOCVD**: Metal-Organic Chemical Vapor Deposition
- **NBED**: Nano Beam Electron Diffraction
- **NLO**: Nonlinear Optics
- **PACBED**: Position-Averaged Convergent Beam Electron Diffraction
- **PANBED**: Position-Averaged Nano Beam Electron Diffraction
- **PED**: Precession Electron Diffraction
- **PL**: Photoluminescence
- **POA**: Phase Object Approximation
- **PSF**: Point Spread Function
- **PVD**: Physical Vapor Deposition
- **SAD**: Selected Area Diffraction
- **SEM**: Scanning Electron Microscopy
- **SFG**: Sum Frequency Generation
- **SHG**: Second Harmonic Generation
- **STEM**: Scanning Transmission Electron Microscopy
- **TEM**: Transmission Electron Microscopy
- **THG**: Third Harmonic Generation
- **TMD**: Transition Metal Dichalcogenides
- **WPOA**: Weak Phase Object Approximation
- **ZA**: Zone Axis
- **ZLP**: Zero-Loss Peak
- **ZOLZ**: Zero Order Laue Zone
- **ZZ**: Zigzag

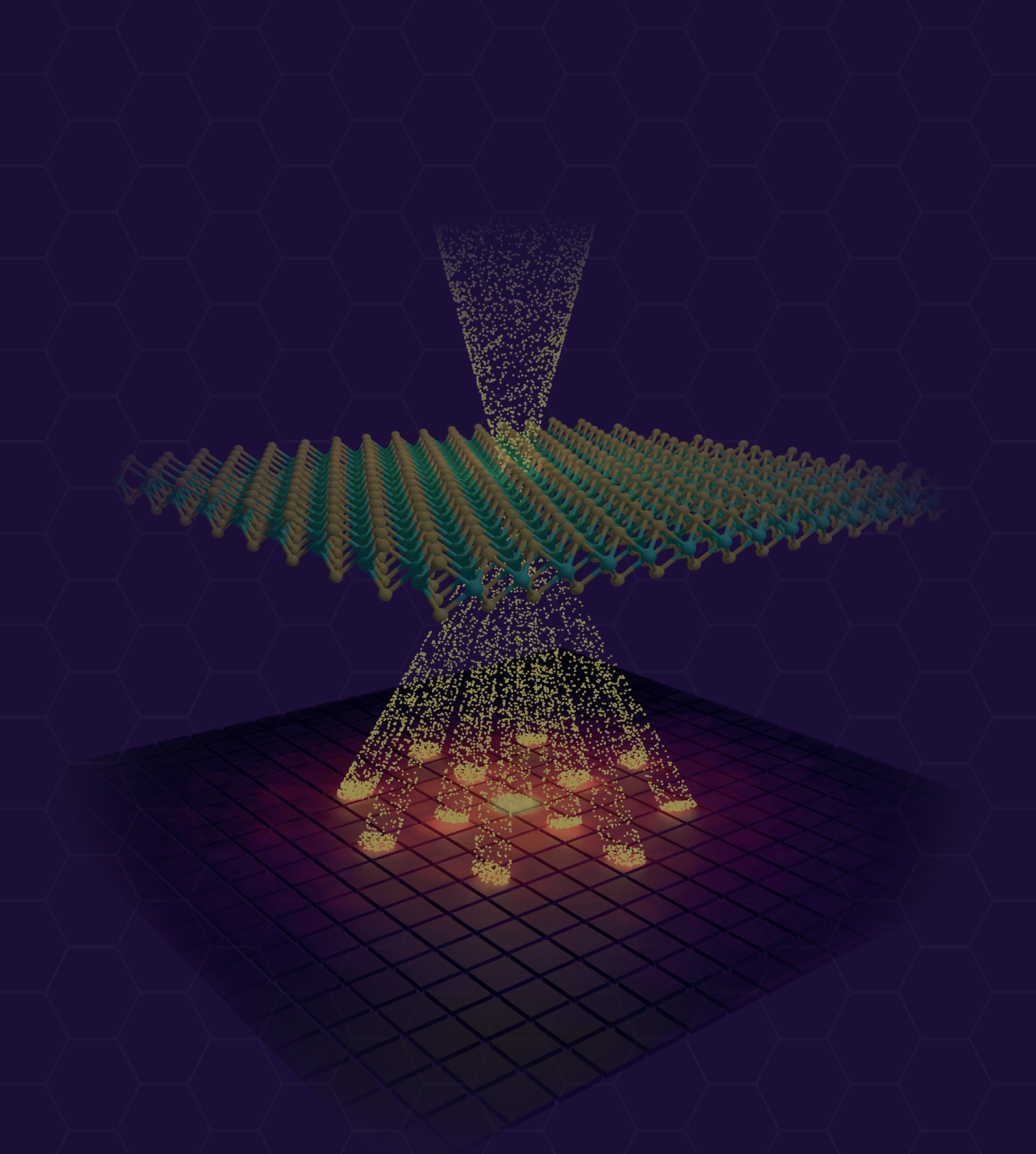

ISBN: 978-94-6384-762-9

TU Delft